INVESTIGATIONS OF THIN FILMS OF RARE EARTH MANGANITES, MAGNETOFERROELECTRICS AND RELATED MATERIALS

A THESIS SUBMITTED FOR THE Ph. D. DEGREE

BY

SACHIN PARASHAR

TO

JAWAHARLAL NEHRU CENTRE FOR ADVANCED SCIENTIFIC RESEARCH

(A Deemed University)

BANGALORE, INDIA

APRIL 2003

STATEMENT

Certified that the work described in this thesis was carried out under our supervision at Jawaharlal Nehru Centre for Advanced Scientific Research, Jakkur, Bangalore, India.

Prof. C N R Rao

Dr. A R Raju

PREFACE

The thesis consists of four parts. Part 1 describes the results of investigations of thin films of rare earth manganites and Part 2 deals with investigations of biferroic manganites. Part 3 discusses the results of investigations of copper and copper-cobalt thin films. Part 4 presents the results of investigations of single crystals of charge ordered rare earth manganites.

Electric-field-induced insulator-metal transitions in the thin films of rare earth manganites $Ln_{1-x}A_xMnO_3$ (Ln = Nd, Pr, Gd and Y and A = Ca and Sr) constitute a major part of Part 1. Particularly noteworthy is the memory effect in the electric-field effects. Broad band noise studies suggest that there is a threshold to the electric-field-induced nonlinear conduction.

Results of the investigations of magnetoferroelectric $YMnO_3$ and $BiMnO_3$ are discussed in Part 2. The co-existence of ferromagnetism and ferroelectricity in the simple perovskite $BiMnO_3$ is of great interest. $BiMnO_3$ is ferromagnetic with a T_C of 105 K and ferroelectric with a Curie temperature of 450 K. It remains ferroelectric down to low temperatures through the ferromagnetic transition. $YMnO_3$ is an antiferromagnet (T_N = 73 K), becoming ferroelectric below 917 K. Dielectric properties of this manganite show novel features.

In Part 3, investigations of thin films of copper, cobalt and copper-cobalt granular alloys are discussed. The last system exhibits significant magnetoresistance.

In Part 4, studies of single crystals of rare earth manganites grown by the floating zone melting crystal growth technique are presented. The studies include electric-field-induced melting of the charge-ordered states.

ACKNOWLEDGEMENTS

I wish to express my sincere gratitude to my teacher and guide, Prof. C N R Rao, FRS, for suggesting the research problems, invaluable guidance and moral support which have been instrumental in shaping me as a research student. I am sure that I will continue to receive the same forever. He has taught me how to work professionally and to present my research in the best manner possible.

I am extremely thankful to my co-guide Dr. A R Raju who helped me in carrying out the experiments. His systematic way of working and excellent knowledge of instrumentation has made it possible for me to complete my work in a short span of time.

I thank Prof. S B Krupanidhi for the generous support and useful discussions I had with him in the last year on the $YMnO_3$ problem.

My sincere thanks to L Sudheendra for his effort in making me understand few of the basic concepts related to my research.

I am thankful to Dr. U V Waghmare for giving me the hang of theory and calculations which are useful for the research, I have carried out and also for his patient hearing.

Thanks to Manipal Academy of Higher Education and the great Pai's for the fellowship they have provided to me.

I thank Prof. S Chandersekharan and Prof. T N Guru Row for teaching the best courses.

I thank Prof. A K Raychaudhuri for the endless copper wires I have been borrowing from his lab.

I thank Prof. G U Kulkarni for his insistence on efficiency.

Thanks to Dr. Govinda Raj for providing latest hot news on science and surroundings.

Thanks to Srinath for the electronics and instrumentation he has been teaching me.

I thank Anil, Basvaraj, Vasu and Srinivas for consistent help in my research work.

Thanks to my friends and batch mates Sameer, Aparna, Abhijit, Smita, Anupama, Urvashi, Becky, Joy, Moshmi, Supriya, Debanshu, Jayant, Subrutho, Navedh for all the tolerance they have to entertain me.

I thank Prof. D D Sarma and his lab for support.

Thanks to Ms. Raina for instrumentation ideas.

Thanks to friends at the Jakkur campus C P, T Lakshmi, Kripa, Leonard, Gautam, Kundu, Pattu, Vaidhya, John, Dhanshree, Jaya, Pushapa and all the fantastic dashing young biologists and flying mechanics.

I specially thank Dr. S. K. Jain for motivating me to study chemistry and Dr. Ashok Mittal for business ideas.

I specially thank Prof. K. V. Sane for giving me the first opportunity to work in his research laboratory in the University of Delhi.

I thank my Pramod Mamaji for teaching the action of work.

I thank my Parents for Affection, Love and Financial Support.

The administration of JNCASR for speedy processing of purchase orders.

Thanks to Rajesh and Shittal of computer lab.

CONTENTS

PART 1

INVESTIGATIONS OF THIN FILMS OF RARE EARTH MANGANITES DEPOSITED BY NEBULIZED SPRAY PYROLYSIS ON SOLID SUBSTRATES

SUMMARY*

Rare earth manganites of the type $Ln_{1-x}A_xMnO_3$ where Ln is a rare earth and A is an alkaline earth have become known for a variety of fascinating properties such as colossal magnetoresistance (CMR), charge ordering (CO) and orbital ordering. Thin films of some of these manganites have been deposited on different solid substrates by nebulized spray pyrolysis. Electronic properties of these films have been investigated.

Thin films of charge-ordered rare earth manganites of the compositions $Nd_{0.5}Ca_{0.5}MnO_3$, $Gd_{0.5}Ca_{0.5}MnO_3$, $Y_{0.5}Ca_{0.5}MnO_3$ and $Nd_{0.5}Sr_{0.5}MnO_3$ have been deposited on Si(100) and $LaAlO_3$(100) substrates by the nebulized spray pyrolysis of organometallic precursors. Small electric fields induce insulator-metal transitions in the films with the resistivity decreasing with increasing current. The I-V characteristics are non-ohmic and show some hysteresis. The transition is attributed to the depinning of the randomly pinned charge solid. These materials also exhibit an interesting memory effect probably due to the randomness of the strength as well as the position of the pinning centers. The current-induced negative differential resistance found in these manganite films could have potential technological applications.

Thin films of charge-ordered manganites, $Pr_{1-x}Ca_xMnO_3$ ($x = 0.3, 0.4$) undergo electric current-induced insulator-metal (I-M) transitions, the transition temperature increasing with the current. The occurrence of I-M transitions in these films without prior laser irradiation is noteworthy. The films show interesting memory effects and

some non-linearity in the I-V characteristics. The magnetic field induced I-M transition in the films is independent of the current employed. At low magnetic fields, or at low currents, resistance oscillations occur due to temporal fluctuations between the resistive states.

Measurements of the dc transport properties and the low-frequency conductivity noise in films of charge-ordered $Nd_{0.5}Ca_{0.5}MnO_3$ grown on Si substrate reveal the existence of a threshold field in the charge-ordered regime beyond which strong nonlinear conduction sets in along with a large broad band conductivity noise. Threshold-dependent conduction disappears as $T \rightarrow T_{co}$, the charge-ordering temperature. This observation suggests that the charge-ordered state gets depinned at the onset of the nonlinear conduction.

Properties of thin films of hole-doped $Pr_{0.6}Ca_{0.4}MnO_3$ and electron-doped $Pr_{0.4}Ca_{0.6}MnO_3$ have been compared. While both are charge-ordered insulators, the hole-doped manganite undergoes a insulator-metal (I-M) transition on the application of magnetic-fields, but the electron-doped manganite does not. Substitution of 3% Cr^{3+} or Ru^{4+} in the Mn site has greater effect on the hole-doped manganite. Electric fields however have similar effects on these manganites, both exhibiting current-induced I-M transitions. The study not only establishes that the mechanism of the I-M transition brought about by electric and magnetic fields be different, but also suggest that the electronic structures of the hole-doped and electron-doped manganites have basic differences.

Thin films of bilayered manganites of the formula $LnSr_2Mn_2O_7$ (Ln = rare earth),were deposited on LAO(100) substrates by nebulized spray pyrolysis, show charge-ordering transitions in the resistivity data. The transition temperatures decrease from 205 K to 185 K as the rare earth ionic radii decrease from Ln = La to Gd. While magnetic fields up to 6T have little effect on the charge ordering transition, small currents prevent the onset of the

charge-ordered state. Furthermore, the resistance decreases markedly with increasing current, with nonlinear behavior, in polycrystalline films deposited on Si(100) substrates.

*Based on this work papers have been published in Appl. Phys. Lett. (1999): Appl. Phys. Lett. (1999): Phys.Rev. B (2000): Solid State Comm. (2000): Int. J. Inorg. Mater. (2000): J. Phys. Chem. Solids (2001)

1.1 A BREIF OVERVIEW OF RARE EARTH MANGANITES

1.1.1 Introduction

Rare earth manganites of the type $Ln_{1-x}A_xMnO_3$ where Ln is a rare earth and A is an alkaline earth have become known for a variety of fascinating properties such as colossal magnetoresistance (CMR), charge ordering (CO) and orbital ordering[1-5]. While some of these properties were known for nearly 50 years[6], a full appreciation of their importance has been a more recent development[7]. The sensitivity of the CMR in these oxide materials is not found in bulk metallic systems or metallic multilayers (GMR materials[8]) even at low temperatures. These remarkable properties have led to a proper understanding of concepts such as double exchange[9] and Jahn-Teller polarons[10]. The rich magnetic and electronic phase diagram of this family of compounds drives the research on these systems.

The perovskite manganites originally became popular because of the discovery of colossal magnetoresistance[11] (CMR). CMR and related properties essentially arise from the double-exchange mechanism of electron hopping between the Mn^{3+} ($t^{3}_{2g}\ e^{1}_{g}$) and Mn^{4+} ($t^{3}_{2g}\ e^{0}_{g}$) ions. In this mechanism, lining up of spins (ferromagnetic alignment) of the incomplete e_g orbitals of the adjacent Mn ions is directly related to rate of hopping of the electrons, giving rise to an insulator-metal transition in the material at ferromagnetic curie temperature, T_C. In the ferromagnetic phase ($T< T_C$), the material becomes metallic, but is an insulator in the paramagnetic phase ($T>T_C$). In the insulating phase, a Jahn-Teller distortion associated with the Mn^{3+} ions favors the localization of electrons. Charge ordering of the Mn^{3+} and Mn^{4+} ions competes with double-exchange and promotes insulating behavior and antiferromagnetism. It may be recalled that the Mn^{3+}-

O^{2-}- Mn^{3+} and Mn^{4+}- O^{2-}- Mn^{4+} superexchange interaction[12], through the e_g orbitals, is antiferromagnetic. Although charge ordering in the rare earth manganites was investigated by Jirak[13] et al. as early as 1985, the subject has received renewed attention recently.

Charge ordering occurs through a fairly wide range of compositions of $Ln_{1-x}A_xMnO_3$, provided the Ln and A ions are not too large. Large Ln and A ions (e.g. La, Sr) favor ferromagnetism and metallicity, whereas the smaller ones (e.g. La, Ca, or Pr, Ca) favor charge ordering. Charge ordering and spin (antiferromagnetic) ordering may or may not occur at the same temperature. Besides, the Mn^{3+} (d_{Z^2}) orbitals and the associated lattice distortions develop long-range order. Such orbital ordering may or may not occur with charge ordering in the manganites, but it generally accompanies antiferromagnetic (spin) ordering.

All the above properties and phenomena are interesting because they can be easily manipulated by the application of different tools of energy such as magnetic field, electric-field and electromagnetic radiation. Such an unconventional control of the state of matter becomes possible through the properties associated with the *strongly correlated electron*[14] in the manganites. Correlated electrons in solids bear multiple degrees of freedom not only in charge sector but also in the spin and orbital sectors. The mutual interaction between these sectors can produce complex phases and phenomena such as liquid-like, crystal-like, liquid-crystal-like states of electrons and electronic phase separation or pattern formation, as typical of complex system. The electronic/magnetic phase of a material containing correlated electrons can be controlled in unconventional

ways (Fig.1.1) and in an ultrafast means (at teraherz frequencies), thereby enabling correlated electron technology (CET) to provide a seed for a new class of electronics.

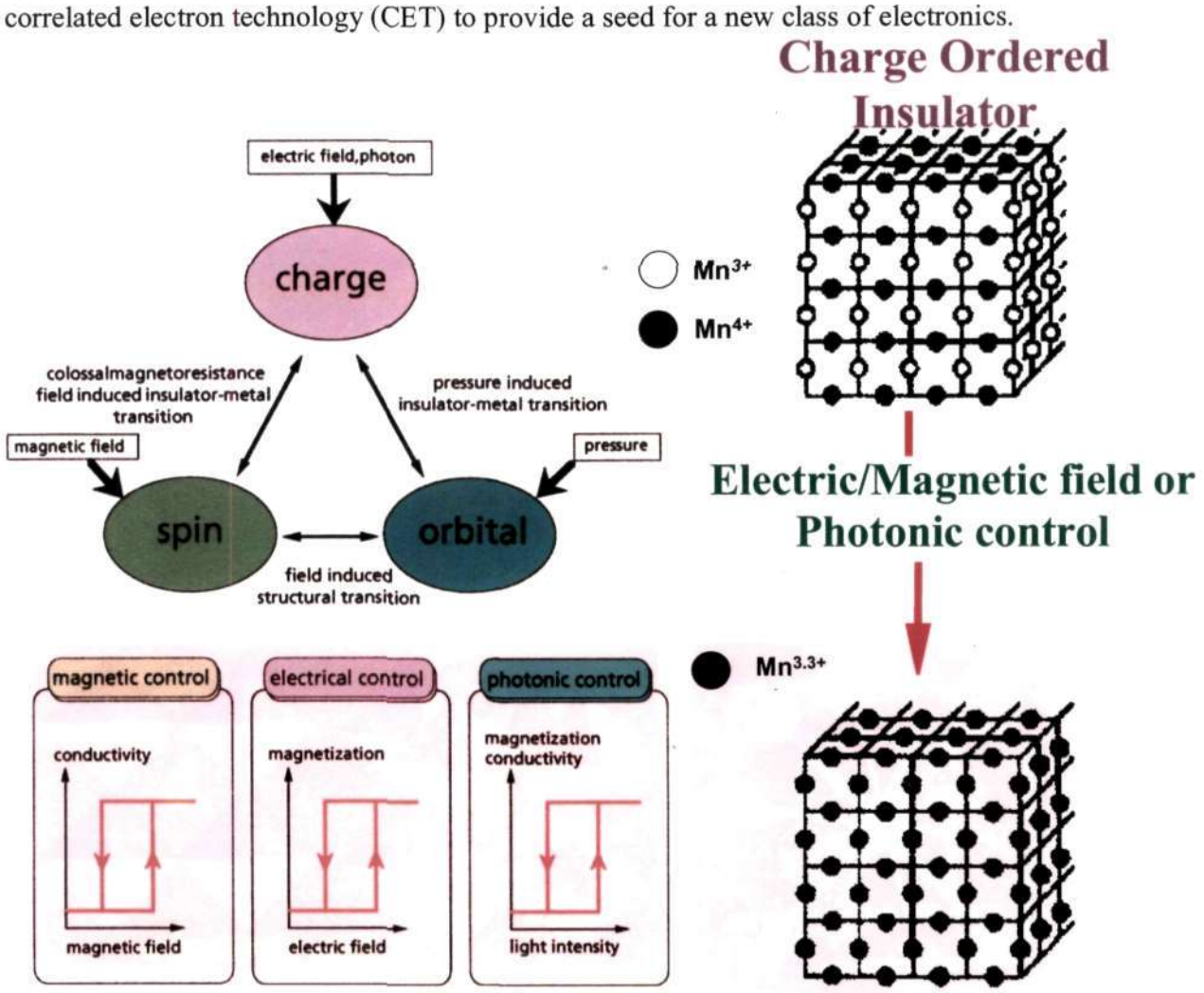

Fig.1.1 Spin-charge orbital coupling for correlated d electron systems (upper) and unconventional phase control (lower). [Taken from ref. 14]

1.1.2 Structural aspects of rare earth manganites

Rare earth manganites of the type $Ln_{1-x}A_xMnO_3$ where Ln is a rare earth and A is an alkaline earth crystallize in perovskite ABO_3 structure as shown the fig.1.2. The cation at the A-site is 12 coordinated and the one in the B-site is 6 coordinated with an octahedral geometry. In an ideal cubic perovskite structure where the atoms are just touching one

another, the B-O distance is equal to a/2 and the A-O distance is $\sqrt{2}(a/2)$ where a is the cube unit cell length and the following relation of radii of ions holds: $(R_A + R_O) = \sqrt{2}(R_B + R_O)$. Goldschmidt[15] found that the perovskite structure is retained in ABO_3 compounds even when this relation is not exactly obeyed and defined a tolerance factor, t, as

$$t = (R_A + R_O)/\sqrt{2}(R_B + R_O)$$

For the ideal perovskite structure, t is unity. The perovskite structure is, however, found for lower values of t ($\sim 0.75 < t \leq 1$) also. In such cases, the structure distorts to tetragonal, rhombohedral or orthorhombic symmetry. This distortion arises from the smaller size of the A ion which causes a tilting of the BO_6 octahedra in order to optimize A-O bonding. The average radius of A-site cations $<r_A>$ plays an important role in determining the

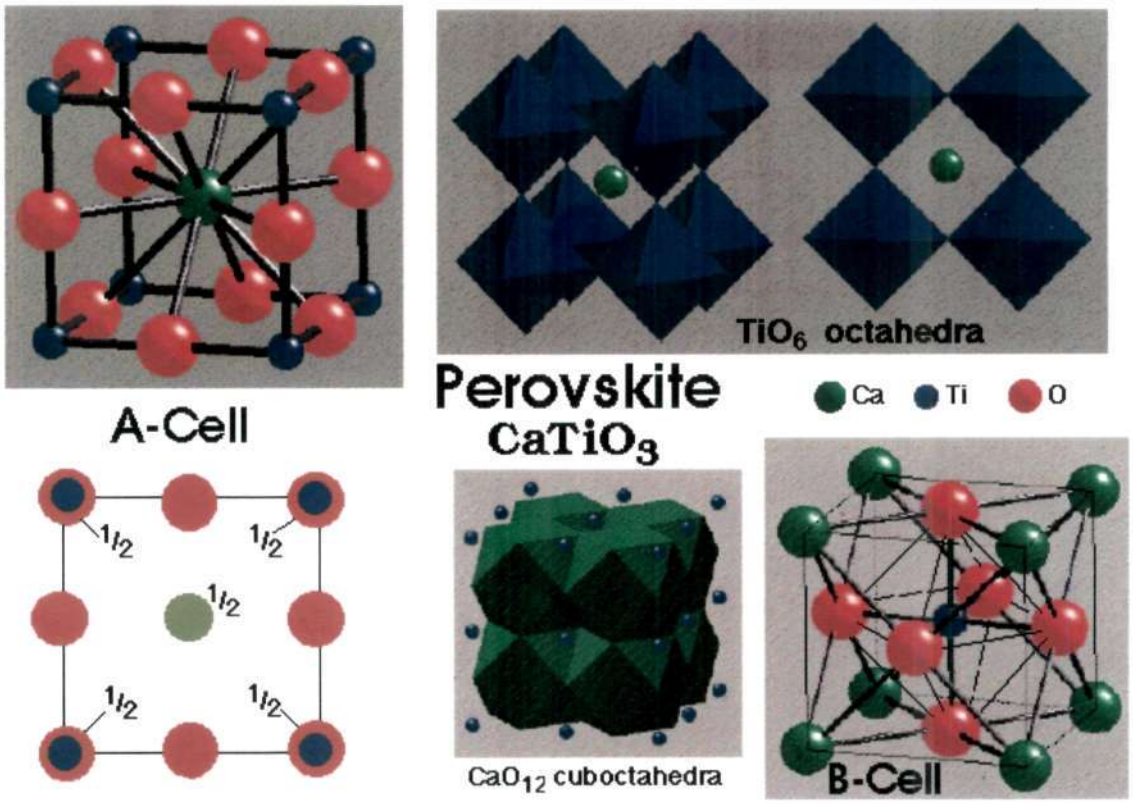

Fig.1.2 Perovskite Structure.

properties of these compounds as it controls the Mn^{3+}- O^{2-}- Mn^{4+} bond angle, which in turn determines type of magnetic ordering and electronic properties. One of the simplest examples where this effect is clearly visible is in the series of charge-ordered manganites such as $Ln_{0.5}A_{0.5}MnO_3$ where with decreasing $<r_A>$ the ferromagnetic state is less pronounced. This happens because the Mn^{3+}- O^{2-}- Mn^{4+} angle starts changing with radius of the A-site cation $<r_A>$.

1.1.3 Magnetic and Electronic Properties

Magnetic properties of rare earth manganites are basically governed by two major factors .i.e. the ratio of Mn^{3+} and Mn^{4+} ions and the Mn^{3+}- O^{2-}- Mn^{4+}, Mn^{3+}- O^{2-}- Mn^{3+} and Mn^{4+}- O^{2-}- Mn^{4+} interactions in the system. Based on these interactions two major type of exchange processes became possible.

a) Double exchange mechanism

b) Super exchange mechanism

(a) Double exchange mechanism

In the perovskite structure, the manganese ion is in an octahedral environment of oxygen atoms and due to crystal-field symmetry, the d-orbitals are split into lower t_{2g} levels and upper e_g levels as shown in fig.1.3. The valence state of manganese as mentioned earlier is either in 3+ or in 4+ state corresponding to the electronic configuration $t^3_{2g}\, e^1_g$ (S = 2) and $t^3_{2g}\, e^0_g$ (S = 3/2). The Mn^{3+} ion is however a Jahn-Teller ion and therefore the degeneracy of the e_g states is lifted. The e_g orbital (say $3z^2$-r^2) are lowered in energy to such an extent that the spin (S = ½) couples with the spin of the t_{2g} level (S = 3/2). This intrasite spin coupling is referred to as the Hund coupling (J_H). The

energetics of the d-orbital splitting due to crystal field (Δ_{Dq}) is around 1 eV whereas the on-site Hund coupling J_H is around 2-3 eV. The t_{2g} levels which lie lower are less

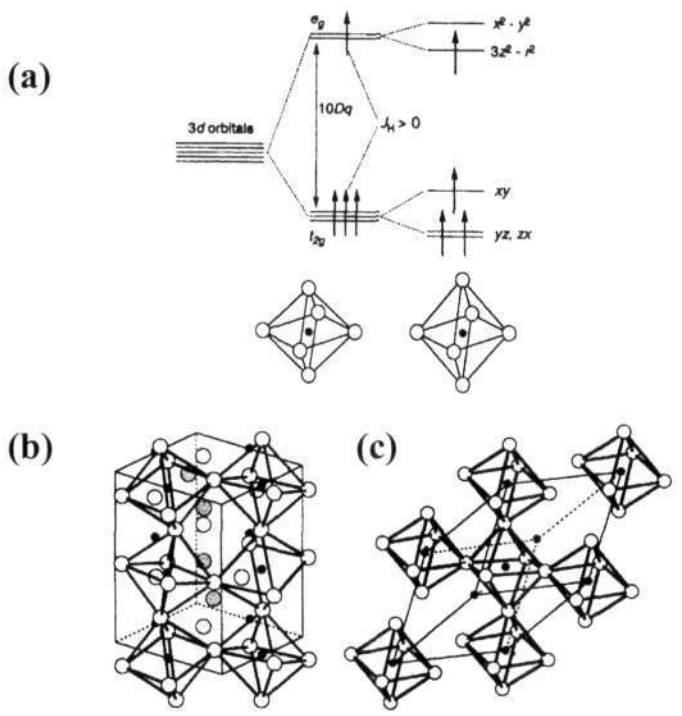

Fig.1.3 (a) Crystal field splitting of five fold degenerate d orbitals in t_{2g} (triply degenerate) and e_g (doubly degenerate) levels. Jahn Teller distortion of MnO_6 octahedra further lifts the degeneracy. Distorted perovskite structures (b) orthorhombic (c) rhombohedral. [Taken from ref. 19]

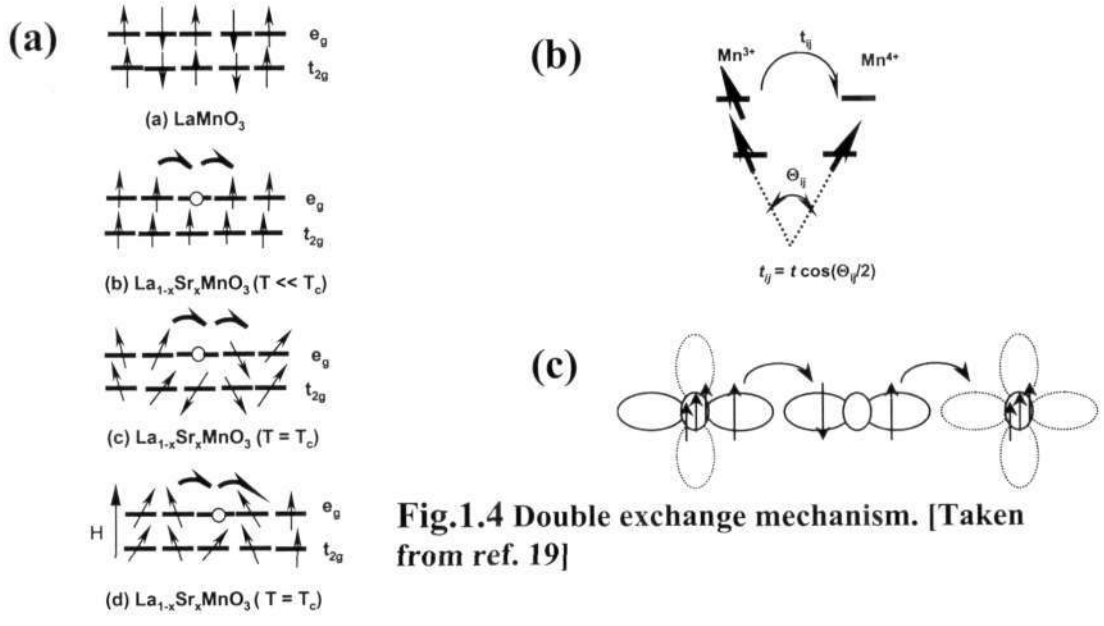

Fig.1.4 Double exchange mechanism. [Taken from ref. 19]

hybridized than the e_g levels. Electrons in the t_{2g} levels are therefore localized whereas the e_g electrons tend to be itinerant. This mobility of the electrons against the backdrop of the spin interaction is governed by the intersite hopping amplitude term t_{ij}, where i,j correspond to indices of neighboring atoms. Mutual repulsion or electron correlation effects (as they are referred to) characterize the electrons in the d-orbitals as a consequence of Hund's rule. This repulsion therefore inhibits the electrons jumping onto the neighboring sites. The ratio J_H/t_{ij} is used to measure the strength of this correlation interaction versus the hopping term. The hopping amplitude t_{ij} is given by the Anderson-Hasegawa[16] relation

$$t_{ij} = t^{o}_{ij}[\cos(\theta_{ij}/2)]$$

where θ_{ij} is the relative angle between neighboring atoms. This is shown in fig.1.4. It can be seen from the equation that the hopping amplitude is maximized when $\theta_{ij} = 0$, corresponding to alignment of the t_{2g} spins. This hopping process is favored only if the neighboring e_g orbital is empty i.e., corresponding to a Mn^{4+} ion. This corresponds to the interaction where spins have to be aligned to give rise to conduction and consequently the ferromagnetic behavior. The process of electron hopping takes place with the electron jumping from the intervening oxygen atom, and from there to the adjacent Mn^{4+} site leading to a double-exchange process[9,16-18].

(b) Superexchange mechanism

Consider the case where Mn^{3+}- O^{2-}- Mn^{3+}, i.e., two adjacent e^1_g orbitals with an intervening orbital of oxygen. Hopping is highly unfavorable due to electron correlation effects. The only way the system can stabilize itself is to align the spins on the e_g orbitals in an antiparallel fashion resulting in an antiferromagnetic behavior. In the octahedral

environment, the e_g orbital x^2-y^2 (say) aligns itself parallel to the 2p orbital (180°) and the electrons couple antiferromagnetically as shown in fig.5. This correlation interaction-giving rise to antiferromagnetic insulating behavior is known as the superexchange mechanism[12]. The 180° antiferromagnetic interaction occurs in more than one way. In fig.1.5 the different arrangements of spins are shown each giving rise to the net antiferromagnetic behavior.

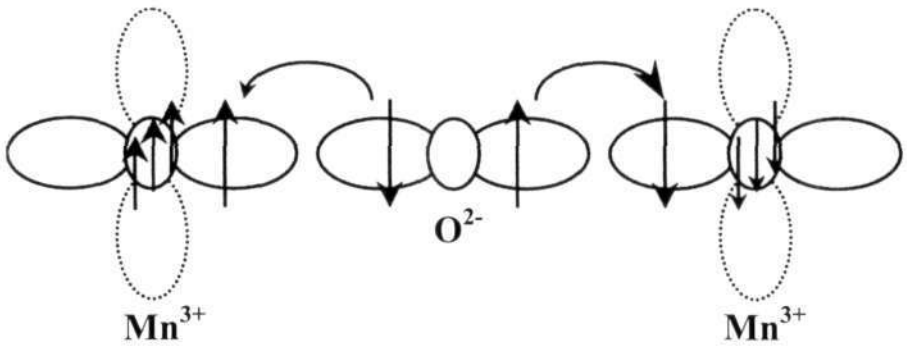

Fig.1.5 Superexchange Interaction leading to antiferromagnetic ordering.

Other types of superexchange interaction exist in which the orbitals interact via an angle of 90 ° giving rise to ferromagnetic-insulating state (fig.1.6). Based on these interactions various kinds of magnetic ordering are possible in these systems as shown in fig.1.7,

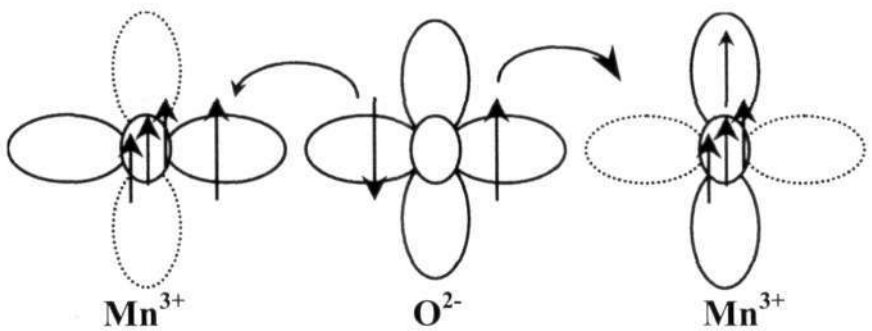

Fig.1.6 Superexchange interaction leading to ferromagnetic ordering.

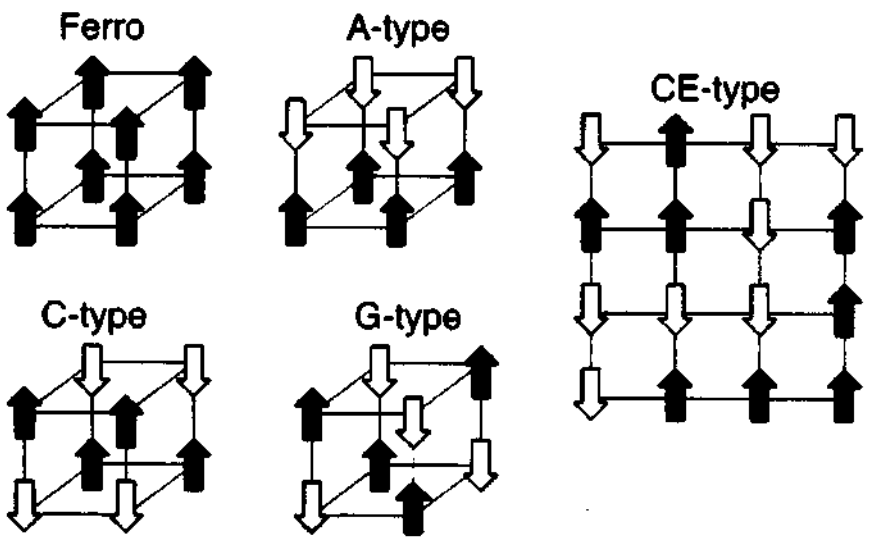

Fig.1.7 Different kinds of magnetic ordering in perovskite manganites.

these are the ferromagnet state F, where all the spins are parallely aligned; A type antiferomagnet, where in a-b layer there is ferromagnetism but along the c-axis it is antiferromagnetic; C type antiferromagnetic ordering; G type antiferromagnetic ordering and the CE type antiferromagnetic ordering. These magnetic orderings are only responsible for the rich phase diagrams of these systems.

1.1.4 Orbital ordering

In a transition metal oxide with the perovskite structure, the transition metal ion is surrounded by six oxygen ions, giving rise to the crystal field potential hindering the free rotation of the electrons and quenching the orbital angular momentum by introducing the crystal field splitting of d orbitals. Wave functions of the metal ion pointing towards O^{2-} ions have higher energy in comparison with those pointing between them. The former's wave functions, $d_{x^2-y^2}$ and $d_{3z^2-r^2}$ (e_g) orbital, and the d_{xy}, d_{yz} and d_{zx} (t_{2g}) orbitals are

shown in the fig.1.8 (see also figs. 1.3 & 1.4). An active role of orbital degree of freedom in the lattice and electronic response can be most typically seen in manganite oxide compounds with perovskite structure. In this class of compounds, colossal magnetoresistance (CMR), i.e., a very large decrease of resistance is observed upon the application of an external magnetic field and has attracted a lot of interest[11,19].

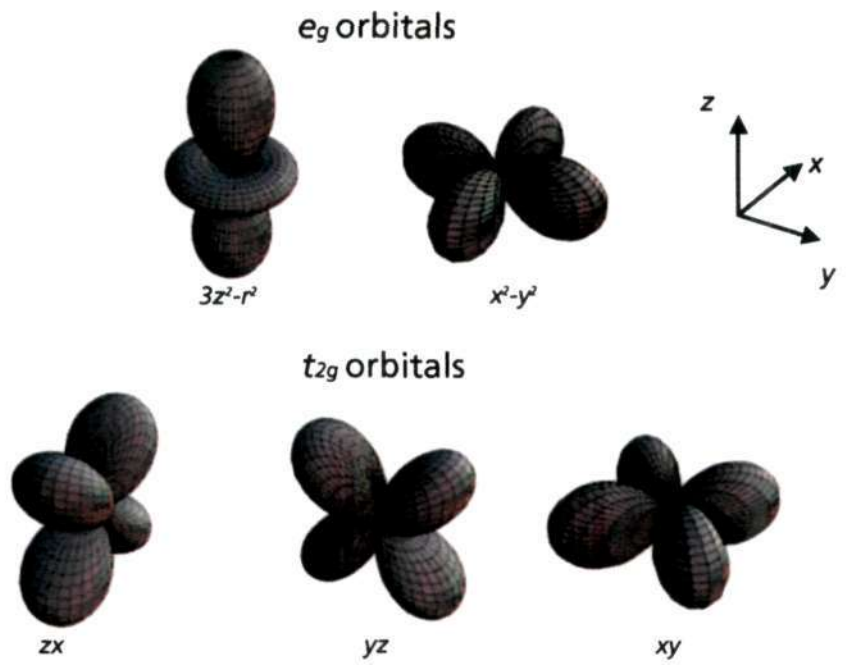

Fig.1.8 Five d orbitals in cubic crystal field, five fold degeneracy is lifted to two e_g ($d_{x^2-y^2}$ and $d_{3z^2-r^2}$) and t_{2g} (d_{xy}, d_{yz} and d_{zx}). [Taken from ref. 14]

The CMR phenomenon itself is, as argued in the following, related to orbital ordering and correlation. Orbital ordering gives rise to the anisotropy of the electron-transfer interaction. This favors or disfavors the double-exchange interaction and superexchange (ferromagnetic or antiferromagnetic) interaction in an orbital direction –dependent manner and hence gives a complex spin-orbital coupled state. One typical example is the case of $LaMnO_3$ with no double-exchange carriers, in which the in-plane (*ab* plane)

alternate ordering of $(3x^2-r^2)$ / $(3y^2-r^2)$ orbitals causes the in-plane ferromagnetic spin coupling. The A-type antiferromagnetic (AF) state is the manifestation of the anisotropic superexchange interactions, that is , ferromagnetic within the plane and AF between the plane, due to the orbital ordering.

The importance of the orbital and lattice degrees of freedom has long been recognized theoretically[20]. As for the e_g electrons in the 3D perovskite structure, the A-type AF state is obtained with alternating $(z^2-x^2)/(y^2-z^2)$ orbitals within the plane. In addition to this superexchange interaction, the Jahn-Teller interactions (JTI) also contribute to determining the orbital ordering. When JTI prefers the planar orbitals, such as (z^2-x^2) and (y^2-z^2), it does not contradict with the above orbital ordering; however, JTI could also prefer the rod-type orbitals, such as $(3z^2-r^2)$. In the former case and/or when JTI is weak, the A-type AF state with alternating $(z^2-x^2)/(y^2-z^2)$ orbitals should be realized as observed in $KCuF_3$[21]. The A-type AF state with alternating $(3x^2-r^2)$ / $(3y^2-r^2)$ in $LaMnO_3$, on the other hand, is attributed to the JT distortion[22-24].

In the hole-doped manganese oxides, in which the double-exchange interaction emerges with the strength being dependent on the doping level, various orbital-ordered and disordered states show up, accompanying the respective spin-ordering features (top of fig.1.9). Let us here take the case of $Nd_{1-x}Sr_xMnO_3$ under ambient pressure[25-28]. With appreciable doping on the parent compound $NdMnO_3$, the orbital order melts into a quantum-disordered state, and the compound shows the ferromagnetic-metallic (F) state for $0.3<x<0.5$. When doped further, the kinetic energy of carriers decreases, and the compound shows the 2D metallic state with layered-type antiferromagnetic (A) state for

0.5<x<0.7. Doping above x = 0.7 further alters the magnetic structure to the chain type (C).

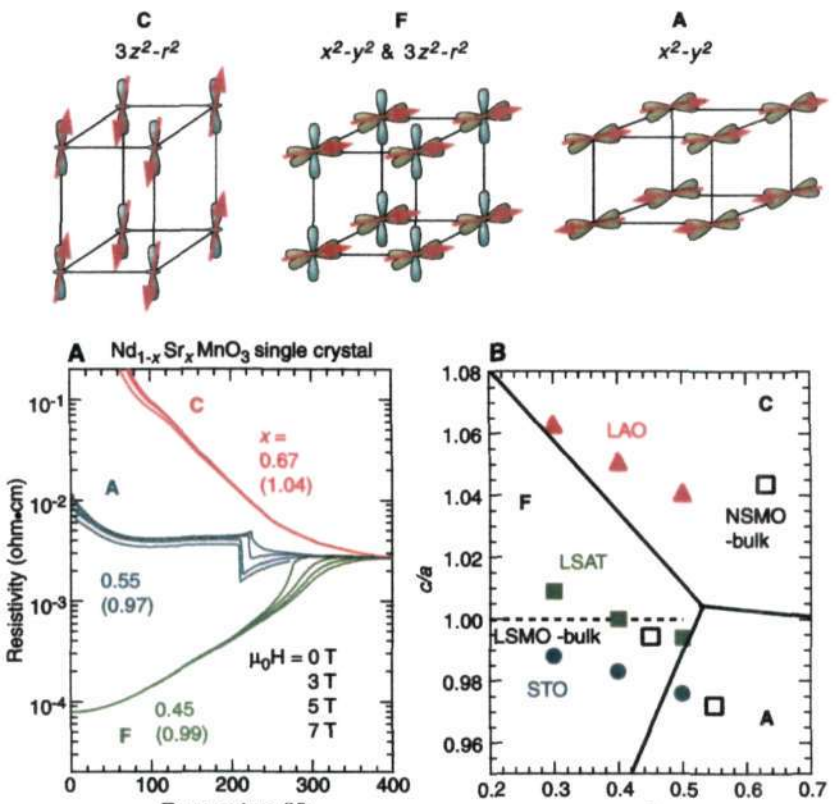

Fig.1.9 Spin orbital phase diagram of manganites. [Taken from ref. 14]

This rich phase diagram can be reproduced and understood theoretically in terms of mean field approximation applied to the generalized Hubbard model[29]. The A state is realized as the compromise between the AF superexchange interaction between the t_{2g} spins and the double-exchange interaction through the ferromagnetic (homogenous) order of (x^2-y^2) orbital[29]. In cubic perovskite, the electron transfer is almost prohibited along the c-axis because of the (x^2-y^2) orbital order, which is also the origin for the interplane AF coupling. In fact, the charge dynamics in this A-type AF state is almost 2D[27].

The C-type AF state for $x > 0.7$ is accompanied by the $(3z^2\text{-}r^2)$ orbital. This state is perhaps affected also by the charge ordering and shows an insulating feature (fig.1.9A). The large orbital polarization T is indispensable for the wave function is well defined, and the anisotropy appears only in this case, i.e., the dimensional control by the orbital occurs. Otherwise, it would become a boring phase diagram in which the ferromagnetic state dominates.

Instead of changing the carrier's kinetic energy with doping level, one can use the lattice strain as a biasing field on the orbital state through the JT channel; namely, the uniaxial strain with respect to MnO_6 octahedron can serve as a pseudo magnetic field on the pseudospin T. Fig.1.9B shows a schematic spin-orbital phase diagram in the moderately doped $(0.3<x<0.7)$ manganese oxides on the plane of the uniaxial strain measured as the ratio of lattice parameter c/a (or almost equivalent the ratio of the apical to equatorial Mn-O bond length) and the doping x. The phase diagram was based on the local density functional calculation as well as the experimental results for the epitaxial single crystalline films of $La_{1-x}Sr_xMnO_3$ with coherent lattice strain due to the lattice mismatch with the substrate[30]. The entanglement of the doping and the strain causes the slanted phase boundaries for the F (orbital-disordered), A $[(x^2\text{-}y^2)$-ordered] and C $[(3x^2\text{-}r^2)$- ordered] states. As a general trend, the decrease of hole doping enlarges the F region, whereas the increase (decrease) in the c/a ratio stabilizes the C(A) state as excepted. In fact, thin films of $La_{1-x}Sr_xMnO_3$ $(x = 0.5)$ epitaxially grown on three different perovskite substrates show the respective ground states (F, A and C) and the similar transport properties to those shown in the case of $Nd_{1-x}Sr_xMnO_3$ (fig.9A). The orbital ordering in the manganese oxides occasionally accompanies the

concomitant charge ordering. The most prototypical case, namely the CE type shown in fig.1.10, is realized at doping level (x) of 0.5. In the pseudo cubic perovskite, the ab planes are coupled antiferromagnetically while keeping the same in-plane charge and orbital pattern[31,18].

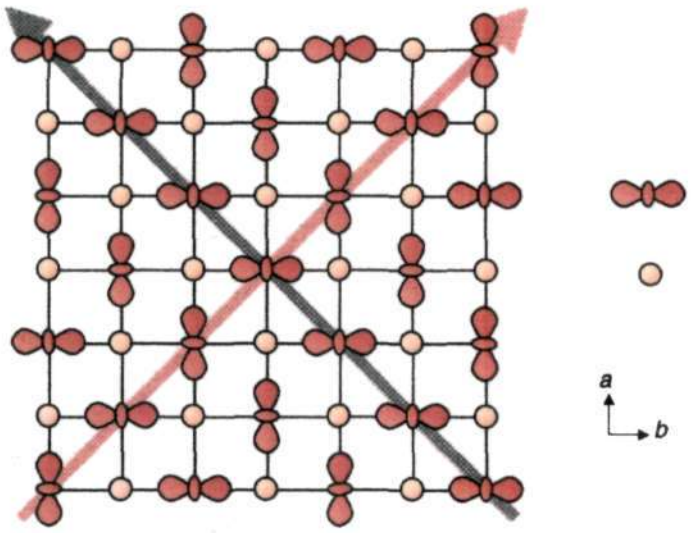

Fig.1.10 The orbital $[(3x^2-r^2) / (3y^2-r^2)]$ and charge order of CE type projected on MnO_2 sheets (ab plane). [Taken from ref. 14]

1.1.5 Charge Ordering

Charge ordering refers to the ordering of the metal ions in different oxidation states in specific lattice sites of a mixed valent material. Such ordering generally localizes the electrons in the material, rendering it insulating or semiconducting because when the charges are localized, electrons cannot readily hop from one cation site to another. Charge ordering is not a new phenomenon in metal oxides. One of the earliest examples of charge ordering in inorganic solids is that of Fe_3O_4 (magnetite), which undergoes a disorder-order transition, popularly known as the Verwey transition, at 120 K[32]. Complex charge ordering is also found in the perovskite, $La_{1-x}Sr_xFeO_3$[33] and quasi-two-

dimensional $La_{1-x}Sr_xNiO_4$[34]. The charge ordering transition in $La_{1.67}Sr_{0.33}NiO_4$ occurs around 240 K , accompanied by a structural change and opening up of a gap[34]. Charge ordering in rare earth manganites of the general formula $Ln_{1-x}A_xMnO_3$ (Ln = rare earth, A= alkaline earth) is particularly fascinating, being associated with novel properties that are sensitive to electronic and geometric factors. The study of charge ordering in these manganites has recently received much attention because of the colossal magnetoresistance (CMR) exhibited by these materials, although charge ordering itself had been noticed by Wollan and Koehler[35] in 1955 and later by Jirak et al[13]. in 1985.

To understand typical scenarios of charge ordered manganites, it is instructive to examine the properties of two manganites with different sizes of the A-site cations. For this purpose, we choose $Nd_{0.5}Sr_{0.5}MnO_3$ with a weighted average radius of the A-site cations, $\langle r_A \rangle$, of 1.24 Å and $Pr_{0.6}Ca_{0.4}MnO_3$ with an $\langle r_A \rangle$ of 1.17 Å (Shannon radii are

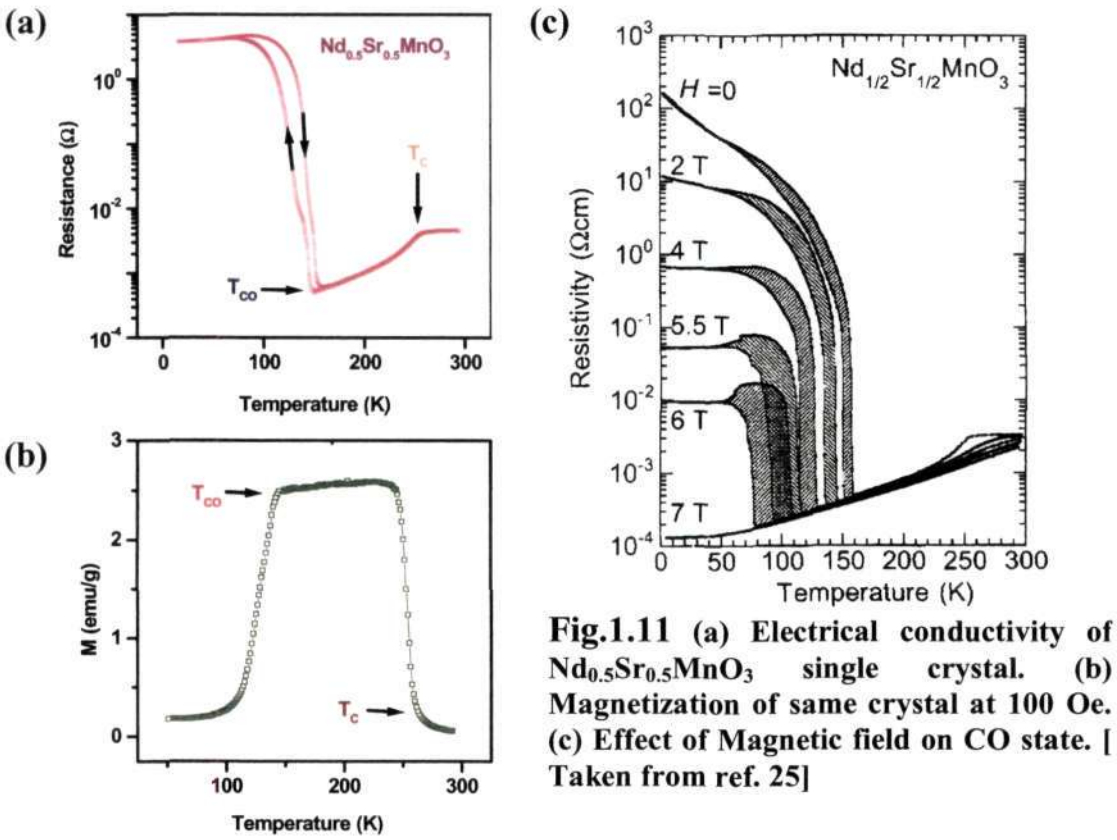

Fig.1.11 (a) Electrical conductivity of $Nd_{0.5}Sr_{0.5}MnO_3$ single crystal. (b) Magnetization of same crystal at 100 Oe. (c) Effect of Magnetic field on CO state. [Taken from ref. 25]

used here). $Nd_{0.5}Sr_{0.5}MnO_3$ is ferromagnetic metal a T_C of ~250 K and transforms to an insulating CO state at about 150 K (fig.1.11). The CO transition is accompanied by spin ordering, and the CO insulator is a CE-type antiferromagnet[36] (fig.1.12). The orbital ordering therefore involves $(3x^2\text{-}r^2/3y^2\text{-}r^2)$ orbitals as in fig.1.12. Application of a magnetic field of 7T destroys the CO state, and the material becomes metallic (fig.1.11), the sharpness of the transition decreasing with increasing strength of the field. The transition is first order, showing hystersis and is associated with changes in unit cell parameters. The unit cell volume of the CO state is considerably smaller than that of the FMM state. The properties of $Nd_{0.5}Sr_{0.5}MnO_3$ can be described in terms of the phase diagram shown in fig.1.13.

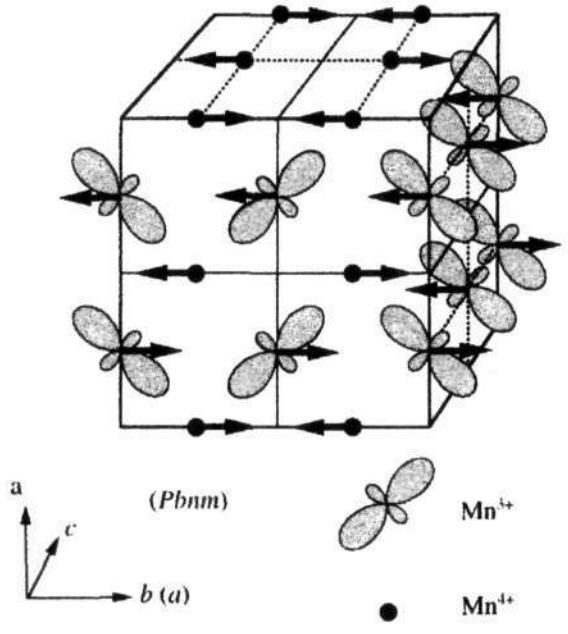

Fig.1.12 Spin, charge and orbital ordering pattern of CE type observed for most of x~0.5 manganites. [Taken from ref. 5]

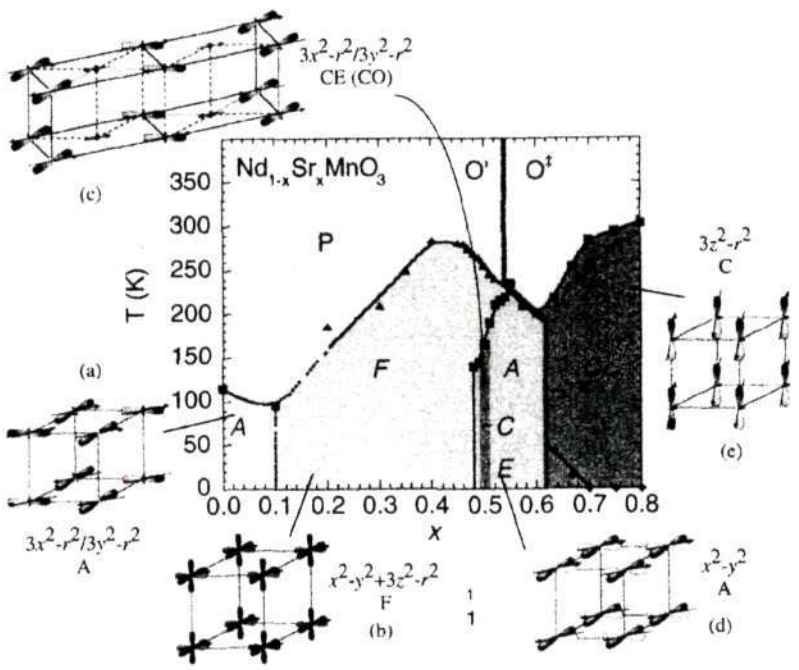

Fig.1.13 Phase-diagram of $Nd_{1-x}Sr_xMnO_3$ system. [Taken from ref. 5]

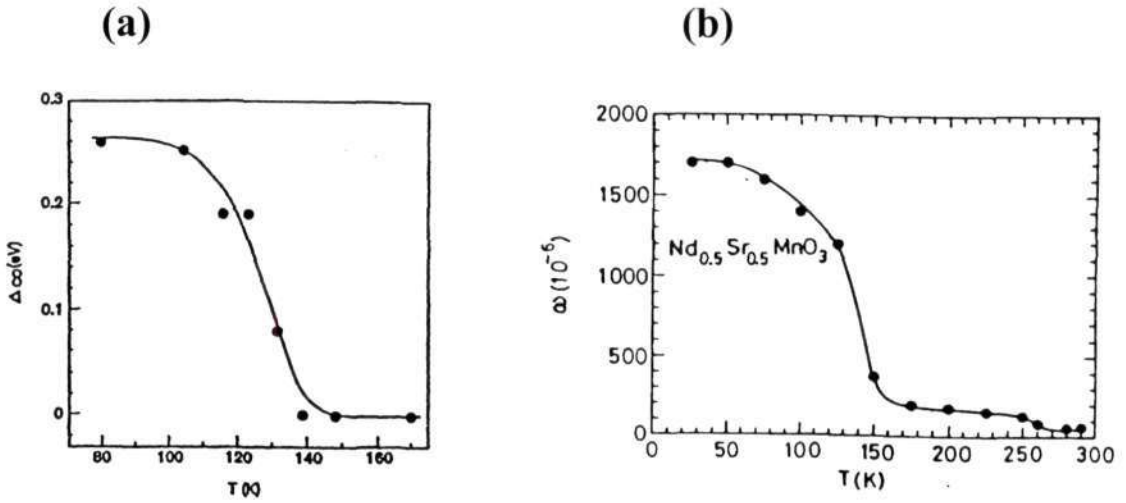

Fig.1.14 (a) Vacuum tunneling measurements of $Nd_{0.5}Sr_{0.5}MnO_3$ (b) Magnetostriction behavior of $Nd_{0.5}Sr_{0.5}MnO_3$. [Taken from ref. 37 and 39]

The Imma space group of this manganite renders the Mn-O-Mn angle in the ab plane closer to 180°, promoting the overlap of the Mn(e_g) and O(2p) orbitals. Vacuum tunneling measurements[37] show that a gap of 250 meV opens up below T_{CO} (fig.1.14 (a)). The gap collapses on applying a magnetic field, suggesting that a gap in the density of states at E_F is necessary for the stability of CO state. Photoemission studies indicate a sudden change in electron states at the transition and give an estimate of 100 meV for the gap[38]. These estimates of the gap are considerably larger than the T_{CO} (12 meV) can destroy the CO state. $Nd_{0.5}Sr_{0.5}MnO_3$ shows anomalous magnetostriction[39] behavior, with a large positive magnetovolume effect (fig.1.14 (b)), owing to the magnetic field-induced structural transition accompanying a change from the AFM CO state to FMM state.

$Pr_{0.6}Ca_{0.4}MnO_3$ is an insulator at all temperatures and becomes charge ordered at about 230 K (T_{CO}). At this temperature, anomalies are found in the magnetic susceptibility[40,41], as well as in the resistivity, as shown in fig.1.15. In the CO state, the

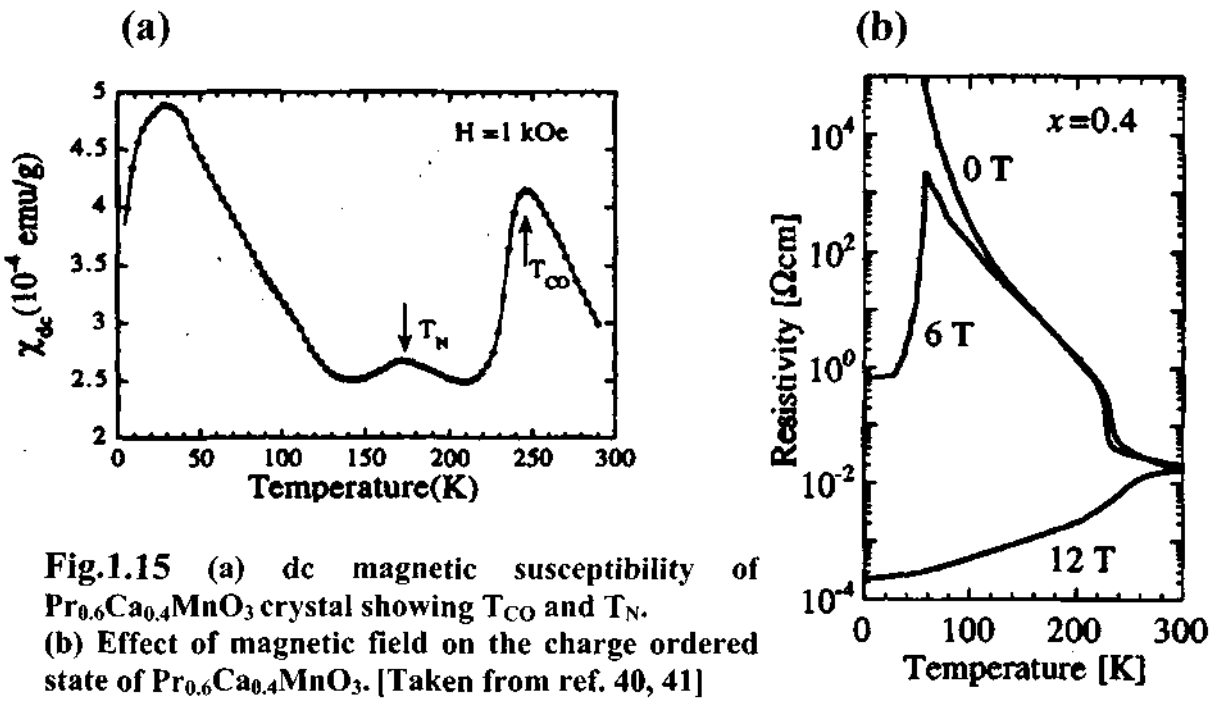

Fig.1.15 (a) dc magnetic susceptibility of $Pr_{0.6}Ca_{0.4}MnO_3$ crystal showing T_{CO} and T_N.
(b) Effect of magnetic field on the charge ordered state of $Pr_{0.6}Ca_{0.4}MnO_3$. [Taken from ref. 40, 41]

Mn^{3+} and Mn^{4+} ions are regularly arranged in the ab plane with the associated ordering of the $3x^2$- $r^2/3y^2$-r^2 orbitals. On cooling, AFM ordering (CE-type) occurs at 170 K (T_N). At about 40 K, $Pr_{0.6}Ca_{0.4}MnO_3$ exhibits canted AFM ordering. Application of an external magnetic field transforms the CO state to an FMM state, as shown in fig.1.15(b), but the field required is much larger than in $Nd_{0.5}Sr_{0.5}MnO_3$. The transition is associated with hysteresis. The properties of $Pr_{0.6}Ca_{0.4}MnO_3$ can be represented by the phase diagram in fig.1.16. The basic features of the CO state in $Pr_{0.6}Ca_{0.4}MnO_3$ are exhibited by several other rare earth manganites with relatively small A-size cations, in that the CO state is the ground state. Thus $Nd_{0.5}Ca_{0.5}MnO_3$ ($<r_A>$ = 1.17 Å) is a paramagnetic insulator with a charge ordering transition at about 240 K.

Charge ordering occurs in the paramagnetic state in $Pr_{1-x}Ca_xMnO_3$ ($0.35 \leq x \leq 0.5$) with the T_{CO} increasing with x. The paramagnetic state is characterized by FM spin fluctuations with a small energy scale[42]. At T_{CO}, these fluctuations decrease and

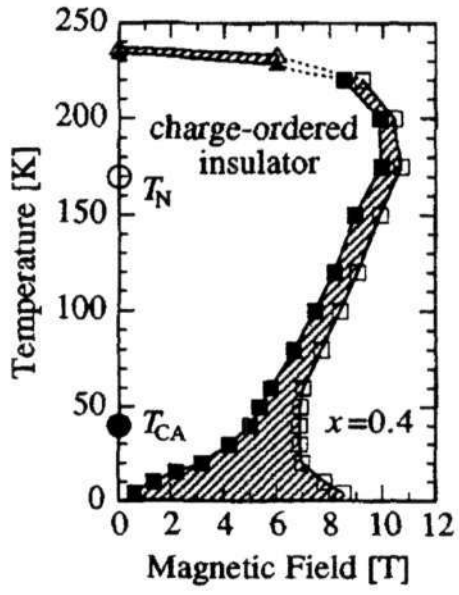

Fig.1.16 Phase diagram of $Pr_{0.6}Ca_{0.4}MnO_3$ system in the presence of magnetic field. [Taken from ref 40]

disappear at T_N. Electron diffraction and dark field transmission electron microscopy (TEM) images show the presence of incommensurate charge ordering in the paramagnetic insulating state (180-260 K) of the x = 0.5 composition[43] at T_N, there is an incommensurate – commensurate CO transition. In the incommensurate CO structure, partial orbital ordering is likely to be present. Similar charge, orbital and spin ordering has been found in the 0.3 composition as well[44]. Optical conductivity spectra of the x = 0.4 composition show evidence of spatial charge and orbital ordering at 10 K[45]. The CO state has a gap of 0.2 eV, and the gap remains up to 4.5 T. The gap value is the order parameter of the CO state and couples with spin ordering. $Pr_{0.67}Ca_{0.33}MnO_3$ shows thermal relaxation effects from the metastable FMM state (produced by the application of 10 T magnetic field) to the CO state. A metal-insulator transition is observed as a abrupt jump in resistivity at a well defined time, depending on the temperature. This observation seems to indicate a percolate nature of current transport.

As mentioned earlier the average size of the A-site cations controls the deviation of Mn-O-Mn bond angle from 180° and hence the e_g electron-hopping interaction through a change in Mn 3d and O 2p hybridization. One of the simplest examples where this effect is clearly visible are the series of charge-ordered manganites namely $Ln_{0.5}A_{0.5}MnO_3$ where as we are decreasing the $<r_A>$ ferromagnetic state is slowly getting disappeared as shown in Table 1.1[46]. All this can only happen when the Mn^{3+}-O^{2-}- Mn^{4+} starts changing with radius of the A-site cation $<r_A>$. Fig.1.17 shows a typical scenario of the variation of $<r_A>$ verses the temperature and the possible magnetic ordering present in the system[47].

Table 1.1

A = Ca				A = Sr		
Ln	$\langle r_A \rangle$, Å	Stable phase	T_{CO} (K)	$\langle r_A \rangle$, Å	Stable phase	T_{CO} (K)
Y	1.127	CO	260			
Dy	1.132	CO	260			
Gd	1.143	CO	260	1.206	Spin glass	
Nd	1.172	CO	240	1.236	FMM	150
Pr	1.179	CO	240	1.244	FMM	
La	1.198	PMI	170	1.263	FMM	0

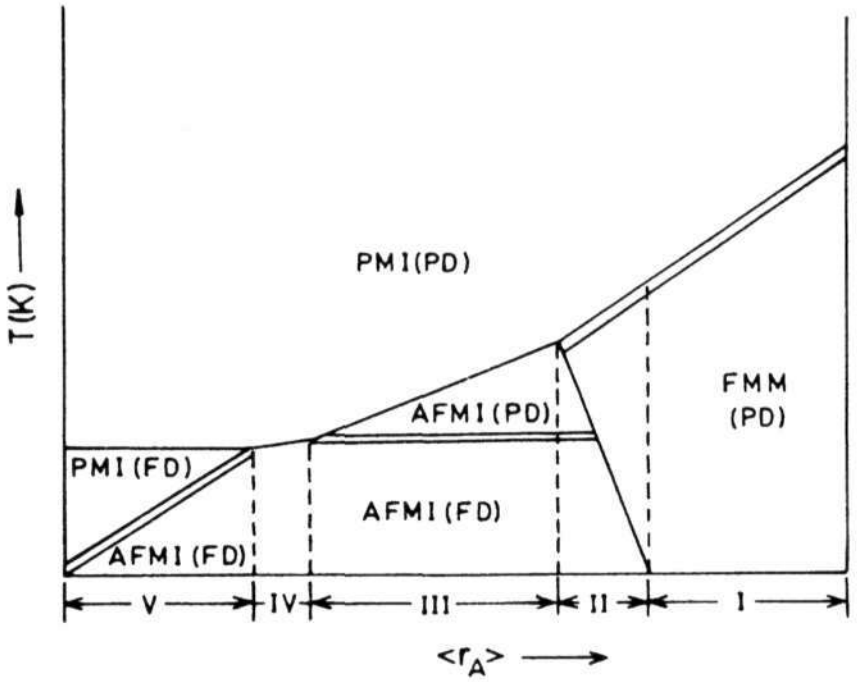

Fig.1.17 Phase diagram showing variation of $\langle r_A \rangle$ verus Temperature with the type of magnetic ordering. [Taken from ref. 47]

In fig.1.18 we show the phase diagrams of $Ln_{0.5}Sr_{0.5}MnO_3$ and $Ln_{0.5}Ca_{0.5}MnO_3$ which show the variation of the magnetic, charge/orbital ordering with respect to $<r_A>$[50].

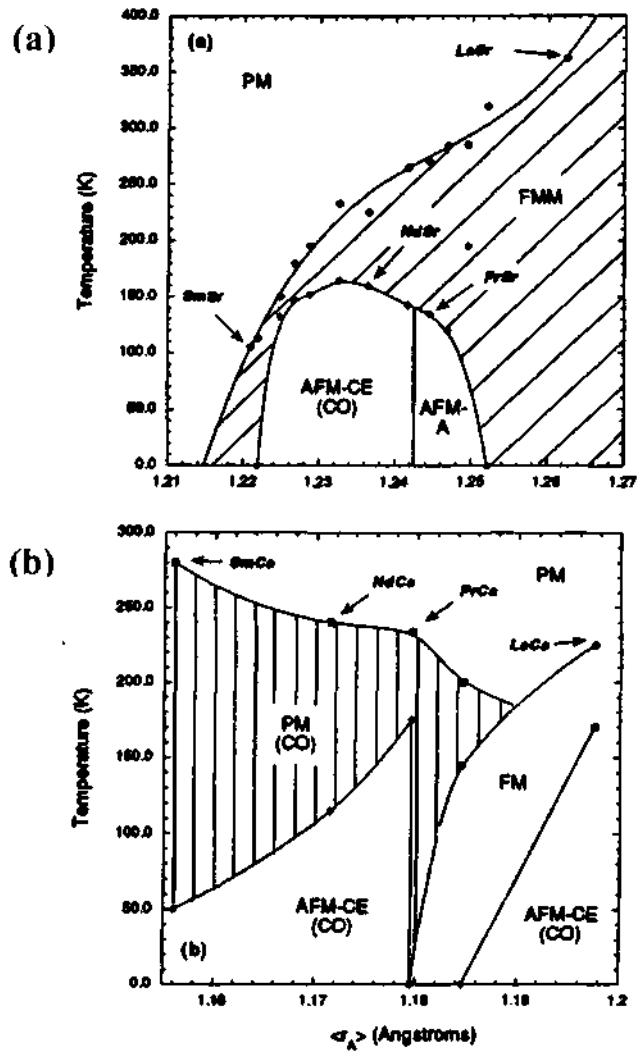

Fig.1.18 The phase diagrams of A. $Ln_{0.5}Sr_{0.5}MnO_3$ and B. $Ln_{0.5}Ca_{0.5}MnO_3$. [Taken from ref. 46]

1.1.6 Effect of magnetic fields on charge ordered manganites

The melting or the destruction of the charge ordered state by magnetic fields has been a major aspect of research in these systems. Unlike the CMR systems where the fields of few tesla have very drastic effect on the resistance of the system, the effect of magnetic

field is limited to very few charge ordered systems, like $Nd_{1-x}Sr_xMnO_3$ and $Pr_{1-x}Ca_xMnO_3$ for a few prototype to mention. As the $<r_A>$ of the system decrease the CO state becomes more and more robust and the magnetic fields needed to melt go extremely high. In the case of $Y_{0.5}Ca_{0.5}MnO_3$, ($<r_A>$ 1.13 Å) a magnetic field of 100 T does not have

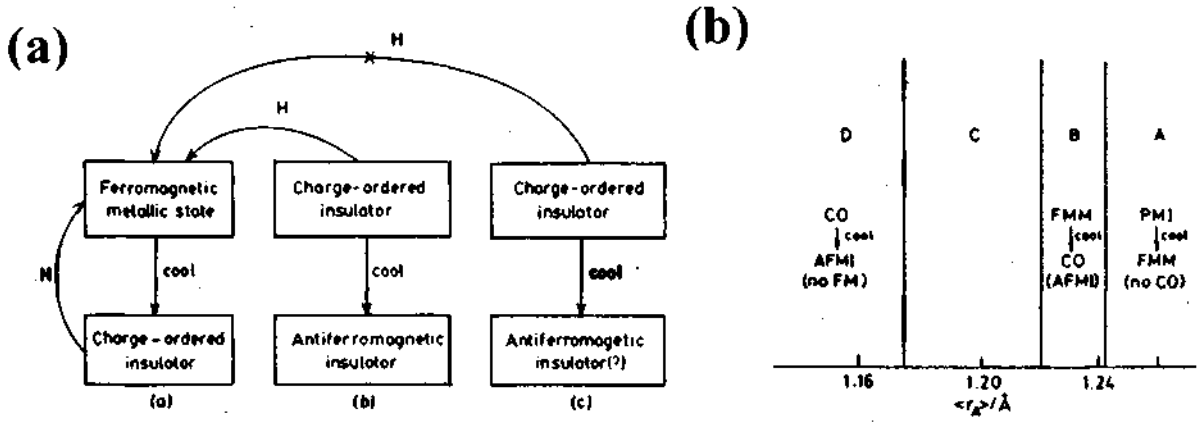

Fig.1.19 (a) Different types of CO states in rare earth manganites as deloneated by the effect of magnetic fields. (b) Schematic diagram showing different charge ordering behaviors of $Ln_{0.5}A_{0.5}MnO_3$ depending on $<r_A>$. [Taken from ref. 46]

any effect on the CO state of this system. Fig.1.19 describes the different $<r_A>$ regimes and their sensitivity to the magnetic fields. In $Pr_{1-x}Ca_xMnO_3$, the dependence of the magnetic field-induced transition (or collapse of the charge/orbital – ordered state in a magnetic field) on the doping level has systematically been investigated[39,48] for $0.3<x<0.5$. The x-dependent features are well demonstrated by the charge/orbital ordering phase diagram displayed on the magnetic field temperature (H-T) plane shown in fig.1.20[34]. In this figure, the phase boundaries have been determined by the measurements of the magnetic field dependence of resistivity (ρ-H) and magnetization (M-H) at fixed temperatures.

The charge/orbital ordering for x = 0.5 is so strong that the critical field to destruct the charge/orbital – ordered state becomes as large as about 27 T at 4.2 K, and a similar feature is also seen for x = 0.45[48]. For x<0.4, by contrast, the charge/orbital-ordered phase-region becomes remarkably shrunk, in particular at low temperatures. The averaged value (H_{av}) of the critical fields in the H - increasing and decreasing runs at a constant temperature below ~ 175 K ($dH_{av}/dT < 0$). In the case of x = 0.3, collapse of the charge/orbital-ordered state (i.e., appearance of FM metallic state) is realized by applying an external magnetic field of only several tesla when the temperature is set below 50 K. Another noteworthy aspect in fig.1.20 is expansion of field hysteresis with decreasing temperature, which is characteristic of first order phase transition as mentioned above[25]. Such a variation of the charge/orbital-ordered phase with the doping level has been

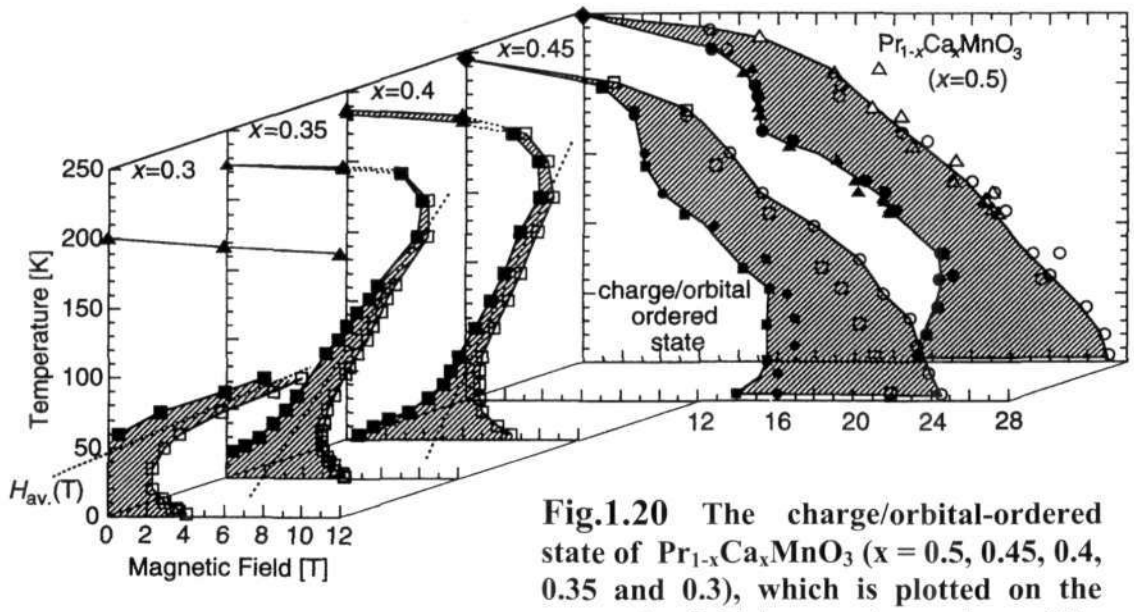

Fig.1.20 **The charge/orbital-ordered state of $Pr_{1-x}Ca_xMnO_3$ (x = 0.5, 0.45, 0.4, 0.35 and 0.3), which is plotted on the magnetic field-temperature plane. The hatched area indicates the hysteresis region. [Taken from ref. 34]**

observed similarly for a further W-reduced system[48,49], $Nd_{1-x}Ca_xMnO_3$. The common feature for the modification of the phase diagram with x seems to be correlated with the action of the extra electron-type carriers in the CE-type structure[50]. Thermodynamically excess entropy may be brought about in the charge/orbital – ordered state by the extra-localized carriers and their related orbital degrees of freedom, which are pronounced as x deviates from 0.5. The excess entropy may reduce the stability of the charge-ordered state with decreasing temperature and cause the reduction in the critical magnetic field ($dH_{av}/dT < 0$) as observed in the case of $x<0.4$ in fig.1.20. In reality, however, the microscopic phase separation into $x\sim 0.5$ charge-ordered state and the $x<0.5$ ferromagnetic state should also be taken into account for a deeper understanding of the present features for $x<0.5$ systems.

Fig.1.21 shows the charge/orbital ordering phase diagrams for various $Ln_{1-x}A_xMnO_3$ crystals, which are presented on the magnetic field-temperature (H-T) plane. The phase

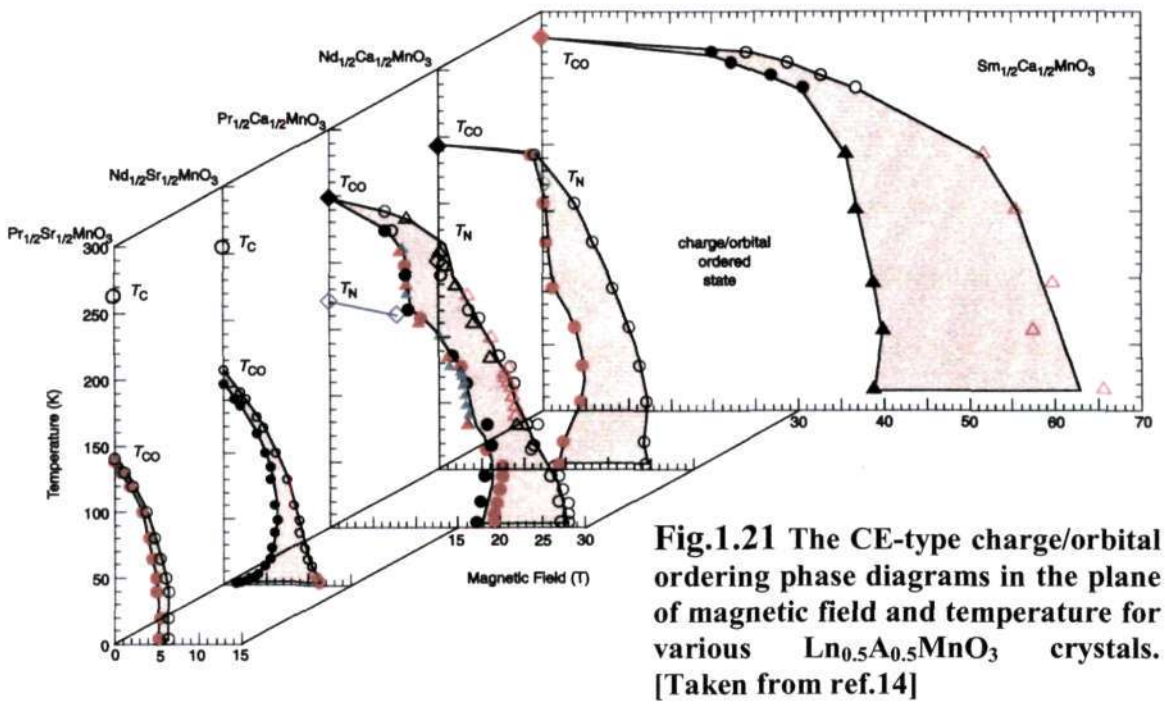

Fig.1.21 The CE-type charge/orbital ordering phase diagrams in the plane of magnetic field and temperature for various $Ln_{0.5}A_{0.5}MnO_3$ crystals. [Taken from ref.14]

boundaries have been determined by the measurements of the magnetic field dependence of resistivity (ρ-H) and magnetization (M-H) at fixed temperatures[25,51] and those of $Ln_{0.5}Ca_{0.5}MnO_3$ (Ln = Pr, Nd and Sm) have been obtained by measurements utilizing pulsed high fields up to 40 T[48]. In this figure, the critical field to destroy the charge/orbital-ordered state in $Nd_{0.5}Sr_{0.5}MnO_3$ is about 11 T at 4.2 K, while that in $Pr_{0.5}Ca_{0.5}MnO_3$ increases to about 27 T. In the case of $Sm_{0.5}Ca_{0.5}MnO_3$, charge / orbital ordering is so strong that the critical field becomes as large as about 50 T at 4.2 K. Fig.1.21 thus demonstrates that the robustness of charge/orbital ordering at x = 0.5 critically depends on the W, which represents the competition between the DE interaction and the ordering of Mn^{3+}/ Mn^{4+} with a 1:1 ratio accompanied by the simultaneous ordering of the e_g orbitals of Mn^{3+}. To be further noted in fig.1.21 is the large hysteresis of the transition (hatched in the figure) which is characteristic of the first-order transition coupled with the change of crystal lattice. The change in the lattice parameters originates from the field destruction of orbital ordering. As seen in the fig.1.21, the hysteresis region (hatched area) expands with decreasing temperature especially below ~20 K. In the case of the first-order phase transition, the transition from the metastable to the stable state occurs by overcoming a free-energy barrier. Since the thermal energy reduces with the decrease in temperature, a larger (smaller) field than the thermodynamic value is needed to induce the transition from (to) the AF charge/orbital-ordered to (from) the FM metallic state. Thus, the hysteresis between the runs with increasing and decreasing runs increases with the decrease of temperature. It is noteworthy that charge ordering in some of the manganite compositions is destroyed by substitution of transition metal ions in the B-site.

Thus, Cr^{3+} or Ru^{4+} substitution (1-3%) in $Pr_{0.6}Ca_{0.4}MnO_3$ or $Nd_{0.5}Ca_{0.5}MnO_3$ destroys charge ordering in these materials and renders them ferromagnetic and metallic.

1.1.7 Effect of Photoexcitation on charge ordering

In fig.1.22, we show an example of the photo-induced[52,53] dielectric breakdown for the crystal of $Pr_{1-x}Ca_xMnO_3$ (x = 0.3). The sample resistance across the gold electrodes with a gap of 200 μm was more than 1GΩ at 30 K. A single nanosecond laser pulse with a photon energy well-above the charge gap (0.5 eV) extremely decreases the resistance to a

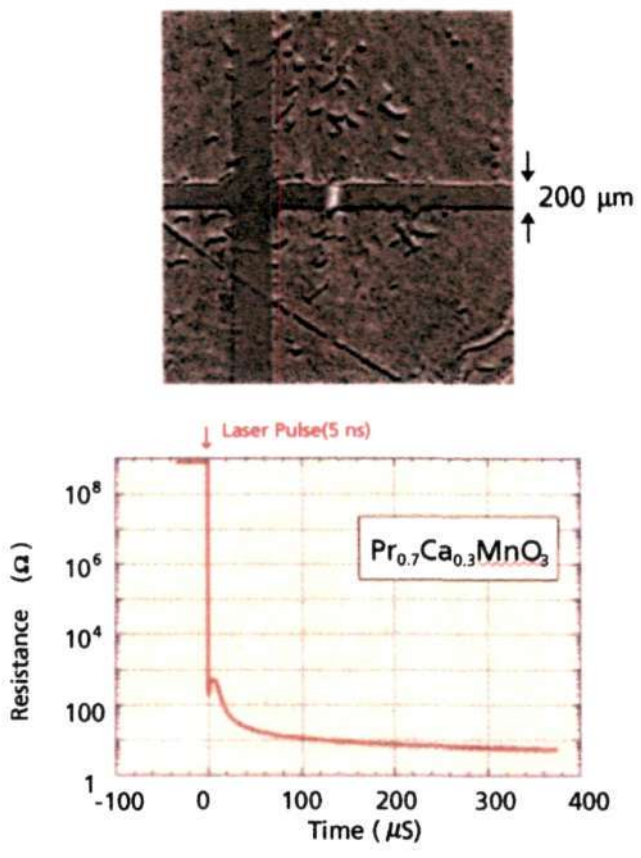

Fig.1.22 The Photo-induced insulator-metal transition for a $Pr_{1-x}Ca_xMnO_3$ (x = 0.3) crystal at 30 K. The resistance measured with the electrode gap of 200μm shows a gigantic decrease from above 1GΩ to a few tens of ohms. The photo-excitation with a single shot of nanosecond laser (2.4 eV) pulse. Upper panel shows the image (a bright region) of the photo-induced metallic current path between the electrodes (gold). [Taken from ref. 52,53]

few tens of ohm or generates a large persistent photoconductivity. Under a microscope, the local insulator-metal transition between the electrode gap (200 μm) is quite visible as the current path (the brightened image) in the upper panel of fig.1.22. Such a local light-induced insulator-metal transition is due to the local melting of the charge/orbital ordered state, which gives rise to a large change of reflectivity even in the visible region. The metallic path can be sustained by passing the current. According to pump-probe experiment using 100 fs light pulses, the photo-induced melting of the charge/orbital ordered state or the local insulator-metal transition is completed within 1 ps, and is accompanied by a large change in optical reflectivity and perhaps also by the onset of ferromagnetism. Such an ultrafast phase-control would be a great advantage in use of correlated-electron materials.

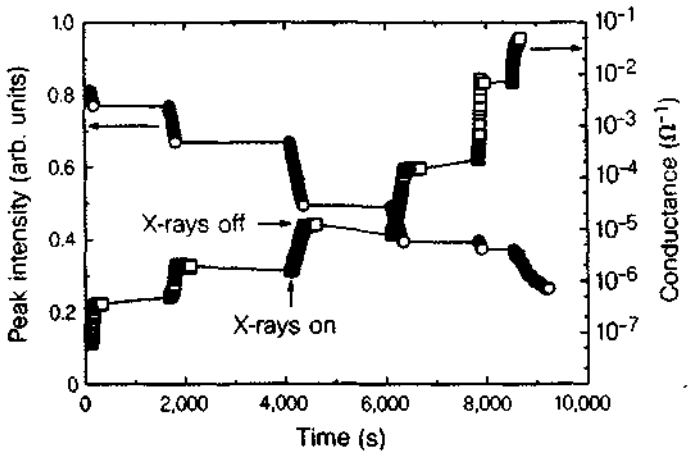

Fig.1.23 X-ray exposure dependence of the peak intensity of the (2,15,0) bragg reflection characteristic of charge ordering (left axis), and of the electrical conductance (right axis), at temperature T = 4 K. The measurements were taken with a monochromatic X-ray beam (energy 8 keV, flux 5 x 10^{10} s^{-1}, beam size 1 x 1mm) at beamline X22B National Synchrotron Light Source. [Taken from ref. 54]

1.1.8 Effect of X-rays on charge ordering

Yet another method to get an I-M transition is to use another powerful tool of energy like X-rays[54]. Fig.1.23 shows that the intensity of reflection decreases continuously with X-rays illumination; no change is observed when the X-ray beam is switched off. The diminution of charge order is associated with a dramatic change in transport properties. The conductance measured between two contacts spaced ~1mm apart on a polished surface of the sample increases by more than six orders of a magnitude after ~20 min of total X-ray exposure (fig.1.23). With the X-ray beam off, the conductivity persists for many hours without measurable degradation.

Although the metallic state generated after prolonged X-ray exposure exhibits

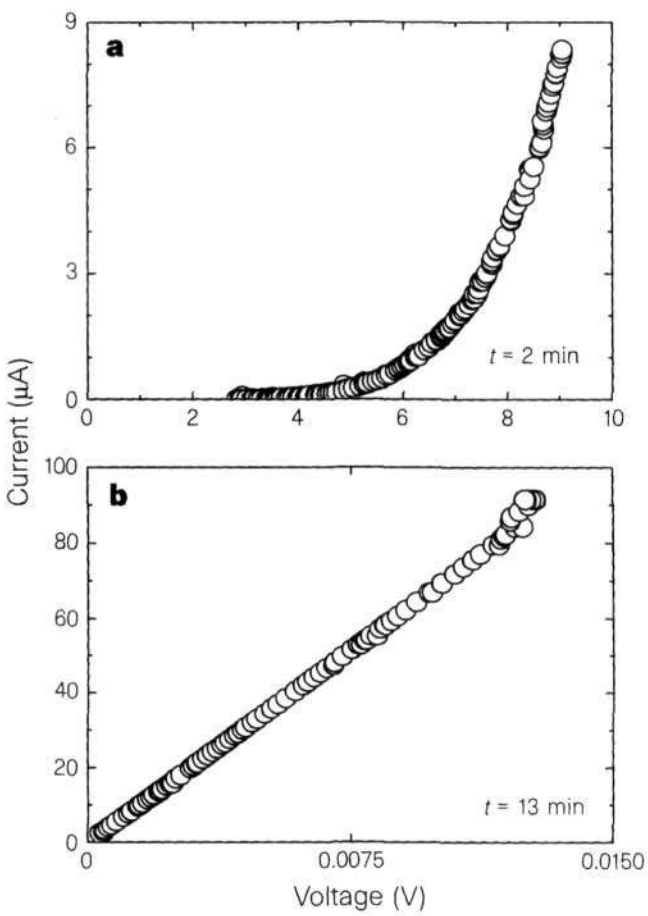

Fig.1.24 Current–voltage characteristics measured after different X-ray exponsures at temperature T = 4 K. [Taken from ref. 54]

conventional ohmic conductivity (fig.1.24 (b)), in (fig.1.24 (a)) current-voltage characteristics after short exposure are remarkably nonlinear. (Because of this conductance is quoted rather than conductivity in fig.1.23). The non-ohmic conductivity in this regime is a consequence of a much more general current-switching behavior that will be discussed separately. We obtain $\rho \sim 5 \times 10^{-4}$ Ωcm for the ohmic resistivity after prolonged X-ray exposure, using the calculated X-ray penetration depth of 1.5 μm as the

Further evidence for this assertion comes from a comparison of the metastablilty boundaries of these two metallic states. Fig.1.25 shows that the X-ray-induced conductivity is annealed out on heating above 60 K, which is the annealing temperature for the magnetic-field-induced phase. Fig.1.23 also shows phase coexistence of insulating (charge-ordered) and metallic states for short exposures, which may indicate that the

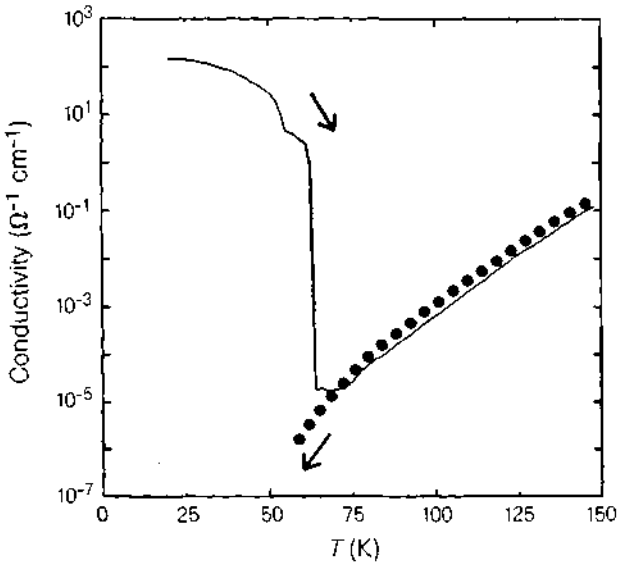

Fig.1.25 Conductivity measured on cooling before X-ray illimination (dotted curve) and heating after illumination with X-rays for a moderate amount of time (solid curve). [Taken from ref. 54]

photoinduced transition is first order, as is the field-induced transition. Repeated our X-ray measurements in magnetic fields up to H_C and foud that the photoinduced transition

occurs faster under these conditions. Though the magnetization was not measured directly, the close analogy to the magnetic-field-induced transition implies that the magnetic properties of the sample change dramatically with illumination, from canted antiferromagnetic to ferromagnetic state. To our knowledge, a photoinduced antiferromagnetic-to-ferromagnetic transition has thus far not been observed.

1.1.9 Phase Separation

A fascinating phenomenon, recently found to occur in certain transition-metal oxides, is phase separation where in pure, nominally monophasic oxides of transition metals with well-defined compositions separate into two or more phases over a specific temperature range. Such phase separation is entirely reversible, and is generally the result of a competition between charge localization and delocalization, the two situations being associated with contrasting electronic and magnetic properties. Coexistence of more than one phase, therefore, gives rise to electronic inhomogeneity and a diverse variety of magnetic, transport, and other properties, not normally expected for the nominal monophasic composition. An interesting feature of phase separation is that it covers a wide range of length scales anywhere between 1 ± 200 nm. While cuprates and manganites, especially the latter, provide excellent examples of phase separation, it is possible that many other transition-metal compounds with extended structures will be found to exhibit phase separation.

A macroscopically homogeneous mixed oxide with no tendency towards chemical phase separation, for example in $RMnO_3$ and $RAMn_2O_6$, must nevertheless be inhomogeneous on an atomic scale due to distribution of R^{3+} and A^{2+} on the A-sites of the perovskite structure. A random potential due to A-site cation disorder (or the stronger

effect of cation vacancies in nonstoichiometric oxides) creates localized states in the tail of the conduction band(s) derived from the e_g (Mn) and 2p(O) orbitals. In orthorhombic end-members such as $LaMnO_3$, and in compounds with a small value of x (≤ 1), this e_g band is split by a static Jahn-Teller (JT) distortion (Mn^{3+}-$3d^4\{t_{2g}^3 e_g^1\}$ in an octahedral site is a strong JT ion). Hence the Fermi level lies in a band tail. However, in the conduction rhombohedral phase at $x \leq 0.3$, where the JT distortion is dynamic or entirely absent, the Fermi level is expected to lie far from a mobility edge.

The phase diagrams of manganites are temperature versus composition plots. Even if the oxides are chemically homogeneous in the sense that x is macroscopically uniform, there is the possibility of 'electronic' phase separation into electron-rich and electron-poor regions with short range spatial range fluctuations in the local 3d electron density. Phase separation on a large scale is impossible because the coulomb fields created would return a conducting system to some semblance of local charge neutrality, but electronic heterogeneity on a short length scale can be envisaged.

The experimental phase diagrams published for the various manganite systems, where R=La, Pr; A= Ca, Sr, Ba, do not generally take phase separation into account. In this sense, they are unlike normal binary phase diagrams where two-phase regions and the associated eutectoid and peritectoid structures separate regions of extended solid solubility. On the manganite diagrams, every region appears either as a line compound or as a region of solid solubility; there seem to be no two-phase diagram.

Phase separation can be classified into two broad categories[55] i.e. reversible and irreversible phase separation as shown in fig.1.26.

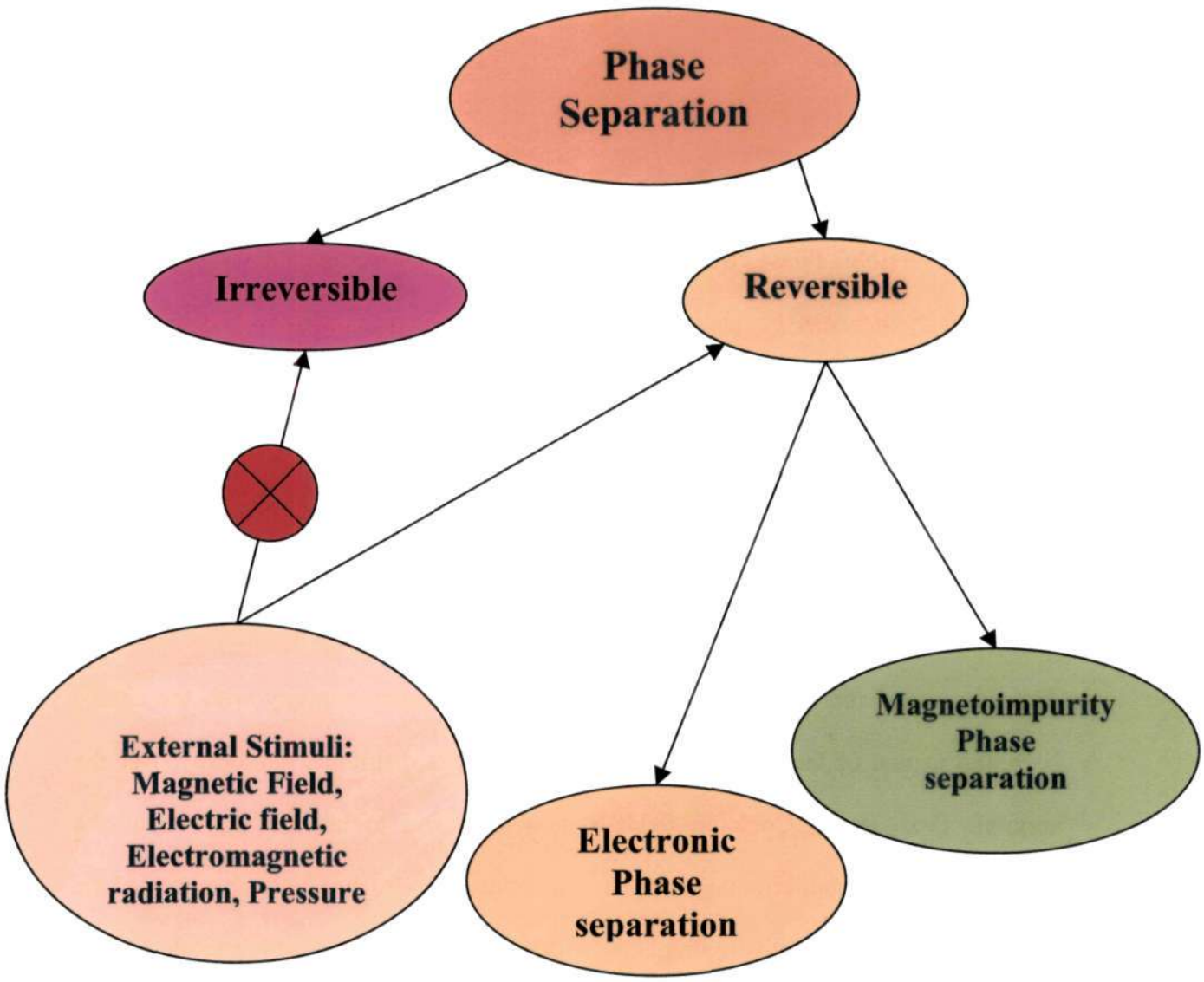

Fig. 1.26 Phase separation and its classification.

a) Irreversible Phase Separation: This phase separation is caused by inhomogeneity of the chemical composition of a sample, for example, due to the nonuniformity of the impurity distribution over a sample, which arises at the moment of its synthesis at elevated temperatures and remains frozen after its cooling. Such a phase separation is not sensitive to external factors (temperature or magnetic field) and for this reason it is an individual property of each concrete sample.

b) Reversible Phase Separation: Reversible phase separation is the phase separation, which can be changed under external factors, and this change happens normally by two mechanisms. i.e. electronic phase separation and magnetoimpurity phase separation.

Electronic Phase Separation: In the case of electronic phase separation, concentration of the charge carriers in a portion of the crystal, where they cause appearance of the ferromagnetic ordering, leads to the mutual charging of both the phases. This is a consequence of the fact that the ionized donor or acceptor impurity with the charge opposite to that of the charge carriers, unlike them, is distributed uniformly over the crystal. Thus, strong Coulomb fields arise which tend to intermix regions of the ferromagnetic and antiferromagnetic phases and thus to lower the Coulomb energy of the system involved. At relatively small carrier densities, the high-conducting ferromagnetic regions form separated, not making contacts with each other, droplets inside the insulating antiferromagnetic host (fig.1.27 (a)). As they are separated from each other by the insulating layers, the crystal as a whole is an insulator at $T = 0$ (if one neglects the tunnel currents flowing between droplets).

On increase in the carrier density, the volume of the ferromagnetic phase also increases and, beginning from a certain critical density n_p, the ferromagnetic droplets begin to make contacts with each other, i.e. percolation of the ferromagnetic ordering, as well as of the charge carrier liquid, occurs. This means that the concentration insulator-to-metal transition takes place. On further increase in density, the geometry of the two-phase state changes drastically: the ferromagnetic region transforms from multiply-connected to simply-connected. In other words, the ferromagnetic portion of the crystal consists of separated droplets inside the ferromagnetic host (fig.1.27 (b)). And lastly, at still more higher carrier density, the entire crystal becomes ferromagnetic.

Such an electronic phase separation realizes in heavily doped antiferromagnetic EuSe and EuTe semiconductors (see experimental verification of this statement[55])

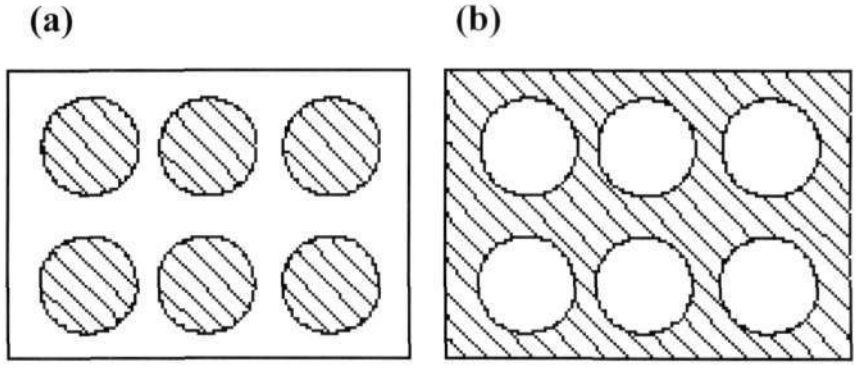

Fig.1.27 The phase-separated state of a degenerate antiferromagnetic semiconductor: (a) insulating state; (b) conducting state (hatched is the ferromagnetic part and nonhatched is the antiferromagnetic part of the crystal). [Taken from ref. 55]

Impurity phase separation: An alternative to the electronic phase separation is the magnetoimpurity phase separation which is caused by two factors simultaneously:

(1) Interaction between impurity donor or acceptor atoms resulting in the formation of an 'impurity metal', which consists of them. In other words, delocalization of the charge

carriers occurs according to the well-known Mott mechanism. In full analogy with the conventional metal, the tendency appears to establish such an interatomic spacing, which provides the minimum to the total energy of the system. If the mean impurity density over the crystal is less than this optimal density, then it is energetically favored for the impurity atoms to concentrate in a certain portion of the crystal. Then the remaining part of the crystal will not contain them at all.

(2) The same tendency of charge carriers to establish the ferromagnetic ordering, as at the electronic phase separation, makes the electrons or holes to assemble together in a portion of the crystal where they establish jointly this ordering. But, along with them, in one or another area of this portion the 'parent' impurity atoms also assemble.

An essential difference between the impurity phase separation and the electronic phase separation is the absence of the mutual charging of the phases at the former, as the electron or hole charges are compensated for the charges of impurity ions diffusing together with carriers. As a result, the ferromagnetic regions can be sufficiently large in size even at small carrier densities. But here the region size is limited by the elastic forces, which do not allow, for example, a crystal of a macroscopic size to be separated only into two regions of different phases. For this reason, on increase in the carrier density, the topology of the high-conducting ferromagnetic portion should change here at a certain percolation density n_p, which occurs jointly with the concentration phase transition from the insulating state to the high-conductive one.

In principle, at the impurity phase separation the magnetic field should also increase the size of the ferromagnetic regions, thus facilitating the electron tunnelling between

them. Hence, the very fact of the phase separation serves here as one of the possible mechanisms of negative magnetoresistance, too.

On increasing the temperature, the phase-separated state should be broken, and the impurity distribution over the crystal should become uniform. Thus, the mean impurity density will be less than the local density in impurity-rich regions. Meanwhile, the delocalization of electrons belonging to the donor impurity or holes belonging to the acceptor impurity can take place only at sufficiently large impurity densities. Hence, the situation is possible principally, when, on destruction of the insulating impurity-phase-separated state of the fig.1.27 (a)-type, the crystal does not go over into the high-conductive state. Actually, if the impurity density in the impurity-rich regions was sufficiently large for the electron (hole) delocalization, the mean density may turn out to be insufficient for this aim after destruction of the phase-separated state. The mean impurity density may also be sufficient for the metallization, though, and then destruction of the phase-separated state will lead to the crystal transition to the high conductive state. In the case of the fig.1.27 (b)-type geometry, destruction of the phase-separated state does not change the metallic type of the conductivity. Certainly, in order to realize the impurity phase separation, the impurity-atom diffusion coefficient must be sufficiently large at actual temperatures. There is direct experimental evidence that the oxygen diffusion coefficient is high in many perovskites: at room temperatures it may reach values of the order of 10^{-9} cm^2 s^{-1}, which ensure oxygen rapid diffusion at these temperatures. Moreover, in the $La_2CuO_{4+\delta}$ perovskite, separation into the oxygen-rich and oxygen-poor regions occurs even at 265 K. There exist many other HTSCs in which the impurity phase separation was discovered[55].

For the case of manganite which are the focus of this thesis the phase diagram of $La_{1-x}Ca_xMnO_3$ serves as a typical example of phase separated system is shown in fig.1.28 and (b). $La_{0.5}Ca_{0.5}MnO_3$ changes to a FM phase on cooling to 220 K (T_C) and then to a charge-ordered AFM phase around 150 K (T_{CO}). This manganite is best described as magnetically phase separated over a wide range of temperatures[56]. At low temperatures

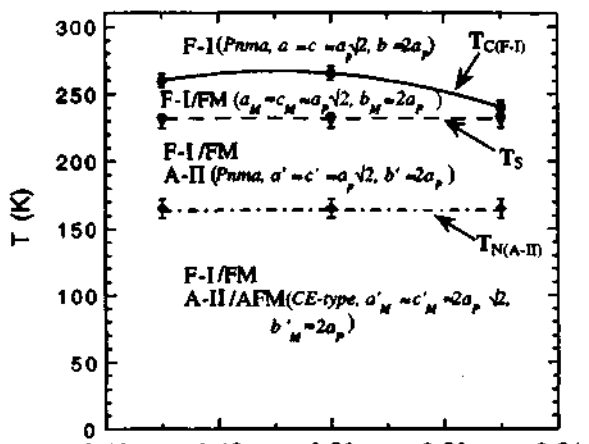

Fig.1.28 Phase diagram of $La_{1-x}Ca_xMnO_3$ in the range of compositions $0.47 \leq x \leq 0.53$. The horizontal curves separate, going from top to bottom: i) the FM transition of the F-I crystallographic phase at ~260 K; ii) the formation of the low-temperature A-II phase, which appears at ~230 K; and iii) the AFM transition that occurs in the A-II structure at ~160 K (T_N). As shown in the diagram, the ferromagnetically ordered F-I phase and the antiferromagnetically ordered A-II phase coexist at low temperatures. [Taken from ref. 55]

($T < T_{CO}$), FM metallic domains are trapped in the charge-ordered AFM matrix, giving rise to percolative metallic conduction. The fraction of the FM phase at low temperatures is highly dependent on the thermal treatment. Even within the FM phase, in the $T_{CO} < T < T_C$ region, there is phase separation. A second crystallographic phase, probably without magnetic order, has been identified[56]. The phase diagram of $La_{1-x}Ca_xMnO_3$ in the $0.47 \leq x \leq 0.5$ range (fig.1.28) reveals the nature of phase separation. Magnetization studies

show three phase separated regimes: $T_C>T>T_O$, $T_O>T>T_{CO}$ and $T<T_{CO}$, in which T_O is the onset temperature below which the cooling field plays an unbalancing role in favor of the FM state[56]. It is in the last regime that minority FM domains are embedded in the AFM matrix. In the first regime near the T_C, the FM phase grows freely with the application of a magnetic field. In fig.1.29 the phase diagram of $La_{1-x}Ca_xMnO_3$ is shown which includes

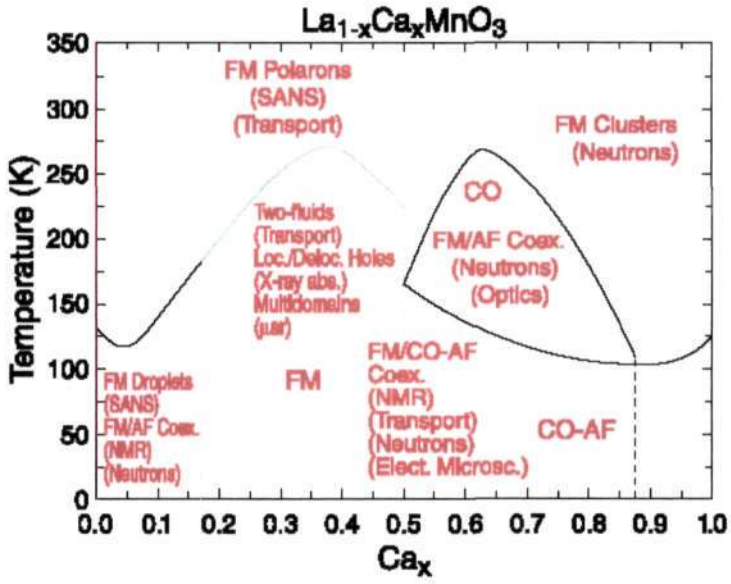

Fig.1.29 Schematic phase diagram of $La_{1-x}Ca_xMnO_3$. The use of words such as droplets, domains, polarons, clusters, and others indicate a tendency toward inhomogeneous behavior, present in most of the phase diagram. [Taken from ref.55]

i showing the experimental techniques applicable in the different regimes.

Phase separation in metal oxide systems has emerged to become a phenomenon of importance, because of the diversity of properties found in the rare earth manganites. We have seen few possible scenarios of phase separation schematically. These scenarios roughly represent the experimental observations in the rare-earth manganites. Phase separation has been observed recently in real space with atomic-scale resolution[57]. It seems likely that phase separation will be found in materials in which the electronic or

magnetic properties vary strikingly over extremely narrow composition ranges. For most classes of materials this is not the case, but in highly correlated systems, instability towards phase separation and formation of inhomogeneous states may be an intrinsic property[34]. For example, phase separation is suspected to be responsible for the occurrence of two magnetic transitions in Sr_3CuIrO_6[58]. The compositional FM±AFM transition accompanying changes in electron bandwidth found in $La_{1-x}Y_xTiO_3$, coexistence of FM and paramagnetic phases in $La_{1-x}Sr_xCoO_3$, and the compositional AFM ± FM transition in $Ca_{2-x}La_xRuO_4$ are all likely to be associated with phase separation[59] What is important to note is that phase separation occurs over a large length scale from a few angstroms to a few hundred nanometers. The domain sizes of the component phases clearly determine the properties of the material.

1.2 SCOPE OF THE PRESENT INVESTIGATIONS

Rare earth manganites of the formula $Ln_{1-x}A_xMnO_3$ (Ln=rare earth, A=alkaline earth) exhibit important phenomena such as colossal magnetoresistance (CMR) and charge ordering and phase separation[1-6]. Charge ordering in the manganites is specially interesting since it competes with double exchange, giving rise to interesting properties. Charge ordering, favored in certain compositions such as those with x = 0.5 is associated with insulating behavior and antiferromagnetism. Charge ordering and other properties of the manganites is highly sensative to the average radius of the a-site cation $\langle r_A \rangle$ which in turn is related to e_g bandwidth. Two types of charge ordering can be distinguished in the manganites. In manganites such as $Nd_{0.5}Sr_{0.5}MnO_3$ with a relatively large average radius of the A-site cations, $\langle r_A \rangle$, a ferromagnetic metallic (FMM) state (T_c= 250 K) transforms to a charge-ordered (CO) state on cooling to ~150 K. Manganites with a small $\langle r_A \rangle \leq$

1.17 Å, do not exist in the FMM state at any temperature, but instead are charge-ordered at relatively high temperatures. The CO state in a manganite with a relatively large A-site ion radius ($\langle r_A \rangle \geq 1.17$ Å) can be transformed to the FMM state by the application of magnetic fields. On the other hand, large magnetic fields ($\geq$ 20 tesla) have negligible effect on the CO state of $Nd_{0.5}Ca_{0.5}MnO_3$ with a $\langle r_A \rangle$ of 1.17 Å. In the case of $Y_{0.5}Ca_{0.5}MnO_3$ ($\langle r_A \rangle = 1.13$ Å), even fields close to ~100 tesla have no effect[75]. The CO state in single crystals of $Pr_{1-x}Ca_xMnO_3$ has been transformed to the FMM state by applying electric fields or by laser irradiation[67,70].

An examination of the literature showed that there was little or no effort to prepare thin films of the charge-ordered manganites, although thin films of the manganites showing CMR have been prepared by various means[76-79]. In this thesis, the successful preparation of thin films of the charge-ordered manganites, $Nd_{0.5}Ca_{0.5}MnO_3$(NCM), $Y_{0.5}Ca_{0.5}MnO_3$(YCM) and $Nd_{0.5}Sr_{0.5}MnO_3$(NSM) on single crystal substrates by employing nebulized spray pyrolysis of organometallic precursors is investigated in detail[60-62]. More importantly, the electric current-induced transition from the insulating CO state to the metallic state in these films is noteworthy. It is noteworthy that the insulator-metal (I-M) transition in the thin films of the CO manganites is brought about by passing small currents. Even $Y_{0.5}Ca_{0.5}MnO_3$ with a very small $\langle r_A \rangle$ exhibits this phenomenon although high magnetic fields have no effect on the CO state in this material. Furthermore, the films show nonohmic behavior and interesting memory effects. There was no need to create photocarriers by laser irradiation prior to carrying out the electrical resistivity measurements as suggested by some of the workers. We have also carried out low frequency conductivity noise studies on $Nd_{0.5}Ca_{0.5}MnO_3$ films on

Si(100) which reveal the existence of a threshold field in the charge ordered regime beyond which strong nonlinear conduction sets in along with a large broad band conductivity noise.

Since the study of films of $Ln_{0.5}A_{0.5}MnO_3$ showed that the CO states are destroyed by small electric currents in these materials, independent of $\langle r_A \rangle$, giving rise to interesting I–M transitions. It appeared important to investigate the effect of electric fields on epitaxial films of $Pr_{1-x}Ca_xMnO_3$ which is a prototype CO system. The I–M transition in thin films of $Pr_{1-x}Ca_xMnO_3$ (x = 0.3 and 0.4) induced by electric field alone as well as by a combination of electric and magnetic fields are examined.

A comparative study of hole-doped $Pr_{0.6}Ca_{0.4}MnO_3$ and electron-doped $Pr_{0.4}Ca_{0.6}MnO_3$ has also been carried out, since properties of the later are considerably different. Thus, the electron-doped manganites do not exhibit the FMM state and the CO state is not affected by magnetic fields[80]. The study includes the effect of both magnetic and electric fields on the properties of the films. Small electric fields are shown to produce marked effects on the properties of both these types of manganites and bring about an insulator-metal (I-M) transition with the concomitant melting of the charge ordered state. We have also examined the effect of doping $Pr_{0.6}Ca_{0.4}MnO_3$ and $Pr_{0.4}Ca_{0.6}MnO_3$ with 3% Cr^{3+} and Ru^{4+}. These impurities are known to significantly effect on the properties of certain charge-ordered manganites rendering them ferromagnetic and metallic in certain instances.

Since charge-ordering in the three-dimensional manganites is sensitive to a variety of factors, such as the average radius of the A-site cation, impurity doping in the Mn-site, pressure, as well as magnetic and electric fields, one would expect dimensionality to

affect the CO states as well. Dimensionallity has a marked effect on the colossal magnetoresistance (CMR) and related properties in these materials[1]. Charge-ordering occurs in $La_{0.5}Sr_{1.5}MnO_4$, which is a single layered manganite with K_2NiF_4 structure. It has been shown to occur in bilayered $LaSr_2Mn_2O_7$ at around 210 K, but the CO state collapses at low temperatures. It is suggested that charge ordering in $LaSr_2Mn_2O_7$ is dominated by A-type antiferromagnetic ordering rather than CE-type ordering, implying that $d(x^2-y^2)$ orbital ordering is more important than $d(3x^2-r^2)$/ $d(3y^2-r^2)$ orbital ordering. Charge-ordering in thin films of bilayered rare earth manganites deposited on different substrates has been investigated, in order to explore the nature of changes in the electrical resistivity at the charge ordering transition and the effects of magnetic and electric fields. For this purpose, thin films of the bilayered $LnSr_2Mn_2O_7$ where Ln = La, Nd and Gd were prepared by nebulized spray pyrolysis.

1.3. EXPERIMENTAL

The films of the various metal oxides were prepared employing the simple, low cost, solution based chemical technique called nebulized spray pyrolysis.

1.3.1. Nebulized Spray Pyrolysis

Pyrolysis of sprays is a well-known method for depositing films and for making fine powders. A novel improvement in this technique is the so-called pyrosol process or nebulized spray pyrolysis involving the transport and subsequent pyrolysis of a spray generated by an ultrasonic atomizer as demonstrated by Joubert and coworkers[60-62]. Wold and coworkers[63-66] have employed this method to prepare thin films of a variety of oxides. This method seem to be an excellent compromise for obtaining thin films economically, which are adhesive homogeneous and with excellent physical properties.

The advantage of this technique is the ultrasonic atomization process. When a high frequency (100 kHz to 10 MHz) ultrasonic beam is directed at a gas-liquid interface, geyser forms at the surface and the height of the geyser is proportional to the acoustic intensity and the physical properties of the liquid (vapor pressure, viscosity and surface tension). The generation and cavitation at the gas-liquid interface accompany its formation.

(a) Ultrasonic Atomization

If a liquid is irradiated ultrasonically, above a certain excitation power threshold, leads to the atomization of fine droplets forming a spray. The correlation between the capillary wavelength (λ_c) at the liquid surface and the mean diameter of the atomized droplets (D) is one of the fundamental principles of ultrasonic atomization

$$D = \alpha \ \lambda_c \qquad (1)$$

Where α is the proportionality constant. Based on Kelvin's equation, the capillary wavelength can be written as,

$$\lambda_c = (8\pi\sigma / pf^2)^{1/3} \qquad (2)$$

where σ is the surface tension of the liquid, p its density and f the ultrasonic excitation frequency. The droplet diameter is therefore expressed in terms of σ, p and f.

$$D = \alpha (8\pi\sigma / pf^2)^{1/3} \qquad (3)$$

In the case of water, the most probable diameter of the atomized droplets varies from 2 to 30 microns when the frequency varies from 3 MHz to 70 kHz. In addition, the frequency dependence expressed by the relation (3) gives rise to a very narrow distribution in terms of number and volume of atomized droplets as shown in fig.1.30(a). This narrow distribution over more conventional pneumatic atomization techniques which give droplets whose size is difficult to control and a spray that always contain a certain percentage of large droplets fig.1.30(b)[60].

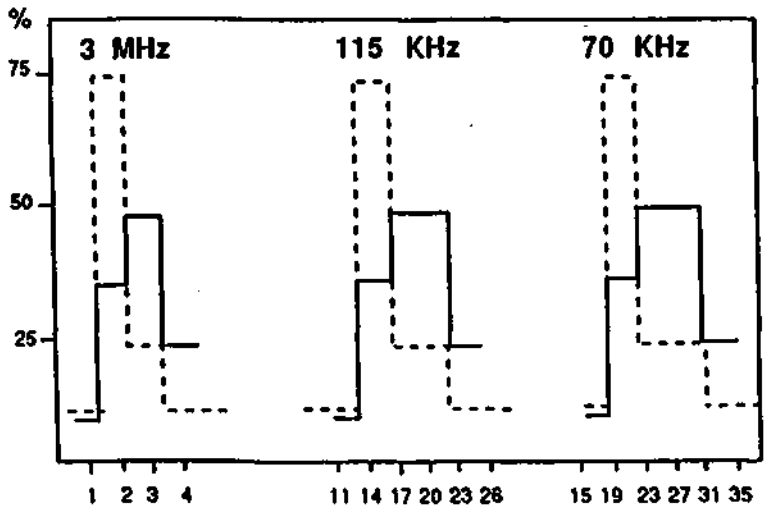

Fig.1.30 (a).The distribution of droplet diameter verses volume percentage for different frequencies for nebulized spray. [Taken from ref.60]

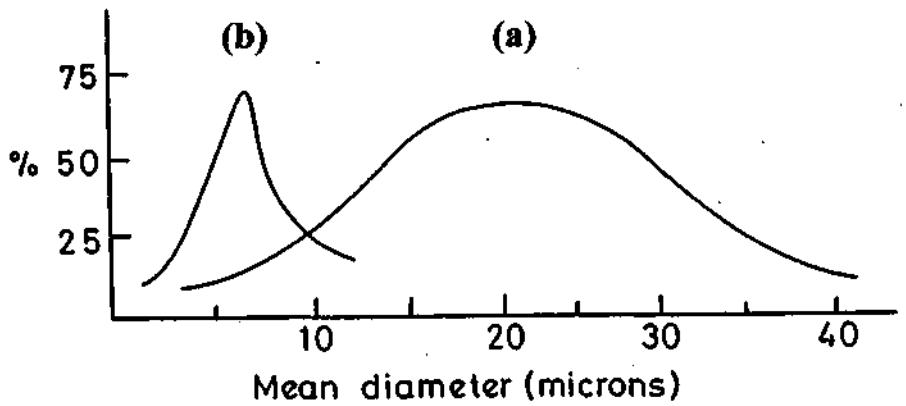

Fig.1.30 (b) The distribution of droplet diameter for the pneumatic spray.

The relation clearly shows that the mean diameter of the atomized droplets depends not only on the excitation frequency, but also on the characteristics of the irradiated liquid. The same is true for the quantity of the spray produced. It has been shown that, at constant carrier gas feed and flow rate, this production was an increasing function of the ratio,

$$\gamma = p_s/\sigma\eta \qquad (4)$$

where p_s represents the saturated vapor pressure of the liquid, σ its surface tension and η its dynamic viscosity. It is therefore theoretically possible to predict the atomization kinetics of the liquid if its physical properties are known.

(b) Atomization Process

The source liquid containing the relevant cations in the form of salts dissolved in an organic solvent is kept in the atomization chamber. A piezoelectric transducer (PZT) crimped to the base of the chamber is connected to a high frequency (1.72 MHz) generator of 10-40 watts power. By varying the voltage (with the frequency fixed at a value close to the resonant frequency of the PZT ceramic), the intensity of the geyser

which appears at the liquid surface, where the acoustic waves are focused, also varies. Liquid atomization occurs when the amplitude of the acoustic vibrations exceeds a certain value, considered to be a threshold for that liquid. Just above this threshold the mist produced is intermittent and corresponds to irregular disintegration of the geyser. At much higher values than the threshold, mist emission becomes continuous and regular. A constant level burette is used to ensure liquid level stability in the chamber and for in-situ measurement of the volume of the deposited liquid. The liquid height above the transducer is equivalent to the load of the PZT transducer and the mist formation also depends on this height.

During the atomization process, the liquid is heated at the tip of the geyser where the acoustic intensity is maximum. At this point, the temperature exceeds 375 K. Consequently a small portion of the atomized spray may change into the vapor state, which is detrimental to the spray homogeneity. To avoid this problem, the nozzle carrying the mist from the atomization chamber to the reactor must be designed sufficiently narrow and long to leave the vapors to re-condense into droplets during the transport stage. However, the nozzle should not be too long as collisions between the droplets during the transport may give rise to a considerable change in size distribution through a coalescence process. The length and diameter of the pyrosol reactor are 50 cm and 3 cm respectively.

(c) Pyrolysis

The pyrolysis reaction, which determines the deposition kinetics, takes place when the spray passes near the hot substrate. The temperature is controlled by a thermocouple placed at the heating support-substrate interface. This method of measurement and

substrate temperature control is the one most frequently used as it enables in-situ measurement without disturbing the deposition process.

Depending on the substrate temperature, several deposition processes can be considered and can be described in a simplified form by one of the four schemes (fig.1.31)

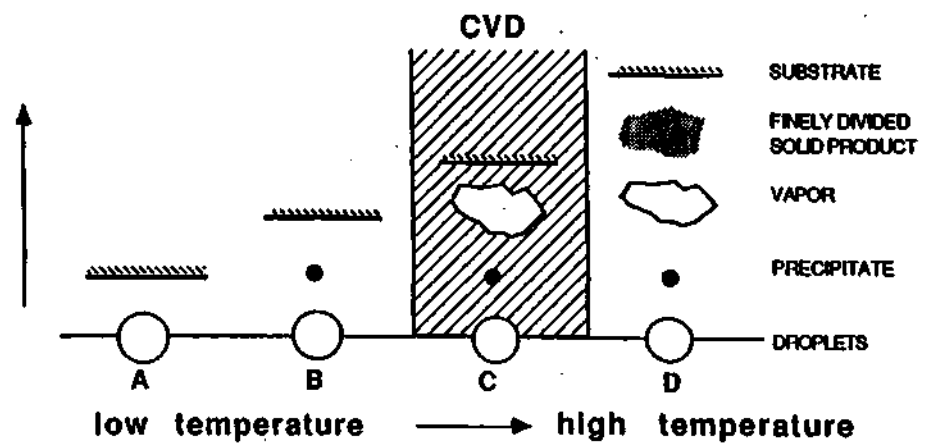

Fig.1.31 Various deposition reaction schemes for the nebulized spray pyrolysis process. [Taken from ref.60]

(a) At low temperatures (case A), the droplets reach the substrate in liquid state. The solvent in which the source compounds dissolved slowly evaporates leaving a finely divide precipitate on the substrate.

(b) At high temperatures (case B), the solvent has time to evaporate before reaching the substrate and the precipitate impacts the substrate in the solid state.

(c) At still high temperatures (case C), the solvent evaporation and precipitate sublimation occurs in succession. The vapors obtained will diffuse towards the substrate where they react chemically in heterogeneous gas-solid phase to give the final compound. This is a typical case of CVD.

(d) At excessively high temperatures (case D), the chemical reaction takes place before the vapor reaches the substrate. The product of this chemical reaction deposits on the substrate in fine powder form.

Although it is possible to obtain a coating in each case, the adherence is very poor in cases A, B and D. The adherence can be improved by appropriate annealing, although the resulting films will never have optical quality. However, the films obtained with the reaction process C, have excellent adherence and high optical quality, without the need for annealing. These deposits are perfectly crystalline. It is easy to see the advantage of a narrow droplet size range likely to react chemically before reaching the substrate, thereby giving a homogeneous deposits.

(d) Apparatus

The schematic diagram showing different parts of the nebulized spray pyrolysis apparatus fabricated by us is shown Fig.1.32. It consists of two independent zones.

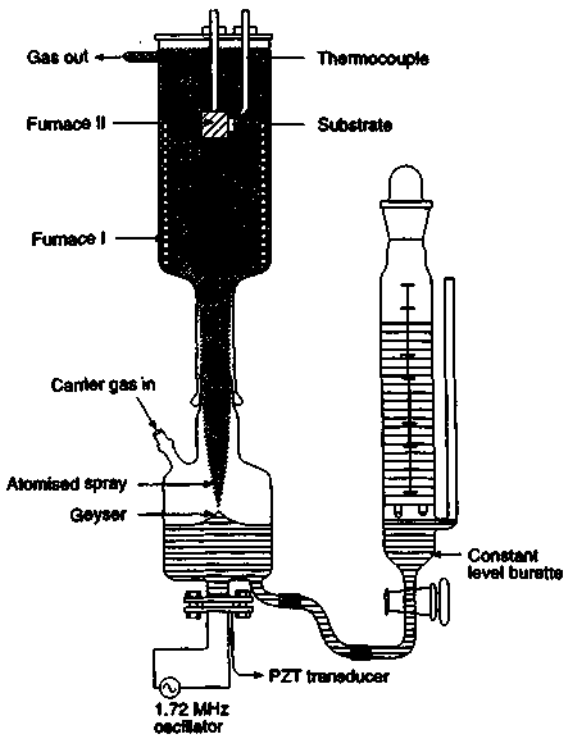

Fig.1.32 Nebulized Spray Pyrolysis Assembly.

1. The atomization chamber

2. The pyrolysis chamber

Atomization Chamber

The atomization chamber is constructed such that the bottom of the chamber is having 20 mm diameter and 1mm thickness. The special feature of our design is that the transducer is in direct contact with the liquid, thereby the energy transfer to the liquid is highest when compared to the non-contact methods. The disadvantage being the liquid pH has to be maintained at around 7. The liquid level in the atomizer chamber is maintained by using a constant level burette. A carrier gas introduced through a side port transports the spray produced in the first chamber.

Pyrolysis Chamber

The second zone is a long glass tube consisting of a heater (nichrome wire wounded on a ceramic tube), a substrate holder and a chromel-alumel thermocouple fixed to the substrate holder. The pyrolysis reaction product consists of a thin film, whose composition, adherence and morphology depend on the experimental conditions. These two zones can be completely dismantled for cleaning purposes. They are made off borosilicate glass as it gives excellent heat resistance and ease of fabrication. One of the features that make the whole process so simple is that this technique does not employ vacuum systems.

Ultrasonic atomization is accomplished by using an appropriate transducer (PZT) located at the bottom of the liquid container. The atomized spray is transported to the heater chamber by the carrier gas and is deposited on a suitable solid substrate.

1.3.2. Preparation of rare earth manganite films

Thin films of the charge ordered manganites of the formula $Ln_xA_{1-x}MnO_3$, where (Ln = Nd, Gd,Y and Pr; A = Ca and Sr; and x = 0.5) were deposited on Si(100) as well as on LAO(100) single crystal substrates by employing nebulized spray pyrolysis described in section 1.3.1. The precursors employed were $Nd(acac)_3$ (tris acetylacetanato neodymium), $Gd(acac)_3$ (*tris acetylacetanato gadolinium*), $Y(acac)_3$ (*tris acetylacetanato yttrium*), $Pr(acac)_3$ (tris acetylacetanato presynodium), $Ca(acac)_2$ (bis acetylacetanato calicum) and $Mn(acac)_3$ (tris acetylacetanato manganese) for $Nd_{0.5}Ca_{0.5}MnO_3$, $Gd_{0.5}Ca_{0.5}MnO_3$, $Y_{0.5}Ca_{0.5}MnO_3$, $Pr_{0.7}Ca_{0.3}MnO_3$, $Pr_{0.6}Ca_{0.4}MnO_3$, $LaSr_2Mn_2O_7$, $NdSr_2Mn_2O_7$, $GdSr_2Mn_2O_7$ and $Nd_{0.5}Sr_{0.5}MnO_3$. For $Pr_{0.6}Ca_{0.4}A_{0.03}Mn_{0.97}O_3$ and $Pr_{0.4}Ca_{0.6}A_{0.03}Mn_{0.97}O_3$ where A = Cr or Ru, $Cr(acac)_3$ (tris acetylacetanato chromium) and $Ru(acac)_3$ (tris acetylacetanato ruthinium) were employed. All the precursors were prepared from commerically available ligands and chloride/nitrate salts of the required elements. Films of ~1000 nm thickness were deposited at 650 K by using air as the carrier gas (1.5 liters/min).

1.3.3 Characterization techniques

The deposited films were studied by X-ray diffraction using a Seifert (xrd, xdl, θ-θ, Cu target) instrument. Conventional θ-θ scans were collected with a Bragg-Brentano goniometer and high resolution (169 eV) Si(Li) solid state detector with 0.5 mm/1 mm slits. The surface morphology of the films was observed by scanning electron microscopy (SEM) with a Leica S-440 i SEM. The film thickness was confirmed by cross-sectional scanning electron microscopy. The EDX analysis was done using Links

ISIS of Oxford intruement. Temperature-dependent resistivity measurements were carried out by employing close cycle refrigerator and sputtered gold electrodes. A constant d.c current was suuplied by Keithley constant current source (model 220). These gold electrodes had a constant distance of separation between them and sputtered with the help of a mask. Typical separations were 1mm, 0.5 mm and 0.2 mm and the length of electrodes were 10 mm, 8 mm and 5 mm. Magnetoresistance measurements were carried out by employing 15 tesla close-cycle cryocooled superconducting magnet (Cryo Industries of America).

1.4 Results and Discussion

1.4.1 X–ray diffraction studies of thin films of $Ln_{0.5}A_{0.5}MnO_3$ (Ln = Nd, Gd and Y; A = Ca or Sr)

The films of the manganites had a polycrystalline nature on a Si(100) substrate, but were oriented in the (100) direction on LAO(100) substrate. Fig.1.33 shows the X-ray

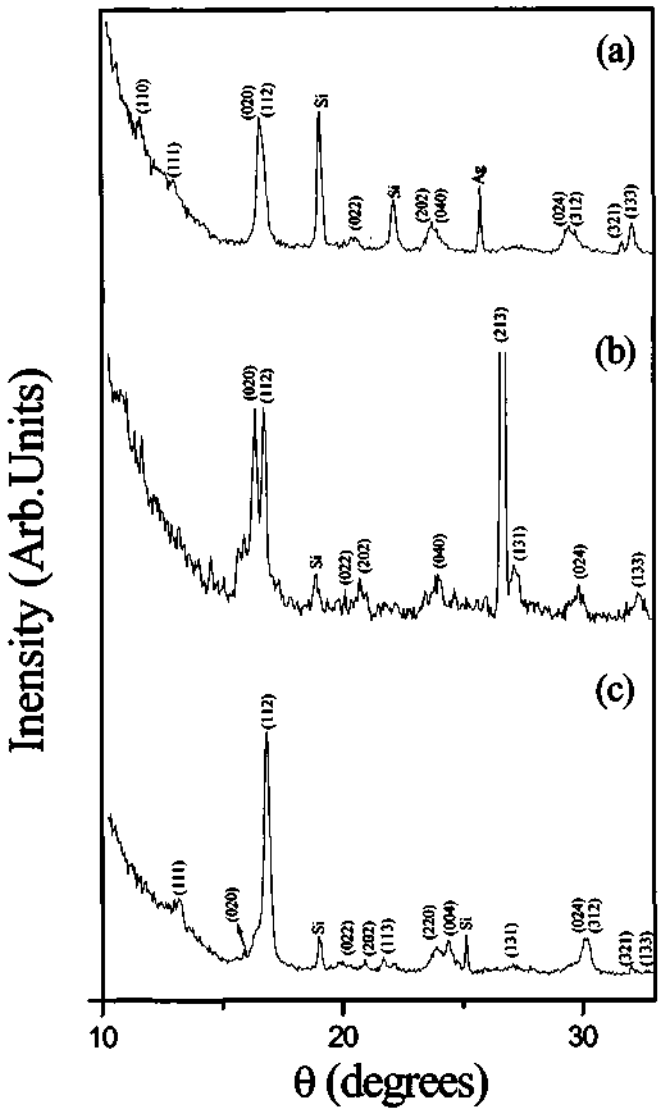

Fig.1.33 X-ray diffraction patterns of films of (a) $Nd_{0.5}Ca_{0.5}MnO_3$ (b) $Gd_{0.5}Ca_{0.5}MnO_3$ (c) $Y_{0.5}Ca_{0.5}MnO_3$ on Si(100).

diffraction patterns of the films of $Nd_{0.5}Ca_{0.5}MnO_3$, $Gd_{0.5}Ca_{0.5}MnO_3$ and $Y_{0.5}Ca_{0.5}MnO_3$

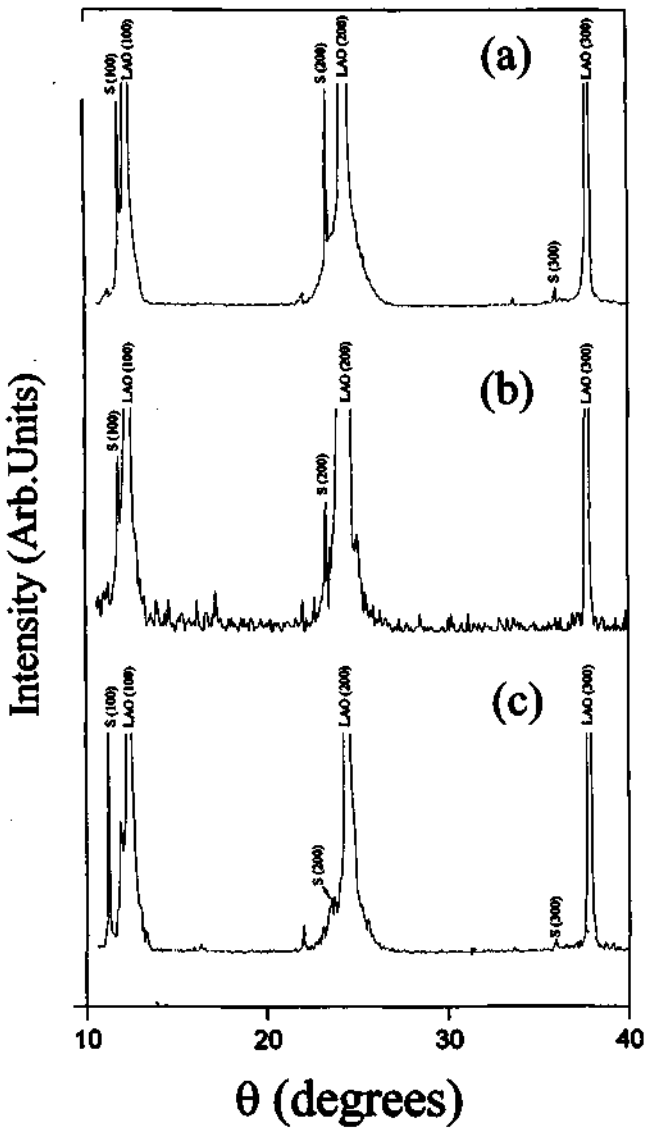

Fig.1.34 X-ray diffraction patterns of films of (a) $Nd_{0.5}Ca_{0.5}MnO_3$ (b) $Gd_{0.5}Ca_{0.5}MnO_3$ (c)$Y_{0.5}Ca_{0.5}MnO_3$ on LAO(100) `S' denotes reflections due to the rare earth manganite.

on Si(100). Fig.1.34 shows X-ray diffraction patterns of the films of $Nd_{0.5}Ca_{0.5}MnO_3$, $Gd_{0.5}Ca_{0.5}MnO_3$ and $Y_{0.5}Ca_{0.5}MnO_3$ on a LAO (100) substrate. In the patterns we see

only three reflections i.e. (100), (200) and (300) of the substrate LAO(100) and of the manganites. The reflections due to the manganites are weaker than those of the substrate. From this, we conclude that the films on LAO (100) are oriented in nature.

Figs.1.35 (a) and (b) show the x-ray diffraction patterns of the $Nd_{0.5}Sr_{0.5}MnO_3$ films on Si(100) and LAO(100). The films have polycrystalline nature on Si(100) and are oriented in (100) direction on LAO(100). The films show a metallic behavior from ~300 K.

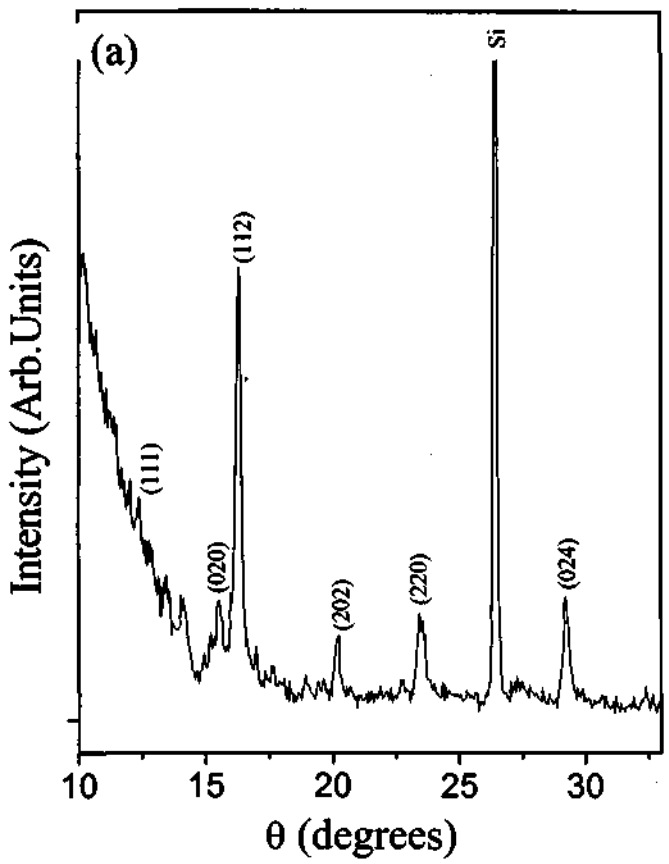

Fig.1.35 (a) X-ray diffraction pattern of a polycrystalline $Nd_{0.5}Sr_{0.5}MnO_3$ film on Si(100).

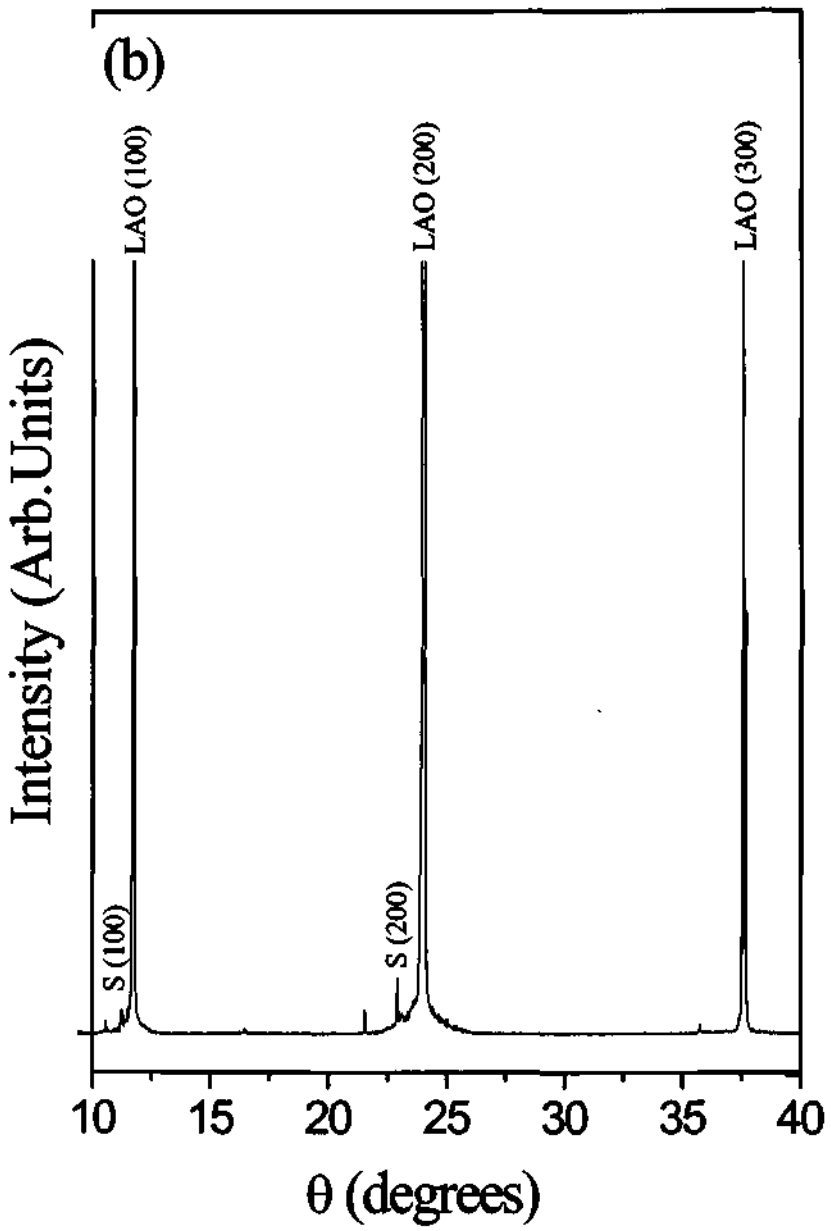

Fig.1.35 (b) X-ray diffraction pattern of a oriented $Nd_{0.5}Sr_{0.5}MnO_3$ film on LAO(100).

1.4.2 Electrical Transport Properties

$Ln_{0.5}Ca_{0.5}MnO_3$ (Ln = Nd, Gd or Y)

The electrical resistivity of the films was studied by the four-probe method. In fig.1.36, we show the temperature variation of the resistance of $Nd_{0.5}Ca_{0.5}MnO_3$ (NCM) films deposited on Si(100) and LAO(100) respectively, for different values of dc current passed. When the current is small (0.05 μA), the film on Si(100) shows insulating behavior. Upon increasing the current, we observe the occurrence of an insulator-metal (I-M) transition [fig.1.36 (a)]. It is noteworthy that even a current of 0.1 μA causes the I-M transition. (The values of the current density are 1.25 Acm^{-2} and 1.25 x 10^4 Acm^{-2} for 1 μA and 10 mA, respectively). The effects observed are not due to local Joule heating, which becomes appreciable only at high currents (≥ 50 mA). In fact, the irrelevance of the joule heating can be clearly seen in the low temperature metallic [temperature coefficient of resistance (TCR) > 0] regime accessible in fig.1.36 (a). Here the resistance for a given current increases with increasing temperature, while for a given temperature the resistance decreases with increasing current. Just the opposite would be true for a Joule heating. It is reasonable, therefore, to assume that joule heating is quiet irrelevant to our transport results, qualitatively at least. The temperature of the I-M transition shifts from 100 to 150 K with increase in current. The I-V curves show nonohmic behavior as shown in the inset of fig.1.36 (a) measurements on the oriented NCM film deposited on LAO (100) also shows a marked decrease in resistance with increasing current [fig.1.36 (b)]. We donot clearly see a metal-like decrease in resistance at low temperatures, and the behavior is comparable to that of laser-irradiated $Pr_{1-x}Ca_xMnO_3$ crystals reported by Ogawa[67] et. al. The oriented NCM films also show nonohmic behavior [see inset fig.1.36

(b)]. On the LAO substrate, a higher current is required to reduce resistance of the NCM film to the same extent as on the Si substrate.

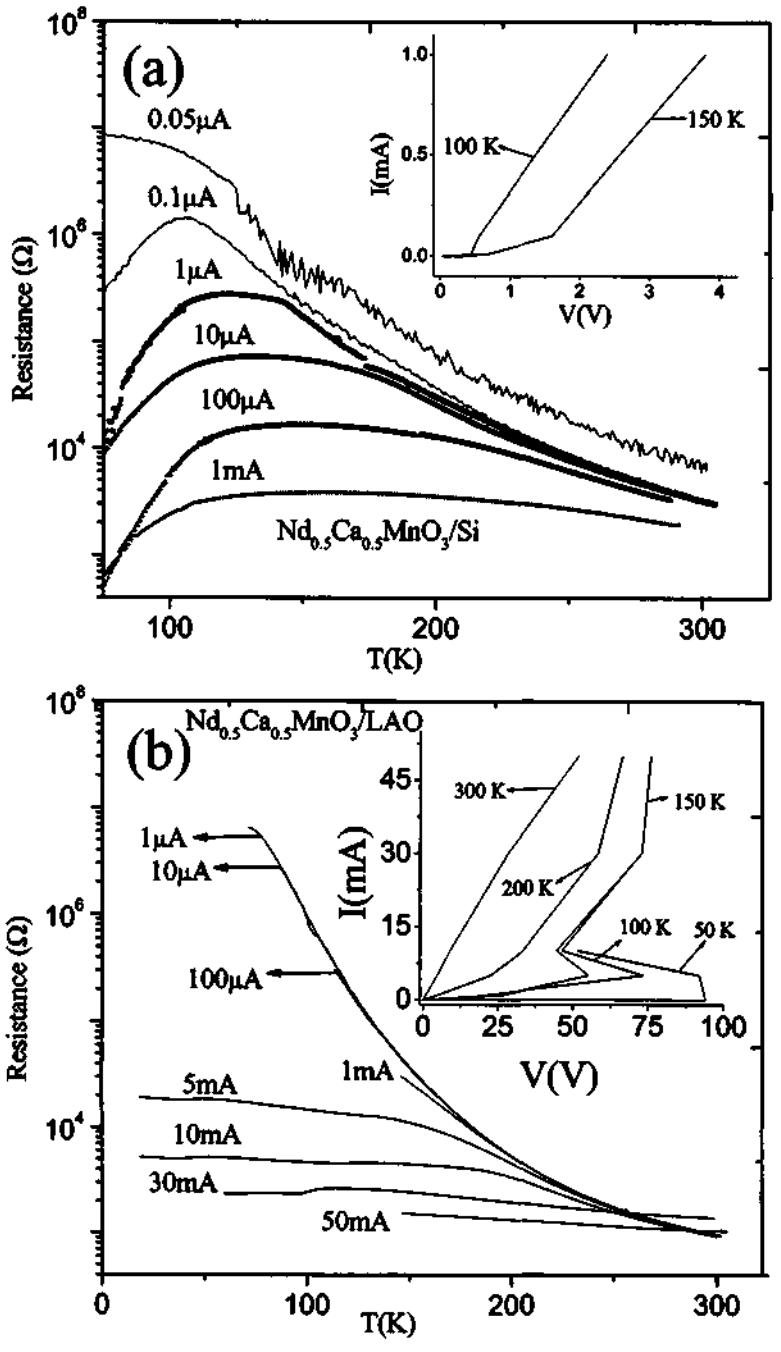

Fig.1.36 Temperature variation of the resistance of $Nd_{0.5}Ca_{0.5}MnO_3$ (NCM) films deposited on (a) Si(100) and (b) LAO(100) for different values of current. The insets show I-V characteristics at different temperatures.

In figs.1.37 (a) and (b), we show the effect of increasing the electric current on the resistance of $Gd_{0.5}Ca_{0.5}MnO_3$ (GCM) films deposited on Si(100) and LAO(100) substrates, respectively. The behavior is comparable to that of NCM films, particularly on LAO substrate. On Si(100) substrate, the GCM films show essentially flat resistance curves with almost no change with temperature, reminiscent of degenerate materials.

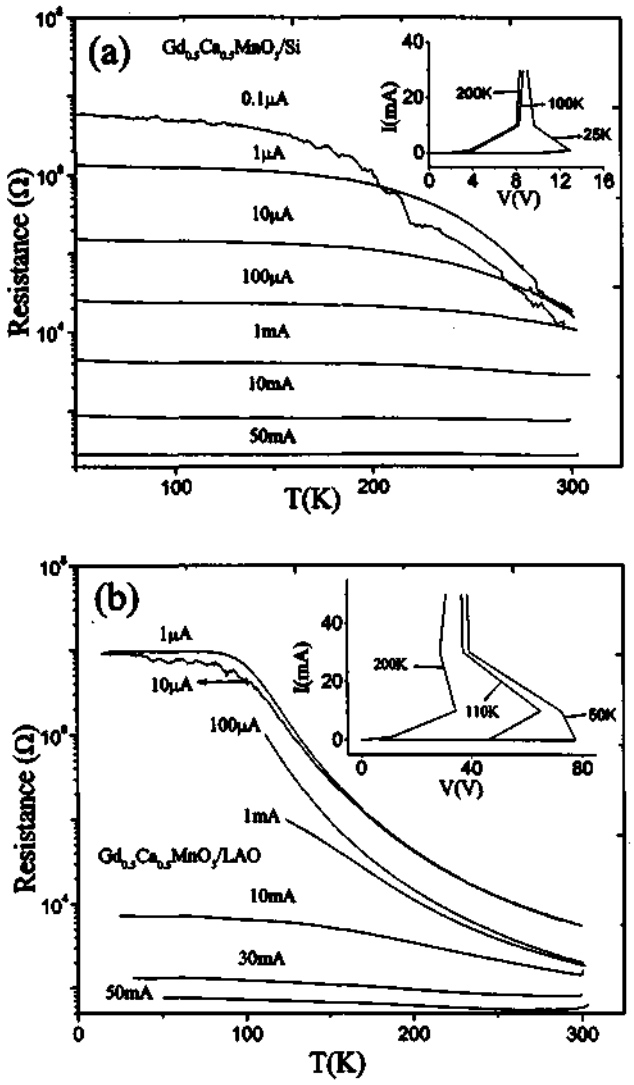

Fig.1.37 Temperature variation of the resistance of $Gd_{0.5}Ca_{0.5}MnO_3$ (GCM) films deposited on (a) Si(100) and (b) LAO(100) for different values of current. The insets show I-V characteristics at different temperatures.

This is especially noticeable when the current is ≥ 100 μA. On the LAO substrate, such near constancy of resistance is seen when the current is greater than 10 mA. Nonohmic behavior is found in the GCM films as well, as can be seen from the insets in figs.1.37 (a) and (b).

A particularly remarkable feature of NCM and GCM films deposited on LAO (100) substrates is the occurrence of a hysteretic I-M transition driven by transport current. We

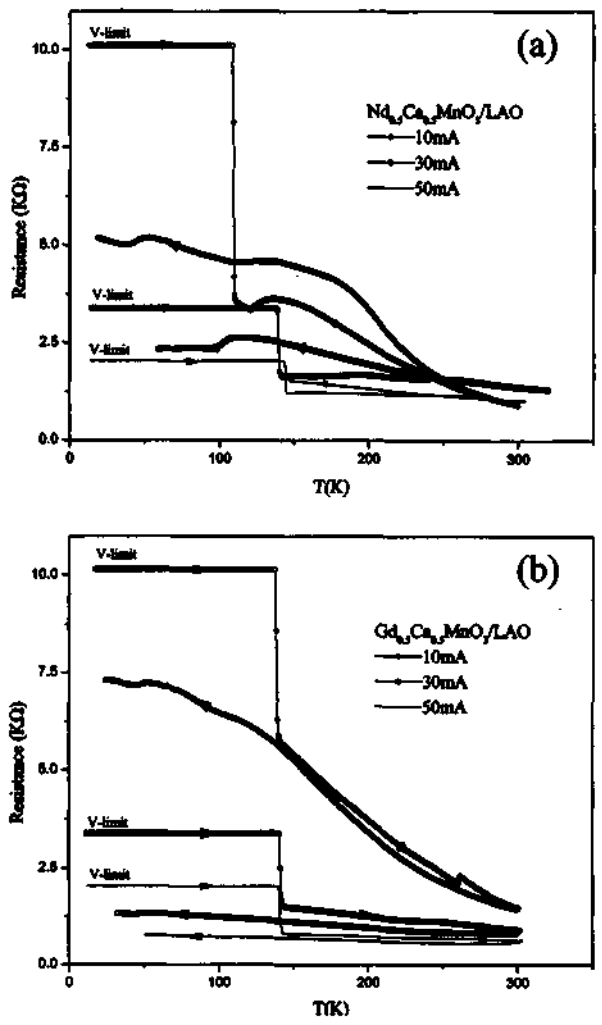

Fig.1.38 Resistance Vs temperature plots of (a) $Nd_{0.5}Ca_{0.5}MnO_3$ and (b) $Gd_{0.5}Ca_{0.5}MnO_3$ films deposited on LAO(100) for three different current values, recorded over cooling and heating cycles. The current was switched off after cooling curve was completed and turned on again to record the heating curve.

show typical data on these films in fig.1.38. The resistance temperature plots (at constant transport current) are as described earlier when the sample is cooled from room temperature. After attaining the lowest temperature the current is switched off and switched on again to carry out measurements as the films are heated. Note that at the current switching, the large resistance increases overloads the available current source used. Our current source overload was 105 V, thus causing overload when resistance is 105 MΩ, for a current of 10mA. (We do not have a source of higher voltage). The heating curves first show an abrupt increase in resistance followed by an equally abrupt drop around a temperature at which the charge solid apparently melts. The jumps in resistance to the original value on the cooling curve in the charge liquid state in indeed remarkable. Such a memory of the current-specific resistance value registered in the charge liquid state is an interesting property

In fig.1.39 we show the resistance Vs temperature curves for a YCM film on Si(100) for different values of the current. We observe substantial decrease in resistance with increase in current in YCM as well and the I-V behavior is non-ohmic. In fig.1.40, we show the resistance Vs temperature curves of $Y_{0.5}Ca_{0.5}MnO_3$ (YCM) film on LAO(100) for different values of the current. We observe a substantial decrease in the resistance with increase in the current and the I-V behavior is nonohmic [see inset of fig.1.40 (a)]. The occurrence of a current-induced I-M transition in the YCM film is noteworthy as the CO state in this material is very robust, being unaffected by magnetic fields or substitution of Mn^{3+} by Cr^{3+} and such ions[38]. The value of resistance at a given current varies as YCM > GCM > NCM, in same order as the $\langle r_A \rangle$. The memory effect discussed earlier is also found in the YCM film, as shown in fig.1.40 (b).

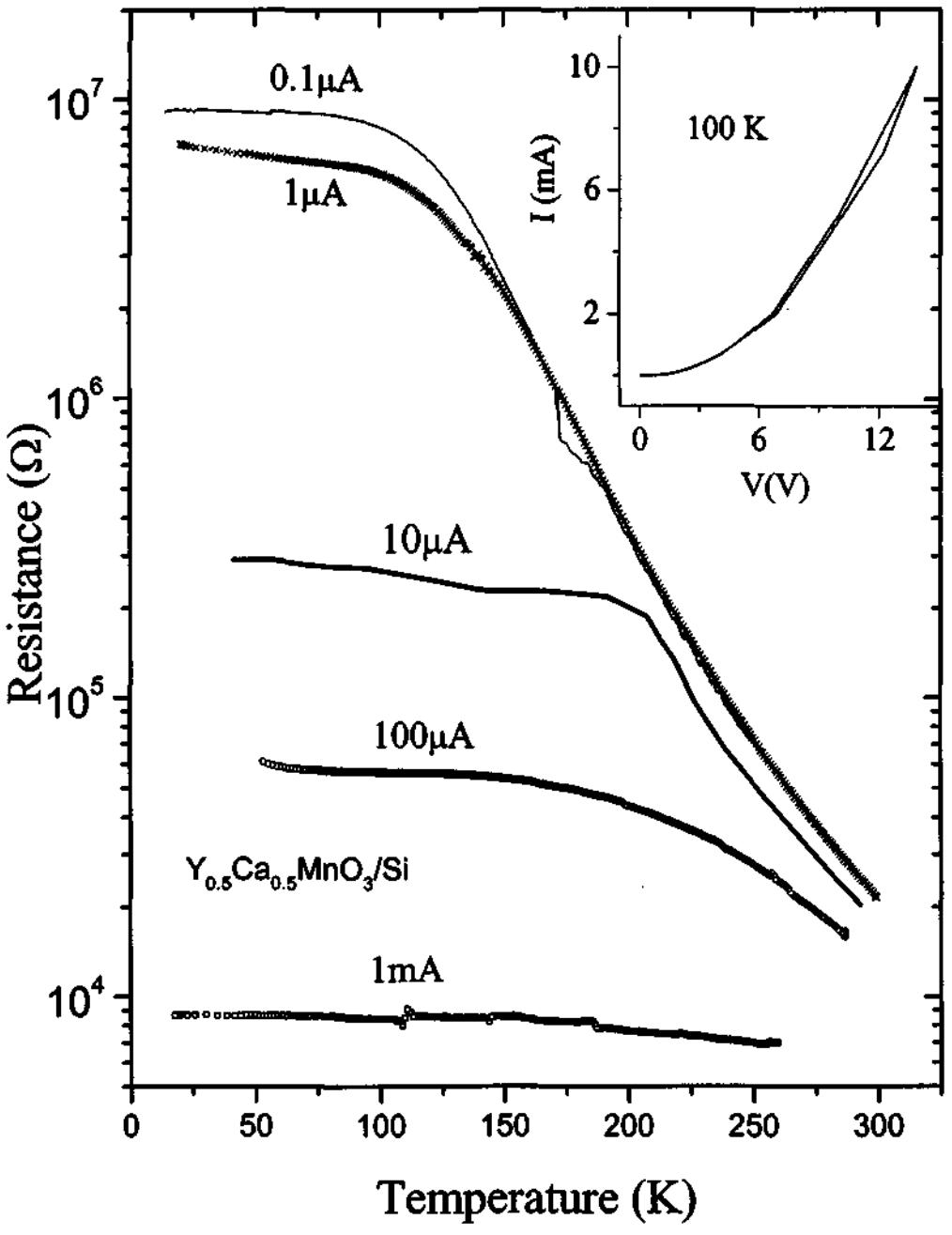

Fig.1.39 **Temperature variation of the resistance of a polycrystalline $Y_{0.5}Ca_{0.5}MnO_3$ film deposited on Si(100) for different values of current. Inset shows I-V characteristics at 100 K.**

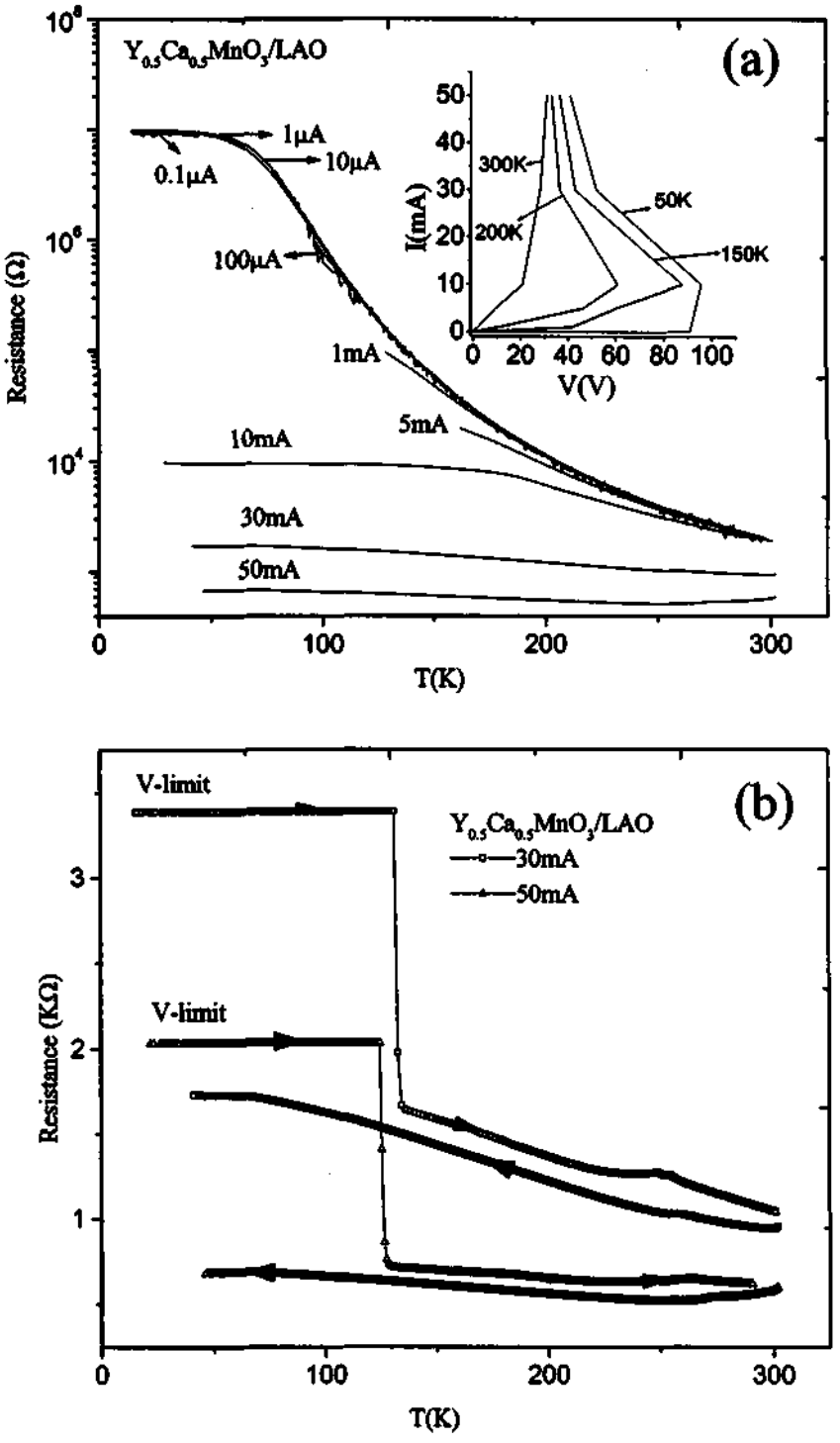

Fig.1.40 (a) Temperature variation of the resistance of a $Y_{0.5}Ca_{0.5}MnO_3$ (YCM) film deposited on LAO (100) for different values of current. The inset shows I-V characteristics at different temperatures. (b) Cooling and heating curves obtained as showing switching behavior.

$Pr_{0.7}Ca_{0.3}MnO_3$

In fig.1.41, we show the temperature variation of the resistance of a polycrystalline $Pr_{0.7}Ca_{0.3}MnO_3$ film deposited on Si(100), for different values of the dc current. With a current of 0.01 μA, the film shows a insulator-metal (I-M) transition at around 120 K. With increasing current, however, the resistance of the film decreases drastically and around 1 mA, the film shows a nearly metal-like behavior. The temperature of the I-M transition shifts from 120 to 150 K with increase in current. It is again ascertained that the observed effects were not to be due to Joule heating, which becomes apparent only at higher current values (>50 mA). In fact,

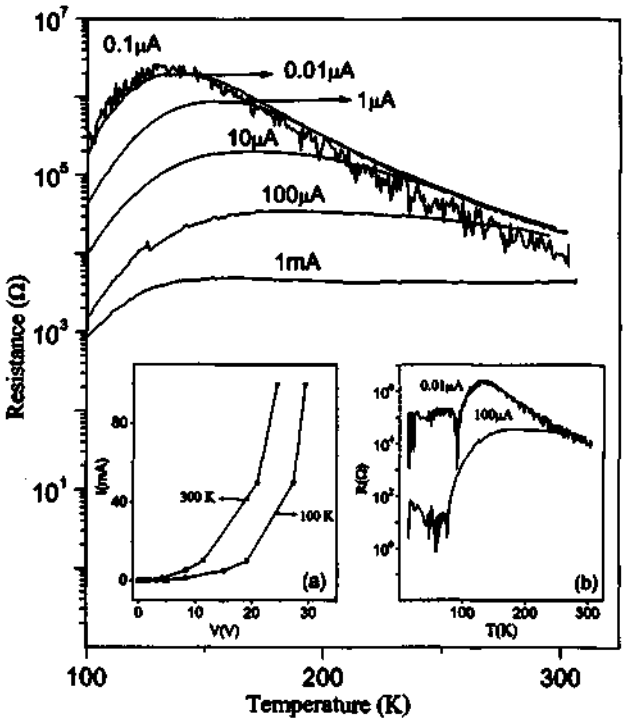

Fig.1.41 Temperature variation of resistance of a polycrystalline $Pr_{0.7}Ca_{0.4}MnO_3$ film deposited on Si(100) for different values of the current. Inset (a) shows I-V curves at different temperatures. Inset (b) illustrates the resistance oscillations found at low temperatures.

the irrelevance of the Joule heating can be clearly seen in the low temperature metallic (TCR>0) regime accessible in fig.1.41. Here the resistance for a given current increases with increasing temperature, while for a given temperature the resistance decreases with increasing current. Just the opposite would be true for a Joule heating. It is reasonable, therefore, to assume that the joule heating is quite irrelevant, to our transport results, qualitatively at least.

The current-voltage (I-V) curves show non-ohmic behavior as shown in the inset (a) of fig.1.41. In the low-temperature region, below 70 K, a noisy behavior is observed in the resistance-temperature plots due to temporal fluctuations between resistive states (see inset (b) of fig.1.41). Such fluctuations are suppressed at high currents.

Measurements on the highly oriented $Pr_{0.7}Ca_{0.3}MnO_3$ films deposited on LAO also show a marked decrease in resistance, with the resistance decreasing markedly with increasing current [fig.1.42 (a)]. We do not clearly see a metal-like decrease in the resistance at low temperatures,

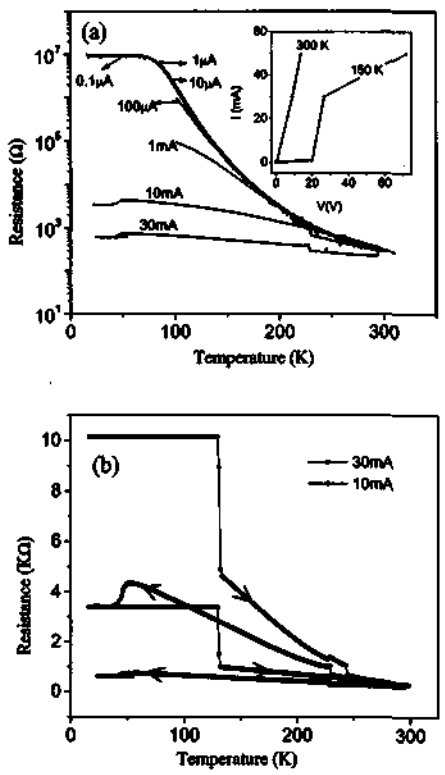

Fig.1.42 (a) Temperature-variation of resistance of an oriented $Pr_{0.7}Ca_{0.3}MnO_3$ film deposited on LAO(001) for different values of the current. (b) Resistance-temperature plots for two current values recorded over cooling and heating cycles showing memory effect. Inset in (a) shows I-V curves at different temperatures.

the behavior being similar to that in the I-M transition of laser-irradiated $Pr_{1-x}Ca_xMnO_3$ crystals[67,68]. Fig.1.42 (a) shows that the current-independent temperature-variation of resistance occurs when the current is lower than 10 μA. $Pr_{0.7}Ca_{0.3}MnO_3$/LAO films also show non-ohmic behavior [see inset of fig.1.42 (a)]. More interestingly, we observe the hysteretic I-M transition shown in fig.1.42 (b). The resistance-temperature plots at constant current in the cooling run are

as described earlier. When the current is turned off after reaching the lowest temperature (20 K), and switched on again, to carry out measurements in the heating run, the heating curves show an abrupt drop around a temperature at which the charge solid apparently melts. The

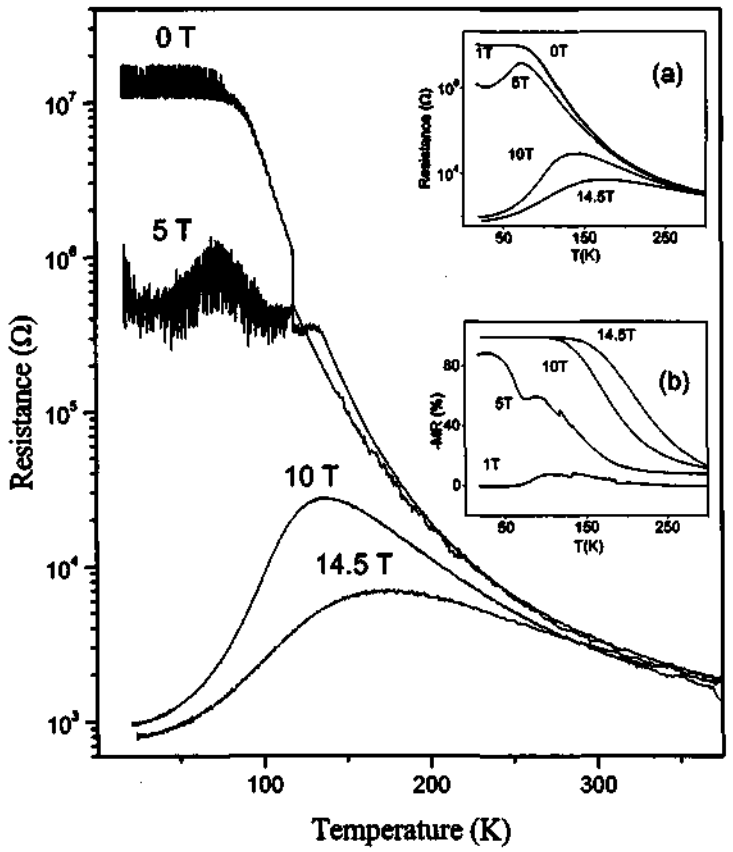

Fig.1.43 Temperature-variation of resistance of an oriented $Pr_{0.7}Ca_{0.3}MnO_3$ film deposited on LAO (001) substrate for different applied magnetic fields at a fixed current of 100 nA. Inset (a) is for 100 μA current. Inset (b) give temperature variation of magnetoresistance (MR).

jump in resistance to the original value of the cooling cycle is truly remarkable and such a memory of the resistance value in the CO states constitutes a novel property. The hysteretic curves could be reproduced after several cycles.

The temperature-variation of the resistance of the $Pr_{0.6}Ca_{0.4}MnO_3$ films deposited on Si(100) as well as on LAO(001) are similar to that of the $Pr_{0.7}Ca_{0.3}MnO_3$ films on the same substrates. These films also show the non-linear behavior.

We have examined the combined effect of electric and magnetic fields on the $Pr_{0.7}Ca_{0.3}MnO_3$ films deposited on LAO substrates. For this purpose, we have measured the

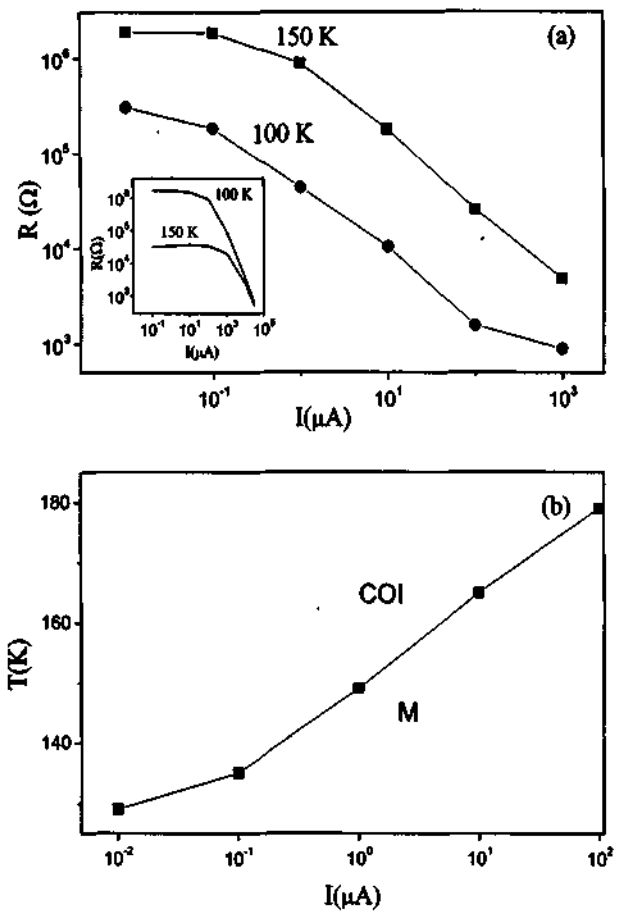

Fig.1.44 **(a) Current-induced variation in resistance at two different temperatures ; (a) $Pr_{0.7}Ca_{0.3}MnO_3$/Si, inset shows the curves for $Pr_{0.7}Ca_{0.3}MnO_3$/LAO. (b)Temperature-current phase diagrams showing the metallic (M) and charge-ordered insulator (COI) regimes.**

temperature-variation of the resistance at different magnetic fields for different fixed values of the current. In fig.1.43 we show the temperature-variation of the resistance at a low value of the current (100 nA) for different magnetic fields. At this current value, the oscillations at high resistance occurring at low temperatures are prominent up to 5 tesla, but disappears at higher magnetic fields. The oscillations disappear in the absence of magnetic field when the current is above 100 μA. Thus, at a current of 100 μA, we do not observe any oscillations as can be seen from the inset (a) of fig.1.43. The temperature of the magnetic-field-induced I-M transition increases from 70 K at 5 tesla to 160 K at 14.5 tesla when the current is 100 nA. The variation in the I-M transition temperature with the magnetic field is nearly the same when the current is

100 μA. The magnetic field induced I-M transition can be considered to be the colossal magnetoresistance of these films. The variation of magnetoresistance with temperature shown in the inset (b) of fig.1.43, reveals that colossal magnetoresistance between 60 and 80% occurs below 100 K at 5T and below ~165 K at 10 or 14.5 T.

In fig.1.44 (a) we have given the resistance-current curves at fixed temperatures to illustrate the current-induced I-M transitions. We observe a marked decrease in resistance above a value of the current. On the basis of current-induced I-M transition data, we have drawn the phase diagram in fig.1.44 (b). The I-M transition discussed here is not due to conventional dielectric breakdown. These transitions and associated properties can be considered to be due to electric-field induced depinning in the CO solid. A given transport current appears to select the same subset of pinning centers, hence giving the same resistance. This behavior in not unlike that found in charge density wave solids.

$Nd_{0.5}Sr_{0.5}MnO_3$

In fig.1.45, we show the temperature variation of resistance of a $Nd_{0.5}Sr_{0.5}MnO_3$ (NSM) film deposited on Si(100). The NSM films show metallic resistivity from ~300 K down to ~140 K and resistance increases below 140 K due to charge ordering. The increase in resistance in the CO state is not as sharp in the film as in a single crystal[36]. We, however, observe the high-temperature metallic behavior for all current values and the resistance decreases substantially in the charge-ordering regime, with increasing current. At 50 mA, the material remains metallic from 300 to 20 K, although there is a slight heating of the sample at this current value. The resistance values in NSM are considerably lower than in NCM and other films at similar currents. The NSM films also shows nonohmic behavior (see inset of fig.1.45). Mori[68] has recently observed effects in

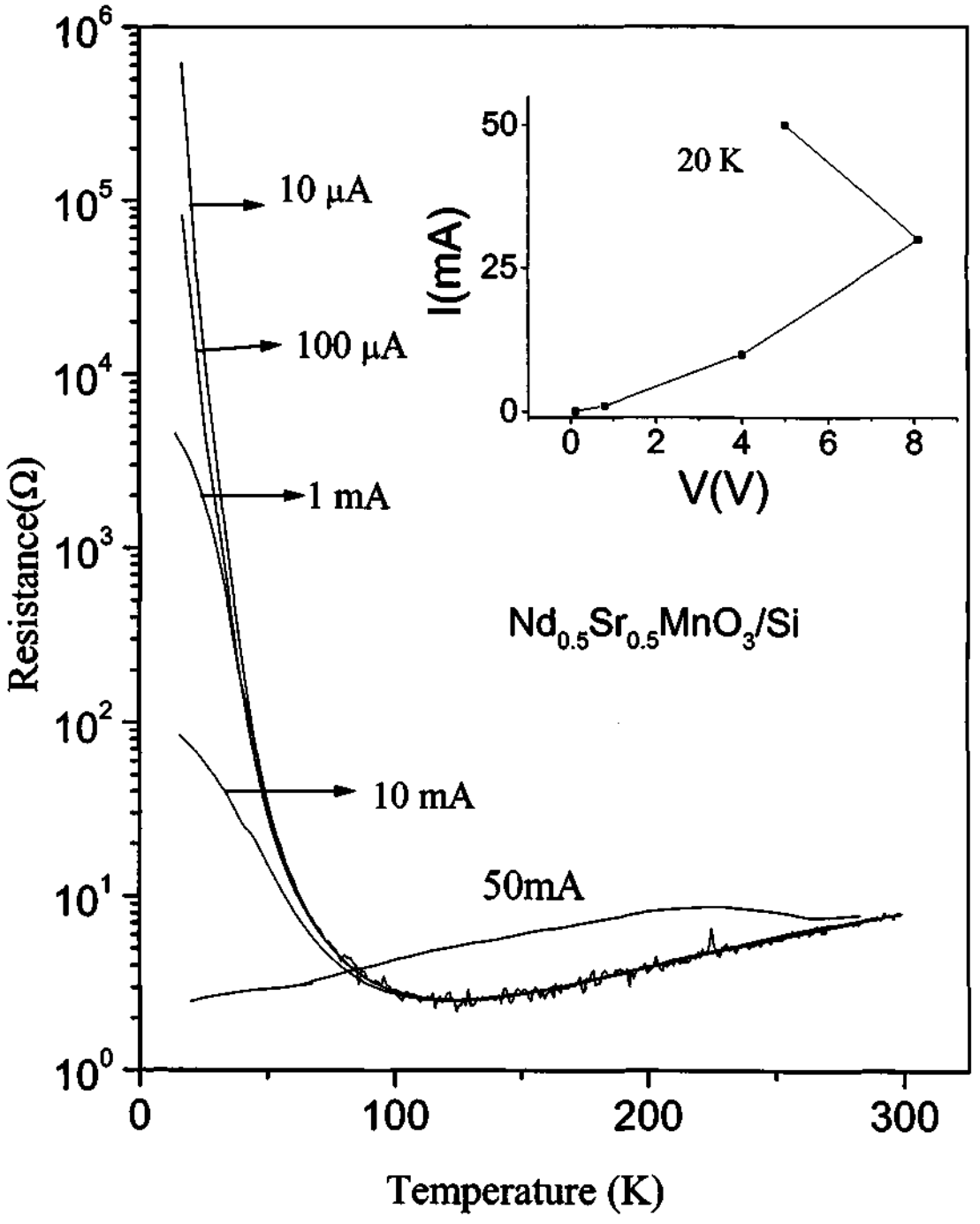

Fig.1.45 Temperature variation of resistance of a $Nd_{0.5}Sr_{0.5}MnO_3$ (NSM) film deposited on Si(100) for different values of current. The inset shows I-V characteristic at 20 K.

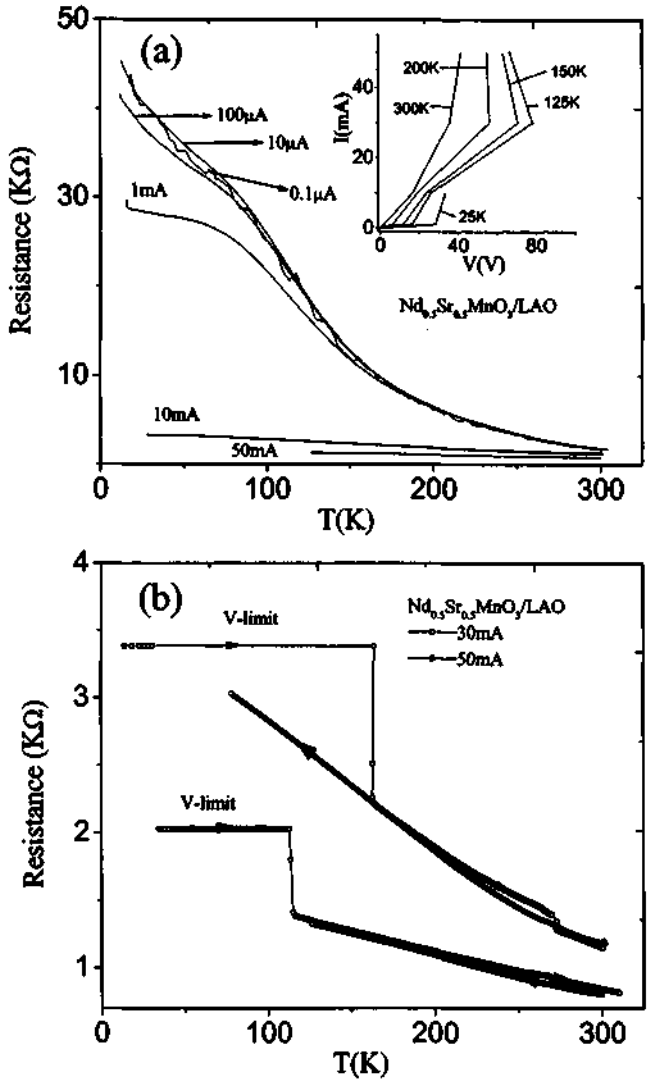

Fig.1.46 (a) Temperature variation of a $Nd_{0.5}Sr_{0.5}MnO_3$ (NSM) film deposited on LAO (100) for different values of current. The inset shows I-V characteristic at a low temperature.(b) Switching behavior of NSM films on LAO substrate.

NSM crystals somewhat comparable to the memory effects [fig.1.38 and fig.1.40 (b)] found by us. In fig.1.46 we show the resistance Vs temperature curves of $Nd_{0.5}Sr_{0.5}MnO_3$ (NSM) film on LAO(100) for different values of the current. We observe a substantial decrease in the resistance with increase in the current and the I-V behavior is nonohmic [see inset of fig.1.46 (a)]. Fig.1.46 (b) shows the same switching behavior of the NSM films on LAO (100) substrate for high currents.

Nonlinear electrical conduction and broad band noise in $Nd_{0.5}Ca_{0.5}MnO_3$ *

Electric field induced melting of the CO state leads to a strong nonlinear conduction as seen in the bulk as well as in films. This raises a very important question whether there is threshold field associated with the nonlinear conduction. In driven system pinned by a periodic potential there exists a threshold force beyond which the system is depinned. If the system is charged and the driving force comes from an electric field then this shows as a threshold field or bias for the onset of a nonlinear conduction. Existence of a th*reshold field would imply that the melting of the CO state by an applied electric field can actually be a depinning phenomena. We investigated this in films of the CO system $Nd_{0.5}Ca_{0.5}MnO_3$ by careful measurement of field dependent dc transport at various temperatures and also followed it up with a measurement of electrical noise (voltage fluctuation) as a function of applied dc bias. We made the following important observations: (1) There indeed exists a threshold field (E_{th}) below the CO temperature T_{co} and for $E > E_{th}$ a strong nonlinear conduction sets in; (2) E_{th} strongly depends on T and $E_{th} \rightarrow 0$ as $T \rightarrow T_{co}$; (3) For $T < T_{co}$, a large voltage fluctuation ($\langle \delta V^2 \rangle / V^2$) appears at the threshold field. Both E_{th} and $\langle \delta V^2 \rangle / V^2$ reaches a maximum at T~90K (~$0.4T_{co}$); (4) The spectral power distribution of the voltage fluctuation is broad band and has nearly $1/f$ character.

In $Nd_{0.5}Ca_{0.5}MnO_3$, a system with relatively small $\langle r_A \rangle$, the CO transition takes place from a high temperature charge-disordered insulating phase to a charge-ordered insulating phase (COI). Polycrystalline films of $Nd_{0.5}Ca_{0.5}MnO_3$ (average thickness ~1000 nm) were deposited on Si(100) single crystal substrates by nebulized spray

* Thanks are due to Drs. A Guha, A Ghosh and Prof. A K Raychaudhauri for collaboration.

pyrolysis of organometallic compounds were used in the present study. Electrical contacts were made by sputtering gold on the films and connecting the current and voltage leads on the gold contacts by silver paint. The I-V characteristics were measured by dc current biasing and the voltage between the voltage leads was measured by a nanovoltmeter. For measuring the electrical noise, the fluctuating component of the voltage δV was amplified by $5x10^3$ times by a low noise preamplifier. The output of the preamplifier was sampled by an ADC card and the data were directly transferred to the computer. The temperature was controlled to within 10 mK for both measurements. The films have a T_{co}~ 250 K as seen from the resistivity data. The resistivity was measured at a measuring current of 3 nA, which is much lower than the current where nonlinear conductivity sets in. The experiment was conducted down to 80 K where the sample resistance becomes more than 100 MΩ, the limit of our detection electronics.

In fig.1.47, we show the typical I-V curves at few characteristic temperatures. At all the temperatures (except at 220 K) there is a clear signature of a threshold voltage V_{th} beyond which the current rises significantly signaling the onset strong nonlinear conduction. (The separation of electrodes in our experiment is 2 mm, so that $E_{th} = 5V_{th}$ V/cm). I-V curves show two components of conduction: a normal component which exists at all V and a strongly nonlinear component starting at $V > V_{th}$. We fit our I-V data using following empirical expression which allows us to separate the two components I_1 and I_2 :

$$I = I_1 + I_2 = g_1 (V-V_{th}) + g_2 (V) = C_1 (V-V_{th})^{n1} + C_2 V^{n2} \qquad \text{Eq.(1)}$$

where g_1, a function of $(V-V_{th})$, is the component of current (I_1) that has a threshold associated with it and $C_1 = 0$ $V < V_{th}$. The component g_2 is the normal conduction

component of current (I_2). C_1, C_2, n_1, and n_2 are constants a given temperature. The data at all temperatures can well fitted to Eq. (1) for T > 90 K as shown by the solid lines fig.1.47. The dashed and dashed–dotted lines give the contributions of each of the terms.

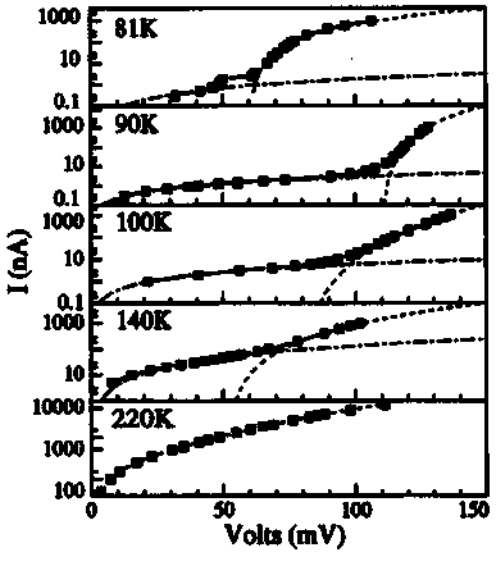

Fig.1.47 I-V curves at different temperatures, solid line shows the total I, dashed and dashed-dotted lines show the components I_1 and I_2 as obtained from fit to data using eq.(1).

For T < 90 K certain additional features show up (see data at 81 K) in the I-V data which give the impression that there may be multiple thresholds. In fig.1.48 (b) we have plotted the threshold voltage V_{th} function of T as obtained from Eq.(1). It can be seen that $V_{th} \rightarrow 0$ as $T \rightarrow T_{co}$. Within the limitations of our detachability, we could see a finite nonzero V_{th} up to T~170 K ~0.7 T_{co}. Beyond this temperature it is difficult to distinguish between the

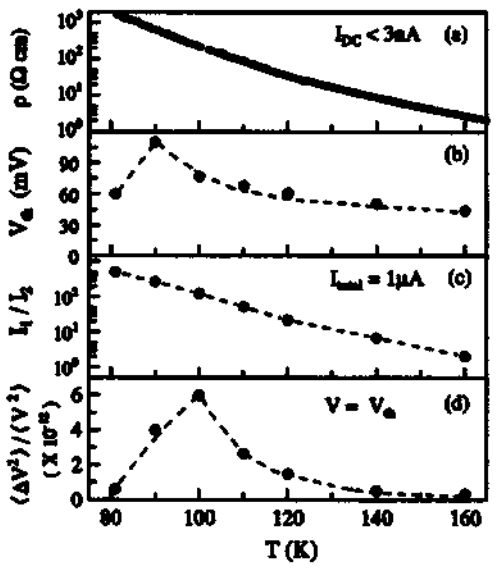

Fig.1.48 Temperature variation of (a) resistivity (b) magnitude of threshold voltage (c) relative contributions of I_1 and I_2 and (d) noise magnitude at the threshold voltage. The values of I_1 and I_2 are obtained from eq.(1).

two conduction components. At voltages much below the threshold voltage the I-V can be fitted to linear equation. However, for $V < V_{th}$ (but comparable to V_{th}) best fit obtained needs a nonlinear dependence on Equation (1) therefore is valid for a range $V > 0.1\ V_{th}$. It must be pointed out that the normal component I_2 also has small nonlinearly since n_2~1.1-1.4. This is much less nonlinear than the I_1 component seen above V_{th}. The relative contributions of I_1 and I_2 to the total current (expressed as the ratio I_1/I_2 evaluated at I = 1 μA) has been obtained from Eq. (1) and has been plotted as a function of T in fig.1.48 (c). At $T << T_{co}$, the nonlinear component is orders of magnitude larger than the normal conduction component and they are comparable as $T \rightarrow T_{co}$. The exponent n_1 is strongly temperature dependent and from a value ~2 at 160 K it reaches a value more than 5 at T~100 K. The exponent n_2 does not have much of a temperature dependence and is ~1.1–1.4 for T ≤180 K. In a pinned driven system one often sees the onset of broad band noise as the system is depinned at the threshold voltage. We find that such is indeed

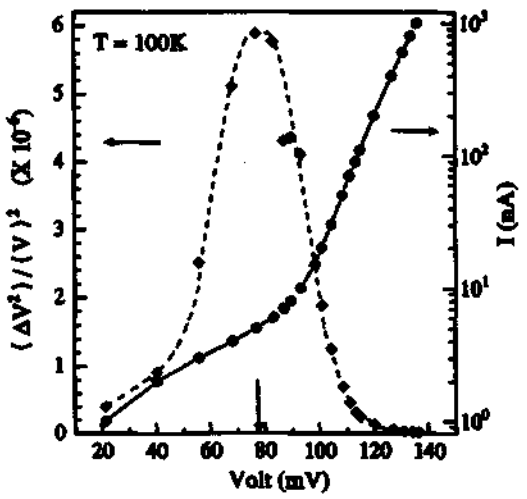

Fig.1.49 The noise magnitude and I-V characteristics at 100 K. The arrow indicates the threshold voltage.

the case in this system. In fig.1.49 we show the magnitude of the voltage fluctuation $\langle \delta V^2 \rangle / V^2$ as a function of the applied bias V at T = 100 K along with the I-V curve. The

arrow indicates V_{th}. It is clear that the voltage fluctuation has a nonmonotonous dependence on V and reaches a peak at V~V_{th}. This fluctuation has been seen at all T< $0.7T_{co}$ where we can detect measurable V_{th}. The peak values of the fluctuation measured at different T are shown in fig.1.48 (d). The fluctuation→0 T →T_{co} and has a peak at 90 K where T_{th} also shows a peak. Frequency dependencies of the spectral power $S_v(f)$ measured at 100 K with biases V< V_{th}, V~ V_{th} and V> V_{th} are shown in fig.1.50. We have plotted the data as S_v/V^2 vs *f*. For a pure 1/*f* noise ($S_v \propto 1/f$), this should be straight line

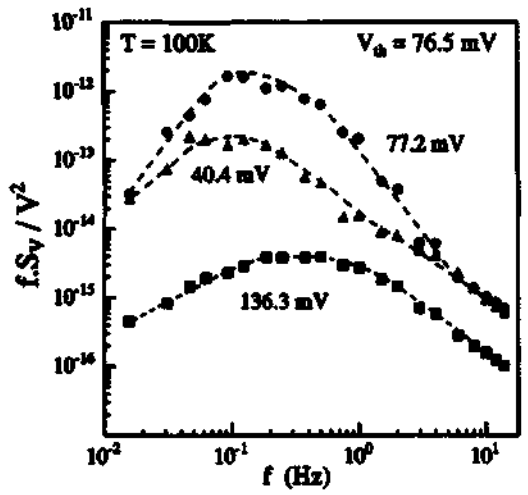

Fig.1.50 Frequency spectrum the noise at 100 K for different bias values.

parallel to the *f* axis. It can be seen that the predominant contribution to noise has 1/*f* character and the noise becomes more 1/*f* at higher voltages.

1.4.3 Discussion

The effect of electric fields on the thin films of charge ordered (CO) manganites has been considered to arise due to filamentary conduction. Such filamentary conduction arises due to phase separation. In the case of $Nd_{0.5}Ca_{0.5}MnO_3$, below the charge ordering transition there is phase separation. Since phase separation involves conducting and insulating regions, the following simple scenario can explain the observations on the electric field effects. The onset of the NDR (negative differential resistance) region in the

I-V curve beyond a certain value of I is due to the appearance of the metallic filaments, which carry most of the current. This decreases the voltage across the sample. On passing more I, the volume fraction of the filament increases, leading to a further decrease of voltage, and the NDR regime is sustained. SQUID observations show that the filaments so formed have ferromagnetically aligned Mn moments, which enhance the magnetization. We may thus consider the filaments as made up of the FMM phase. This is reasonable since the metallic (conducting) property of the rare earth manganites arises from double exchange which also causes ferromagnetism. NDR is also seen in the I-V characteristics of single crystals of the same system on application of laser light. Direct observation using reflection measurements show that in this region there is formation of ''metallic'' filaments. Interestingly, a small jump in magnetization was also seen in laser induced melting.

What is also interesting to be noted is that the electric field makes the system metallic in the charge ordered state at low temperatures. The effects can be understood similar to that of magnetic field. That is, the electric field generates a magnetic field inside the sample, which leads to the formation of ferromagnetic domains, hence leading to conducting states.

We discuss now the electric-field-induced insulator-metal transition and the nonohmic transport in the charge-ordered rare-earth manganites. These materials are to be viewed as charge solids pinned randomly to the underlying lattice, and can be depinned by an externally applied electric field, and, of course, melted thermally. The random pinning is expected on general grounds, e.g., the L/A substitutional disorder in $L_{0.5}A_{0.5}MnO_3$ that acts as a quenched randomness, other lattice defects or possible in homogeneities,

including the occurrence of domains or clusters of CO and metallic phases. Charge ordering in the cubic manganites is, however, not a charge-density wave (CDW) arising from a nesting of the Fermi surface and the associated Peierls instability, as presumably is the case for the effectively low-dimensional layers system[70] Sr_2IrO_4. Charge ordering in the manganites is driven by Coulomb interaction among the charge carriers, and is stabilized by the background lattice potential, with which it is ideally commensurate for the 1/1 ordered Mn^{3+} / Mn^{4+} case. The charge carriers themselves are expected to be polarons specifically, the lattice polarons associated with the Jahn-Teller ions Mn^{3+} for the manganites with a small average A-cationic radius as, e.g., in NCM, YCM, or GCM. Charge transport in these manganites, again unlike a CDW with its sliding or unpinned condensate, is expected to proceed through the correlated motion of the polarons, depinned by the applied electric field. This picture is qualitatively consistent with the observed facts, namely, the observed threshold of electric field, or applied current, for electrical conduction, nonohmic transport, metal insulator transition, negative differential resistance, and certain hysteretic and memory effects associated with the melting transition from a charge solid to a charge liquid as discussed below.

At the lowest temperature (77 K) and current ($I \leq 0.05$ μA) employed, the NCM film [fig. 1.36 (a)] is highly insulating (TCR < 0) with R ~10^7 Ω. The resistance then falls by an order of magnitude for a small increase of the current to ~0.1 μA, but finally levels off to a gradual decrease around 1 mA. The corresponding variation in the applied voltage, and, therefore, of the electric field, is small, from ~0.5 to ~0.6 V. This nonlinear threshold conduction, qualitatively of the Zener type $R \propto \exp(E_0 / E)$, is characteristic of a pinned charge solid (insulator), and its field-induced depinning gives a conductor. The

field-induced depinning also accounts for the nonohmic decrease of resistance with increasing applied current at a given temperature as observed in these manganites. Let us next consider the temperature dependence of resistance at a given current. At low enough temperatures, the depinning energy far exceeds the thermal energy (k_BT) and the conduction is dominated by a coherent tunneling step. A positive TCR is to be expected because of the decohering thermal effects, as indeed observed [fig.1.36 (a)]. At higher temperatures, the transport crosses over from this quantum coherent tunneling through pinning barrier to an incoherent thermal escape over the barrier giving a change in sign of the (TCR < 0) as expected of a thermally activated process. This is again exactly what is observed [fig.1.36 (a)]. Indeed, such a crossover from a low-temperature coherent conduction with a positive TCR to a higher temperature incoherent conduction with a negative TCR is well known for independent small polarons. In the present case, the single polaron is replaced by the polarons entrained in a correlation volume due to interaction. With increasing temperature, the coherence volume must decrease thereby lowering the depinning energy. It is very apt to point out here that the field-induced depinning of the randomly pinned charge solid has a close analogue in the well-known phenomenon of shear induced melting, which is not the result of heating.

The picture discussed above with reference to fig.1.36 (a) for NCM/Si also covers the NCM/LAO, GCM/Si or LAO and YCM/LAO films depicted in figs.1.36 (b), 1.37 and 1.40 (a), respectively. In these cases, the metallic-type regime with TCR > 0 (found in NCM/Si at low temperatures) is absent. This suggests that the correlation volume, or the pinning barrier, is sufficiently small for the thermally activated depinning to dominate over tunneling even at low temperatures, thus making the regime with TCR > 0

parametrically inaccessible. In the case of NSM (fig.1.45), charge ordering and its pinning involve antiferromagnetic (AFM) ordering, and hence the depinning occurs at relatively lower temperatures. The idea of pinning/depinning, and of the associated coherence volume entraining a number of charge carriers, is general and has a much wider applicability. Thus, it is applicable to the classic Wigner crystal pinned by random substrate imperfections, to which the CO state considered here approximates best but with the proviso that the electrons have to be replaced by JT polarons whose higher effective mass favors charge solid formation in the parameter regime of interest.

The negative differential resistance in the case of the magnetic CO manganites (as in NSM) can be understood in terms of local ferromagnetic (FM) ordering forced by a sufficiently large transport current impressed as an external constraint. This is the spin-valve effect acting in the reverse [reverse spin valve effect fig.1.51 (c)], assuming that the Hund's coupling is far larger than the antiferromagnetic coupling. The transport-induced local FM order leads to a lower resistance because of the spin-valve effect [fig.1.51 (a) and (b)], and hence the negative differential conductance. Such a transport driven (magnetic) structural change is a particular case of the general nonequilibrium phenomenon of ordering caused by transport. Similar transport driven instability is expected in the other systems showing negative differential conductance.

Finally, we turn to the remarkable hysteretic I-M transitions driven by the transport current in the CO systems shown in figs.1.38 and 1.40 (b). The R-T plot at constant transport current along the heating curve shows an abrupt drop at the transition temperature (~150 K) at which clearly the charge solid melts to a charge liquid. On the cooling curve, the charge liquid shows appreciable undercooling (stays liquid below 150

K) which is not surprising for a melting transition. What is surprising, however, is that on the heating curve (following the switching of the applied current at the lowest temperature) the resistance jumps back at melting to its original current-specific value on the cooling curve in the charge liquid melt. This memory of the current specific-resistance value registered in the charged liquid state, and addressed uniquely by that *specific value of the transport current, can be understood in terms of the quenched* randomness of the strength as well as the position of the pinning referred to earlier[69]. Accordingly, at a given transport current, the charge solid is depinned only at a subset of pinning centers. We suggest that effectively only this depinned fraction melts cooperatively at the melting point, and then contributes to the conductance in the charge liquid state. This subset increases with the increasing applied current, giving therefore, lower resistance for higher currents in the charge liquid state, as is clearly seen in figs.1.38 and 1.40 (b). [Here again, the Joule heating is irrelevant as is evident from the fact that the observed melting temperature is unaffected by the applied current magnitude]. Thus, the charge liquid just above the melting temperature also conducts nonohmically. It is the transport-current specificity of the charge liquid resistance that sets it apart from the hysteresis usually associated with the first-order melting transition.

The onset of strong nonlinear conduction at a threshold voltage and the accompanied broad band noise has been seen in solids like $NbSe_3$, TaS_3 which show depinning of charge density waves (CDW) by a threshold field. Though the physics of CDW and CO states are entirely different, the underlying phenomenological description of depinning can be similar. To conclude, the present study demonstrates that there is a threshold field associated with the onset of nonlinear conduction in the CO system along with the

Spin Valve Effect

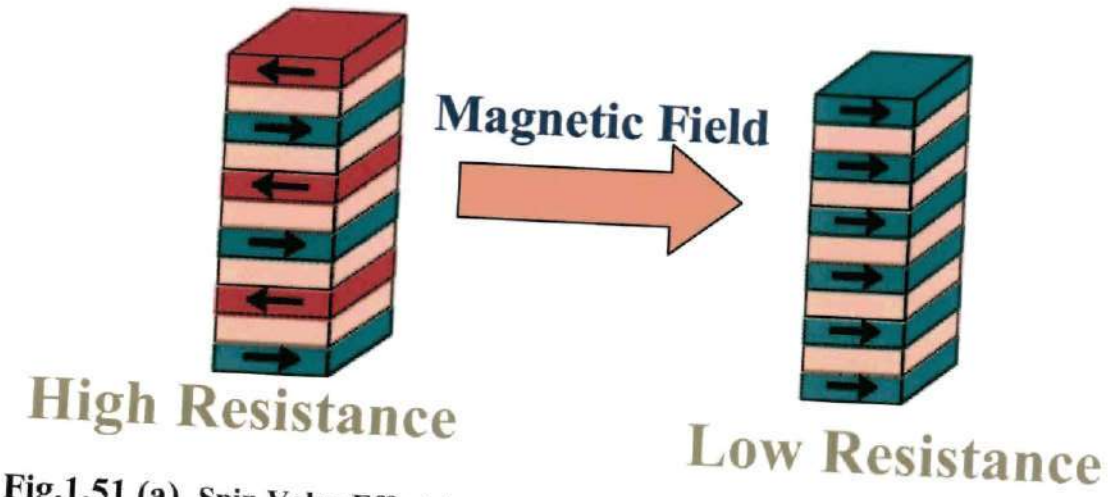

Fig.1.51 (a) Spin Valve Effect in magnetic multilayers giving rise to lower resistive states.

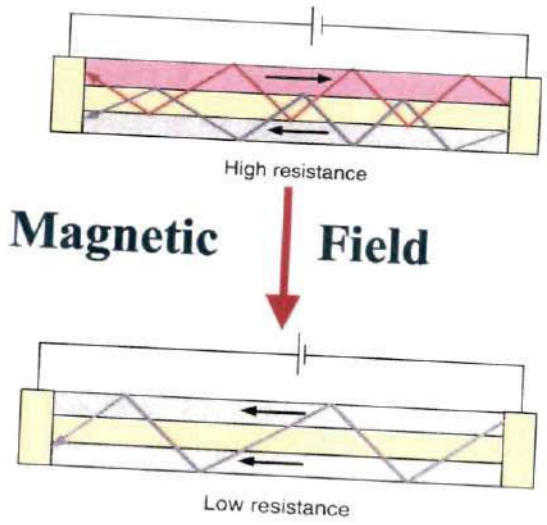

Fig.1.51 (b) Spin Valve Effect.

Inverse Spin Valve Effect

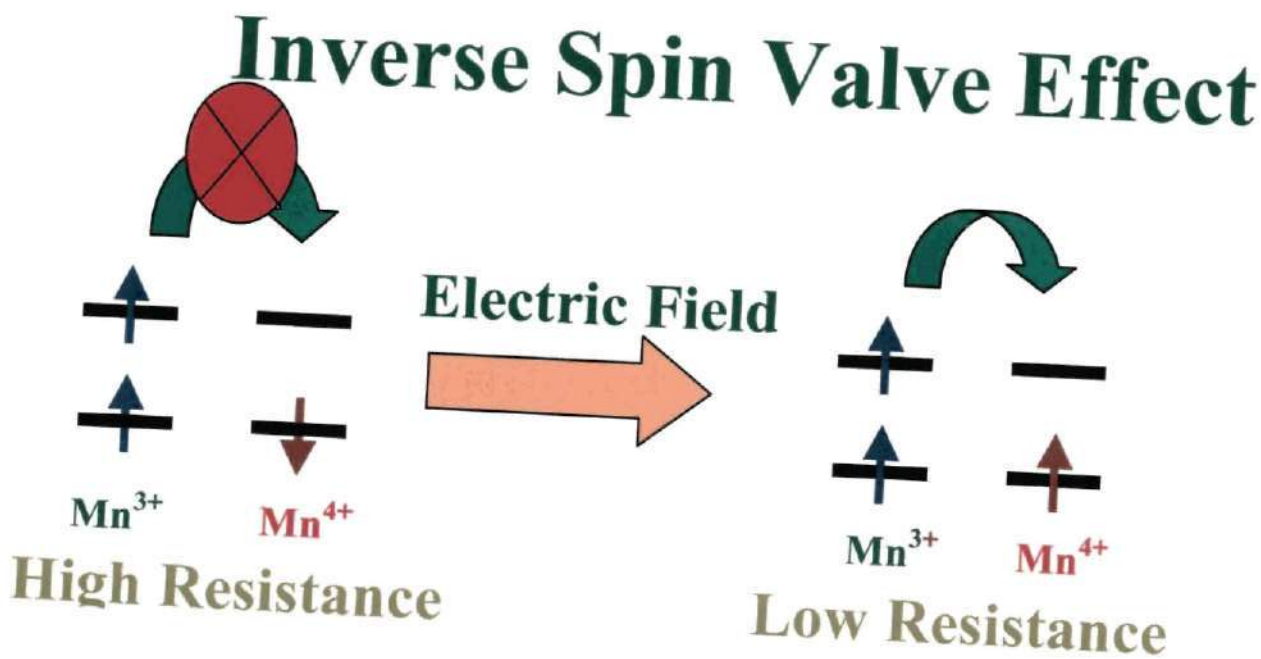

Fig.1.51(c) Proposed Inverse Spin-Valve Effect as the possible mechanism for melting of charge ordered states by Electric fields.

existence of a broad band noise. The observation is taken as evidence of depinning of the CO state as the origin of nonlinear conduction in these solids.

1.4.4 A comparative study of thin films of hole-doped $Pr_{0.6}Ca_{0.4}MnO_3$ and electron-doped $Pr_{0.4}Ca_{0.6}MnO_3$

Thin films of the $Pr_{1-x}Ca_xMnO_3$ (x = 0.4, 0.6) as well as the compositions with 3% Cr^{3+} and Ru^{4+} doping were prepared by nebulized spray pyrolysis. The films of $Pr_{0.6}Ca_{0.4}MnO_3$ and $Pr_{0.4}Ca_{0.6}MnO_3$ deposited on Si(100) were polycrystalline in nature while those deposited on LAO(100) were oriented along the (100) direction as determined by X-ray diffraction. Fig.1.52 shows typical EDAX data on the films of

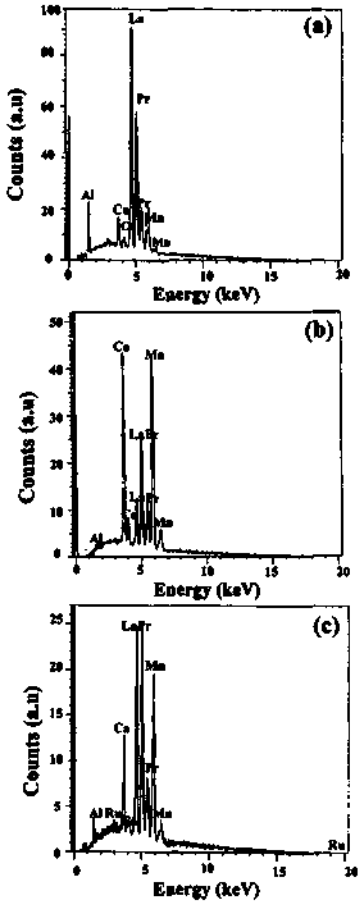

Fig.1.52 EDX spectra of thin films of (a) $Pr_{0.6}Ca_{0.4}MnO_3$ (b) $Pr_{0.4}Ca_{0.6}MnO_3$ and (c)$Pr_{0.6}Ca_{0.4}Ru_{0.03}Mn_{0.97}O_3$ deposited on LAO(100) substrates.

$Pr_{0.6}Ca_{0.4}MnO_3$, $Pr_{0.4}Ca_{0.6}MnO_3$ and $Pr_{0.6}Ca_{0.4}Ru_{0.03}Mn_{0.97}O_3$ deposited on LAO substrates. The compositions obtained from the EDAX spectra were generally close to the expected calculated compositions.

In fig.1.53 (a) we show the temperature-variation of electrical resistance of a $Pr_{0.6}Ca_{0.4}MnO_3$ film deposited on LAO at different magnetic fields. It is insulating down to lowest temperature in the absence of a magnetic field, but on the application of a magnetic field of 5 T, there is an insulator-metal (I-M) transition. The I-M transition temperature increases from 175 K at 5 T to 235 K at 10 T. Magnetoresistance (MR) is

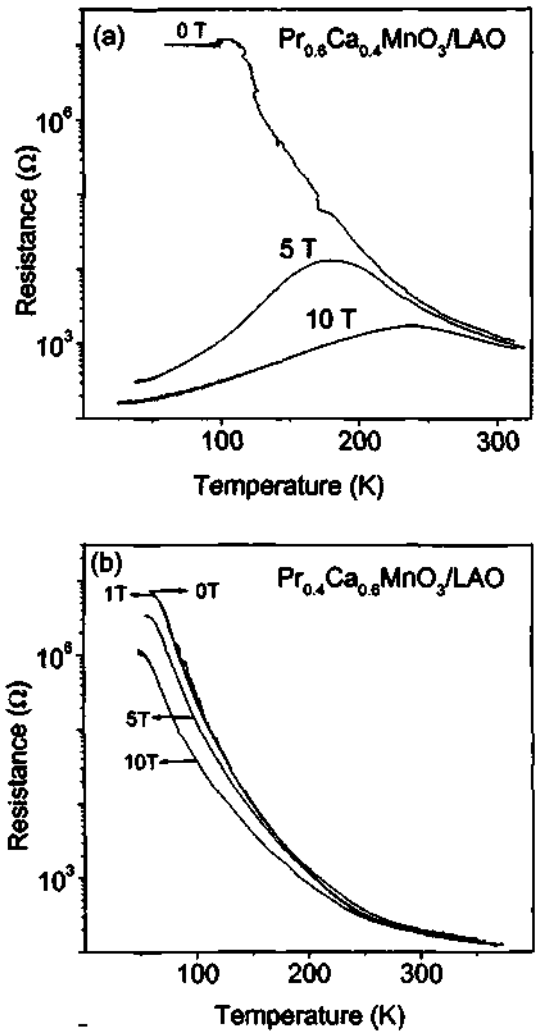

Fig.1.53 Temperature-variation of the electrical resistance of thin films of (a) $Pr_{0.6}Ca_{0.4}MnO_3$ and (b) $Pr_{0.4}Ca_{0.6}MnO_3$ deposited on LAO(100) substrates at different magnetic fields.

~98 % and 46 % respectively at 150 K and 200 K at 5 T. This behavior is similar to that reported in literature for a single crystal of this material. In contrast to films of $Pr_{0.6}Ca_{0.4}MnO_3$, films of the electron-doped $Pr_{0.4}Ca_{0.6}MnO_3$ on LAO show insulating behavior down to lowest temperature, even on the application of magnetic fields, as can be seen from fig.1.44 (b). The magnitude of MR is also low and reaches only 19 % at 5 T at 150 K.

In figs.1.54 (a) and (b), we show the effect of electric currents on the resistance of polycrystalline films of $Pr_{0.6}Ca_{0.4}MnO_3$ and $Pr_{0.4}Ca_{0.6}MnO_3$ respectively, deposited on Si(100) substrates. In the case of $Pr_{0.6}Ca_{0.4}MnO_3$, we clearly observe melting to a metallic state with even a modest current of 10μA. The temperature of the I-M transition increases with increasing current. The effect of electric fields on films of the electron-doped

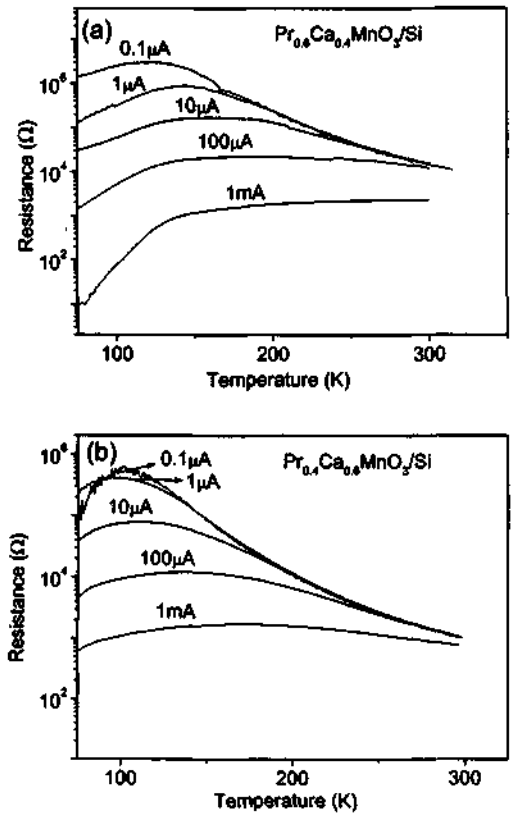

Fig.1.54 Temperature-variation of the electrical resistance of thin films of (a) $Pr_{0.6}Ca_{0.4}MnO_3$ and (b) $Pr_{0.4}Ca_{0.6}MnO_3$ deposited on Si(100) for different values of the current.

manganite, $Pr_{0.4}Ca_{0.6}MnO_3$, is comparable to that found with hole-doped $Pr_{0.6}Ca_{0.4}MnO_3$. However, the resistance of the films of the electron-doped composition is slightly higher than that of the hole-doped composition. Furthermore, the I-M transition is not as distinctive in the electron-doped sample as in the case of the hole-doped sample. In figs.1.55 (a) and (b), we show the temperature-variation of resistance of the films of $Pr_{0.6}Ca_{0.4}MnO_3$ and $Pr_{0.4}Ca_{0.6}MnO_3$ deposited on LAO (100) substrates. Although these

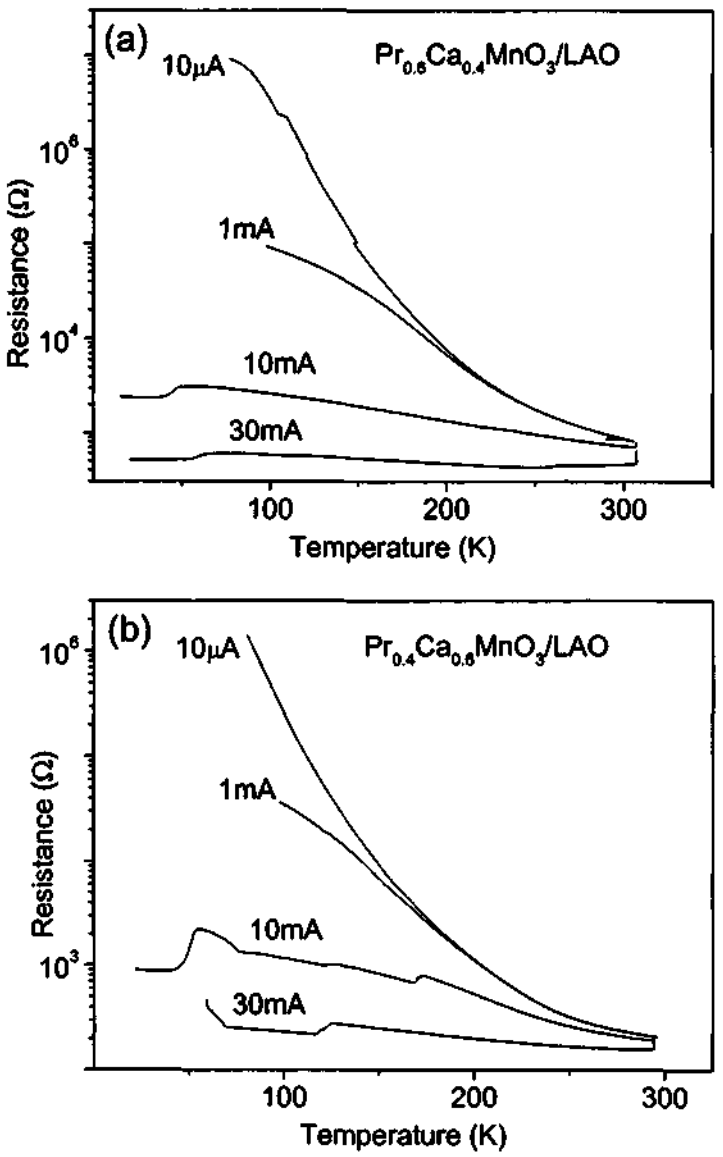

Fig.1.55 Temperature-variation of the electrical resistance of the thin films of (a) $Pr_{0.6}Ca_{0.4}MnO_3$ and (b) $Pr_{0.4}Ca_{0.6}MnO_3$ deposited on LAO(100) for different values of the current.

films do not exhibit a clear I-M transition with increasing current, they show a marked decrease in the resistance when the current is increased. The electric-field induced I-M transitions and the marked decrease in the resistance with increasing current for these films can be understood in terms of the depinning of the charge-ordered state brought about by electric-fields.

When a charge-ordered manganite such as $Nd_{0.5}Ca_{0.5}MnO_3$ is doped with 3% Ru^{4+}, it becomes ferromagnetic and undergoes an I-M transition[71]. In figs.1.56 (a) and (b), we show the temperature-variation of electrical resistance of the films of 3% Cr^{3+} doped $Pr_{0.6}Ca_{0.4}MnO_3$ and $Pr_{0.4}Ca_{0.6}MnO_3$ respectively, in comparison with the data for the undoped parent compositions. Although 3% Cr^{3+} doping does not render either of the materials metallic, there is a marked decrease in resistance in the case of the hole-doped

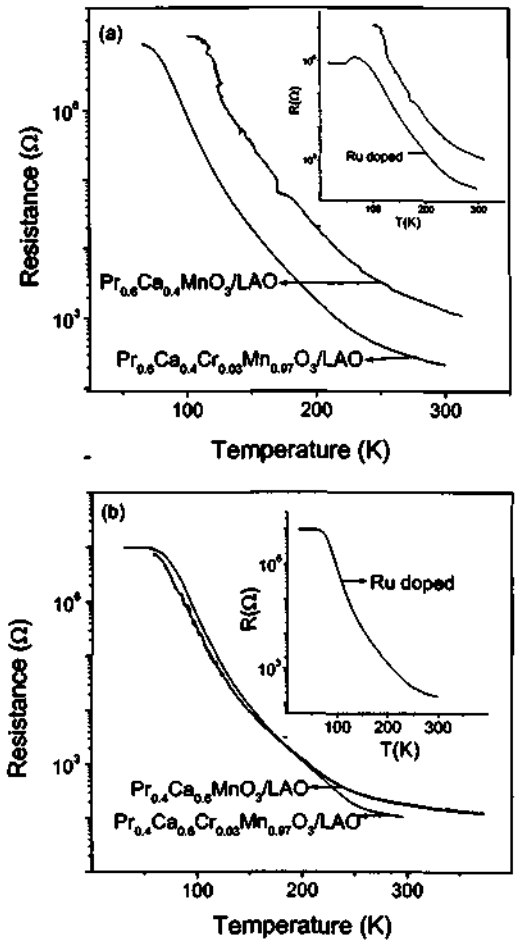

Fig.1.56 Temperature-variation of the electrical resistance of thin films of (a) $Pr_{0.6}Ca_{0.4}MnO_3$ and $Pr_{0.6}Ca_{0.4}Cr_{0.03}Mn_{0.97}O_3$, and (b) $Pr_{0.4}Ca_{0.6}MnO_3$ and $Pr_{0.4}Ca_{0.6}Cr_{0.03}Mn_{0.97}O_3$ deposited on LAO(100) substrates. Insets show similar effects for the pure and 3% Ru^{4+} samples.

sample. This observation is also verified in the case of Ru^{4+} doped $Pr_{0.6}Ca_{0.4}MnO_3$ and $Pr_{0.4}Ca_{0.6}MnO_3$ films as can be seen from the insets in figs.1.56 (a) and (b). In figs.1.57 (a) and (b), we show the temperature-variation of electrical resistance in the absence and presence of a magnetic field of 5 tesla for the films of $Pr_{0.6}Ca_{0.4}Cr_{0.03}Mn_{0.97}O_3$ and $Pr_{0.6}Ca_{0.4}Ru_{0.03}Mn_{0.97}O_3$ deposited on LAO(100) substrate. On application of the

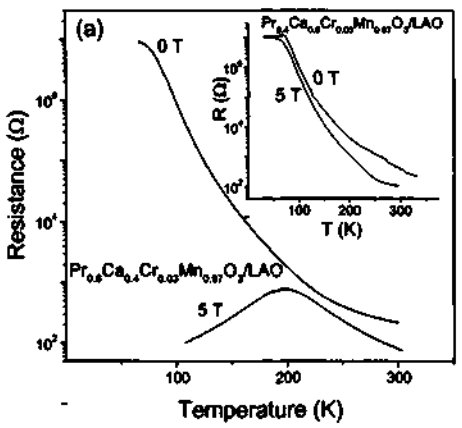

Fig.1.57 Temperature-variation of the electrical resistance of the thin films of (a)$Pr_{0.6}Ca_{0.4}Cr_{0.03}Mn_{0.97}O_3$ and (b) $Pr_{0.6}Ca_{0.4}Ru_{0.03}Mn_{0.97}O_3$ at 0 and 5 tesla. Insets show similar effects for the electron-doped samples, $Pr_{0.4}Ca_{0.6}Cr_{0.03}Mn_{0.97}O_3$ and $Pr_{0.4}Ca_{0.6}Ru_{0.03}Mn_{0.97}O_3$.

magnetic field an I-M transition manifests itself in both the cases. The I-M transition temperatures are 198 K and 216 K respectively in the Cr^{3+} and Ru^{4+} doped samples. Similar measurements for the electron-doped $Pr_{0.4}Ca_{0.6}Cr_{0.03}Mn_{0.97}O_3$ and $Pr_{0.4}Ca_{0.6}Ru_{0.03}Mn_{0.97}O_3$ compositions are shown in the insets of figs.1.57 (a) and (b) respectively. Unlike the hole-doped compositions magnetic field has no effect on the

resistance of the electron-doped samples. This is in accordance with the behavior of parent hole doped $Pr_{0.6}Ca_{0.4}MnO_3$ and electron doped $Pr_{0.4}Ca_{0.6}MnO_3$ compositions. Thus the combined effect of doping and magnetic field fail to render the electron doped $Pr_{0.4}Ca_{0.6}MnO_3$ metallic even at low temperatures. The effect of electric fields is however found to be comparable in the films of Cr^{3+} and Ru^{4+} doped $Pr_{0.6}Ca_{0.4}MnO_3$ and $Pr_{0.4}Ca_{0.6}MnO_3$ films, although the resistance of the electron-doped samples is somewhat higher than that of the hole doped samples. This is clearly seen in figs.1.58 (a) and (b) for

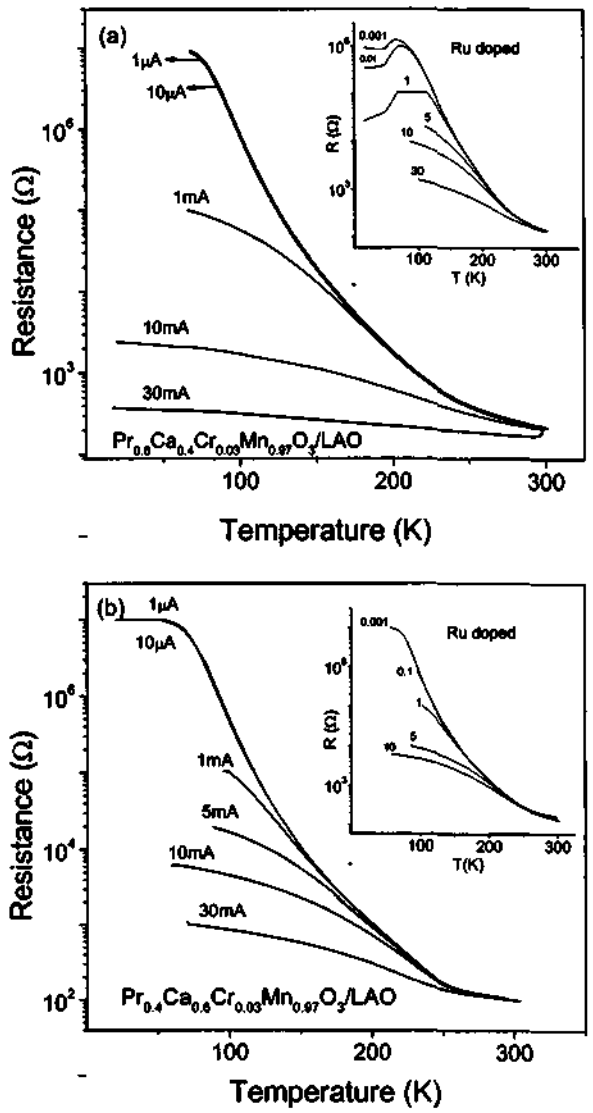

Fig.1.58 Temperature variation of the electrical resistance of thin films of (a) $Pr_{0.6}Ca_{0.4}Cr_{0.03}Mn_{0.97}O_3$ and (b) $Pr_{0.4}Ca_{0.6}Cr_{0.03}Mn_{0.97}O_3$ deposited on LAO (100) for different values of the current. Insets show similar effects for 3% Ru^{4+} samples (numbers are in mA).

the 3% Cr^{3+} doped $Pr_{0.6}Ca_{0.4}MnO_3$ and $Pr_{0.4}Ca_{0.6}MnO_3$. The insets in these figures show similar electric-field effects on the 3% Ru^{4+} doped samples.

1.4.5 Charge ordering in thin films of bilayered rare earth manganites

Fig.1.59 shows the EDAX spectra of the films of $LaSr_2Mn_2O_7$ and $NdSr_2Mn_2O_7$ deposited on the LAO(100) substrates. The compositions obtained from the EDX spectra

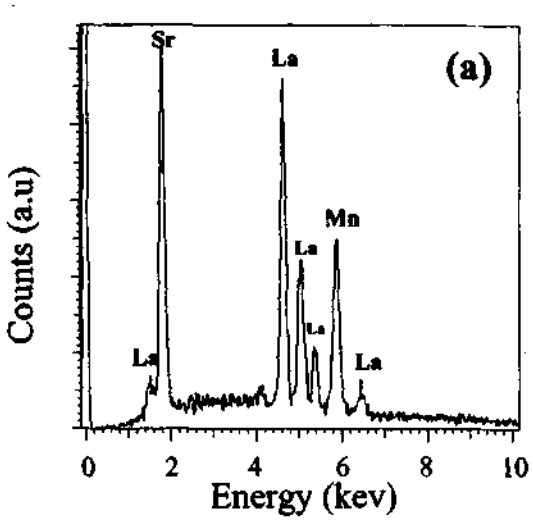

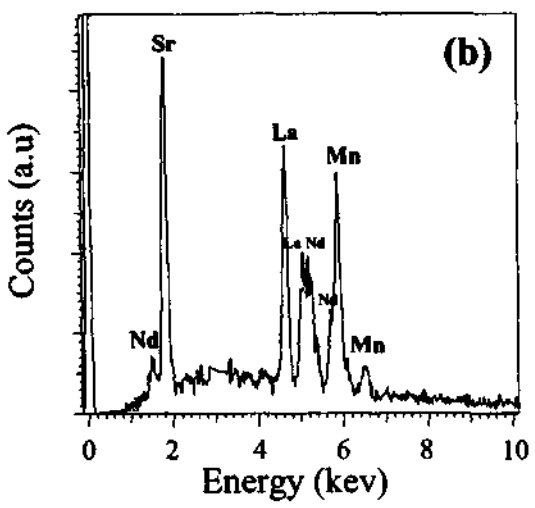

Fig.1.59 EDAX spectra of thin films of (a) $LaSr_2Mn_2O_7$ (b) $NdSr_2Mn_2O_7$ deposited on LAO(100) substrates. In the case of $LaSr_2Mn_2O_7$ we have compared the elemental ratios of Sr and Mn as the La concentration couldnot be compared because of the interference by substrate.

were close to the theoretical compositions. Fig.1.60 shows the XRD patterns of two representative films deposited on LAO (100) substrate. The XRD patterns show the reflections due to the manganites besides those due to the substrate.

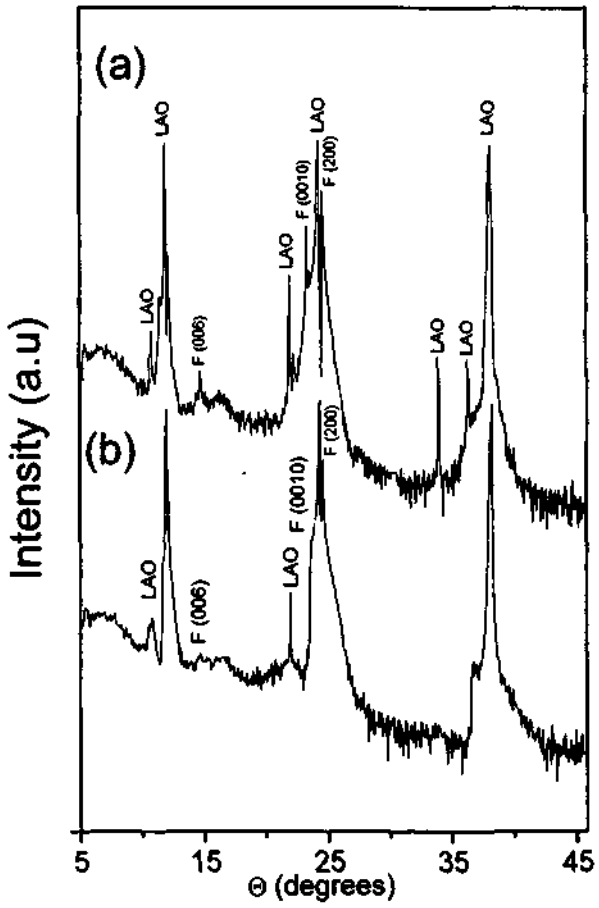

Fig.1.60 XRD pattern of thin films of (a) $LaSr_2Mn_2O_7$ and (b) $GdSr_2Mn_2O_7$ deposited on LAO(100) substrates. `*F*' denotes the peaks due to manganite films.

In particular, they contain strong (006) and (0010) reflections, confirming that the films are predominantly oriented with the c-direction [001] perpendicular to the surface. However, the presence of a (200) reflection reveals that some of the crystallites are oriented with the [100] direction perpendicular to the substrate. The tetragonal lattice parameters (a = 3.876 Å, c = 20.010 Å) were in agreement with bulk values in the literature ref. Scanning electron micrographs of the films confirm that the surfaces of the

films are reasonably smooth, with small crystallite shaped grains, typical of epitaxial films. The films on Si(100) were polycrystalline in nature.

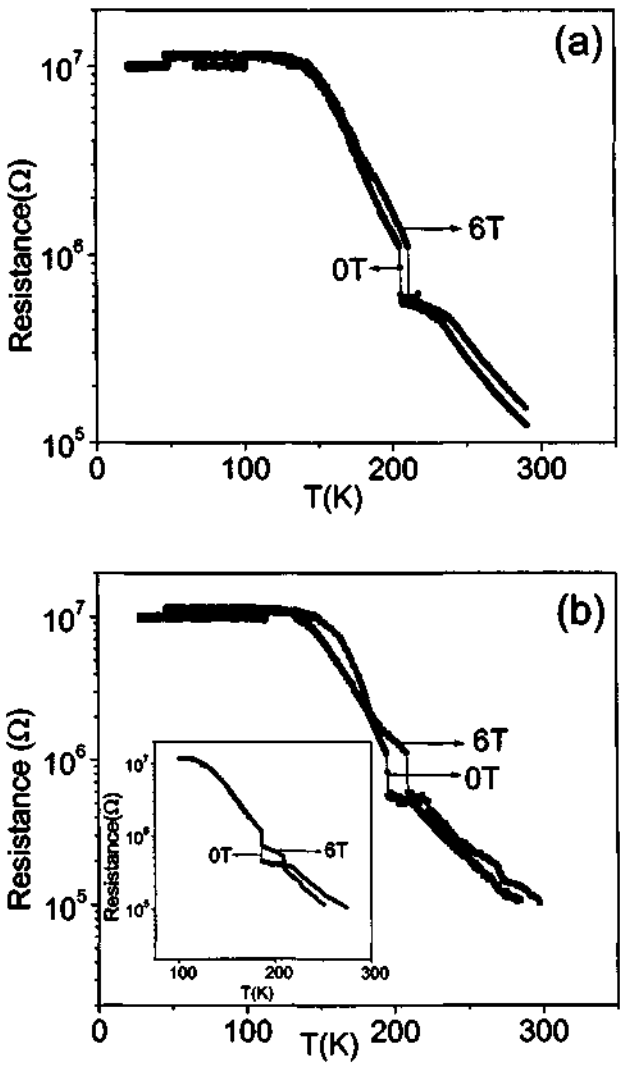

Fig.1.61 Temperature-variation of resistance of thin films of (a) $LaSr_2Mn_2O_7$ and (b) $NdSr_2Mn_2O_7$ at 0 and 6 tesla deposited on LAO(100) substrate. Temperature-variation of resistance of the film of $GdSr_2Mn_2O_7$ deposited on LAO(100) substrate is shown in the inset of (b).

Oriented films of $LaSr_2Mn_2O_7$ and $NdSr_2Mn_2O_7$ on LAO (100), show definitive changes in resistance due to charge-ordering, unlike the polycrystalline films on Si(100) substrate. The resistivity transition is found at 205 K in $LaSr_2Mn_2O_7$ and at 195 K in $NdSr_2Mn_2O_7$ as can be seen from fig.1.61 (a) and (b) respectively. Application of a magnetic field of 6 T has negligible effect on the resistance but the CO transition temperature increases slightly. Resistivity maxima in single crystals are found to be shifted to higher

temperatures[72,73]. The $GdSr_2Mn_2O_7$ film deposited on LAO shows a resistivity transition due to charge ordering at 185 K [see inset of fig.1.57 (b)]. We thus find a decrease in the CO transition temperature as we go from La to Gd. This is the effect of the size of the rare-earth ion is somewhat unusual compared to the perovskite manganites of composition $Ln_{1-x}A_xMnO_3$.

The effect of electric fields on the bilayered manganite films is interesting. In fig.1.62 we show the effect of a small electric currents on the resistance of the bilayered

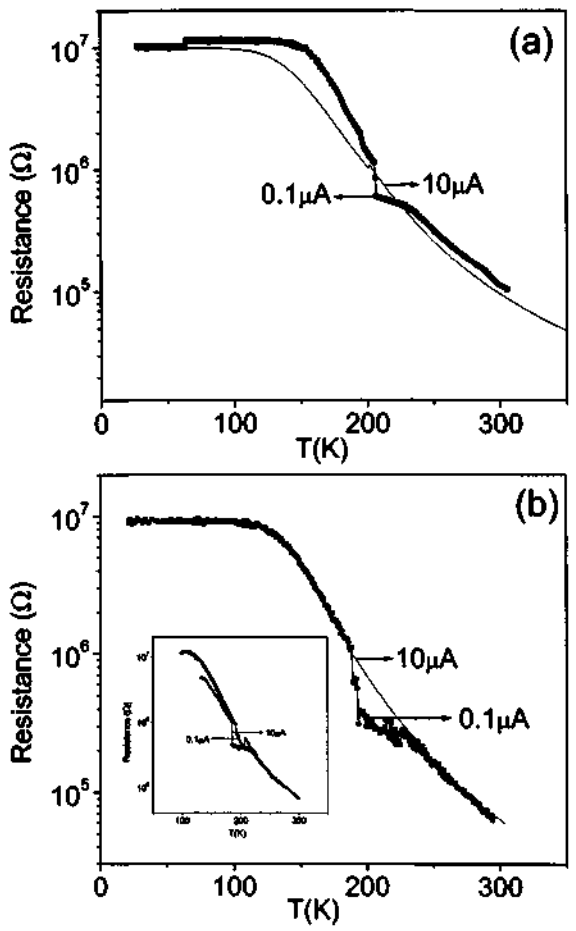

Fig.1.62 Temperature-variation of resistance of thin films of (a) $LaSr_2Mn_2O_7$ and (b) $NdSr_2Mn_2O_7$ deposited on LAO(100) substrate at different currents. Inset in (b) shows similar effect for $GdSr_2Mn_2O_7$ film on LAO(100).

manganite films deposited on LAO substrates. Even on increasing the current from 0.1μA to 10μA, the charge-ordering transition disappears in $LaSr_2Mn_2O_7$ and

$NdSr_2Mn_2O_7$. In the case of $GdSr_2Mn_2O_7$, the transition is shifted slightly to a higher temperature, and its magnitude is diminished. We did not measure the resistance of these films at higher currents, since there was no negative differential resistance of the type found in charge-ordered perovskite manganites. Measurements on polycrystalline films deposited on Si(100) substrates, however, showed that with increasing current, the

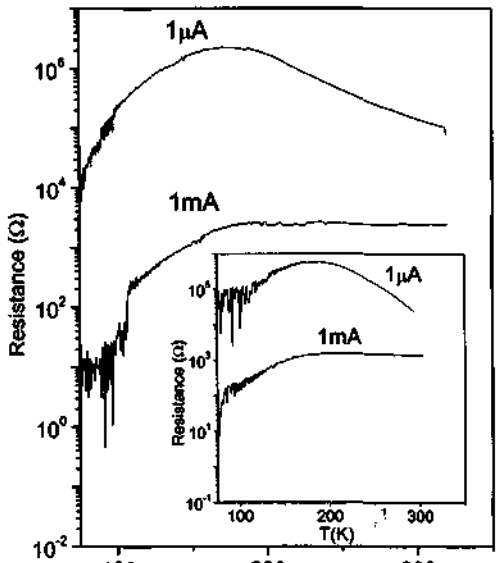

Fig.1.63 Temperature-variation of resistance of thin film of $LaSr_2Mn_2O_7$ deposited on Si(100) substrate at different currents. Inset shows similar effect for $GdSr_2Mn_2O_7$ film on Si(100).

resistance decreases substantially as shown in Fig.1.63. Furthermore, the behavior is non-linear.

1.5 Referenecs

1. Rao C N R and Raveau B Eds. Colossal Magnetoresistance, Charge Ordering and Related Properties of Manganese Oxides; World Scientific: Singapore, **1998**: Rao C N R, Arulraj A, Santosh P N and Cheetham A K Chem. Mater. 1998 **10** 2714: Rao C N R J. Phys. Chem. B 2000 **104** 5877
2. Ramirez A P J. Phys.: Condens. Matter 1997 **9** 8171
3. Imada M, Fujimori A and Tokura Y Rev. Mod. Phys. 1998 **70** 1039
4. Coey J M D, Viret M and Molnar S V Adv. Phys. 1999 **48** 167
5. Salamon M B and Jaime M Rev. Mod. Phys. 2001 **73** 583
6. Van Santen J H and Jonker G Physcia (Ansterdam) 1950 **16** 599
7. Jin S, Tiefel T, McCormack M, Fastnacht R, Ramesh R and Chen L Science 1994 **264** 413
8. Baibich M N, Broto J M, Fert A, Dau Van Nguyen F, Petroff, Eitenne P, Creuzet G, Friederich A and Chazelas J Phys. Rev. Lett. 1988 **61** 2472
9. Zener C Phys. Rev. 1951 **2** 403
10. Jahn H A and Teller E Proc. Roy. Soc. (London) 1937 **A161** 220: Kanamori J J. Appl. Phys. 1960 **31** 14S: Pollert E, Krupicka S and Kuzwicova E J. Phys. Chem. Solids 1982 **43** 1137: Zhao G, Conder K, Keller H and Muller K A Nature 1996 **381** 676
11. Rao C N R, Cheetham A K and Mahesh R Chem. Mater. 1996 **8** 2421: Rao C N R and Cheetham A K Adv. Mater. 1997 **9** 1009
12. Anderson P W Phys. Rev. 1950 **79** 350

13. Jirak Z, Krupicka S, Simsa Z, Dlouha M and Vratislav S J. Magn. Magn. Mater. 1985 **53** 153

14. Tokura Y JSAP International 2000 **July No. 2** 12: Tokura Y and Nagaosa N Science 2000 **288** 462

15. Goldschmidt V M Naturwissenschaften 1926 **14** 477

16. Anderson P W and Hasegawa H Phys. Rev. *1955* ***100*** *675*

17. DeGennes P G Phys. Rev. 1960 **118** 141

18. Goodenough J B Phys. Rev. 1955 **100** 564

19. For review, see, Tokura Y Ed., Colossal Magnetoresistive Oxides (Gordon and Breach Science, New York, 2000), and reference therein.

20. For a review on theories of manganese oxides see, an article by Millis A J in (19), pp 53-86.

21. Kugel K I and Khomskii D I Sov. Phys. JETP 1981 **52** 501

22. Solovyev I, Hamada N, and Terakura K Phys. Rev. Lett. 1996 **76** 4825

23. Mizokawa T and Fujimori A Phys. Rev. B 1996 **54** 5368

24. Ishihara S, Inoue J and Maekawa S Phys. Rev. B 1997 **55** 8280

25. Kuwahara H, Tomioka Y, Asamitsu A, Moritomo Y and Tokura Y Science 1995 **270** 961

26. Kawano H et. al Phys. Rev. Lett. 1997 **78** 4253

27. Kuwahara H, Okuda T, Tomioka Y, Asamitsu A, and Tokura Y Phys. Rev. Lett. 1999 **82** 4316

28. Kajimoto R et. al Phys. Rev. B 1999 **60** 9506

29. Maezono R, Ishihara S and Nagaosa N Phys. Rev. B 1998 **58** 11583

30. Konishi Y et. al. J. Phys. Soc. Jpn. 1999 **68** 3790

31. Zimmermann M V et. al. Phys. Rev. Lett. 1999 **83** 4872

32. Verwey E J W Z. Phys. 1935 **91** 65

33. Li J Q, Matsui Y, Park S K and Tokura Y Phys. Rev. Lett. 1997 **79** 297

34. Blumberg G, Klein M V and Cheong S W Phys. Rev. Lett. 1998 **80** 564: Katsufuji T, Tanabe T, Ishikawa T, Fukuda Y, Arima T and Tokura Y Phys. Rev. B 1996 **54** 14230

35. Wollan E O and Koehler W C Phys. Rev. 1955 **100** 545

36. Radaelli P G, Cox D E, Marezio M and Cheong S W Phys. Rev. B 1997 **55** 3015: Kuwahara H, Tomioka Y, Asamitsu A, Moritomo Y and Tokura Y Science 1995 **270** 961

37. Biswas A, Raychaudhuri A K, Mahendiran R, Guha A, Mahesh R and Rao C N R J. Phys. Condens. Matter 1997 **9** L355

38. Arulraj A, Gundakaram R, Biswas A, Gayathri N, Raychaudhuri A K and Rao C N R J. Phys. Condens. Matter 1998 **10** 4447: Arulraj A, Santosh P N, Gopalan R S, Guha A, Raychaudhuri A K, Kumar N and Rao C N R J. Phys. Condens. Matter 1998 **10** 8497

39. Mahendiran R, Ibarra M R, Maignan A, Millange F, Arulraj A, Mahesh R, Raueav B and Rao C N R Phys. Rev. Lett. 1999 **82** 2191

40. Tomioka Y, Asamitsu A, Kuwahara H, Moritomo Y and Tokura Y Phys. Rev. B 1996 **53** 1689

41. Lees M R, Barrat J, Balakrishnan G, Paul D M C K and Yethiraj M Phys. Rev. B 1995 **52** 14303

42. Kajimoto R, Kakeshita T, Oohara Y, Yoshizawa H, Tomioka Y and Tokura Y Phys. Rev. B 1999 **58** R11837

43. Mori S, Katsufji T, Yamamoto N, Chen C H and Cheong S W Phys. Rev. B 1999 **59** 13573

44. Cox D E, Radaellli P G, Marezio M, Cheong S W Phys. Rev. B 1999 **57** 3305

45. Okimoto Y, Tomioka Y, Onose Y, Otsuka Y and Tokura Y Phys. Rev. B 1999 **59** 7401

46. Woodward P M, Vogt T, Cox D E, Arulraj A, Rao C N R, Karen P and Cheetham A K Chem. Mater. 1998 **10** 3652

47. Kumar N and Rao C N R J. Solid State Chem. 1997 **129** 363

48. Tokunaga M, Miura N, Tomioka Y and Tokura Y Phys. Rev. B 1998 **57** 5259

49. Liu K, Wu X W, Ahn K H, Sulcek T, Chien C L and Xiao J Q Phys. Rev. B 1996 **54** 3007

50. Yoshizawa H, Kawano H, Tomioka Y and Tokura Y Phys. Rev. B **52** R1345

51. Tomioka Y, Asamitsu A, Moritomo Y, Kuwahara H and Tokura Y Phys. Rev. Lett. 1995 **74** 5108

52. Miyano K, Tanaka T, Tomioka Y and Tokura Y Phys. Rev. Lett. 1997 **78** 4257

53. Fiebig M, Miyano K, Tomioka Y and Tokura Y Science 1998 **280** 1925

54. Kiryukhin V et. al Nature 1997 **386** 813

55. Dagotto E, Burgy J and Moreo A Solid State Commun. 2003 **126** 9; Rao C N R and Vanitha P V Curr. Opin. Solid State Mater. Sci. 2003 **6** 97; Rao C N R, Vanitha P V and Cheetham A K 2003 **9** 824; Dagotto E, Hoota T and Moreo A Phys. Rep. 2001 **344 1**; Nagaev E L Phys. Uspekhi 1996 **39** 781; Nagaev E L Fizika Magnitnykh

Poluprovodnikov (Physics of Magnetic Semiconductors) (Moscow: Nauka, 1979) [Translated into English (Moscow: Mir, 1983)]; Nagaev E L Phys. Status Solidi (b)1994 **186** 9; Nagaev E L Phys. Usp. 1995 **38** 497

56. Fontcuberta J 40th Annual Conference on Magnetism and Magnetic Materials Abstracts (Philadelphia, Pennsylvania, 1995) p.167 (Phys. Rev. Lett. 1996 **76** 1122); Srinivasan G40th Annual Conference on Magnetism and Magnetic Materials Abstracts (Philadelphia, Pennsylvania, 1995) p.167;
57. Yankel H L Acta Crystalloigr. 1955 **8** Pt7 394
58. Fesenko E G Perovskite Family and Segnetoelectricity Moscow: Atomizdat 1972
59. Zhang S 40th Annual Conference on Magnetism and Magnetic Materials Abstracts (Philadelphia, Pennsylvania, 1995) p.21
60. Langlet M and Joubert J C Chemistry of Advanced Materials, Edited Rao C N R, IUPAC 21st Century Monographs series, Blackwell Sci. Pub. Oxford, **1993** 55
61. Langlet M, Labeau M, Bochu B and Joubert J C IEEE Trans. Mag. 1986 **22** 151
62. Labeau M, Reboux V, Dharhi D and Joubert J C Thin Solid Films 1986 **136** 257
63. Desisto W, Sosnowski M, Smith F, Deluca J, Kershaw R, Dwight K and Wold A Mat. Res. Bull. 1989 **24** 753
64. Qian Y T, Kershaw R, Dwight K and Wold A Mat. Res. Bull. 1990 **25** 1243
65. Xu W W, Kershaw R, Dwight K and Wold A Mat. Res. Bull. 1990 **25** 1385
66. Haertling G H J. Vac. Sci Tech. 1991**A9** 414
67. Ogawa K, Wei W, Miyano K, Tomioka Y and Tokura Y Phys. Rev. B 1998 **57** R15033
68. Mori T Phys. Rev. B 1998 **58** 12543

69. Gruner G Rev. Mod. Phys. 1988 **60** 1129

70. Cao G, Bolivar J, McCall S, Crow J E and Guertin R P Phys. Rev. B 1998 **57** R11039

71. Vanitha P V, Sarathy K V, Cheetham A K and Rao C N R Solid State Comm. 2000 **115** 463

72. Kimura T, Kumai R, JQ Li, Matsui Y and Tokura Y Phys. Rev. B 1998 **58** 11081

73. Battle P D, Breen M A, Laskey N S, Millburn J E, Murphy L and Rosseinsky M J Chem. Mater. 1997 **9** 552

74. Asamitsu A, Tomioka Y, Kuwahara H and Tokura Y Nature 1997 **388** 50

75. Tokunaga M, Miura N, Tomika Y and Tokura Y Phys. Rev. B 1999 **60** 6219

76. Xiong G C, Li Q, Ju H L, Green R L and Venkatesan T Appl. Phys. Lett. 1995 **66** 1689

77. Snyder J G, Hiskes R, DiCarolis S, Beasley M R and Geballe T H Phys. Rev. B 1996 **53** 14434

78. Wang J Q, Barker R C, Cui G J, Tamagawa T and Halpern B L Appl. Phys. Lett. 1997 **71** 3418

79. Raju A R, Aiyer H N, Nagaraju B V, Mahendiren R, Raychaudhuri A K and Rao C N R J. Phys. D 1997 **30** L71

80. Vijayasarathy K, Vanitha P V, Seshadri R, Cheetham A K and Rao C N R Chem. Mater. 2001 **13** 787

PART 2

INVESTIGATIONS OF MAGNETOFERROELECTRIC $BiMnO_3$ AND $YMnO_3$

SUMMARY*

In this part of the thesis, studies of $BiMnO_3$ and $YMnO_3$ with paired ferroic properties are presented. While $BiMnO_3$ is a ferromagnetic-ferroelectric, $YMnO_3$ is a antiferromagnetic-ferroelectric.

Polycrystalline samples of $BiMnO_3$, synthesized at high-pressures as well as of thin films deposited on n-type Si(100) substrates by nebulized spray pyrolysis have been investigated. The investigations show that $BiMnO_3$ is ferromagnetic with a T_C of 105 K and ferroelectric with a Curie temperature of around 450 K. It remains ferroelectric down to low temperatures, through the ferromagnetic transition.

$YMnO_3$ thin films were grown on n – type Si(111) substrates by nebulized spray pyrolysis in the Metal – Ferroelectric – Semiconductor (MFS) configuration. The C-V characteristics of the film in the MFS configuration exhibit hysteretic behavior consistent with the polarization charge switching direction, with the memory window decreasing with increase in temperature. The density of interface states decreases with the increase in the annealing temperature. Mapping of the silicon energy band gap with the interface states has been carried out. The leakage current measured in the accumulation region is lower in well-crystallized thin films and obeys a space-charge limited conduction mechanism. The calculated activation energy from the dc leakage current characteristics corresponds to oxygen vacancy motion. Deep level trap spectroscopy (DLTS) of

$YMnO_3$/Si(111) films has revealed the defect structure of the films. The results clearly indicate the presence of oxygen ion vacancy defects.

*Based on this work papers have been published in Solid State Commun. (2002), J. Phys. D: App. Phys. (To be published)

2.1 A BRIEF OVERVIEW OF BIFERROICS

2.1.1 Introduction

Ferroics are materials possessing two or more orientation state domains, which can be switched from one to another through the application of one or more appropriate forces[1]. Thus, in a ferroelectric, the orientation state of spontaneous electric polarization can be altered by the application of an electric field; in a ferromagnet the orientation state of magnetization in domains can be swtiched by the application of magnetic field; in a ferroelastic, the direction of spontaneous strain in a domain can be swtiched by application of mechanical stress. Such transitions are described as ferroic transitions. The boundaries of domains are moved by the application of force in order to accomplish changes in orientation.

Ferroics can be classified in two board classes namely primary ferroics and secondary ferroics as shown in fig.2.1.

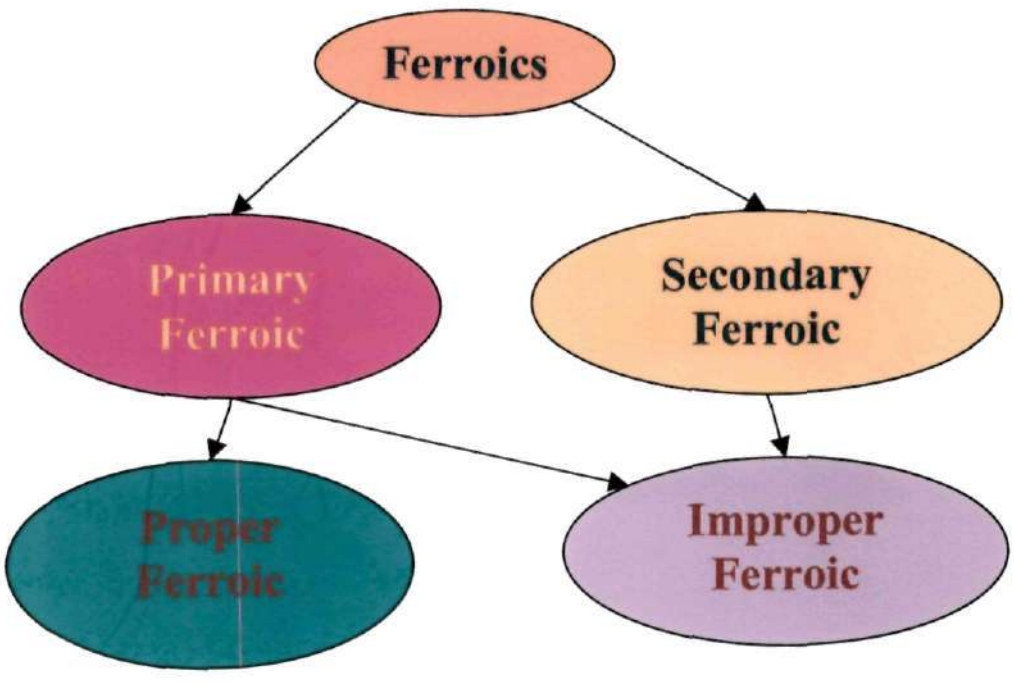

Fig.2.1 Ferroic Phase diagram.

a) Primary Ferroics – Those ferroics where the directionality change of the extensive property like electric polarization, magnetic polarization and elastic strain directly determines the free energy of the system are known as primary ferroics. For example, $BaTiO_3$ is a typical ferroelectric, CrO_2 is a ferromagnet(ic) and $CaAl_2Si_2O_8$ is a ferroelastic.

b) Secondary Ferroics – These are ferroics where the above mentioned extensive properties are induced with the help of another property. The orientation states in these compounds will differ in derivative quantities, which characterize the induced effects. Thus, the induced electric polarization is characterized by dielectric susceptibility, K_{ij}, induced magnetic polarization by magnetic susceptibility, χ_{ij}, and the induced strains by the elastic compliance's, C_{ijkl}. The orientation states in secondary ferroics, therefore, differ in K_{ij}, χ_{ij} and C_{ijkl}; these are tensor quantities and the rank of the tensor is equal to the number of subscripts. The induced effects such as polarization or magnetization can also result from cross-coupled effects such as stress induced polarization (piezoelectric), stress induced magnetization (piezomagnetic) or as a combined effect of two types of fields such as in elastoelectric or elastomagnetic effects. The directional change can then be visualized to occur in the corresponding derivative quantities. Following Newnham, we have listed different types of ferroic effects in Table I where we have also indicated the switching field with an example of each type of ferroic.

Table I

Ferroic class	Ferroic property	Switching field	Example
Primary			
Ferroelctric	Spontaneous polarzation	Electric field	$BaTiO_3$
Ferromagnetic	Spontaneous magnetization	Magnetic field	CrO_2
Ferroelastic	Spontaneous strain	Mechanical stress	$CaAl_2Si_2O_8$
Secondary			
Ferrobielectric	Dielectric susceptibility	Electric field	$SrTiO_3$
Ferrobimagnetic	Magnetic susceptibility	Magnetic field	NiO
Ferrobielastic	Elastic compliance	Mechanical stress	α- Quartz
Ferroelastoelectric	Piezoelectric coefficients	Electric field and mechanical stress	NH_4Cl
Ferromagnetoelastic	Piezomagnetic coefficients	Magnetic field and mechanical stress	$FeCO_3$
Ferromagnetoelectric	Magnetoelectric coefficients	Magnetic field and electric field	Cr_2O_3

As shown in fig.2.1 primary and secondary ferroelectric can further be classified into proper and improper ferroelctric. This second classification is based on order parameters driving the transition. For example polarization, magnetization and strain are proper

parameters for the ferroelectric, ferromagnetic and ferroelastic transitions respectively. Whenever transitions are governed by the expected variations of these order parameters, they are called ***proper ferroics***. The coupled nature of the ferroic phenomena is such that the order parameter, which determines the transition, can often be different from the proper order parameter. Ferroics where the order parameter does not represent a proper property are called ***improper ferroics***. It is possible that the order parameter driving the transition in the primary ferroics is none of the obvious quantities in the expression for free energy, and the ferroic can then be considered to be totally improper. A good example is terbium molybdate in which the order parameter is a condensed optical mode[2]. The optic mode causes a spontaneous strain, which in turn causes a spontaneous polarization through piezoelectric coupling; terbium molybdate is therefore both a improper ferroelectric and an improper ferroelastic. A hexagonal representation of proper and improper ferroics as proposed by Newnham and Cross in given in fig.2.2. The proper order parameter appears on the diagonals of the hexagon while the sides of the hexagon represents improper ferroics. They indicate the cross-coupled origin of ferroic phenomena. An improper primary ferroic in this classification is distinguished from a true secondary ferroic by the appearance of prefix ferro only with the primary ferroic quantity and not for both the coupled quantities. Thus, the term magnetoferroelectric (e.g. Cr_2BeO_4) implies that the material is an improper ferroic where as the term ferromagnetoelectric (e.g. Cr_2O_3) would mean that the material is a secondary ferroic. Based on the above classification of ferroics, a new class of compounds known as multiferroics, are readily understood.

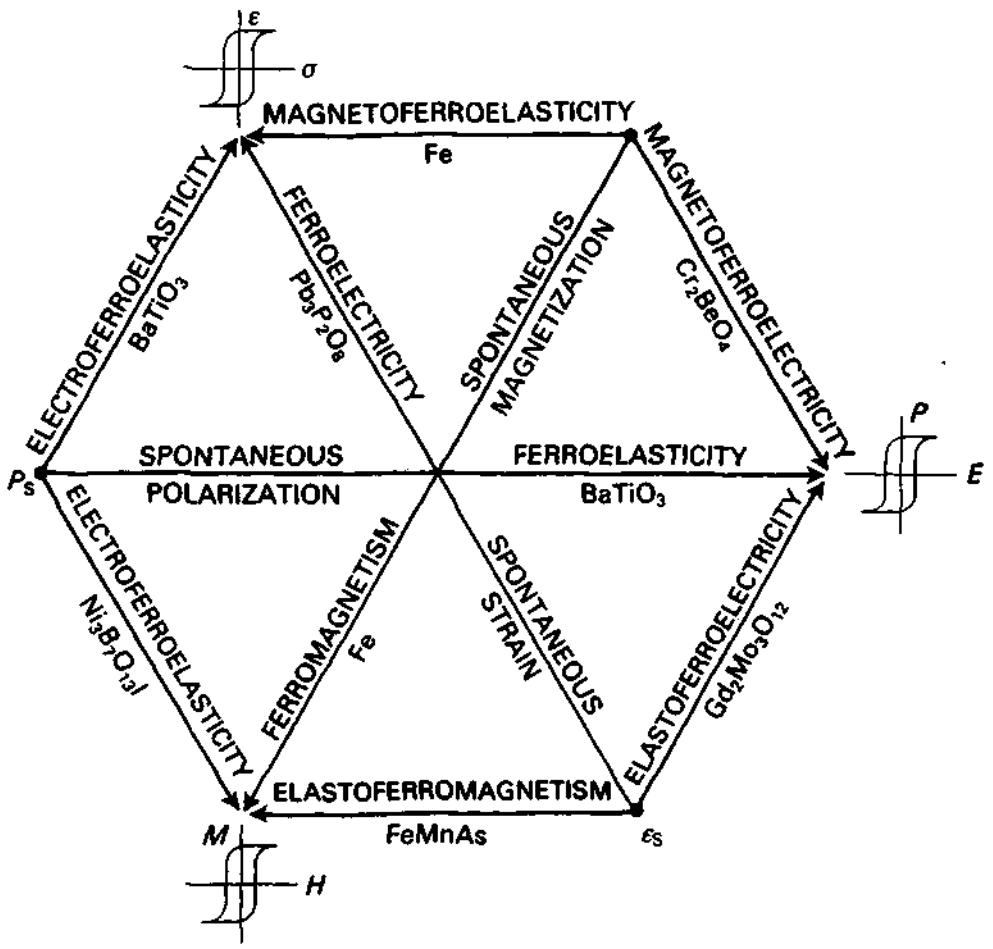

Fig.2.2 Diagram showing several types of order parameters involved in proper and improper ferroics. [Taken from ref. 2]

2.1.2 Multiferroism: The term multiferroism has been coined[3] to describe materials in which two or three of the properties, ferroelectricity, ferromagnetism, and ferroelasticity, occur in the same phase. This means that they have a spontaneous magnetization that can be reoriented by magnetic field, a spontaneous polarization that can be reoriented by applied electric field and a spontaneous deformation that can be reoriented by an applied mechanical stress. Specific device applications that have been suggested for such "multiferroic materials"[4] include multiple state memory elements, electric-field-

controlled ferromagnetic resonance devices and transducers with magnetically modulated piezoelectricity. In addition, the ability to couple with either the magnetic or the electric polarization offers an extra degree of freedom in the design of conventional actuators, transducers and storage devices. In this part of the thesis we are concerned with magnetoelectric multiferroics, which are simultaneously ferromagnetic and ferroelectric, with or without ferroelasticity.

Magnetoelectric Multiferroics: The first ferromagnetic ferroelctric material to be discovered[5] was nickel iodine boracite, $Ni_3B_7O_{13}I$. This was followed by the synthesis of many more multiferroic boracite compounds, all of which have complex structures with many atoms per formula unit and more than one formula unit per unit cell. The large number of inter-ionic interactions in those materials prevented the isolation of the essential factors causing multiferrocity and of the nature of the coupling between the magnetic, electric polarization and structural order parameters. Nickel iodine boracite can be thought of as the Rochelle salt of magnetic ferroelectrics – invaluable for demonstrating the proof of the concept, but unlikely to find applicability.

a) Mixed Perovskites: The search for ferromagnetic ferroelectrics began in Russia in 1950s, with the replacement of some of the d^0 B cations in ferroelectric perovskite oxides by magnetic d^n cations[6]. The first synthetic ferromagnetic ferroelectric material, $(1-x)Pb(Fe_{2/3}W_{1/3})O_3 - xPb(Mg_{1/2}W_{1/2})O_3$, was produced in the early 1960s by this approach[7]. Here, the Mg and W ions are diamagnetic and cause the ferroelectricity, and Fe^{3+} (d^5) ion is responsible for the magnetic ordering. Other examples include B-site-ordered $Pb_2(CoW)O_6$[8], which is ferroelectric and ferromagnetic. $Pb_2(FeTa)O_6$[8], is ferroelectric and antiferromagnetic. $Pb_2(FeTa)O_6$[9] and $Pb_2(FeTa)O_6$[10], are both

ferroelectric and antiferromagnetic, with weak ferromagnetism below around 10 K. As a result of dilution of the magnetic ions, these materials all have rather low Curie and Neel temperatures.

b) Other Perovskites: A number of other perovskite materials are known to have ferroelectric as well as magnetic (mostly of the antiferromagnetic type) ordering. These include the manganites of the small rare earth elements and yttrium and a few compounds in which Bi is the A-site large cation. These materials will be discussed in detail later.

Requirements for Magnetoelectric Multiferroicity: A material to be magnetoelectric multiferroic must be ferroelectric and ferromagnetic in the same phase and temperature window. Therefore, its allowed physical, structural and electronic properties are restricted to those that occur both in ferromagnetic and in ferromagnetic materials. In this section, we analyze a range of properties and discuss how these properties limit our choice of potential materials. We discuss those that are the limiting factors in preventing the simultaneous existence of ferromagnetism and ferroelectricity.

a) Symmetry: A primary requirement for the existence of ferroelectricity is a structural distortion from the prototypical high-symmetry phase that removes the center of symmetry and allows an electric polarization. There are 31 point groups that allow a spontaneous electric polarization, P, and 31 that allow a spontaneous magnetic polarization, M[3]. Thirteen point groups (1, 2, 2', m, m', 3, 3m', 4, 4m'm', m'm2', m' m'2', 6 and 6m'm') are found in both sets, allowing both properties to exist in the same phase. Although this represents a considerable reduction from the total number of possible crystal structures (the total number of Shubnikov point groups is 122), it is not an insignificant number, and many candidate materials that are not in fact ferromagnetic

and ferroelectric exist in one of the allowed symmetries. Therefore, it is unlikely that symmetry considerations are responsible for the scarcity of ferromagnetic ferroelectric materials.

b) **Electrical Properties:** A ferroelectric should be an insulator (otherwise, an applied electric field would be inducing an electric current, rather causing an electric polarization). Ferromagnets, although not required to have specific electrical properties, are often metals. For example, the driving force for ferromagnetism in the elemental ferromagnets Fe, Co and Ni and their alloys is high density of states at the Fermi level, which also, of course results in metallicity. Therefore, one could assume that the lack of the simultaneous occurrence of magnetic and ferroelectric ordering is simply the result of a dearth of magnetic insulators. However, if we extend our search to include ferrimagnets or weak ferromagnets (which have canted antiferromagnetic ordering, resulting in a weak magnetic moment in the direction of canting), this argument no longer holds, because most ferrimagnets or weak ferromagnets are, in fact, insulators. In addition, there are also very few antiferromagnetic ferroelectrics, even though antiferromagnets are usually insulating materials. Therefore, it appears that we cannot blame the lack of magnetically ordered ferroelectrics simply on a shortage of magnetically ordered insulators.

c) **Chemistry of Multiferroism:** We know the common perovskite ferroelctric materials have B-site cations with a formal charge corresponding to the d^0 electron configurartion. Clearly, if there are no d electrons creating localized magnetic moments, then there can be no magnetic ordering of any type. It appears however that, in most cases, as soon as the d shell on the small cation is partially occupied, the tendency for it to make a distortion that removes the center of symmetry is eliminated. This could be the

result of a number of effects, including size, the tendency to undergo a different more dominant distortion, electronic properties, magnetic properties or some combination of the above. We now consider the likely influence of each of these factors.

d) Size of Small Cation: We now compare the ionic radii of typical d^0 cations in perovskite ferrolectrics with those of typical d^n cations in nonferroelectrics perovskite oxides to see if this argument is correct.

The Shannon radii[11] of some common d^0 small cations found in ferroelectric perovskite oxides are Ti^{4+}, 0.745 Å; Nb^{5+}, 0.78 Å and Zr^{4+}, 0.86 Å. Some representative d^n cations that are found as the small cations in nonferroelectric perovskite oxides include $Mn^{3+}(d^4)$, $Ti^{3+}(d^1)$ and $V^{4+}(d^1)$ with radii of 0.785 Å, 0.81 Å and 0.72 Å, respectively. Therefore, typical B-site cations with d electron occupation do not have systematically larger radii than d^0 B-site cations. We conclude that the size of the B-cation is not a deciding factor in the existence or otherwise of ferroelectriciy.

e) Structural Distortions: Ferroelectric materials must undergo a phase transition to a low-temperature phase that does not have a center of symmetry. This is most often achieved in conventional perovskite ferroelectrics by an off-center displacement of the small (B) cation from the center of oxygen octahedron. However, for cations with certain d-orbital occupancies, the tendency to undergo a Jahn-Teller distortion is strong and will likely be the dominant structural effect. The Jahn-Teller distorted structure might have a lower driving force for off-center displacement than the otherwise undistorted structure.

Examples of this effect are seen in lanthanum manganite, $LaMnO_3$, in which the Mn^{3+} ion has a d^4 configuration, and yttrium titanate, $YTiO_3$, in which the Ti^{3+} ion is d^1. Both materials have a d-type Jahn-Teller distortion, in which the elongated axes of the oxygen

octahedra are oriented parallel to each other along the crystallographic c-axis[12]. Orbital ordering is observed to occur simultaneously with the Jahn-Teller ordering[12]. $LaMnO_3$ is insulating and an A-type antiferroamagnet, in which planes of ferromagnetically algined Mn^{3+} ions are aligned antiparallel to each other. $YTiO_3$ is strongly correlated ferromagnetic Mott-Hubbard insulator. Neither material is ferroelectric. The relevance of formal charge on the B cation can be seen from above examples. In $BaTiO_3$, the actual occupation of the 3d electrons is closer to d^1 than to d^0 because of donation of charge density from the oxygen ligands[13]. A d^1 cation should undergo a Jahn-Teller distortion. No Jahn-Teller distortion is observed in $BaTiO_3$ however, which is consistent with the d^0 formal charge.

f) Magnetism versus d-Orbital Occupancy: It is clear that the existence of d electrons on the B-site reduces the tendency of perovskite oxides to display ferroelectricity. However, it is not clear whether it is merely the presence of d electron density or the influence of the magnetic spin polarization that is the dominant factor in creating this effect. Using first-principles density functional theory calculations, it is possible to answer this question by artificially removing the spin polarization in materials that are experimentally found to be magnetic and determining whether they then become ferroelectric.

2.1.3 Bismuth Manganite

Bismuth manganite can be regarded as the " hydrogen atom" of multiferroics. Although information about $BiMnO_3$ is sparse[14], indications are that it is simultaneously ferromagnetic and ferroelectric at low temperatures, and, because it has a simple structure, it is amenable to detailed study using first principles[15]. $BiMnO_3$ crystallizes at high pressure in a highly distorted perovskite structure as shown in fig.2.3, which is both ferromagnetic and insulating. Ferromagnetic insulators are unusual; another example is

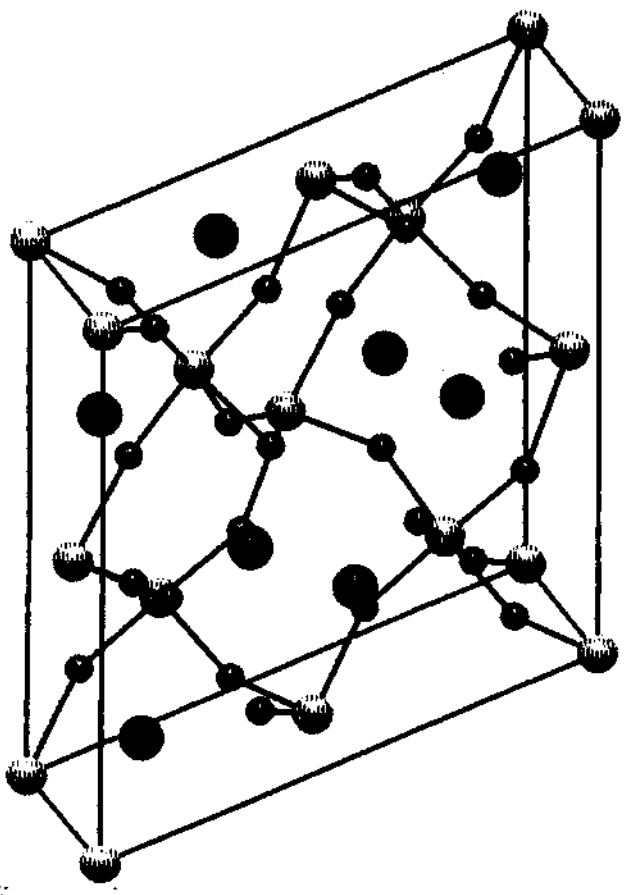

Fig.2.3 Crystal structure of monoclinic $BiMnO_3$ projected nearly down the b axis. The large black spheres are Bi, and the smaller white spheres are Mn, six-coordinate with oxygen. [Taken from ref.21]

$SeCuO_3$, which is also a highly distorted perovskite[16,17]. By contrast, $LaMnO_3$ and all the rare earth manganites are antiferromagnetic insulators, as excepted from the usual superexchange argument[18]. This difference in behavior is particularly surprising in light of

the similarity in ionic radii of La^{3+} and Bi^{3+}, which are respectively, 1.216 and 1.24 Å (in nine coordination). In addition to its fundamental interest as a ferromagnetic insulator, it has also been suggested that $BiMnO_3$ is ferroelectric[15]. Ferroelectricity and magnetism are rarely found in the same system because the off-center distortion responsible for polar behavior is usually incompatible with the partially filled d-levels which are a prerequisite for a magnetic ground state[19,20].

There has been much interest as to why $BiMnO_3$ is a ferromagnetic insulator unlike all other manganites which are antiferromagnetic insulators. This has been the motivation for the theoretical[21] and experimental[22] efforts to study the difference between properties of $BiMnO_3$ and other rare earth manganites like $LaMnO_3$. The origin of the differences between (proposed) ferroelectric $BiMnO_3$ and the nonferroelectric rare earth manganites can be understood by comparing the calculated electronic properties of $BiMnO_3$ with those of $LaMnO_3$. This has been done by calculating the electronic structure for the high

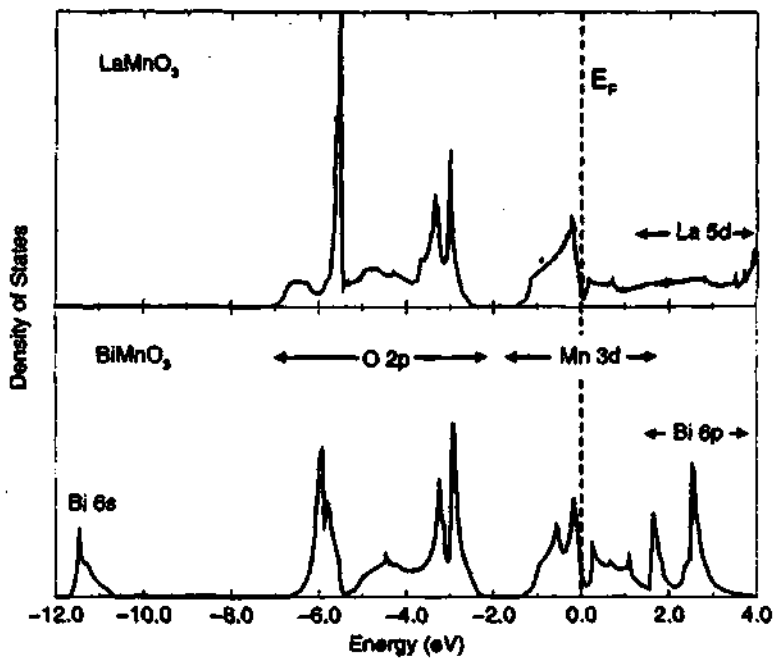

Fig.2.4 Calculated densities of states for cubic paramagnetic $LaMnO_3$ and $BiMnO_3$. [Taken from ref. 19]

symmetry cubic phases, without including magnetic effects [the so-called paramagnetic (PM) phase], then lower the magnetic symmetry to the ferromagnetic (FM) phase, and than the structural distortions are introduced in both paramagnetic and ferromagnetic calculations. This ability to isolate structural and magnetic distortions is unique to computational studies and allows for an identification of the essential microscopic interactions that cause the observed macroscopic behavior. There are two important questions to answer here. First, why is $BiMnO_3$ ferromagnetic, when the superexchange mechanism causes the other rare earth manganites to be antiferromagnetic? Second, what may cause $BiMnO_3$ to be ferroelectric, when the rare earth manganites do not show a ferroelectric distortion?

(a) Cubic Paramagnetic Structures: Fig.2.4 shows the calculated densities of states for cubic paramagnetic $LaMnO_3$ and $BiMnO_3$. One striking *difference* between the two DOS plots is the presence of a band between -10 and -12 eV in the $BiMnO_3$ band structure that does not exist in the $LaMnO_3$ case. This band corresponds to the high-lying occupied Bi 6s electrons. In addition, the high-energy La 3d electrons have a very different form than the Bi 6p electrons, which occupy a similar energy range.

Fig.2.5 shows the corresponding band structures along the high-symmetry axes of the simple cubic Brillouin zone. Note that the Mn 3d bands in $BiMnO_3$ overlap with the partially occupied Bi 6p orbitals, whereas in $LaMnO_3$, the next highest bands are the unoccupied La 5d bands.

Differences between the two band structures show up clearly in the bands along the $\Gamma \rightarrow X$ line. This region of the band structure is shown in fig.2.6 with the symmetry labels added and the energy scale extended to include the lower energy O 2*s* and La 5p bands.

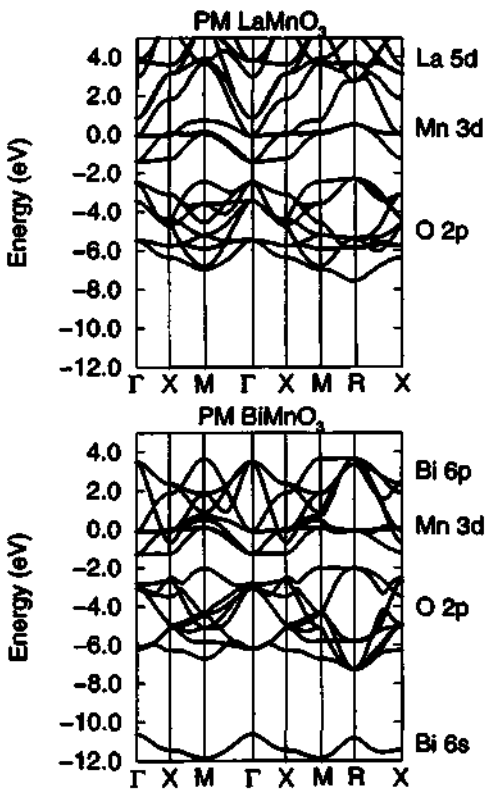

Fig.2.5 **Calculated band structures for cubic paramagnetic $LaMnO_3$ and $BiMnO_3$ along the high-symmetry axes of the Brillouin zone. [Taken from ref. 19]**

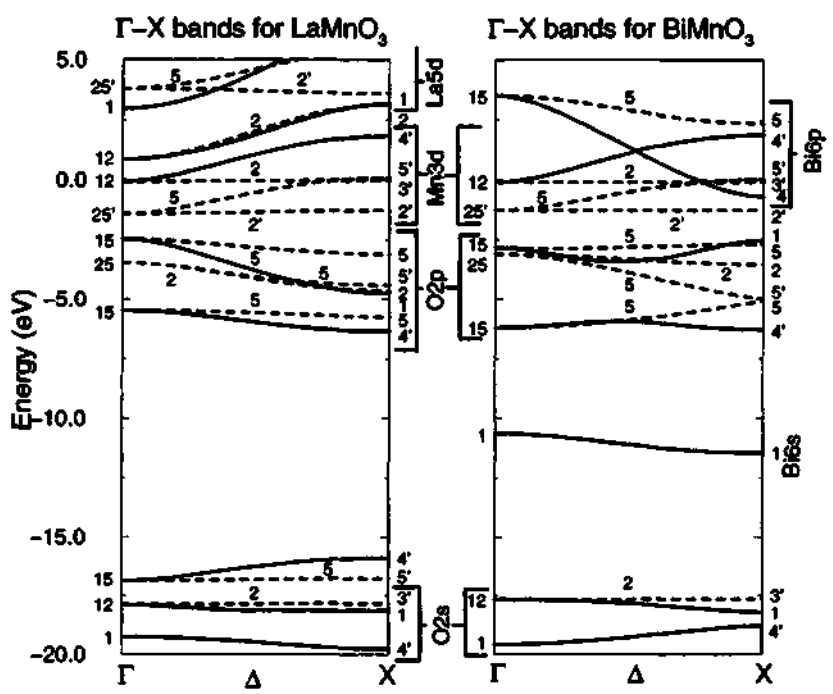

Fig.2.6 **Calculated band structures for cubic paramagnetic $LaMnO_3$ and $BiMnO_3$ along the $\Gamma \rightarrow X$ axis. The solid lines show the bands of Δ_1 symmetry. [Taken from ref. 19]**

In $LaMnO_3$, the two oxygen 2p Δ_1 bands decrease monotonically in energy from Γ to X, and the Mn 3d Δ_1 band increases monotonically from Γ to X. Analysis of the charge density shows that the Fermi surface at the Γ point consists largely of Mn 3d electrons, with contributions from other atoms being very small. The charge density at the X point is very similar, except that there is a small oxygen contribution, indicating that the amount of Mn 3d-O 2p hybridization increases along the Γ to X line.

In $BiMnO_3$, the behavior is quite different. The X_1 symmetry of the Bi 6s band at the X point causes the X_1 O 2p band to be "pushed up" in energy, resulting in a different ordering of the O 2p bands at the X point. The very dispersive Bi 6p Δ_1 band crosses the Mn 3d Δ_1 band and moves below the Fermi level near the X point. As a result, the charge distribution at the Γ point is similar to that of $LaMnO_3$; however at X, there is significant amount of charge density around the Bi atoms. Further analysis reveals that the Bi component is in the X'_4 band, which crossed the highest Mn 3d band.

TABLE 1: Tight-Binding Parameters (in eV) for $BiMnO_3$, $LaMnO_3$ and $YMnO_3$. [Taken from ref.19]

	$BiMnO_3$	$LaMnO_3$	$YMnO_3$
E_{O2s}	−17.6806	−17.8364	−17.9649
E_{O2p}	−3.4444	−4.5140	−4.7382
E_{Mn3d}	−1.2024	−1.1913	−1.4097
$V_{O2s-O2s}$	−0.2521	−0.2437	−0.2461
$V_{(O2p-O2p)\sigma}$	0.7352	0.6206	−0.7167
$V_{(O2p-O2p)\pi}$	−0.1322	−0.0635	−0.1069
$[V_{(O2p-O2p)\sigma}]_2$	−0.2119	0.1826	0.1688
$[V_{(O2p-O2p)\pi}]_2$	−0.0448	0.0830	0.0620
$V_{O2s-Mn3d}$	−1.7207	−1.7358	−1.9711
$V_{(O2p-Mn3d)\sigma}$	−1.9642	−1.8385	−2.0601
$V_{(O2p-Mn3d)\pi}$	1.0363	0.8790	1.0837
$V_{(Mn3d-Mn3d)\delta}$	−0.0034	0.0663	0.0488

[a] Parameters obtained by nonlinear least-squares fitting to the ab initio eigenvalues along Γ to X. [b] E indicates an orbital energy, and V, an interatomic transfer integral. All transfer integrals are between nearest neighbors, except those with the subscript "2", which are between next-nearest neighbors. Only the parameters listed in the table were allowed to be nonzero in the fitting procedure.

To quantify the differences between cubic PM $BiMnO_3$ and $LaMnO_3$, tight-binding analyses of the Γ to X regions of the respective band structures has been done. Tight-

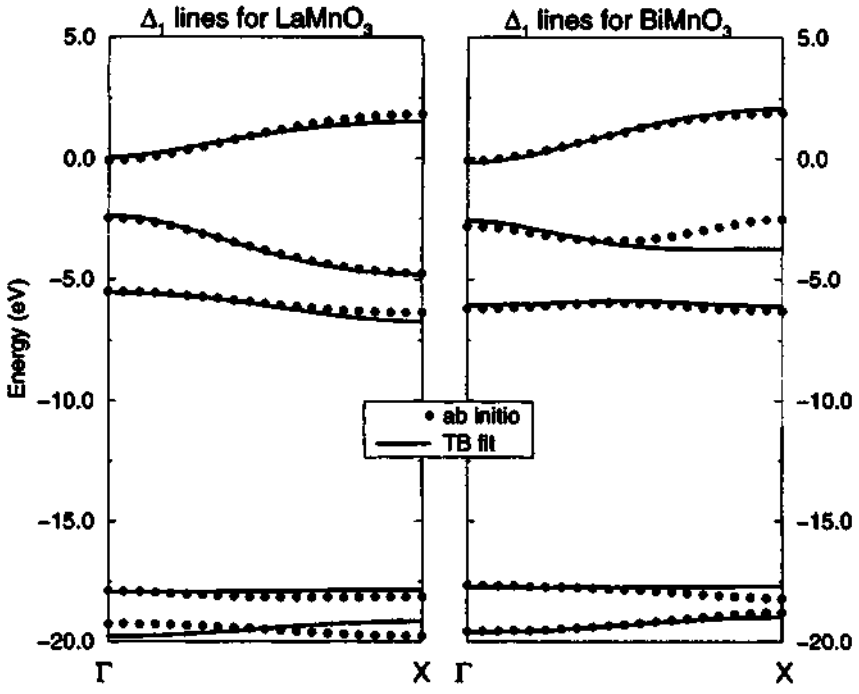

Fig.2.7 Comparison of ab initio Δ_1 bands with those obtained from a tight-binding for using only Mn and O orbitals in the basis. The fit for $LaMnO_3$ is good, indicating that only the Mn and O ions are significantly involved in covalent bonding. The fit for $BiMnO_3$ has a higher RMS deviation and, in particular, misses the additional curvature at around –3eV near the X point. This shows that additional interactions are present. [Taken from ref.19]

binding parameters were obtained by nonlinear least-squares fitting[23] to the calculated ab initio energies at the high-symmetry Γ and X points and at 19 points along the Δ axis. The tight-binding parameters thus obtained are given in Table 1. The band structures for the bands of symmetry are compared with the ab initio values in fig.2.7. The limited basis set reproduces the $LaMnO_3$ bands well, consistent with an early proposal by Goodenough[24] that the magnetic properties of $LaMnO_3$ are determined by the Mn 3d-O 2p hybridization only. Note that the fit to the lower-energy O 2s bands is the least good; these bands are very close in energy to the La 5p bands, which have not been included in the fit. The behavior of the $BiMnO_3$ Δ_1 bands is less well reproduced, confirming that additional orbital overlaps are essential in producing the observed band structure. In $BiMnO_3$ with Bi 6s and 6p orbitals added to the basis. Transfer integrals between nearest-neighbor Bi 6s-O 2p, Bi 6p-O 2p, Bi 6p-Mn 3d, and Bi 6p-Bi 6p orbitals were allowed to

be nonzero. This significantly improved the quality of the fit to the ab initio bands (see fig.2.8) and reduced the root-mean-square deviation to 0.12. The values of the new tight-binding parameters are given in Table 2. The largest transfer integrals involving Bi are the Bi 6s-O 2p and Bi 6p-O 2p σ interactions, with the magnitude of the σ-bonded Bi 6p-O 2p interaction being approximately 30% larger than that of the Bi 6s-O 2p. Also large are the Bi 6p-Bi 6p σ interactions, which cause the Bi 6p Δ_1 band to be pushed down below the Fermi level.

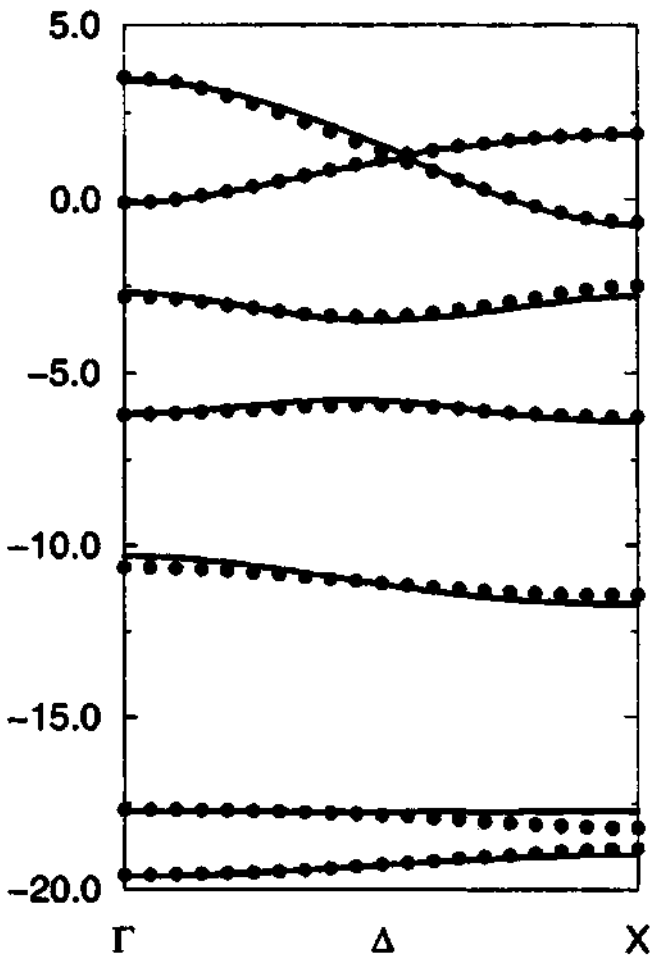

Fig.2.8 Comparison of ab initio Δ_1 bands with those obtained from a tight-binding fit including Bi 6s and 6p orbitals in addition of Mn 3d and O 2s and 2p. The fit improved over the fit using only Mn and O orbitals. [Taken from ref. 19]

TABLE 2: Tight-binding Parameters (in eV) for $BiMnO_3$[a, b]. [Taken from ref. 19]

	$BiMnO_3$		$BiMnO_3$
E_{Bi6s}	−10.310688	$V_{(Bi6p-Mn3d)\pi}$	0.078144
E_{Bi6p}	0.202695	$V_{O2s-O2s}$	−0.237506
E_{O2s}	−17.717958	$V_{(O2p-O2p)\sigma}$	0.652059
E_{O2p}	−3.725773	$V_{(O2p-O2p)\pi}$	−0.125450
E_{Mn3d}	−1.167871	$[V_{(O2p-O2p)\sigma}]_2$	−0.010196
$V_{(Bi6p-Bi6p)\sigma}$	0.848443	$[V_{(O2p-O2p)\pi}]_2$	−0.002797
$V_{(Bi6p-Bi6p)\pi}$	0.166061	$V_{O2s-Mn3d}$	−1.645508
$V_{Bi6s-O2p}$	−0.812502	$V_{(O2p-Mn3d)\sigma}$	−1.926533
$V_{(Bi6p-O2p)\sigma}$	−1.061660	$V_{(O2p-Mn3d)\pi}$	0.959768
$V_{(Bi6p-O2p)\pi}$	−0.145201	$V_{(Mn3d-Mn3d)\delta}$	0.029347
$V_{(Bi6p-Mn3d)\sigma}$	0.170850		

[a] Parameters obtained by nonlinear least-squares fitting to the ab initio eigenvalues along Γ to X. [b] An expanded tight-binding basis including the Bi 6s and 6p orbitals was used. The labeling scheme for the parameters is the same as in Table 1. Only the parameters shown were allowed to be nonzero.

(b) Some Experimental Results: The tight-binding analysis clearly shows that there is strong hybridization between the O 2p and Bi 6p orbitals, consistent with the observed enhancement of charge ordering in Bi-doped $CaMnO_3$[25]. Rao[25] et. al have observed that the charge-ordered state in $Bi_{0.3}Ca_{0.7}MnO_3$ persists to a higher temperature than does the charge-ordered state in $La_{0.3}Ca_{0.7}MnO_3$. They explained their observations by noting that the electronegativity of Bi enhances Bi-O hybridization and, in turn, reduces the amount of Mn-O hybridization. This also provides a plausible explanation for the existence of ferromagnetism in $BiMnO_3$. The combination of structural distortion and reduced Mn 3d-O 2p overlap (both driven by bismuth-oxygen covalency) reduces the strength of the antiferromagnetic superexchange interaction, making ferromagnetic coupling more favorable.

Additional evidence in support of this phenomenon is found from ref. 26, in which a temperature-composition phase diagram for $Bi_{1-x}Ca_xMnO_3$, showing the charge-ordered

transition and the Neel temperature, is plotted. Comparison with similar data for $La_{1-x}Ca_xMnO_3$ (for example, in ref. 27) confirms that the charge-ordered phase persists to higher temperature in Bi-doped $CaMnO_3$ than in La-doped $CaMnO_3$. Therefore, in addition to their potential utility as multiferroic materials, Bi compounds provide the ability to tune the positions of phase boundaries by substitution of Bi for the rare earth ions, which might prove valuable in optimizing material properties for specific device applications.

(c) Cubic Ferromagnetic Structures: The results of calculations in which the high-symmetry cubic structure is retained, but the electrons are allowed to spin polarize are instructive. The introduction of spin polarization reduces the energy of both $BiMnO_3$ and $LaMnO_3$ by around 1 eV per unit cell compared with the paramagnetic case. The most

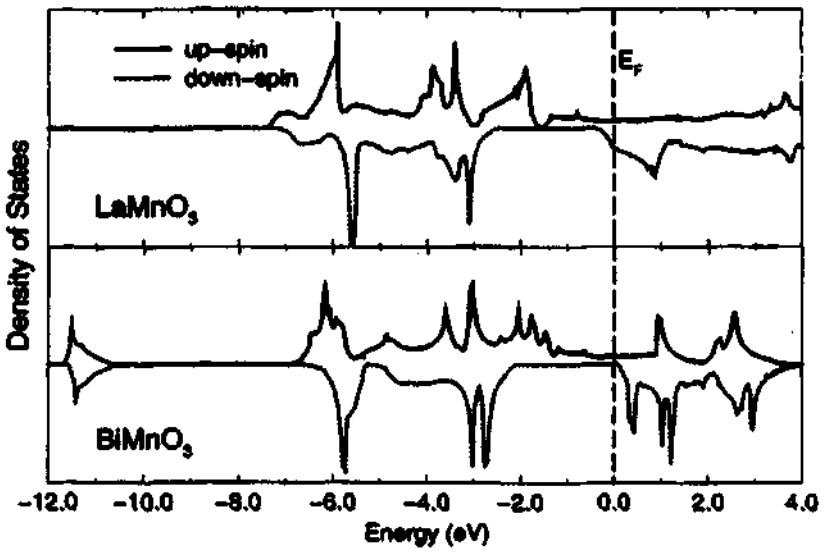

Fig.2.9 Calculated densities of states for cubic ferromagnetic $LaMnO_3$ and $BiMnO_3$. [Taken from ref.19]

important observation is that the *differences* between $BiMnO_3$ and $LaMnO_3$ observed in the paramagnetic calculations persist into the ferromagnetic phase, with the PM to FM transition introducing the same kind of changes in both materials.

Fig.2.9 shows the calculated densities of states for cubic ferromagnetic $LaMnO_3$ and $BiMnO_3$[15,19]. The majority spins are represented by the solid line on the positive *y* axis, and the minority spins by the dotted line on the negative *y* axis. In both $LaMnO_3$ and $BiMnO_3$, the down-spin Mn 3d band is split off from the O 2p band and has a similar form to the corresponding paramagnetic band. The up-spin Mn 3d hybridizes strongly with the O 2p, and there is no band gap for the majority carriers. The up-spin DOS at the Fermi level in $LaMnO_3$ is still high, indicating that the cubic FM state has a high energy. This is consistent with the fact that the lowest-energy spin polarization in *structurally relaxed* $LaMnO_3$ is antiferromagnetic[28]. The DOS at the Fermi level in $BiMnO_3$ is somewhat lower, suggesting that the FM phase should be more stable in $BiMnO_3$ than in $LaMnO_3$. For both compounds, the Fermi level cuts through the very bottom of the down-spin Mn 3d bands, and the conduction band is occupied almost entirely by up-spin electrons. Again, the most obvious differences between the two electronic structures are the presence of the Bi 6s band between -10 and -12 eV and the contrasting forms of the Bi 6p and La 5d bands.

The spin band structures for $BiMnO_3$ and $LaMnO_3$ along the high-symmetry axes of the simple cubic Brillouin zone also show many similarities between the FM and PM energy bands, and the earlier conclusions regarding the origin of the differences between $BiMnO_3$ and $LaMnO_3$ hold valid[15]. For both materials, the up-spin Mn 3d and O 2p bands are strongly hybridized, and there is no gap between them. However, the down-spin Mn 3d are split off from the O 2p bands by a larger gap than in the PM case. Finally, the $BiMnO_3$ minority conduction electrons have a large directional Bi 6p component, in striking contrast to those in $LaMnO_3$, in which the electrons are localized entirely in the

Mn 3d orbitals. The fact that the conduction electrons partly occupy p-type atomic orbitals should produce quite different transport characteristics than those observed in conventional rare earth manganites, in which the conduction bands are entirely Mn 3d-type.

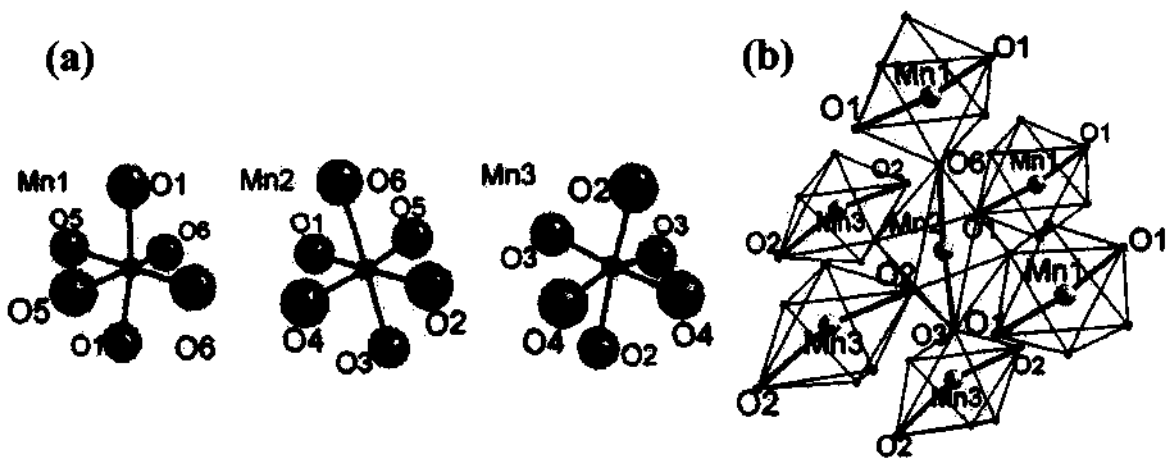

Fig.2.10 (a) Coordination environment of Jahn–Teller distorted Mn cations. (b) Three-dimensional magnetic exchange between the Mn atoms; the thick lines correspond to the occupied d_z^2 orbitals. [Taken from ref. 22]

Recently, the unusual ferromagnetism in $BiMnO_3$ has been explained by Rao et. al[22] to be due to orbital ordering. Each of the three MnO_6 polyhedra shows the axial elongation that is typical of Jahn-Teller distorted d^4 cations in perovskite systems. The orbital ordering that is associated with these distortions in $BiMnO_3$ is the same as that observed at room temperature (fig.2.10), resulting in superexchange interactions that are largely ferromagnetic (Table 3). In four of the six pathways, the orbital ordering ensures that half filled d_z^2 orbitals point towards the empty $d_{x^2-y^2}$ orbitals on the next manganese; such interactions are predicted to be ferromagnetic according to the rules proposed by Goodenough[24] and Kanamori[24]; they are strongest when the M-O-M bond angle is close to 180°. We note that three of the four ferromagnetic Mn-O-Mn angles are significantly

Table 3 Primary superexchange interactions in $BiMnO_3$ at 20 K. The bond angle estimated deviations are ~ 0.3°. [Taken from ref.22]

Pathway	Angle°	Interaction
Mn(1)–O(1)–Mn(2)	154.8	FM
Mn(2)–O(2)–Mn(3)	147.0	FM
Mn(2)–O(3)–Mn(3)	160.4	FM
Mn(2)–O(4)–Mn(3)	148.8	AFM
Mn(1)–O(5)–Mn(2)	149.5	AFM
Mn(1)–O(6)–Mn(2)	158.7	FM

larger than the antiferromagnetic ones (Table 3). There is no instance in which a half filled d_z^2 orbital points towards another half filled d_z^2 orbital (this would be strongly antiferromagnetic), but two cases in which empty $d_{x^2-y^2}$ orbitals point towards each other [(through O(4) and O(5)]. Optimally, these interactions would be weakly antiferromagnetic, but this cannot be accommodated in combination with the constraints of the strong ferromagnetic interactions, so the system must be slightly frustrated.

It is interesting to compare the ferromagnetic structure of $BiMnO_3$ with the *A*-type

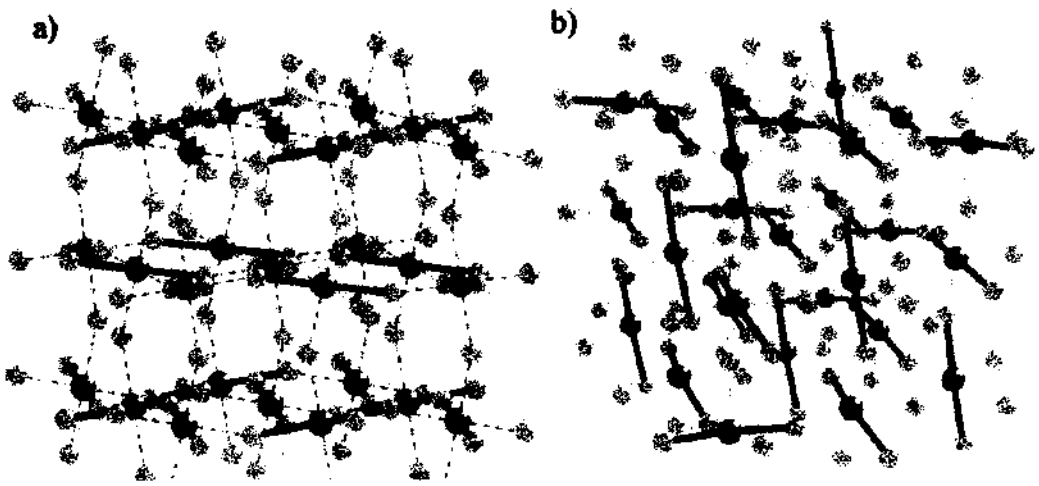

Fig. 2.11 The two-dimensional orbital ordering in (a) $LaMnO_3$ is compared with the three-dimensional orbital ordering seen in (b) $BiMnO_3$. Bold lines represent the orientation of the d_z^2 orbitals, as revealed by the elongations of MnO. [Taken from ref. 22]

antiferromagntic structure found in the related perovskite, $LaMnO_3$. This comparison has recently been discussed by Hill and Rabe[15]. $LaMnO_3$ is also orbitally ordered, but in a simple manner which leads to ferromagnetic sheets that are antiferromagnetically aligned with respect to each other. Half filled d_z^2 orbitals point towards empty $d_{x^2-y^2}$ orbitals within the ferromagnetic sheets, but this results in empty $d_{x^2-y^2}$ orbitals facing each other via the oxygens between the sheets, leading to the overall antiferromagnetic structure see (fig.2.11). It is the substitution of La by Bi that is responsible for stabilizing a different structural distortion with different orbital ordering that leads to ferromagnetism. There are several factors that may be responsible for this crucial difference of covalence of the Bi-O bonds compared with La-O bonds will have an impact on the Mn-O-Mn interactions. Second, the bismuth lone pairs lead to *A* cations displacements along the <111> directions of the cubic perovskite sub-cell that are incompatible with the two-dimensional orbital ordering found in $LaMnO_3$. The more complex orbital ordering pattern found in $BiMnO_3$, which must stem from the distortions imposed by the Bi lone pairs, leads to three dimensional ferromagnetic interactions that result in the observed spin structure.

(d) Soft-Mode Ferroelectric Distortions: The phonon modes in $BiMnO_3$ and $LaMnO_3$ have been analyzed to determine the existence and nature of ferroelectric instabilities[15,19]. The lattice distortions of the high-symmetry cubic phases have been studied and results for $BiMnO_3$ with those for $LaMnO_3$ have been compared. Zone-center phonons are discussed below.

The perovskite manganites have 5 atoms per unit cell, which results in 15 phonon branches, 3 acoustical and 12 optical. At the point, all phonons are 3-fold degenerate, so

there is one acoustical phonon frequency (which is zero) and four optical frequencies. We are interested in the optical phonons that have negative eigenvalues, indicating lattice instabilities.

The force constant matrices for $LaMnO_3$ and $BiMnO_3$ were determined by calculating the Hellmann-Feynman forces resulting from the displacement of each atom in turn 0.1 Å along the *z* direction of the unit cell. The forces exerted on the Mn ions by the other ions were determined using the acoustic sum rule. We calculated the Mn-Mn force by applying the acoustic sum rule to both the columns and the rows of the resulting matrix. The two values differed by less than ~ 0.001 eV/Å.

TABLE 4: Eigenvectors and Eigenvalues of the Dynamical Matrix that Correspond to the Unstable Phonon Modes on Cubic Paramagnetic $BiMnO_3$ and $LaMnO_3$. [Taken from ref. 19]

$BiMnO_3$						$LaMnO_3$					
ν (cm^{-1})	Bi	Mn	Oz	Ox	Oy	ν (cm^{-1})	La	Mn	Oz	Ox	Oy
$72.39i$	0.0	0.0	0.0	$-1/\sqrt{2}$	$1/\sqrt{2}$	$49.04i$	0.0	0.0	0.0	$-1/\sqrt{2}$	$1/\sqrt{2}$
$98.20i$	−0.43	0.09	0.16	0.62	0.62	$44.69i$	−0.59	0.22	0.21	0.53	0.53

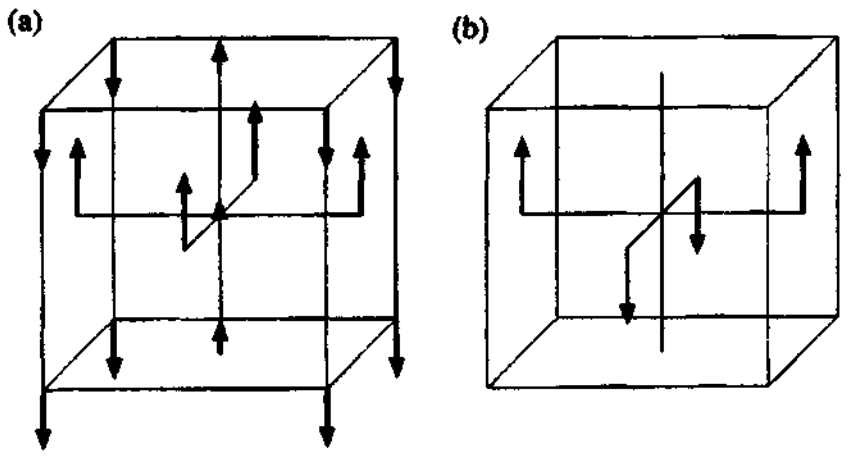

Fig.2.12 (a) Eigenvector of the unstable ferroelectric Γ point phonon mode in $BiMnO_3$. The Mn ion is at the center of the unit cell surrounded by an octahedra of oxygens, with the large cations at the unit cell corners. (b) Nonferroelectric mode that is unstable in $LaMnO_3$. Each mode is 3 fold degenerate. [Taken from ref.19]

instabilities. Although a definitive prediction requires calculation of the phonon dispersion throughout the entire Brillouin zone, it is likely that the weakly unstable zone-center phonon in $LaMnO_3$ will be overshadowed by a stronger instability elsewhere in the Brillouin zone, reproducing theoretically the experimentally observed Jahn-Teller distortion. Similarly, the very unstable ferroelectric mode at the zone center in $BiMnO_3$ is likely to dominate over possible unstable modes at other frequencies, confirming theoretically the suggested existence of ferroelectricity in $BiMnO_3$. This mode is driven by Bi-O covalency and creates a Bi-O electric dipole moment, in contrast to the conventional perovskite oxide ferroelectrics, in which B cation-oxygen covalency is the principal driving force for the ferroelectric distortion. Thus, the d electron occupation on the manganese ion in $BiMnO_3$ inhibits the displacement of the B cation. It is only because of the unusual behavior of the A cation that ferroelectricity can occur at all.

(e) Electronic Ferroelectricity: Ferroelectricity can also occur if the magnetic electronic state in the cubic phase (before the ferroelectric lattice distortion takes place) has a propensity to dipolar instability[30]. In this case, the driving mechanism for ferroelectricity is ***electronic*** instability[30], rather than the usual softening of the phonon mode[13,31]. In these so-called "**electronic ferroelectrics**", the ferroelectric phase transition is driven by a change in the electronic structure rather than the crystal structure. (Of course electron-phonon coupling can cause a lattice distortion as a secondary effect of the transition, but a change in crystal structure is not required). A requirement for the condensation is that the d-f coulomb interaction dominates over the hybridization. The phase transition to the electronic ferroelectric state occurs when the d-f exciton energy goes to zero (instead of when a TO phonon frequency vanishes). Predicted values of the built-in polarization in

an electronic ferroelectric are around 10μC cm^{-2}, similar to the values found in perovskite ferroelectrics. The results obtained for $BiMnO_3$[17] suggest that electronic ferroelectricity might occur in this and other multiferroic materials. In the case of $BiMnO_3$, the localized state will be Mn 3d in origin, and the itinerant state will derive from Bi 6p. A band crossing has been observed between the Bi 6p and Mn 3d bands of the same symmetry in the cubic phase, indicating zero hybridization between these orbitals. In addition, charge transfer occurs from a nominally occupied Mn 3d state into a Bi 6p band, resulting in an on-site d-p coulomb interaction. Confirmation of the existence of electronic ferroelectricity will require further theoretical and experimental work.

Recent neutron diffraction results[22] suggest that there is no crystallographic phase transition on cooling the sample from room temperature upto 20 K. Data analysis reveals a collinear ferromagnetic structure with the spin direction along [010] and a magnetic moment of 3.2 μ_B.

2.1.4 Rare Earth Hexagonal Manganites

The family of manganese perovskites crystallizes in two structural phases. The most common is the cubic or orthorhombic, found in $CaMnO_3$, $LaMnO_3$ and the manganites of the larger rare earths, from $CeMnO_3$ to $DyMnO_3$. The other phase is the hexagonal $P6_3cm$[32,33] and includes $YMnO_3$ and the rare-earth manganites ranging from $HoMnO_3$ to $LuMnO_3$. In the rare-earth perovskites the large cation is generally completely ionized and chemically inert; thus, the occurrence of the hexagonal or cubic structure is determined only by the size of the cation, which is smaller in the class of hexagonal perovskites. These hexagonal perovskites are found to be ferroelectric along the c-axis (i.e., [0001])[33,34] with a spontaneous **P**~5.5 $\mu C/cm^2$, and are magnetically ordered. Among them, $YMnO_3$ is the best known experimentally and also the most feasible for our methodology since the *f* states (troublesome to treat within the pseudopotential method) are empty. Hill *et. al* have done a detailed theortical investigation on these compounds[35]. Also, LDA+U calculations[36] of electronic and optical properties of the hexagonal $YMnO_3$ have been recently published[37, 38].

Both [0001] oriented films[39,40] and single crystals[32,34,40] of hexagonal $YMnO_3$ have been recently grown, and ferroelectric properties and phonon modes[34,41] have been measured. $YMnO_3$ presents some technological advantage with respect to the most common ferroelectric perovskites, like low dielectric constant (~20 at room temperature) and nonvolatile constituent elements. But particular excitement is due to the occurrence of ferroelectric and magnetic ordering in the same compound. The coupling between these two orderings may be eventually exploited in a device where the dielectric properties can be altered by the application of a magnetic field and the magnetic

properties by that of an electric field. Although the big difference between the critical temperature of magnetic and electric orderings (T_N = 80 K and T_C = 900 K), respectively) may suggest that no coupling is present, some evidence of coupling has actually been observed in terms of anomalies in the dielectric constant and loss tangent at the Neel temperature[42,43]. Also, analysis of the second-harmonic optical spectra[44] of Mn^{3+} ion shows the presence of a new kind of nonlinear optical polarization depending on two order parameters. These indications justify the effort of investigating whether magnetic and ferroelectric ordering are reciprocally affected. Since the basic ingredients that favor ferroelectricity and magnetism are known, it is important to see how these elements are combined in hexagonal $YMnO_3$. Note that $YMnO_3$ is also grown in the orthorhombic phase[45], but this phase is not ferroelectric and has similar characteristics to $LaMnO_3$. Although the two phases share the same Mn^{3+} ion, the different crystal fields produces drastic differences in both structural and electronic properties.

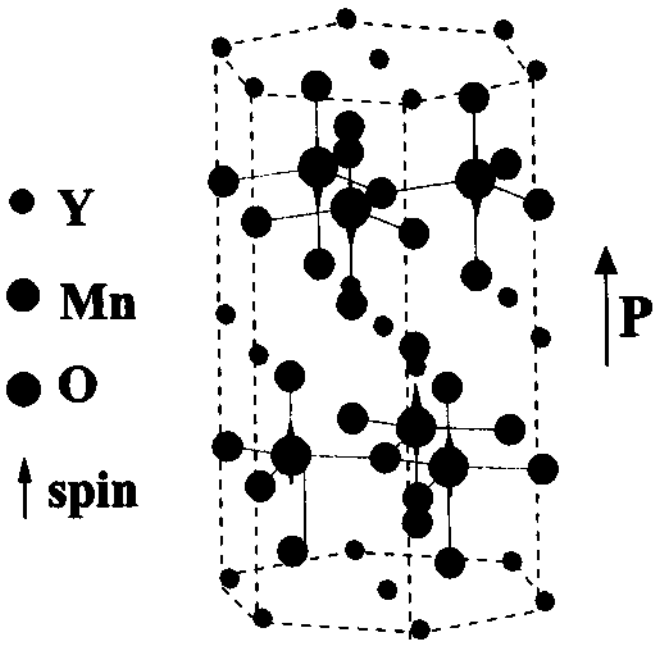

Fig.2.13 Structure of hexagonal ferroelctric $YMnO_3$. The arrows on Mn indicate the spin orientation of A-type AFM ordering. The electric polarization P is directed along the c-axis. [Taken from ref.20]

In fig.2.13 the ferroelectric 30-atom hexagonal unit cell in $P6_3cm$ symmetry of $YMnO_3$ is shown. The Mn ions, sited on close-packed hexagonal positions, are surrounded by corner-sharing bipyramidal cages of oxygens. The stacking along the c-axis consists of a $(MnO)_3$ layer, followed by three $\sqrt{3} \times \sqrt{3}$ layers containing in sequence O_3 ,Y_3, and O_3 (in total there are eight layers per cell). In addition the MnO_5 bipyramids are slightly rotated around the axis passing through the Mn and parallel to one of the triangular base sides. Discarding these small, barely visible tiltings, the atomic positions are those of the paraelectric ($P6_3/mmc$) phase, stable at $T > T_C$. Within the paraelectric symmetry the unit cell has ten atoms distributed on eight 1 x 1 hexagonal layers. Since the electric polarization occurs along the c-axis and the bipyramidal tilting does not alter significantly the features of this compound, the untilted structure is sufficient for the purpose of studying the changes of hybridization in the direction of the ferroelectric displacement.

Hexagonal $YMnO_3$ is found to be A-type antiferromagnetic[46,47] below T_N. The spins on Mn are noncollinear and oriented in triangular fashion. For our calculation we assume the A-type AFM collinear ordering shown in fig.2.13, what we find to be slightly lower in energy than the FM ordering. However, for our purposes this is not an essential feature, since the properties that we want to investigate are determined by the local (i.e., internal to the oxygen cage) spin polarization rather than by the long-range ordering between magnetic moments. The hexagonal paraelectric structure has three independent lattice parameters, i.e., the usual a and c parameters plus an internal u that gives the distance (in units of c) between O_3 and Y_3 layers, and is not fixed by the symmetry. By energy minimization it is found, a = 3.518 Å, c = 11.29 Å, and u = 0.084, in good

agreement with the experimental values a = 3.539 Å, c = 11.3(4) Å, and u = 0.084. This also suggests that the oxygen tilting has only a small effect on the structural properties. The distances between Mn and O are $\Delta_{Mn\text{-}OT}$ = 1.875 Å and $\Delta_{Mn\text{-}Op}$ = 2.03 Å. As a point of comparison, we also calculated the structure of $YMnO_3$ within FM cubic symmetry, and found a = 3.765 Å and $\Delta_{Mn\text{-}O}$ = 1.878 Å. It is notable that the volume enclosed in the bipyramidal cage of the hexagonal structure is much smaller than the octahedral volume of the cubic structure. In other words, in the hexagonal symmetry the Mn charge is enclosed in a smaller and more packed surrounding.

In fig.2.14 a scheme of the majority d-state splitting of Mn^{3+} ion due to the hexagonal crystal field is drawn, in comparison with the splitting due to the orthorhombic field. In the hexagonal field the d states are no longer split into t_{2g} and e_g states, but are ordered in two doublets and one singlet (the Cartesian axes are drawn in fig.2.14).

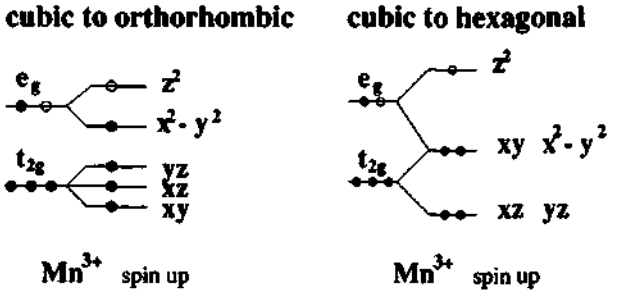

Fig.2.14 Schematic orbital splitting for the majority d states of Mn^{3+} ion within orthorhombic and hexagonal crystal field. [Taken from ref.20]

To determine the effect of the spin polarization the orbital-resolved DOS for the hexagonal phase with both nonmagnetic and AFM ordering has been calculated. The nonmagnetic phase (fig.2.15) shows a large DOS at the Fermi energy, EF, mostly due to the Mn d states located in a narrow region around EF. The degenerate d_{xy} and $d_{x^2-y^2}$ orbitals (of which only one is reported in the figure) lie on the (0001) plane and point

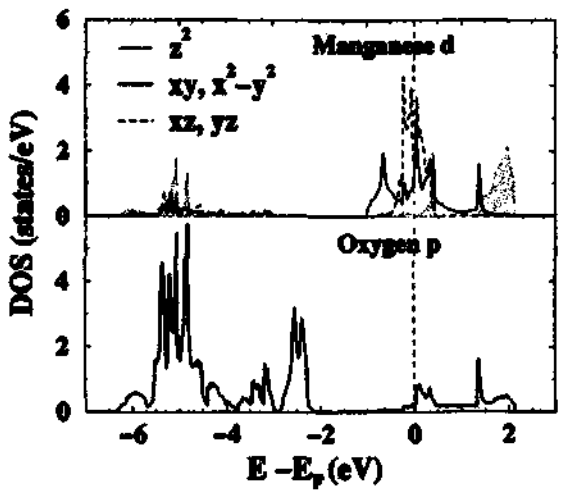

Fig.2.15 Orbital-resolved density of Mn d and O_T p states for the paraelectric, nonmagnetic phase of $YMnO_3$. Since the two couples of Mn d oribitals (d_{xy} and $d_{x^2-y^2}$) and (d_{xz} and d_{yz}). [Taken from ref.20]

towards O_P, thus contributing to the covalent bonding. The d_{xz} and d_{yz} orbital DOS overlap with those of d_{xy} and $d_{x^2-y^2}$, but are localized in a narrower energy region, since they do not point towards oxygens and are more localized in space. Finally, d_{z^2} is the highest in energy and the least occupied, but a certain amount of d_{z2} charge is hybridized with the O_T p_z states located ~5 eV below E_F .

From this energy ordering of the orbitals it follows that each of the four lowest-lying d orbitals is roughly half occupied and contributes to a large DOS at E_F . According to the Stoner exchange argument, this large DOS represents a strong driving force towards a spin-polarized stable phase. Indeed, we find that the transition from nonmagnetic to AFM ordering results in a large energy gain (~1.6 eV per formula unit).

In fig.2.16 the orbital-resolved DOS of individual spin-polarized Mn and O atoms is shown. As in the case of $CaMnO_3$, the AFM symmetry enforces the DOS of the two Mn atoms within the unit cell to be equal under exchange of up and down components. The energies of the Mn *d* manifold are spin split by ~2.5 eV, and the two doublets of Mn *d* states become almost completely spin polarized. Their total up and down charges are 3.93 and 0.47 electrons, respectively, while the occupation numbers of

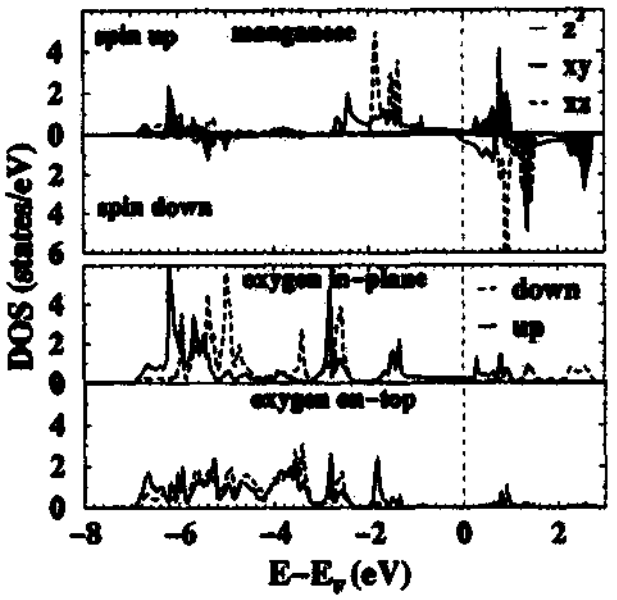

Fig.2.16 Orbital-resolved DOS of single Mn (top panel), O_P (middle) and O_T (bottom) in the paraelectric AFM phase of $YMnO_3$. Due to the exact AFM symmetry, each of the atoms reported in the figure has a corresponding atom in the cell with antialigned spin, i.e., with up and down components of DOS exchanged. [Taken from ref.20]

$d^{\uparrow}{}_{z^2}$ and $d^{\downarrow}{}_{z^2}$ orbitals are 0.53 and 0.30 electrons. The resulting magnetic moment on Mn (3.7 μ_B) is consistent with the high-spin state S = 2, although smaller than 4 μ_B due to the partial hybridization of d_{z^2} with O_T p_z states, and of d_{xy} and $d_{x^2-y^2}$ with O_P p_z and p_y states. There is a tiny DOS at E_F , to which d_{xy} and $d_{x^2-y^2}$ orbitals from Mn and p_x and p_y orbitals from O_P contribute. These orbitals all lie in the hexagonal plane.

The mainly planar distribution of the charge density is also evident from the band energies shown in fig.2.17.

Since the experimental findings suggest that this system is an insulator, the presence of some DOS at E_F must be attributed to the usual inadequacy of the LSDA to describe the magnetic perovskites as insulators. The source of error favoring a metallic ground state is primarily the insufficient spin splitting of the Mn d-state manifold and also a slight overestimation of the hybridization between d_{xy} and $d_{x^2-y^2}$ orbitals and O_P p_x and p_y orbitals. (It is shown in ref. 37 that the introduction of an Hubbard correction U = 8 eV onto the Mn d bands opens a gap ~1.5 eV and decreases the inplane O p–Mn d

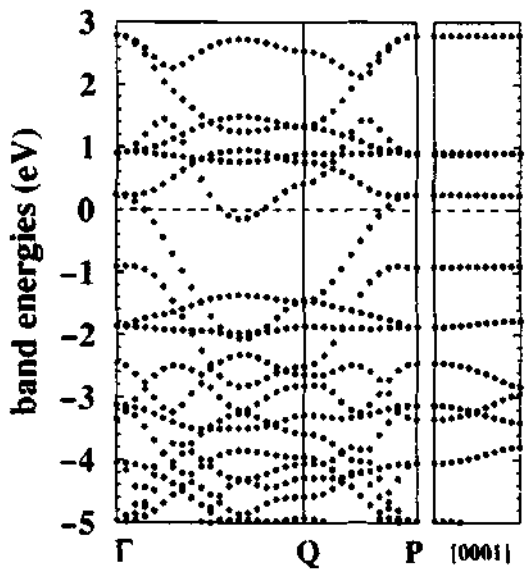

Fig.2.17 Band energies of the paraelectric AFM $YMnO_3$. The left panel shows results for the K = 0 hexagonal plane [i.e., Q = π /a (0, $2/3^{1/2}$, 0), P = π /a (1, $1/3^{1/2}$, 0) = Γ]; the right panel shows the band energies calculated along [0, 0, k_z]. [Taken from ref. 20]

hybridization.) In terms of calculating the ferroelectric properties, the metallic character found in the LSDA calculations is limiting since the metallicity destroys the possibility of sustaining a spontaneous electric polarization.

From the DOS analysis, the peculiar behavior of hexagonal $YMnO_3$ can be understood on the basis of orbital arrangement and crystal field splitting. Unlike the cubic phase, where the partial occupation of the e_g states causes a Jahn-Teller distortion, in the hexagonal phase four d orbitals are filled and one is (nominally) empty. Thus, the latter (d_{z2}) can be actively involved in strong changes of hybridization with the O_T p_z orbitals, realizing the same kind of chemical behavior that drives the ferroelectricity in $BaTiO_3$. However, in contrast to $BaTiO_3$ where all the d states are formally empty and able to contribute to hybridization changes, in hexagonal $YMnO_3$ we expect that the ferroelectric displacement will only be energetically favored along [0001]. This observation leads us to suggest a generalized criterion of *directional* "d^0-ness": in order for a chemical

environment to be favorable to ferroelectric distortions, the *d* orbitals *in the direction of the electric polarization* must be empty.

The chemical environment favorable to the electric polarization along the c-axis is only realized in the spin-polarized phase, and not in the nonmagnetic hexagonal phase. In other words, in hexagonal $YMnO_3$ the spin polarization not only does not prevent, but is actually necessary to enable the ferroelectricity. Also, notice that the transition from the AFM to the paramagnetic phase above T_N = 80 K (i.e., well below the critical temperature of the ferroelectric phase) does not invalidate our argument, since it is the local spin-polarization of Mn^{3+} that matters, independently of the actual presence (or absence) of long-range spin ordering.

At this stage of the investigation we cannot affirm that the chemical activity of Mn d_z^2 and O_T p_z orbitals alone is sufficient to explain the spontaneous polarization. To confirm this, a study of the properties of the ferroelectric phase (which is inaccessible in the LSDA) will be necessary. It will be particularly important to evaluate the BEC. We are not aware of any existing experimental or theoretical determination. However, we might expect anomalous values on Mn and O_T in the direction of the proposed ferroelectric distortion.

2.2 SCOPE OF THE PRESENT INVESTIGATIONS

Ferroics with paired properties are well known and materials with coupled ferroic behavior have the potential to be of considerable practical value[48]. The coexistence of ferromagnetism and ferroelectricity is particularly of interest since such magnetoelectric materials would have spontaneous magnetization that can be switched by a magnetic field and a spontaneous polarization that can be switched by an electric field[19]. In addition, there would be coupling between the order parameters. Most efforts to date have focussed on biphasic mixtures of two different materials individually possessing magnetic or ferroelectric properties[49-51]. To our knowledge there are very few monophasic materials exhibiting magnetoferroelectricity, the double perovskite $Pb_2(CoW)O_6$, being one such material[8]. In $Pb_2(CoW)O_6$, the unique properties of the Co and W ions present in distinct sites come to play. The simple perovskite $BiMnO_3$ with only a simple B-site cation has been suspected to be a biferroic and recent theoretical calculations suggest that it is likely to be both ferromagnetic and ferroelectric because of the covalent bonding between bismuth and oxygen atoms[15]. It should be recalled that $LaMnO_3$ is an antiferromagnetic insulator. Although there have been several reports on the properties of $BiMnO_3$ in the last four decades, nothing definitive is known about the multiferroic nature of the material. Part of the problem is because it can only be synthesized at high pressures. There is, however, sufficient evidence to show that $BiMnO_3$ adopts a polar monoclinic structure at room temperature[52-53] and is ferromagnetic with a T_C of 105 K[54,55]. Ferroelectric properties of $BiMnO_3$ have not been reported hitherto. In order to explore whether there is coexistence of ferromagnetism and ferroelectricity in $BiMnO_3$, we have carried out investigations on bulk samples prepared by high-pressure synthesis as well as

on thin films prepared by nebulized spray pyrolysis. Preliminary results suggest that $BiMnO_3$ is indeed a magnetoferroelectric material, wherein it is ferroelectric, below ~450 K, through the ferromagnetic T_C.

Rare – earth manganites of the type $Ln_{1-x}A_xMnO_3$, where Ln is a rare earth and A is an alkaline earth, have become known for a variety of fascinating properties, such as colossal magnetoresistance, charge ordering and orbital ordering[56,57]. These properties are strongly influenced by the average size of the A-site cation, $\langle r_A \rangle$[58]. The parent manganites of $LnMnO_3$ also show marked effects of the size of A-site cation. $LaMnO_3$ is an antiferromagnetic insulator where the Jahn-Teller distortion around Mn^{3+} plays an important role. However, as the $\langle r_A \rangle$ becomes small, the perovskite structure becomes unstable at ambient conditions, resulting in a hexagonal structure. Thus, $YMnO_3$ crystallizes in the $P6_3cm$ space group[32] with, a = 6.130Å and c = 11.505 Å. The structure is best described as layers of manganase-centred trigonal bipyramids with 5-coordinate Mn but no framework of Mn-O bonds along the axial direction (c-axis). The equatorial oxygens are corner-shared by three polyhedra in the basal plane. This structure leads to an unipolarization axis along [0001], which can be reversed by an electric field, thereby making these manganites exhibit ferroelectric behavior. Although ferroelectrcity as such in the bulk form was discovered in 1963 by Bertaut et al[59], there has been only recent effort to prepare them in thin–film form[60] to investigate ferroelectricity. Various techniques like MBE (moleculer beam epitaxy), PLD (pulsed laser deposition) and sol-gel method have been employed to deposit these films. We considered that it would be most worthwhile to explore a simpler chemical route to provide alternative or even better means of depositing films of novel complex oxides. With this in mind, we have employed

nebulized spray pyrolysis of organometallic precursors to deposit films of $YMnO_3$. In addition, it is also noteworthy that $YMnO_3$ is also antiferromagnetic, thus making it a biferroic[61].

Interest in $YMnO_3$ and related compounds arises from their potential use in ferroelectric random access memories (FRAMs) in the metal-ferroelectric-semiconductor field-effect transistor (MFSFET) mode[62]. An additional advantage of these manganites is the absence of volatile elements such as Pb and Bi. This is especially useful in MFSFET applications as one can directly integrate onto Si substrates. In the present study, we have deposited films of $YMnO_3$ on Si (111) substrates and conducted a detailed study of their ferroelectric properties in terms of C-V characteristics.

2.3 EXPERIMENTAL

The bulk polycrystalline sample of $BiMnO_3$ was prepared by high pressure, high temperature synthesis in a diamond anvil cell. The films of $BiMnO_3$ and $YMnO_3$ were prepared by nebulized spray pyrolysis.

Synthesis of $BiMnO_3$

A polycrystalline sample of bismuth manganite was prepared using a custom-built high-pressure synthesis cell assembly, with a Paris-Edinburgh toroidal anvil cell[63]. The starting material was finely ground mixture of Bi_2O_3 and Mn_2O_3 (Aldrich). The mixture was pelletized and loaded in a BN crucible in the high-pressure setup and heated at 1023 K for 3 hours at a pressure of 6 GPa. At the end of the heating cycle, the product was a hard-densified black-grey pellet, with the X-ray diffraction pattern characteristic of the monoclinic structure[52,53], but containing a minor impurity phase. Variable temperature X-ray diffraction measurements were carried out on the polycrystalline sample in the temperature range 300 – 800 K.

Thin films of $BiMnO_3$

Thin films of $BiMnO_3$ were deposited by nebulized spray pyrolysis. The technique has been described in detail in section 1.3. For depositing the films manganese(II) acetylacetonate and bismuth(III) acetate were used as precursors. A solution of both these precursors was taken in methanol solvent in required composition to be deposited. Films of ~400 nm thickness were deposited on the (100) faces of single crystal substrates of Si at 450 K by using air as the carrier gas. The films so obtained were annealed in air at 723 K for 3 hrs to get the required phase.

Thin films of $YMnO_3$

Thin films of $YMnO_3$ were prepared by nebulized spray pyrolysis. We have employed the acetate of Y and the acetylacetonate of Mn as precursors in the present study. Solutions of stiochiometric quantities of the precursors were prepared in methanol solvent. $YMnO_3$ films of ~1μm to 2μm thickness were deposited on the n-type Si(111) substrates (~ρ = 1 Ω cm, dopant concentration 6.5 x 10^{14} cm^{-3}) at 450 K by using air as the carrier gas (flow rate 1.5 liters/min). The films so obtained were annealed in air at 973 K (denoted as Y33), 1073 K (denoted as Y73), and 1123 K (denoted as Y123) for 6 hrs each in order to study the process of crystallization as a function of annealing temperature.

Characterization

The thin films were studied by X-ray diffraction using a Seifert (xrd, xdl, θ-θ, Cu target) instrument. Conventional θ-θ scans were collected with a Bragg-Brentano goniometer and high resolution (169 eV) Si(Li) solid state detector with 0.5 mm/1 mm slits. The surface morphology of the films was observed by scanning electron microscopy (SEM) with a Leica S-440 i SEM. The film thickness was confirmed by cross-sectional scanning electron microscopy. The EDX analysis was done using Links ISIS of Oxford instrument. The temperature variation of magnetization of polycrystalline $BiMnO_3$ sample was carried out in a vibrating sample magnetometer (VSM) of Lakeshore model 7300.

Ferroelectric polarization of the polycrystalline samples was measured using a sawyer tower circuit as shown in fig.2.18. The samples were in sandwich configuration. The ferroelectric polarization for the films was also measured using the same technique.

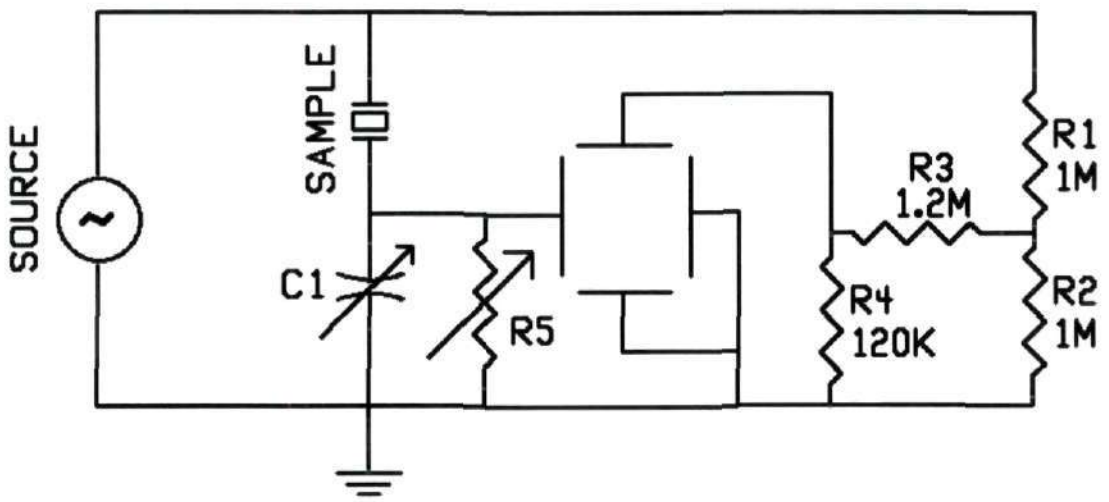

Fig.2.18 Sawyer Tower circuit used to measure the polarization of the ferroelectric $BiMnO_3$ samples

The capacitance-voltage behavior of the $YMnO_3$ films deposited on Si(111) substrate was studied in the sandwich configuration as shown in the fig.2.19. Sputtered gold electrodes on the $YMnO_3$ thin films were used as top electrodes for the Metal - Ferroelectric –

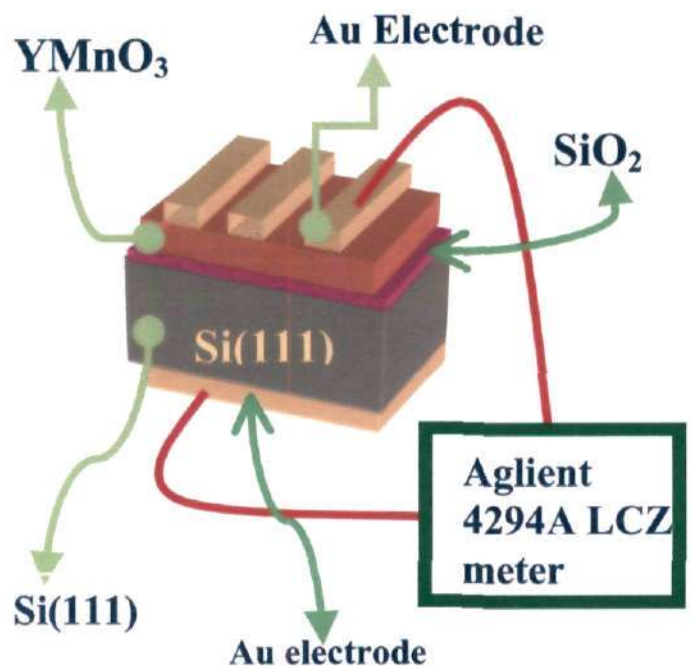

Fig.2.19 The MFS configuration used to study the capacitance-voltage behavior of $YMnO_3$/Si(111)

Semiconductor (MFS) configuration. The bottom electrode was deposited on the back side of the substrate after etching out SiO_2 layer by HF. The dielectric and capacitance – voltage (C – V) measurements were carried by using HP 4284 A LCZ meter to measure capacitance in the range varying from 100 Hz to 1 MHz at oscillating voltage of 500 mV. The current-voltage behavior was using the configuration shown in fig.2.20. The current - voltage measurements were measured using Keithley SMU 236 at elevated temperatures ranging from 300 K to 473 K.

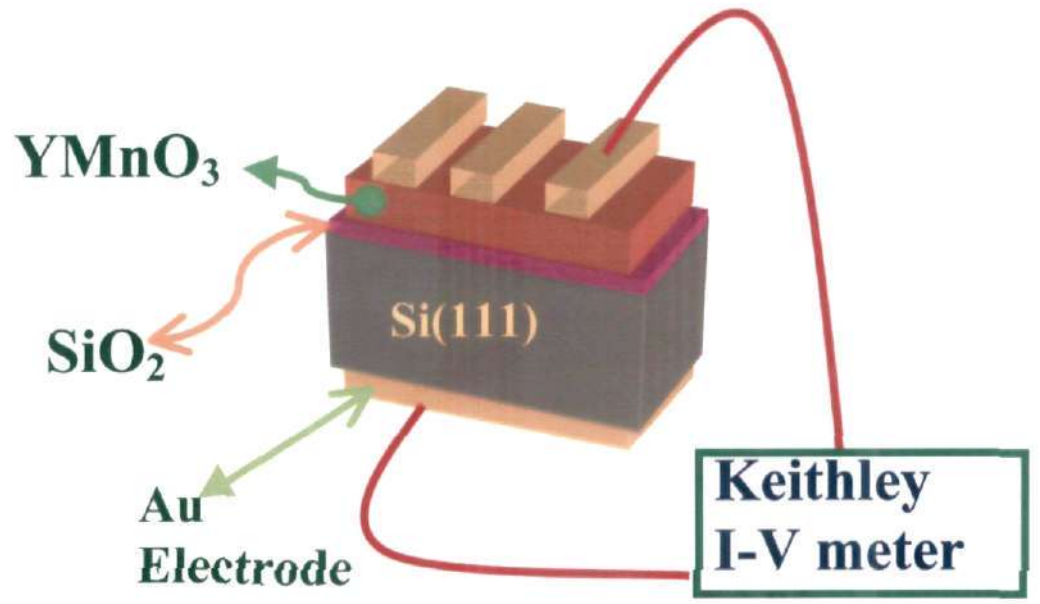

Fig.2.20 The MFS configuration used to study the current-voltage behavior of $YMnO_3$/Si(111)

Deep level trap spectroscopy (DLTS) measurements were carried out in the MFS configuration on thin films of $YMnO_3$ deposited on Si(111).

2.4 RESULTS AND DISCUSSION

2.4.1 Bismuth Manganite

X-ray diffraction study of polycrystalline $BiMnO_3$

Variable temperature X-ray diffraction patterns recorded with a STOE diffractometer show a structural change around 450 K. We show portions of the diffractograms of the room temperature and high temperature phases in fig.2.21. The structural phase transition is reversible and is of second order. We consider this phase transition to represent the transformation of the ferroelectric phase to the paraelectric phase. The transition temperature of 450 K is consistent with the temperature – dependence of the P-E hysteresis loop. The high-temperature (paraelectric) phase also appears to be monoclinic just as the room temperature phase. $BiMnO_3$ shows another transition around 740 K but this is irreversible, being associated with a compositional change[54,64].

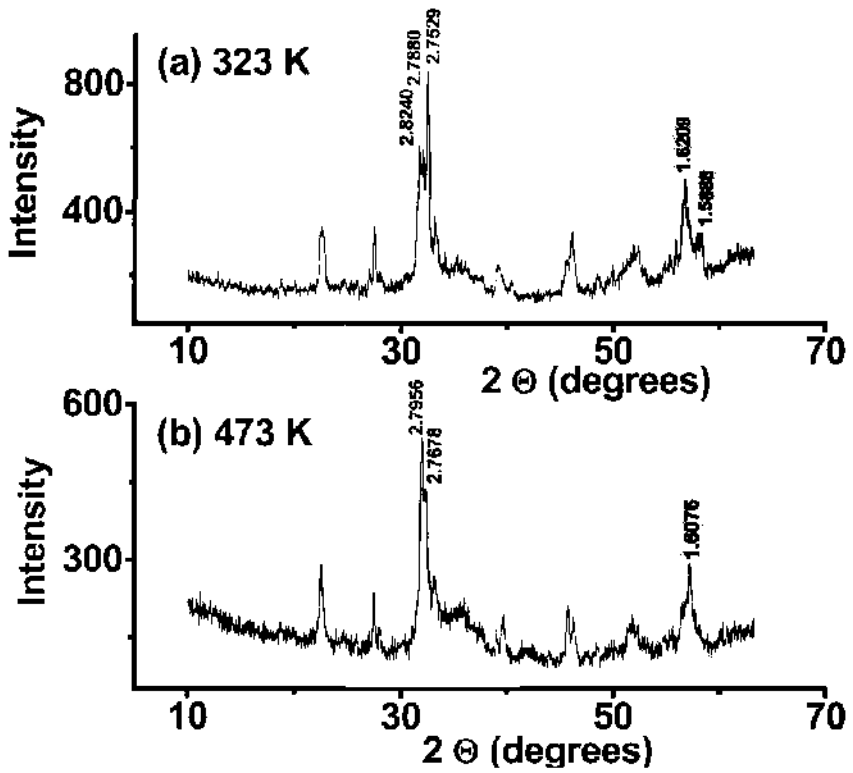

Fig.2.21 X - Ray diffractograms of $BiMnO_3$ at (a) 323 K and (b) 473 K

Magnetization study of polycrystalline $BiMnO_3$

Magnetization measurements on polycrystalline samples of $BiMnO_3$ carried out at 500 Oe show that the compound is ferromagnetic, in agreement with previous work[54,55]. We also obtain a T_C of 105 K as shown in fig.2.22. In the inset of fig.2.22, we show the ferromagnetic hysteresis loops recorded at 75 K and 45 K. The sample shows a magnetic moment of 2.6 μ_B at low temperatures, but the value reaches 3.1 μ_B when measurements are carried out at high fields (10^4 Oe). From the hysteresis measurements, we obtain a coercive field of 470 gauss and a remnant magnetization of 0.2 μ_B at 45 K. We have carefully examined the neutron diffraction data of Atou et. al[53] to understand the magnetic structure of $BiMnO_3$. Orbital ordering in $BiMnO_3$ which is different from that in $LaMnO_3$ seems to be responsible for the ferromagnetic ordering of the spins. The room temperature phase has the polar space group C2 as reported earlier[53], with little change in the structural features across the ferromagnetic transition.

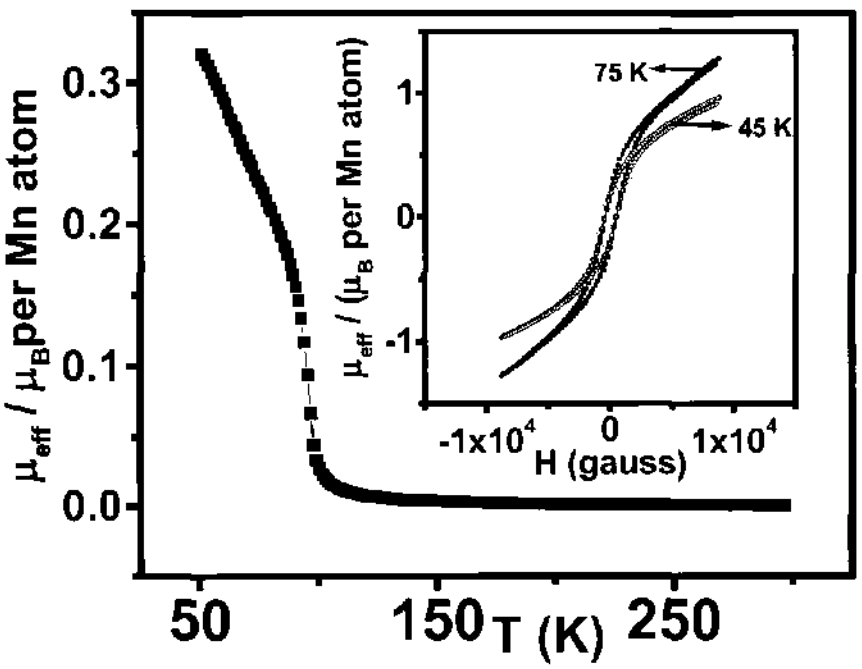

Fig.2.22 Temperature variation of magnetization of $BiMnO_3$ at 500 Oe. Inset shows the ferromagnetic hysteresis loops measured at 75 K and 45 K

Ferroelectric properties of $BiMnO_3$

Ferroelectric hysteresis loop measurements were carried out on the dense pellets of $BiMnO_3$ between 80 K and 400 K. We observe a well-defined P-E hysteresis loop at 300 K which persists down to 80 K, through the ferromagnetic Curie temperature as shown in fig.2.23. The remnant polarization is 43 nC cm^{-2} at 200 K, with a coercive field of 5.6 kV cm^{-1}; at 87 K, these values are 62 nC cm^{-2} and 8.1 kV cm^{-1} respectively. Thin films on Si(100) substrates show the same behavior down to 20 K. Typical ferroelectric hysteresis loops of a film are shown in fig.2.24. The remnant polarization is 4.1 nC cm^{-2} at 120 K, with a coercive field of 330 kV cm^{-1}. Based on the above results we propose that the magnetic phase of $BiMnO_3$ (T< 105 K) is ferroelectric. The P-E hysteresis loop persists up to ~ 400 K, but it was difficult to carry out good measurements at higher temperatures because of the enhanced

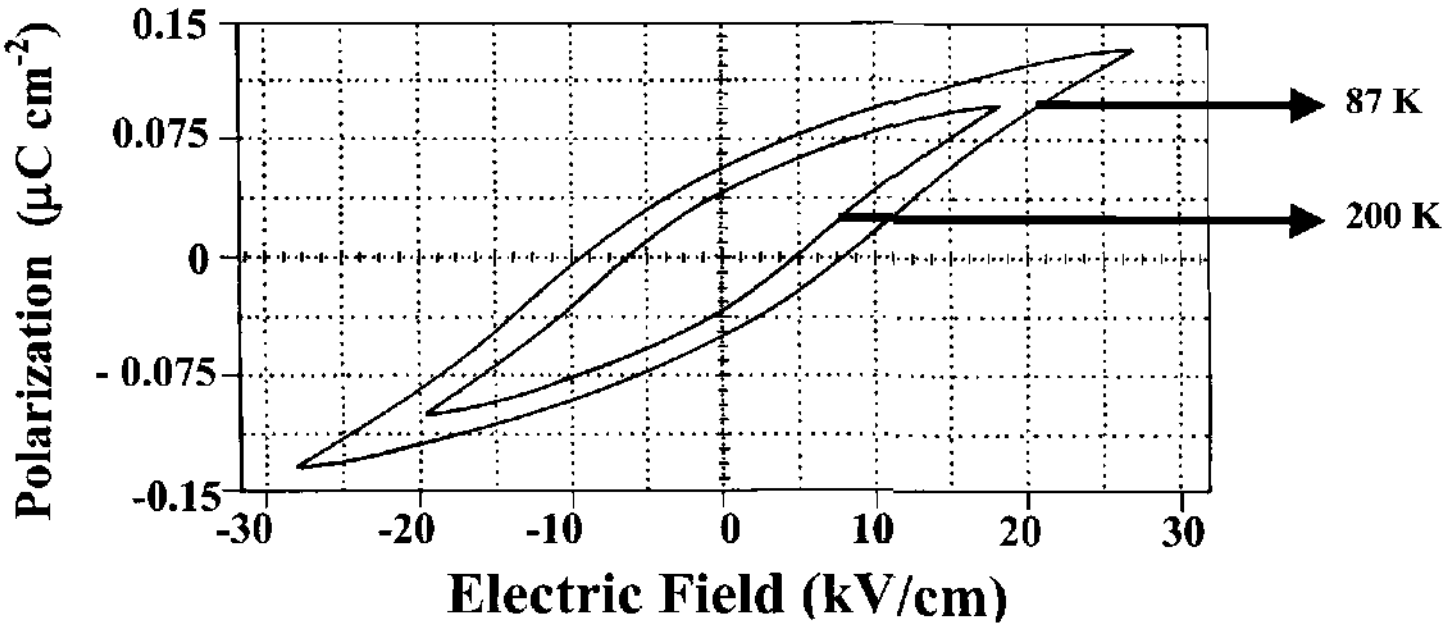

Fig.2.23 P-E hysteresis loops of polycrystalline $BiMnO_3$ through the ferromagnetic T_C

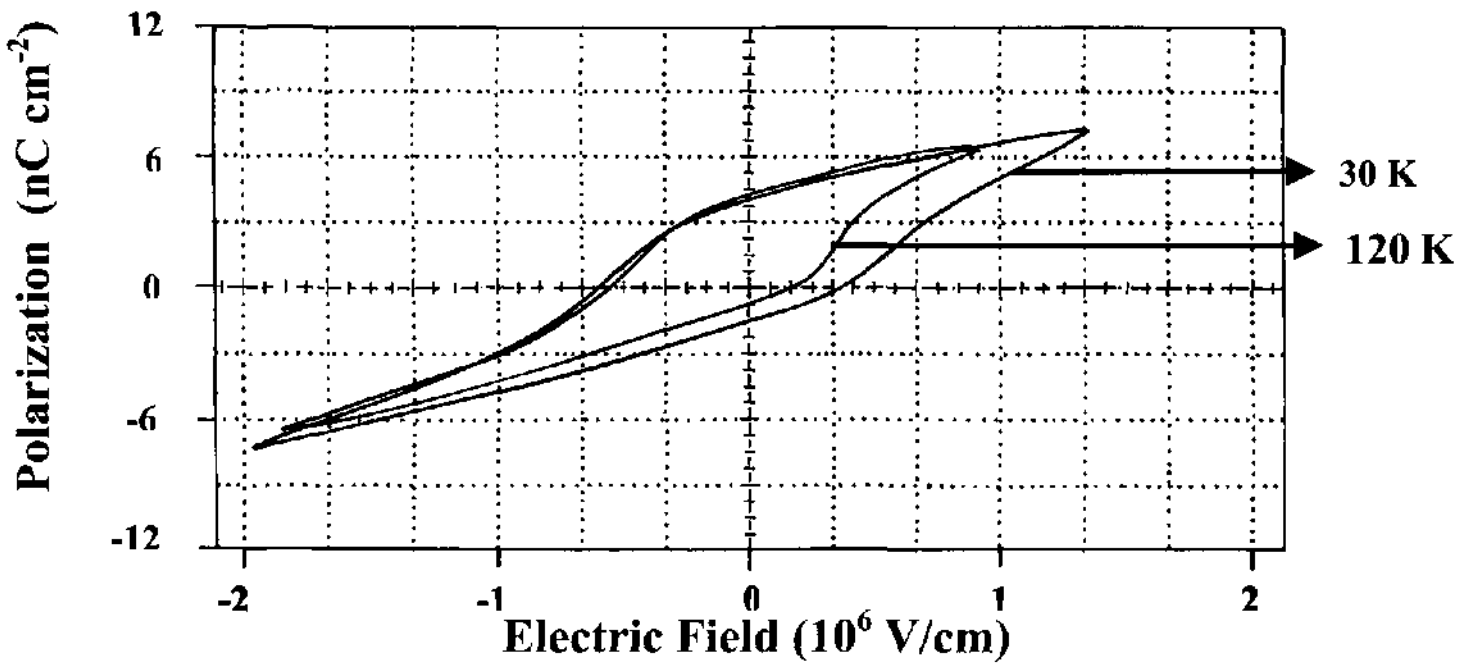

Fig.2.24 P-E hysteresis loops of thin film of $BiMnO_3$ on Si(100) through the ferromagnetic T_C

conductivity of the sample.

2.4.2 Yttrium Manganite

X-ray diffraction and composition analysis of $YMnO_3$/Si(111) films

Fig.2.25 shows the X – ray diffraction (XRD) patterns of the $YMnO_3$/Si (111) films annealed at different temperatures. The XRD patterns reveal that the crystallinity of the films increases as the annealing temperature is increased from 973 K to 1123 K. The evolution of the polarization axis is also seen from the increase in the intensity of the (0004) reflection. Fig.2.26 shows the cross sectional SEM of the $YMnO_3$ thin films crystallized at 1123 K (denoted as Y123) and its morphology is shown in the inset. The morphology was found to be dense and the interface was found to be uniform and coherent from the cross – sectional images. A semi-quantitative analysis of the composition of $YMnO_3$ thin films was found

using energy dispersive analysis of X – rays (EDAX) and the thin films maintained an excellent stoichiometric ratio.

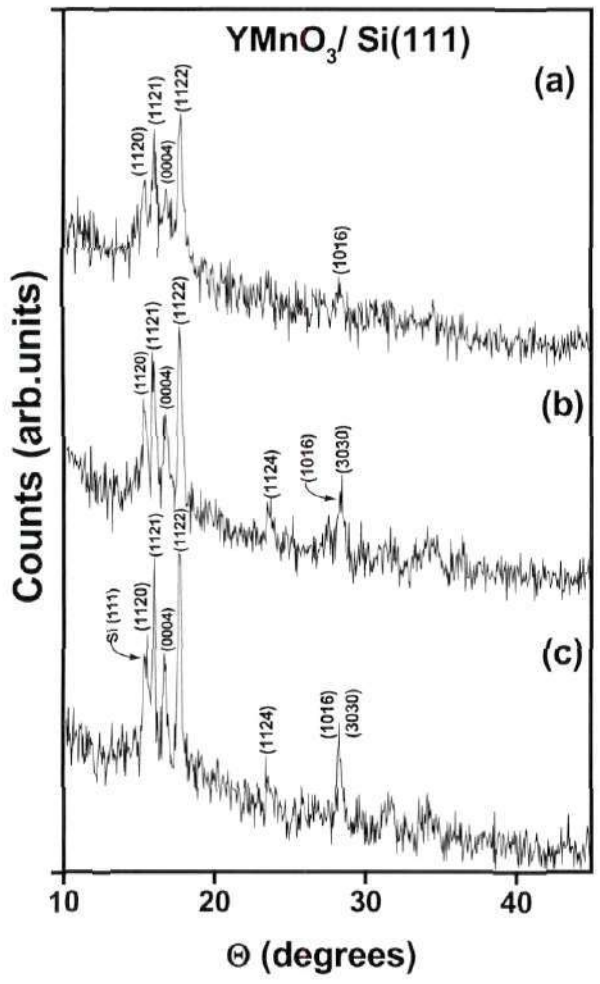

Fig.2.25 X–ray diffraction pattern of the $YMnO_3$ thin films on Si(111) annealed at (a) 973 K (b) 1073 K and (c) 1123 K

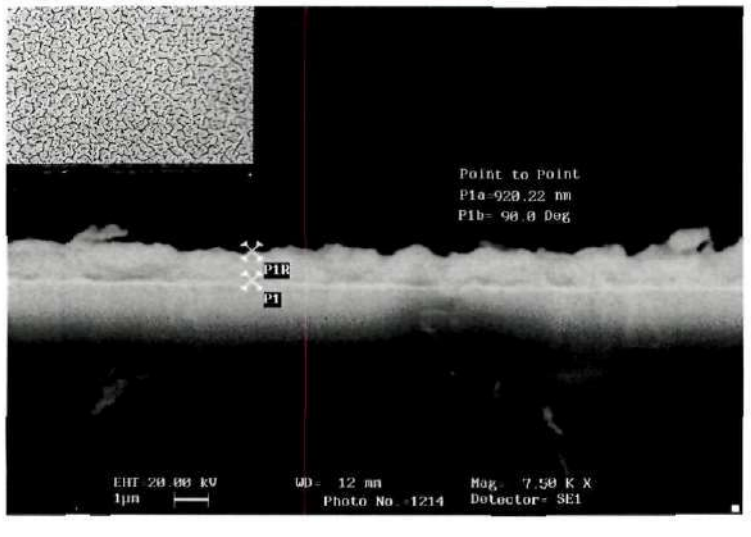

Fig.2.26 Cross-sectional SEM micrograph shows that the interface is uniform and coherent for a Y123 film. Inset shows the morphology of the same film

Electrical Characteristics

Dielectric studies and dc leakage current characteristics of the $YMnO_3$ films deposited on n–type Si substrate were carried out in the Metal – Ferroelectric – Semiconductor (MFS) configuration.

(a) C – V characteristics

C–V measurements were carried out from 100 Hz to 1 MHz for all the well crystallized polycrystalline $YMnO_3$ thin films at elevated temperatures ranging between 300 K to 500 K. The dielectric constant was calculated on taking the account of the thickness of native oxide formation on the silicon based on the annealing conditions and dielectric constant was calculated for 1 MHz in the accumulation region. The capacitance – voltage measurements, the oxide capacitance was determined by using the nonlinear least-square fit algorithm developed by Hauser and Ahmed[65]. Quantum mechanical corrections were not applied, as the films were sufficiently thick, consistent with the work of McNutt and Sah[66]. The dielectric constant obtained for the $YMnO_3$ thin films on Si in the accumulation region was 25, a value close to that reported by Yoshimura et.al[60]. The dielectric constant was found to increase with the annealing temperature. This enhancement of the dielectric constant in the annealed films may be associated with the improved crystallinity, lesser porosity and lesser defects of the thin films.

The gate voltage was swept from $-V_g$ to $+V_g$ and vice versa resulted in a hysteresis behavior. Counter clockwise hysteresis was observed due to the ferroelectric polarization-switching behavior as shown in fig.2.27 for Y123 films[66]. As the bias sweep rate was decreased, the present MFS structure exhibited the same magnitude of hysteresis window, thus demonstrating good memory retention characteristics of the $YMnO_3$ films

on n–type Si, unlike the memory window collapse in case of p–type Si reported by Yoshimura et.al[60].

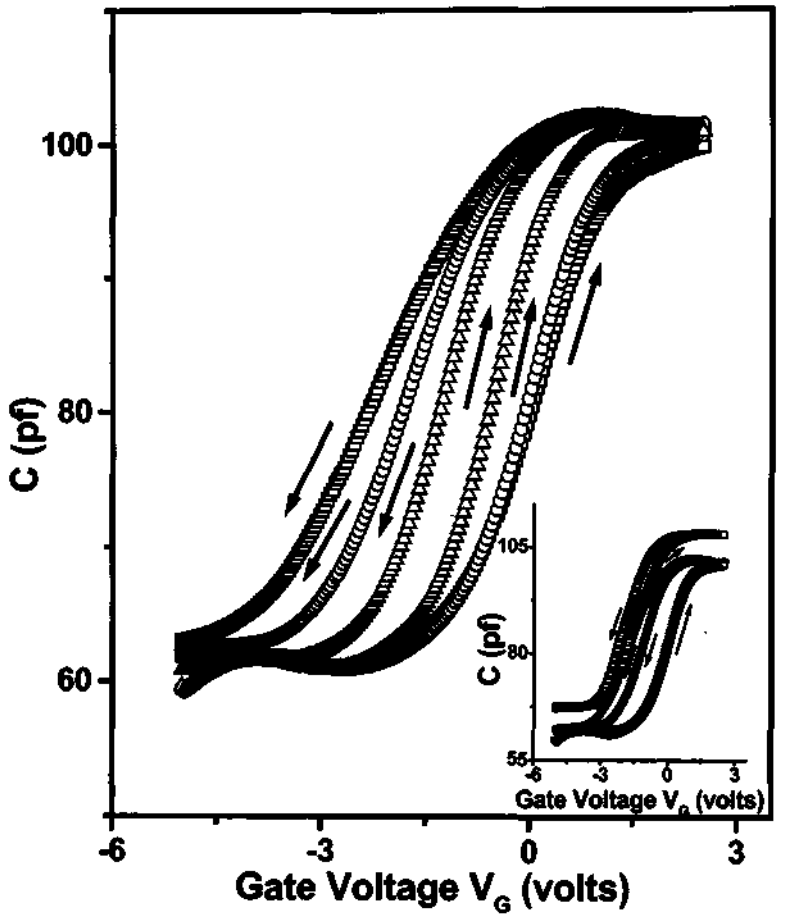

Fig.2.27 C-V characteristics of $YMnO_3$ (Y123) film on n-type Si(111) at different bias sweep rates: 0.75 Vs^{-1}(squares), 0.375 Vs^{-1} (circles), 0.093 Vs^{-1} (up triangles). The inset shows the C-V characteristics of the films at different temperatures. The loop are a decreases as the temperature is increased: 297 K (circles), 313 K (down triangles) and 373 K (squares)

When a ferroelectric film is integrated onto a Si – substrate, the polarization charge density in contact with the Si surface, modifies the surface conductivity. The magnitude of the modulation depends on the applied electric field and follows the normal hysteresis behavior of the ferroelectric. Ito and Tsuchiya[66] clearly identified reversal modes of the memories of ferroelectric thin films integrated on a semiconductor. Polarization mode memory operation clearly establishes the ferroelectric nature of the films on silicon. This approach was taken in the present studies to establish the presence of ferroelectricity in $YMnO_3$ thin films. Polarization mode memory behavior was studied

in terms of C-V hysteresis at different temperatures and results are shown in the inset of fig.2.27. The polarization charge density is expected to reduce as one approaches the Curie temperature, resulting in narrowing or the disappearance of the memory window. This behavior is clearly observed in the present studies, thereby establishing ferroelectricity in the $YMnO_3$ films.

The C – V curves measured at 1kHz and higher were of high frequency type with minimum capacitance at the inversion region. The minority carriers constituting the inversion layer do not respond for frequencies higher than 1 kHz, as the response time of the inversion layer is very long (of 0.01 – 1sec for p-type Si), compared to the time scale of applied ac signal at the room temperature. This indicates that the ac signal is sufficient to induce generation and recombination of the minority carriers in the depletion layer of

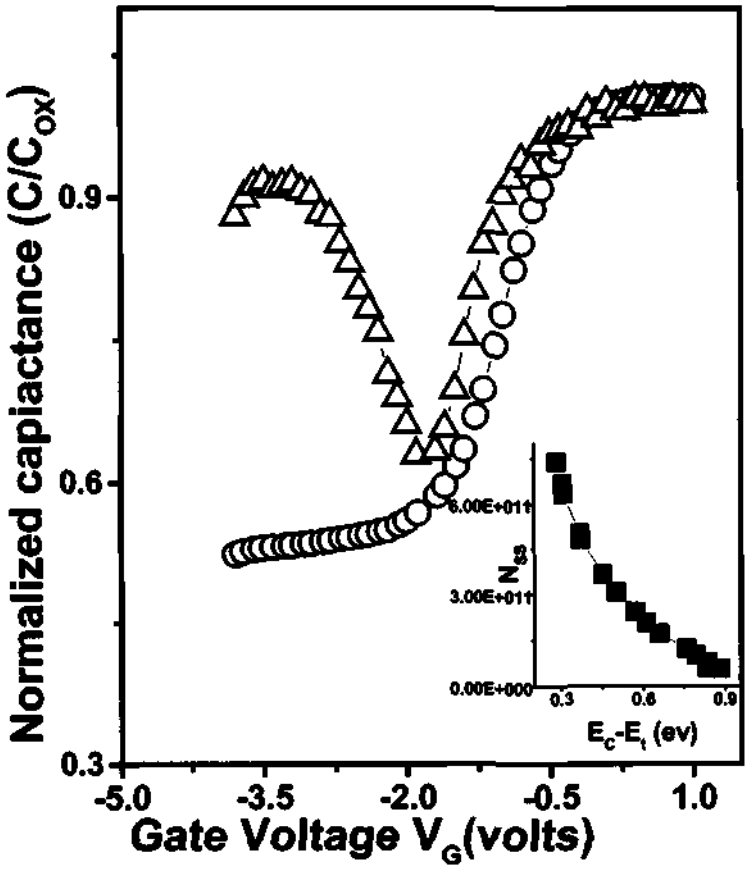

Fig.2.28 C–V characteristics of $YMnO_3$ (Y123) thin films on n – type Si(111) measured at 100 Hz (up triangles) and 1 MHz(circles) at 300 K. The inset shows the mapping of the density of interface states with the energy band gap of Si

the bulk n–type Si, leading to charge exchange with the inversion layer. In our case, the inversion layer was able to respond at the lower frequencies (~ 100 Hz) in Y123 thin films as shown in the fig.2.28. The flat band capacitance was calculated using the following expression

$$C_{fb} = \left(\frac{1}{C_{ox}} + \frac{1}{C_{Ld}} \right)^{-1} \qquad (1)$$

with C_{ox} denoting the maximum oxide capacitance in the accumulation region,

$$C_{Ld} = \left(\frac{\varepsilon_s A}{L_d} \right)$$

ε_s denoting the dielectric constant of the silicon, A denoting the electrode area and $L_d = \left(\frac{\varepsilon_s kT}{q^2 N_a} \right)^{1/2}$. The oxide charges and interface states in a MOS capacitor, plays a crucial role for an efficient performance and to exhibit a thermally stable device. The V_{FB} is calculated as follows:

$$V_{FB} = \phi_{MS} - \frac{Q_I}{C_{OX}} \qquad (1)$$

with ϕ_{MS} denoting the work function difference between metal and semiconductor, C_{OX} as the oxide capacitance and Q_I the effective interface charge[67]. The flat band voltage (V_{FB})[68] was found to shift towards zero voltage with increasing annealing temperature due to better crystallinity as shown in the Table 5. Variation of V_{FB} in the annealed thin films is due to the structural changes in the oxide - semiconductor interface and it reflects the changes in the density of defect states in the insulator. The V_{FB} is found to decrease with increasing oxidation temperatures, indicating a reduction and/or compensation of fixed charges.

Table 5

Flat band voltages and densities of interface traps in $YMnO_3$ thin films.

Annealing temperature (^oK)	V_{FB} (V)	N_{ss} (eV^{-1} cm^{-1})
973	0.505	3.2×10^{12}
1073	0.2275	9.1×10^{11}
1123	0.198	5.1×10^{11}

There are four general types of charges associated in SiO_2 - Si system, such as, fixed oxide charges Q_f, mobile oxide charges Q_m, oxide trapped charges Q_{ot} and interface trapped charges Q_{it}. It may be realized that the Q_f and Q_{it} are vital in degradation of the device. Fixed oxide charges are positive, stable in the oxide and lie close to SiO_2 - Si interface that cannot be charged or discharged by varying the silicon surface potential. Interface states are located at SiO_2 - Si interface and are in direct electrical communication with silicon, and responds rapidly to the changes in the silicon surface potential. Hence the interface states were calculated from the C –V analysis. In order to minimize the D_{it}, an annealing was carried out at higher temperatures in the ambient of dry oxygen. The low temperature annealing was avoided because it induces a transfer of hydrogen, which eventually activates and annihilates the interface traps[69].

The interface states arise due to the dangling bonds or unsaturated bonds at the interface of Si and $YMnO_3$ thin films. The stretch out of the C–V curve at higher frequencies along the voltage axis for the $YMnO_3$/n-Si film is not appreciable, indicating the minor amounts of interface traps present. The interface trap density was obtained by the Castagne–Vaipalle method[70] for the films annealed at 1123 K, as they exhibited both

low and high frequency curves as shown in the fig.2.29. The density of interface states was calculated from the C–V curve as follows:

$$N_{SS}(\psi_S) = \frac{1}{qA}\left(\frac{C_{OX}C_{LF}}{C_{OX} - C_{LF}} - \frac{C_{OX}C_{HF}}{C_{OX} - C_{HF}}\right) \qquad (2)$$

Here ψ_s is the surface potential, C_{ox} is the oxide capacitance, C_{LF} is capacitance at low frequency (100 Hz), C_{HF} is capacitance at high frequency (1MHz), q is charge of electron and A is the area of electrodes. The densities of the interface traps for films annealed at 1073 K and 973 K was calculated using high frequency Terman method[71]. The calculated values of N_{SS} are shown in Table 5. The mapping of the energy band gap of Si with the density of interface states of $YMnO_3$ thin films crystallized at 1123 K is shown as an inset of the fig.2.28. The density of the interface states is lower than that reported earlier[60] while the N_{ss} is higher at the band edges with a dip at the center of the energy band gap of Si for $YMnO_3$ films annealed at 1123 K.

(b) DC leakage current characteristics

Various transport mechanisms of charge flow are involved in the metal – ferroelectric – semiconductor (MFS) configuration. The mechanisms include Poole – Frenkel[69] and Schottky effects[73] resulting from the lowering of a columbic potential barrier by the applied electric field in bulk and electrode – bulk interface respectively, and field ionization of trapping levels known as space charge limited current (SCLC)[73,74]. The dominant current conduction mechanism was analysed from the dc leakage current behavior. Well-crystallized films of $YMnO_3$ (annealed at 1123 K) exhibited lower leakage current than those annealed at lower temperatures as shown in fig.2.29. These $YMnO_3$ thin films didn't obey the Schottky and Poole Frenkel effects as the calculated

high frequency dielectric constant from their respective conduction equations were of one order of magnitude less than the dielectric constant of the $YMnO_3$ bulk ($\varepsilon_\infty \sim 20$).

Space Charge Limited Current Mechanism

A space charge region will be set up in the conduction band on an inexhaustible supply of free carriers in the dielectric near the injecting electrode on assuming the ohmic contact has been formed at the injecting electrode. The space charge limited current (SCLC) for an insulator without traps, obeys Child's law given as

$$J = \frac{9}{8}\frac{\varepsilon\mu}{w^3}V^2 \qquad (9)$$

where ε is the dielectric permittivity, μ the drift mobility of electrons , w the thickness of insulator layer and V the voltage drop across the layer.

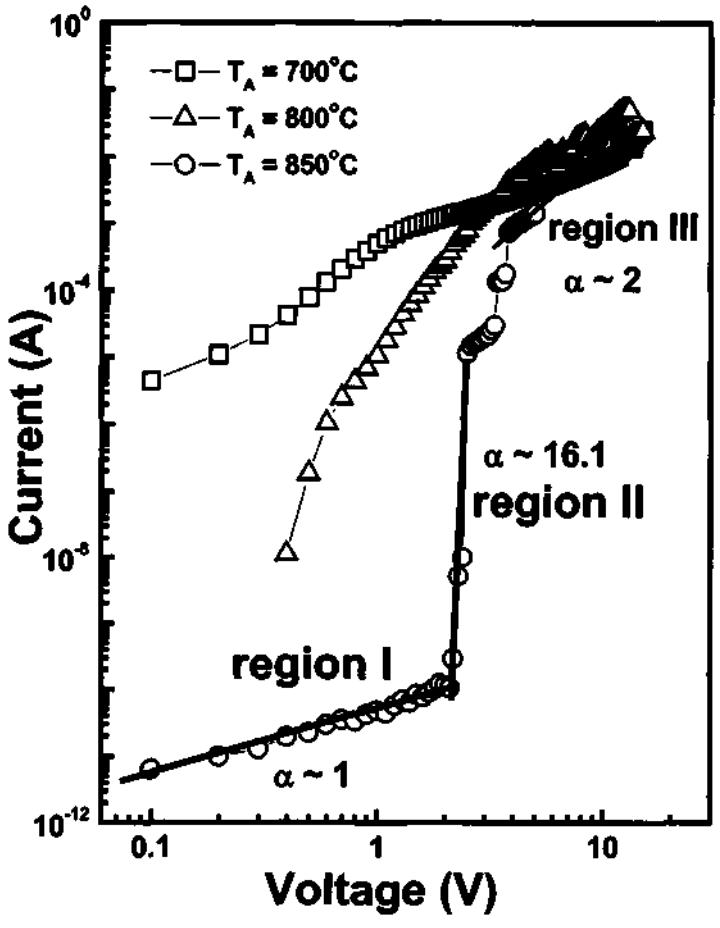

Fig.2.29 Log I – Log V curves in the accumulation region in MFS structure for the different annealing temperature, .i.e. 973 K (squares), 1073 K (up triangles) and 1123 K (circles).

According to the SCLC model, J is proportional to V^2. Fig.2.29, shows that J is proportional to V^2 over a significant range of voltage in the region III. The slope of J(V) in the non - ohmic region is not the same at different temperatures. Suppose electron traps influence the SCLC, then the current obtained is trap filled limited current and these current arises due to both shallow and deep electron traps. $YMnO_3$ films annealed at 1123 K obey the space-charge conduction limited mechanism (SCLC) as shown in the fig.2.29. The J – E plot shows a near linear dependence (region I) upto voltage trap filled limited (V_{TFL} ~ 3.4 V) and curves spikes up with a slope of 15 –18 (region II) and again saturating to a slope of 2 (region III). The sudden increase of current in the *I –V* plot was obtained repetitively, which ruled out the possibility of breakdown phenomenon to be the reason for the sudden increase of current above V_{TFL}. In the region II ($\alpha \sim 16.1$) there is a leap in the slope at voltage trap filled limited (V_{TFL}) which is due to the filling up of the trap levels present in the $YMnO_3$ thin films and in the region III ($\alpha \sim 2$) it exhibits trap free square law

$$J = \left(\frac{9k\mu\varepsilon_o E^2}{8L} \right) \qquad (3)$$

with the J is the current density, k is the Boltzmann constant, μ is free electron mobility, ε_o is the permittivity of vacuum, E is the applied electric field and L is the thickness of the film.

Trap filled voltage (V_{TFL})

It is known in space-charge theory that the trap filled voltage is a voltage where the Fermi level increases well above all the deep trap levels. Above the trap filled limit, all the trap levels would remain filled at a given temperature. If the temperature is increased,

a few of the filled traps re-emit some of the electrons from the trap sites, and those sites would become empty. In other words, the ratio of the free electrons to the trapped electrons increases with temperature. As a result, one would have to apply a higher voltage to inject further electrons in the sample, so that all the trap levels get filled with electrons. This is the possible cause for the increment of V_{TFL} with temperature.In the oresent case, V_{TFL} decreases with the increase in temperature from 300 K to 450 K as shown in the fig.2.30 for $YMnO_3$. This is in contrast to what is predicted by space charge

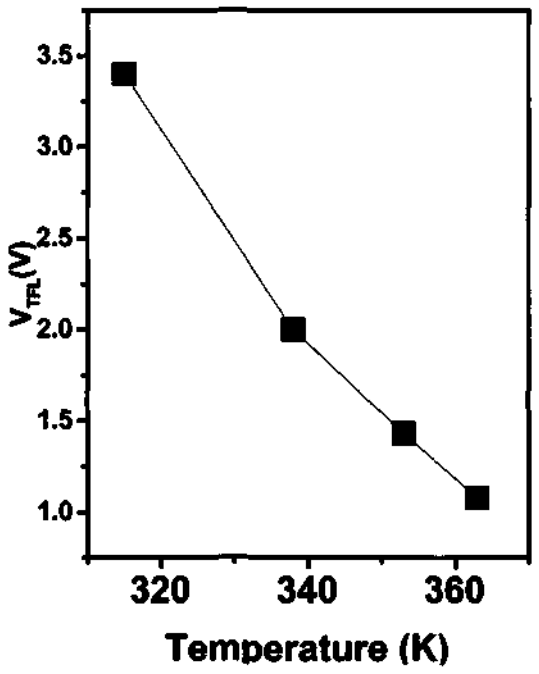

Fig.2.30 Voltage trap filled limited (V_{TFL}) as function of temperature of the Y123 thin films

theory of Lampert as it deals with the conduction mainly by electronic charges. It was assumed that the space charges would be represented by an equilibrium distribution which would be identical to the Fermi–Dirac distribution function, at all temperatures. To achieve equilibrium, a certain time is required. The charges, immediately after being injected into the sample, have to equilibrate with the surroundings, to reach the time

independent distribution of electrons among various energy levels. This has to occur throughout the entire sample. For this to happen, the electrons have to migrate uniformly through the sample, so that they could seek the equilibrium (trap) sites. This means that the space-charge transient would govern the trap distribution, if observed in a short time scale. The space-charge transient in thin films could be of a time scale of several seconds depending upon the sample. The electron distribution would therefore be limited by the competition between the rate of trapping and detrapping of the electrons. The trapping rate is represented by

$$T_{E_c \to E_t} = N(E_c)\sigma(E_t)N(E_t)$$

where, T represents the rate of transition between the energy states mentioned in the suffices, N represents the density of unoccupied energy states at energy E, and $\sigma(E_t)$ is the capture cross section of the traps. The detrapping of electrons is given by

$$T_{E_c \to E_t} = \nu N(E_t)\exp(\Delta E / kT)N(E_c)$$

where the energy difference is denoted by ΔE and the attempt frequency to escape is by ν. At a lower temperature, there would be very few electrons in the upper energy state (from where, it is captured to the trap sites), and the trapping rate also would not change much with temperature. Therefore, the entire process would be limited by the detrapping only. But at a higher temperature, there would be a significant amount of electrons in the conduction band (due to thermal generations and so on) which in turn would increase the rate of trapping, causing a greater number of trapped electrons.

There would be some contribution from the detrapping of electrons also, but the increased trapping rate might overshadow the detrapping rate at a higher temperature. Therefore, one would expect that, the number of electrons required to fill all the traps would be less at a higher temperature, than it was at a lower temperature. This might bring down the trap filled voltage closer to the actual value. This should saturate at the equilibrium value of V_{TFL}. There are reports of the space-charge transients in insulating samples even in this time scale. This was attributed to the movement of oxygen vacancies, which are quite slower compared to electrons. The existence of oxygen vacancies was demonstrated in the preceding section. We can, therefore,

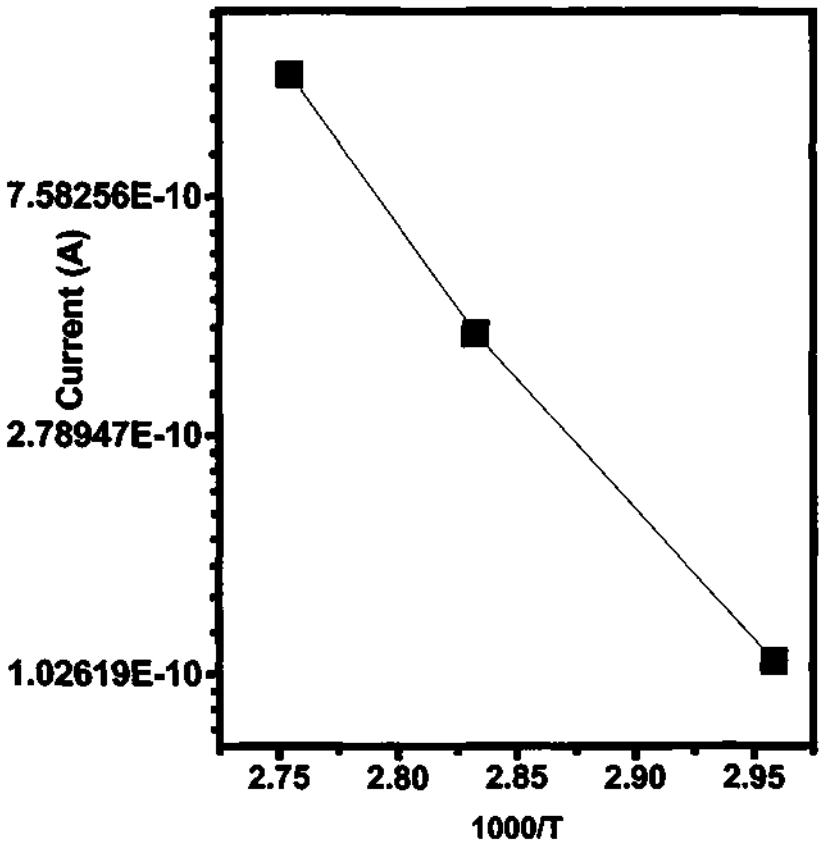

Fig.2.31 **Arhennius plot of current versus temperature at different voltages of $YMnO_3$ thin films.**

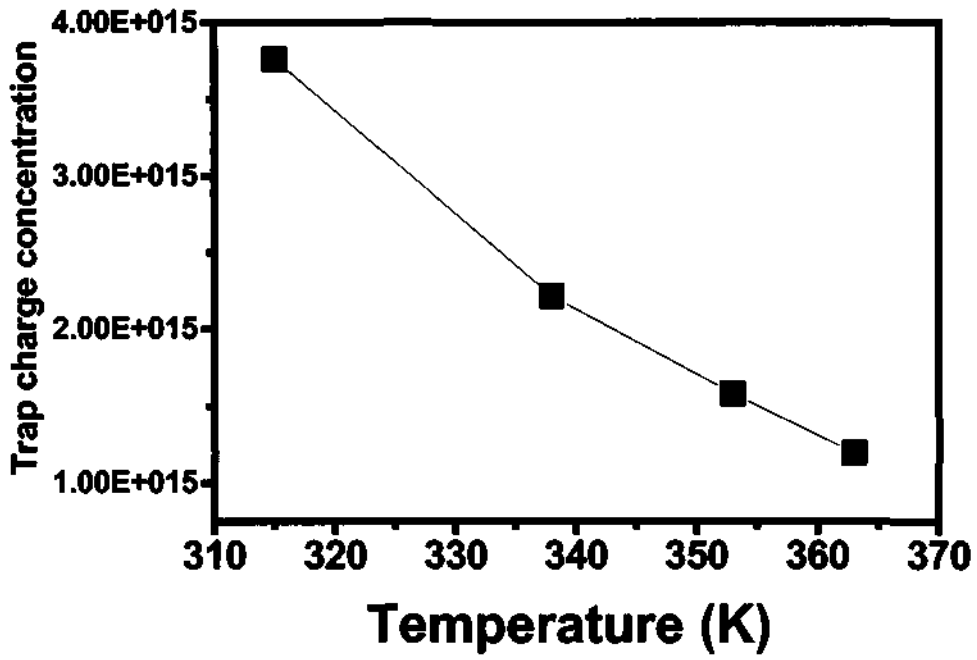

Fig.2.32 Trap charge concentration versus temperature of $YMnO_3$ thin films.

assume that both the electrons and the oxygen vacancies dominate the space-charge phenomenon. At lower temperatures, oxygen vacancies do not respond to higher fields (the nonlinear space-charge region), the highly mobile electronsbeing the majority charge carriers of the current. Due to their higher mobilities, they instantaneously redistribute themselves within the sample according to the space-charge law, and therefore, the expected increase of V_{TFL} with temperature is noticed. However, at high temperatures, even the oxygen vacancies play a significant role in space-charge conduction[75]. Since, oxygen vacancy motion is a slower process, it requires a significant time to respond, and this might be the reason why the linear to nonlinear region transition voltage (or the trap filled voltage) decreases with temperature, or with the increase of delay time. The current in the linear region was found to follow the Arrhenius equation:

$$I \sim \exp(-\Delta E / kT)$$

with ΔE denoting the activation energy obtained, and the calculated activation energy was of 0.92 eV for the 1.1 V on the $YMnO_3$ thin films as shown in the fig.2.31. This order of magnitude of the activation energy can be due to the motion of the oxygen vacancies as reported by many authors. The calculated trap charge concentration was found to decreases with the an increase in the temperature as shown in the fig.2.32 (for $YMnO_3$ films).

Deep Level Transient Spectroscopy

DLTS is an excellent technique to characterize the deep level traps present in crystalline semiconductors and semi-insulators and is also useful to obtain the density of interface states in the MOS capacitor. DLTS is a high frequency (MHz range) junction capacitance technique and advantageous because of its ultimate sensitivity and range of observable trap depths is much greater. In this study, DLTS measurements were carried out by the double boxcar technique developed by Lang[76]. The DLTS signal versus temperature plot is obtained from the DLTS instrument with the quiescent bias voltage V_a and the pulse voltage V_b. The V_a voltage is superimposed on to the V_b voltage for a large duration (t_p) to the gate of the MFS capacitor on a n – type Si substrate. When the pulse is off, the interface states and the bulk traps located below the Fermi level get filled with electrons, which are then emitted with characteristic emission rates. The rate equation for which the electron occupany function f_T of a trap at an energy E_T is given by,

$$\frac{\partial f}{\partial t} = (e_p + nc_n) - (e_n + e_p + nc_n + pc_p) f_T$$

Where e_n and e_p are the thermal emission rates for electrons and holes, c_n and c_p are the capture rates for electrons and holes, and n and p are the densities of the free electrons

and holes respectively. At thermal equilibirium, where the f_T reduces to the Fermi – dirac distribution and the above equation is given as

$$\tau_n^{-1} = e_n(E) = c_n v_n N_c \exp[(E_c - E_T)/kT]$$

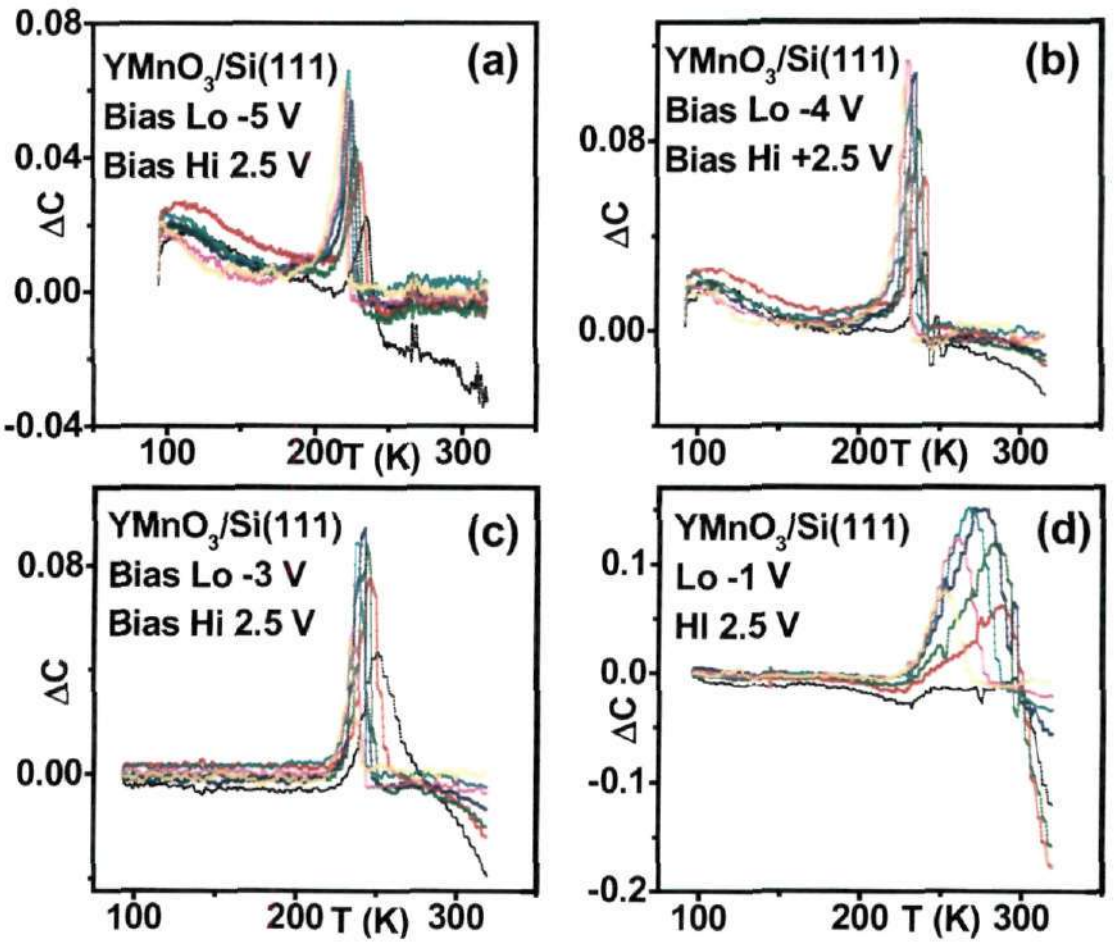

Fig.2.33 DLTS spectra for various applied Bias on $YMnO_3$/Si(111) annealed at 1123 K are shown (a) Lo –5 V Hi 2.5 V (b) Lo –4 V Hi 2.5 V (c) Lo –3 V Hi 2.5 V (d) Lo –1.5 V Hi 2.5 V

Where σ_n is the electron trap capture cross – section, v_n is the thermal velocity of electrons, N_C is the effective density of states in the conduction band, k is the

Boltzmann's constant , T is the absolute temperature and ΔC is the DLTS correlation signal.

In the present experiment the quiescent bias voltage maintained at 2.5 V was applied to the top electrode and the MFS capacitor was biased at different voltages ranging from –5V, -4V, –3V and –1 V as shown in fig.2.33. The transient capacitance was recorded with the emission rate windows e^{-1}_{p} obtained from the maximum peaks in the plot of DLTS signal versus temperature. The defect characteristics of the MFS capacitor were measured by the DLTS signal over a temperature range varying from 90 K to 320 K. Fig.2.33(d) shows the DLTS signal versus temperature for a biased voltage at –1 V with a fixed quiescent voltage of 2.5V. Fig.2.33(d) shows one positive peak representing the electron traps in the thin films, which can arise from the contribution from the structurally disordered interface and bulk states. The possibility of the interface states present in the ferroelectric – semiconductor interface and in the grain – grain interaction in the thin film due to the polycrystalline nature. There are several other possibility of the defects like schottky defect, frenkel defect and other non stoichiometry defects arising due to these constitutent ions of the thin films. The charges are pumped in the accumulation region when the quiescent voltage of 2.5 V and biased pulsed voltage of –1 V, thereby the traps are contributed from the bulk traps rather than the interface traps. The activation energy calculated from the emission rates and the capture cross sections are shown in the fig.2.34. The obtained activation energy was of 0.55 eV which might arise from the traps present near the conduction band.

The density of the interface states N_{ss} were obtained from the equation

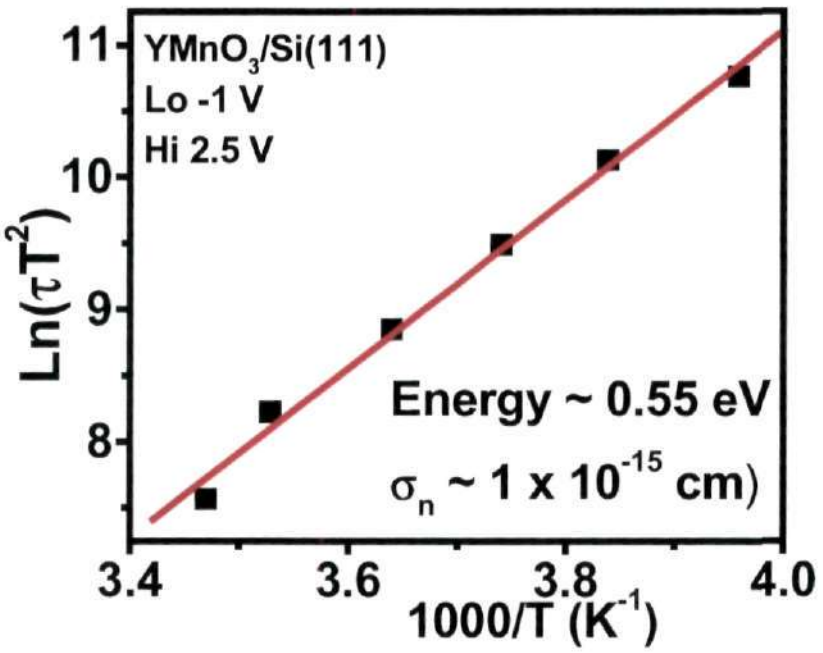

Fig.2.34 Activation energy for bias Lo –1 V Hi 2.5 V

$$N_{ss} = \frac{\Delta C}{(C(t_1) + \Delta C/2)^3} - \frac{C_{ox} A \varepsilon_s N_D}{kT \ln(t_2/t_1)}$$

where ΔC is the DLTS signal, $C(t_1)$ is the capacitance at the sampling time t_1, C_{ox} is the oxide capacitance, A is the area of the field electrode, ε_s is the permittivity of the Si and N_d is the donor density.

Fig.2.33(a) shows the positive peak in the temperature variation of the DLTS spectra for the $V_a \sim -5V$ and $V_b \sim 2.5$ V. The activation energy of traps() from this spectra is plotted in fig.2.35. The superposition of these voltages result in the depletion region of the n – type Si substrate as observed in the C – V plot (fig.2.27). This plot is essential for the calculation of the interfaces states present at the $YMnO_3$ thin films – Si substrate. The calculated N_{ss} was 3.11×10^{11} cm^{-1} eV^{-1} and is found to be close to the N_{ss} calculated from the Capacitance – Voltage measurement. The details on the C – V and its interface states calculation is given in section.

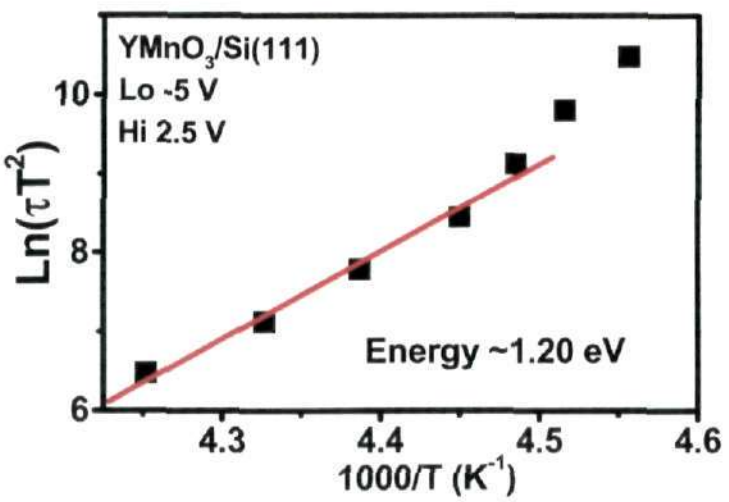

Fig.2.35 **Activation energy for bias Lo –5 V Hi 2.5 V**

2.5 References

1. Newnham R E Am. Mineral. 1974 **57** 906
2. Newnham R E and Cross L E Preparation and characterization of materials (eds. Honig J M and Rao C N R) Academic Press New York 1981
3. Schmid H Ferroelectrics 1994 **162** 317
4. Wood V E and Austin A E Magnetoelectric Interaction Phenomena in Crystals; Freeman A J, Schmid Eds. Gordon and Breach: Newark, NJ, 1975
5. Ascher E, Rieder H, Schmid H and Stossel H J. Appl. Phys. 1966 **37** 1404
6. Smolensky G A, Agranovskaya A I and Isupov V A Sov. Phys. Solid State 1959 **1** 149
7. Smolensky G A, Isupov V A, Krainik N N and Agranovskaya A I Isvest. Akad. Nauk SSSR, Ser. Fiz 1961 **25** 1333
8. Brixel W, Rivera J P, Steiner A and Schmid H Ferroelectrics 1988 **79** 201
9. Astrov D N, Al'shin B I, Tomashpol'skii Y Y and Venevtsev Y N Sov. Phys. JETP 1969 **28** 1123
10. Drobyshev L A, Al'shin B I, Tomashpol'skii Y Y and Venevtsev Y N Sov. Phys. Cryst. 1970 **14** 634
11. Shannon R D Acta Crystallogr. 1976 **A32** 751
12. Mizokawa T, Khomskii D I and Sawatzky G A Phys. Rev. B 1999 **60** 7309
13. Cohen R E and Krakauer H Ferroelectrics 1992 **136** 95
14. Literature search for 1960 and later turned up only the following 5 papers: Troyanchuk I O, Kasper N V, Mantytskaya O and Pastushonok S N JETP 1994 **78** 212; Troyanchuk I O and Derachenko V N Sov. Phys. Solid State 1990 **32** 1436;

Tomashpol'skii Y Y and Venevtsev Y N Sov. Phys. Crystallogr 1972 **16** 905; Bokov V A, Grigoryan N A, Bryzhina M F and Kazaryan V S Bull. Acad. Sci. USSR, Phys. Ser. 1969 **33** 182; Sugawara F, Iida S, Syono Y and Akimoto S J. Phys. Soc. Jpn. 1968 **25** 1553

15. Hill N A and Rabe K B Phys. Rev. B 1999 **59** 8759; Woo H, Tyson T A, Croft M, Cheong S W and Woicik J C Phys. Rev. B 2001 **63** 134412
16. Kohn K, Horie O, Akimoto S I and Inoue K J. Solid State Chem. 1976 **18** 27
17. Subramanian M A, Ramirez A P and Marshall W J Phys. Rev. Lett. 1999 **82** 1558
18. Rao C N R, Cheetham A K and Mahesh R Chem. Mater. 1996 **8** 2421
19. Hill N A J. Phys. Chem. B 2000 **104** 6694
20. Filippetti A and Hill N A Phys. Rev. B 2002 **65** 195120
21. Seshadri R and Hill N A Chem. Mater. 2001 **13** 2892
22. dos Santos A M, Cheetham A K, , Atou T, Syono, Yamaguchi Y, Ohoyama K, Chiba H and Rao C N R Phys.Rev. B 2002 **66** 064425
23. Mattheiss L F Phys. Rev. B 1972 **6** 4718
24. Goodenough J B Phys. Rev. 1955 **100** 564; Goodenough J B J. Phys. Chem. Solids 1958 **6** 287; Kanamori J J. Phys. Chem. Solids 1959 **10** 87
25. Rao C N R, Arulraj A, Cheetham A K and Raveau B J. Phys.: Condens. Matter 2000 **12** R83-R106
26. Bao W, Axe J D, Chen C H and Cheong S W Phys. Rev. Lett. 1997 **78** 543
27. Schiffer P, Ramirez A P, Bao W and Cheong S W Phys. Rev. Lett. 1995 **75** 3336
28. Wollan E O and Koehler W C Phys. Rev. 1955 **100** 545
29. Ghosez Ph., Cockayne E, Waghmare U V and Rabe K M Phys. Rev. B 1999 **60** 836

30. Portengen T, Ostreich Th. and Sham L J Phys. Rev. Lett. 1996 **76** 3384; Phys. Rev. B 1996 **54** 17452

31. Waghmare U V and Rabe K M Phys. Rev. B 1997 **55** 6161

32. Yakel H L, Koehler W C, Bertaut E F and Forrat E F Acta Crystallogr. 1963 **16** 957; Aken B B van, Meetsma A and Palstra T T M Acta Crystallogr. 2001 **57** 230

33. Fujimura N, Ishida T, Yoshimura T and Ito T Appl. Phys. Lett. 1996 **69** 1011

34. Kim S H, Lee S H, Kim T H, Zyung T, Jeong Y H and Jang M S Cryst. Res. Technol. 2000 **35** 19

35. Filippetti A and Hill N A Phys. Rev. B 2002 **65** 195120; Hill N A J. Phys. Chem. B 2000 **104** 6694; Hill N A Annu. Rev. Res. 2002 **32** 1

36. Anisimov V I, Zaanen J and Andersen O K Phys. Rev. B 1991 **44** 943

37. Medvedeva J E, Anisimov V I, Korotin M A, Mryasov O N and Freeman A J J. Phys.: Condens. Matter 2000 **12** 4947

38. Qian M, Dong J and Xing D Y Phys. Rev. B 2001 **63** 155101

39. Yoshimura T, Fujimura N and Ito T Appl. Phys. Lett. 1998 **73** 414

40. Yi W C, Choe J S, Moon C R, Kwun S I and Yoon J G Appl. Phys. Lett. 1998 **73** 903

41. Iliev M N, Lee H G, Popov V N, Abrashev M V, Hamed A, Meng R L and Chu C W Phys. Rev. B 1997 **56** 2488

42. Huang Z J, Cao Y, Sun Y Y, Xue Y Y and Chu C W Phys. Rev. B 1997 **56** 2623

43. Katsufuji T, Mori S, Masaki M, Moritomo Y, Yamamoto N and Takagi H Phys. Rev. B 2001 **64** 104419

44. Frohlich D, Leute St., Pavlov V V and Pisarev R V Phys. Rev. Lett. 1998 **81** 3239

45. Iliev M N, Abrashev M V, Lee H G, Popov V N, Sun Y Y, Thomsen C, Meng R L and Chu C W Phys. Rev. B 1998 **57** 2872

46. Sikora W and Syromyatnikov V N J. Magn. Magn. Mater. 1986 **60** 199

47. Frohlich D, Leute St., Pavlov V V, Pisarev R V and Kohn K J. Appl. Phys. 1999 **85** 4762

48. Rao C N R and Rao K J in A K Cheetham and P Day (Eds.), Solid State Chemistry: Clarendon Press, Oxford, 1992

49. Bokov V A, Myl'nikova, Kizhaev S A, Bryzhina M F and Grigoryan N A Sov. Phys. Solid State 1966 **7** 2993

50. Smolenskii G A and Chupis I E Sov. Phys. Usp. 1982 **25** 475

51. Kanai T, Ohkoshi S, Nakajima A, Watanabe T and Hashimoto K Adv. Mater. 2001 **13** 487

52. Chiba H, Atou T and Syono Y J. Solid State Chem. 1997 **132** 139

53. Atou T, Chiba H, Ohoyama K, Yamaguchi Y and Syono Y J. Solid State Chem. 1999 **145** 639

54. Sugawara F, Ihda S, Syono Y and Akimoto S J. Phys. Soc. Jpn. 1968 **25** 1553

55. Ohshima E, Saya Y, Nantoh M and Kawai M Solid State Commun. 2000 **116** 73

56. Ramirez A P J. Phys.: Condens. Matter 1997 **9** 8171

57. Rao C N R and Raveau B *Colossal Magnetoresistance, Charge Ordering and Related Properties of Manganese Oxides* World Scientific Singapore

58. Rao C N R, Arulraj A, Cheetham A K and Raveau B J. Phys.: Condens. Matter 2000 **12** R83

59. Bertaut E F, Forrat E F and Fang P H Compt. Rend. 1963 **256** 1958

60. FujimuraN, Ishida T, Yoshimura T and Ito T Appl. Phys. Lett. 1996 **69** 1011; Yi W C, Choe J S, Moon C R, Kwun S and Yoon J G Appl. Phys. Lett. 1998 **73** 903; Lee H N, Kim Y T and Park Y K Appl. Phys. Lett. 1999 **74** 3887; Yoshimura T, Fujimura N and Ito T App. Phys. Lett. 1998 **73** 414 ; Kitahata H, Tadanaga K, Minami T, Fujimura N and Ito T App. Phys. Lett. 1999 **75** 719; Yoshimura T, Fujimura N, Ito D and Ito T J.Appl. Phys. 2000 **87** 3444; Yi W C, Seo C S, Kwun S and Yoon J G Appl. Phys. Lett. 2000 **77** 1044; Choi J H, Lee J Y and Kim Y T Appl. Phys. Lett. 2000 **77** 4028; Lee H N, Kim Y T and Choh S H Appl. Phys. Lett. 2000 **76** 1066; Fujimura N, Ito D and Ito T Ferroelectrics 2002 **271** 229

61. Flebig M, Lottermoser Th., Fröhlich, Goltsev A V and Pisarev R V Nature 2002 **419** 818

62. Scott J F and Araujo C A Paz de Science 1989 **246** 1400

63. Zhao Y S, Dreele R B Von and Morgan J G High Pressure Res. 1999 **16** 161

64. Faqir H, Chiba H, Kikuchi M, Syono Y, Mansori M, Satre A and Sebaoun J. Solid State Chem. 1999 **142** 113

65. Hauser J R and Ahmed K edited by D.G.Sciller, A.C.Diebold, W.M.Bullis, T.J.Shaffner, R.McDonald and E.J.Walters 1998 Characterization and Metrology for ULSI technology:The American Institute of Physics, New York pp. 235 – 239

66. Ito K and Tsuchiya H Solid-State Electron. 1977 **20** 529

67. Sze S M 1981 Physics of Semiconductor devices 2nd ed. p 248 Wiley NewYork.

68. Nicollian E H and Brews J R 1982 Metal-oxide-semiconductor (MOS) Physics and Technolgy John Wiley

69. Sze S M, 1981 Physics of Semiconductor devices (Wiley publications, New York)

70. Castagne R and Vaipalle A Surf. Sci. 1997 **28** 557; Castagne R and Vaipalle A C R. Acad. Sci. (Paris) 1970 **270,** 1347

71. Terman L M Solid-State Electron. 1962 **5** 285

72. J.Frenkel Tech. Phys., USSR 1938 **V685**

73. J.G.Simmons Physical Review 1967 **155(3)** 657

74. M.A. Lampert Phys. Rev., 1956 **103** 1648

75. Waser R, Baiatu T and Hardtl K H J. Am. Cer. Soc. 1990 **73** 16451

76. Lang D V J. App. Phys. 1974 **45** 3023

PART 3

INVESTIGATIONS OF THIN FILMS OF COPPER, COBALT AND COPPER-COBALT GRANULAR ALLOYS

SUMMARY*

Metallic copper films have been deposited on Si(100) substrates by nebulized spray pyrolysis of $Cu(acac)_2$, $Cu(hfac)_2$ and $Cu(dpm)_2$ precursors, where acac, hfac anf dpm stand for acetylacetonate, hexaflouroacetylacetonate and dipivaloylmethanate respectively. The structure and morphology of the films have been examined by X-ray diffraction and scanning electron microscopy. The films are polycrystalline in nature with a preferred (111) orientation. Based on the electrical resistivity data, various transport parameters of the films have been estimated. Growth kinetics and the environmental stability of the films from the precursors have been compared. Taking all the factors into account, $Cu(dpm)_2$ seems to yield the best films of copper metal.

Thin films of cobalt have been prepared by nebulized spray pyrolysis in hydrogen atmosphere using the $Co(acac)_2$ precursor. Thin films show excellent magnetic and metallic properties. Granular Cu-Co alloy films of the compositions $Cu_{82}Co_{18}$ and $Cu_{50}Co_{50}$ have been obtained by nebulized spray pyrolysis of mixtures of $Co(acac)_2$ and $Cu(acac)_2$ in hydrogen atmosphere. These films show magnetoresistance at room temperature.

*Based on this work papers have been published in J. Phys. D: App. Phys. (1999), Mater. Chem. Phys. (1999)

3.1 INTRODUCATION

Metallic films have been prepared by employing one of the many physical vapor deposition methods. Of late metallic chemical vapor deposition has also been used to obtain metal films. The demand for reducing feature sizes to below 0.5μm in ultra large scale integrated circuit (ULSI) devices such as the static random access memory, the dynamic random access memory and logic devices with high circuit speed, while at the same time achieving low power dissipation, raises concern over the available metallization technology[1,2]. The increasing resistance – capacitance (RC) time delay at higher clock frequencies and lower interconnect feature sizes creates limitations on achieving high circuit speed. Further more, an increase in the interconnect current density due to miniaturization causes concerns regarding possible electromigration failure[3]. Of late, copper deposition by chemical routes such as the CVD (chemical vapor deposition) process is being considered as a possible means of metallization in multilevel metallization schemes, since copper offers a higher conductivity and greater electronmigration resistance compared to Al alloys used at present in interconnect schemes[4].

Copper has been ignored till recently in IC fabrication schemes because of (i) the lack of an anisotropic, low-temperature Cu etch process[5], (ii) its high diffusion coefficient in both Si and SiO_2[6], (iii) its role as a poison in the active device area due to the formation of deep level acceptor level traps in the forbidden energy gap in Si, (resulting in a reduction of the minority carrier life time) and (iv) the tendency to get oxidized to form Cu_2O and CuO phases below 200°C [7]. However, to enable the use of copper metallization in ULSI (ultra large scale integrated circuits), intense research has been focused recently

on diffusion barrier technology, synthesis of new Cu CVD precursors, blanket as well as selective chemical deposition at low temperature and on chemical mechanical polishing (CMP), needed for planarization in MLM schemes. Because of the use of sputter deposition process, the present Al-based interconnect material suffers from poor step coverage on the highly rugged topography for sub-half-micron level interconnects required in ULSI. As chemical deposition techniques operate at high pressures, it offers better conformal coverage compared to physical vapor deposition processes such as sputtering or e-beam evaporation, which provide line-of-sight deposition due to low operating pressure. In addition, chemical deposition of Cu shows selective deposition, which can reduce etching steps in integrated circuit fabrication. This approach relies on filling trenches selectively by chemical deposition on an exposed seed layer, such as a metal like tungsten, in presence of a non-growth surface like SiO_2.

Cobalt has been an important material of interest over the past decade as the multilayers of copper-cobalt have shown the (GMR) giant magnetoresistance effect. Due to high oxidation resistance of cobalt it has also been a material of interest in interconnect technology. Cobalt films have been generally deposited by physical vapor deposition (PVD) techniques only. Recently due to the availability beta-diketonate precursors of cobalt chemical vapor deposition of cobalt has been initiated as a better alternative to PVD techniques.

In this part of the thesis, results of investigations of copper and cobalt films as well as of Cu-Co granular alloy films prepared by nebulized spray pyrolysis are presented.

3.2 SCOPE OF THE PRESENT INVESTIGATIONS

3.2.1 Copper films

The demand of higher data density storage media has resulted in miniaturization of electronic circuits. This denser media needs a very high speed of processing which should have a minimum time of signal delay. This can only be achieved by having better interconnects in the circuits. Copper is a promising material for metallization in ultra-large scale integrated circuits, such as dynamic random access memories because of its low resistivity, high electromigration resistance and high melting point compared to aluminium and its alloys. Copper films are therefore emerging as useful materials in new technologies. Till now copper has been ignored as interconnect material because of several reasons: (i) Lack of an anisotropic low temperature copper etch process; (ii) High diffusion coefficient of copper in Si and SiO_2; (iii) Low oxidation resistance and (iv) It is a poison to active device area due to formation of deep acceptor level traps in forbidden energy gaps of Si.

In order to overcome these problems, intense research has been carried out by various workers. One of the problems in this area relates to the method of deposition of copper. Physical vapor deposition (PVD) techniques such as sputtering or evaporation employed for depositing films are limited by line of sight deposition and are susceptible to shadowing, poor uniformity and extended defects[8-10], making chemical vapor deposition (CVD) a more desirable choice in such applications[11-14]. CVD has also other advantages of uniform large area coverage and certain processing benefits such as low temperature deposition, deposition selectivity and conformal coverage. Furthermore, precursors for the CVD process can be generally obtained in high purity to allow films to be deposited

with the low impurity levels required in the electronic devices. Several Cu β-diketonates have been used as precursors for CVD of copper films in the literature[11-14] and CVD has been shown to be viable with both Cu(I) and Cu(II) β-diketonates. We have made good copper films by the simple, low-cost solution based chemical technique of nebulized spray pyrolysis. We have used three β-diketonates of copper(II), viz., $Cu(acac)_2$ (bis-acetyalacetonato copper), $Cu(hfac)_2$ (bis-hexafluroacetylacetonato copper) and $Cu(dpm)_2$ (bis-dipivaloylmethanato copper) as precursors in the present study. We have carried out a comparative study of the crystallinity, morphology, growth kinetics, electrical resistivity and environmental stability of the copper films obtained by the nebulized spray pyrolysis of these precursors. In addition, we have estimated the grain boundary and other contributions to the observed resistivity on the basis of known models.

3.2.2 Cobalt and granular Copper-Cobalt films

Thin films of cobalt are known to be useful in memory elements and in microelectronics because of their low resistivity and high oxidation resistance. Although cobalt films have been obtained by thermal evaporation and sputtering techniques, their study has been rather limited. Li *et al*[15] have reported the study of cobalt films deposited by thermal evaporation and chemical vapor deposition (CVD) of β-diketonate compounds. These workers were concerned with the magnetic properties of Co films with respect to their surface roughness. Maruyama[16] deposited Co films of varying thickness by the CVD technique and studied their electrical transport properties with varying thickness. We have deposited thin films of cobalt by nebulized spray pyrolysis using Co (II) acetylacetonate as precursor and ultra high pure H_2 as the carrier gas. These films were grown on Si(100) as well as on borosilicate glass. The films showed hcp and

fcc single and mixed phases on Si(100) and glass substrate at different deposition conditions. Electrical resistivity and magnetic hysterisis measurements were carried out on the Co films.

Copper-cobalt granular films are being investigated extensively in recent years because of the giant magnetoresistance (GMR) exhibited by them. These films have been prepared by dc sputtering[17], magnetron sputtering[18,19] and melt spinning[20]. We have deposited granular copper-cobalt alloy thin films by nebulized spray pyrolysis using similar conditions as those with cobalt. The compositions of $Cu_{1-x}Co_x$ are x=0.2 and 0.5. The films showed a mixed phase of copper and cobalt in the as deposited form but showed a phase separation when annealed in hydrogen. Magnetoresistance properties of the granular films were measured.

3.3 EXPERIMENTAL

Copper Metal Films

Copper films were deposited using a home-made nebulized spray pyrolysis apparatus described in section 1.3 of this thesis. A solution containing the copper precursor in methanol solvent (concentration ~1mM) was nebulized making use of a PZT (1.72 MHz) transducer. We in our study of copper films have used Cu(II)β-diketonates namely $Cu(acac)_2$ (bis-acetylacetanato copper), $Cu(hfac)_2$ (bis-hexaflouroacetylacetanato copper) and $Cu(dpm)_2$ (bis-dipivaloylomethanato copper). The structures of all the three compounds are shown in fig.3.1.

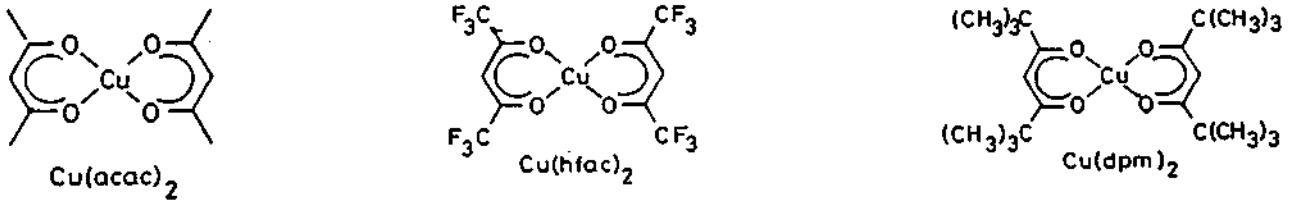

Fig.3.1 Structures of various precursors employed.

All the precursors were prepared by using the commercially obtained β-diketonate ligands and Cu (II) chloride salts in ammonium hydroxide (NH_4OH) medium. Bases like sodium hydroxide and other alkali bases were avoided because the alkaline cation also undergoes a chealation reaction and lead to contamination of the products. In the preparation of all the precursors the ligands were dissolved in methanol and then NH_4OH is added to this solution in excess in order to make ammonium salt β-diketonate and simultaneously dissolve it in NH_4OH to make a clear solution. This solution was then added to the Cu (II) chloride solution in water with constant stirring of the mixture with

the pH maintained at 7 and then left for 1hr. After 1 hr the solution is filtered and the precipitate was thoroughly washed with water in order to remove unreacted chloride salts from the precursor. This precipitate was kept over P_2O_5 in vacuum decicator for drying for 24 hrs.

Films were deposited on Si (100) substrates at substrate temperatures of 523 K-673 K for 3-12 hrs. A mixture of ultrahigh pure N_2 and H_2 (100 sccm) was used as the carrier gas to transport the nebulized precursor with a typical gas flow rate of 1-1.5 l / min. In order to avoid the formation of oxide, the growth chamber was thoroughly purged with N_2/H_2 mixture before and after the deposition run. After the deposition is complete the films were kept in vacuum in other to minimize the rate of oxidation.

The deposited films were studied by X-ray diffraction using a Seifert (xrd, xdl, θ-θ, Cu target) instrument. Conventional θ-θ scans were collected with a Bragg-Brentano goniometer and high resolution (169 eV) Si(Li) solid state detector with 0.5 mm/1 mm slits. The surface morphology of the films was observed by scanning electron microscopy (SEM) with a Leica S-440 i SEM. The film thickness was confirmed by cross-sectional scanning electron microscopy. The EDX analysis was carried out using Links ISIS of Oxford intruement. Scanning tunneling microscope (STM) images were obtained with Nanoscope II (Digital Instruments, USA) to study the surfaces of some of the copper films. STM images were recorded at room temperature (in air) in constant current mode using Pt-Ir tips employing a bias voltage and a tunneling current of 100-500 mV and 0.2-1 nA, respectively. Prior to scanning the film, STM was calibrated by imaging a freshly cleaved highly oriented pyrolytic graphite (HOPG) surface. Electrical resistivity of the deposited films was measured by the four-point probe method.

Cobalt and Granular Copper-Cobalt Alloy Films

Cobalt films and copper-cobalt (Cu-Co) granular alloy films were deposited using the home-built nebulized spray pyrolysis apparatus described in section 3.1. A solution of $Co(acac)_2$ (bis-acetylacetonato cobalt) in methanol solvent (~1mM) was nebulized using the PZT transducer (1.72 MHz). Similarly a solution containing a mixture $Cu(acac)_2$ (bis-acetylacetonato copper) and $Co(acac)_2$ (bis-acetylacetonato cobalt) of required composition was used to deposit Cu-Co granular alloy films. Both the precursors were prepared using comerically obtained ligand and metal chlorides as explained in section 3.2. The composition of the films deposited were $Cu_xCo_{(1-x)}$ (x = 0.5 to 0.9). The films were deposited on Si(100) as well as on borosilicate glass at substrate temperatures ranging from 598 K to 673 K for 7-9 hrs. Zero grade hydrogen was used as carrier gas to transport the nebulized precursor with a typical flow rate of 1-1.5 l/min. In order to avoid the formation of any oxide the growth chamber was purged with hydrogen gas before and after the run. The deposited films were examined by XRD, SEM, electrical transport properties using four probe resistivity technique with a constant current source of Keithley model-220, Lakeshore autotunning temperature controller and digital multimeter Keithley model-2000. The magnetic properties were studied using Lakeshore VSM 7300 vibrating sample magnetometer.

3.4 RESULTS AND DISCUSSION

3.4.1 Copper films

We have carried out a comparative study of crystallinity, morphology, growth kinetics, electrical resistivity and environmental stability of copper films obtained by nebulized spray pyrolysis of $Cu(acac)_2$ (bis-acetylacetanato copper), $Cu(hfac)_2$ (bis-hexaflouroacetylacetanato copper) and $Cu(dpm)_2$ (bis-dipivaloylmethanato copper). In addition, we have estimated the grain boundary and other contributions to the observed resistivity on the basis of known models.

Characterization of films

Fig.3.2 shows X-ray diffracton patterns of Cu films deposited from $Cu(acac)_2$, $Cu(hfac)_2$ and $Cu(dpm)_2$ precursors on Si (100) substrates at 673 K for 12 hr. All the patterns show polycrystalline Cu (111) and Cu (200) reflections, with no indication of any oxide phase within the limits of detection. The peak-height intensity ratio of Cu (111) and Cu (200) reflections is 2.17 in a standard Cu powder sample (JCPDS File No. 4-836). The observed peak height ratios ($I_{(111)}/I_{(200)}$) for our Cu films are however, much larger than the polycrystalline reference and are 11.6, 3.9 and 15.8 respectively for films deposited from $Cu(acac)_2$, $Cu(hfac)_2$ and $Cu(dpm)_2$ precursors. This observation clearly suggests that for the Cu films derived from $Cu(dpm)_2$, the degree of preferred (111) orientation is higher than that obtained from $Cu(acac)_2$ or $Cu(hfac)_2$. The films from $Cu(hfac)_2$ show the least preference for (111) orientation of the film. These differences in the orientation preference of Cu films deposited from different precursors arise from the differences in the energetic of the surface reactions.

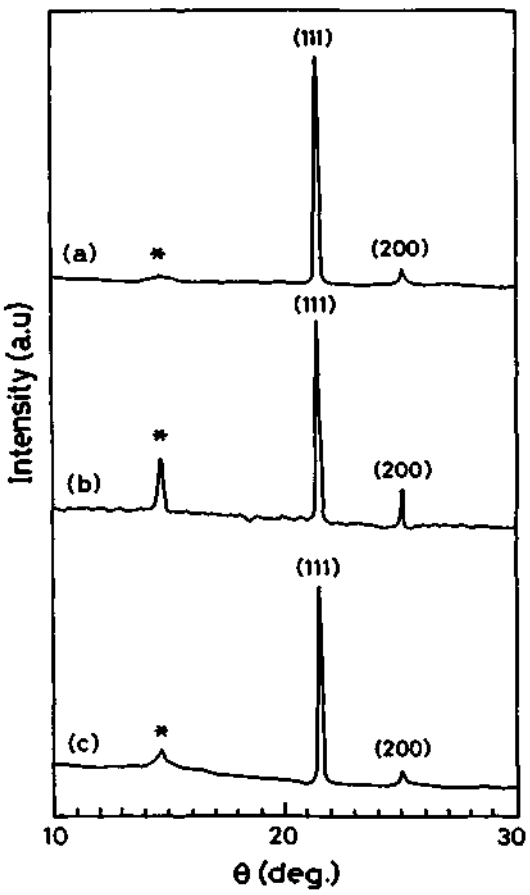

Fig.3.2 XRD patterns of Cu films obtained (a) Cu $(acac)_2$, (b) Cu $(hfac)_2$, (c) Cu $(dpm)_2$ '*' denotes Si(100) reflection.

SEM images of the Cu films deposited at 673 K for 12 hrs using different precursors is shown in fig.3.3. The variation of the surface morphology of the films with precursor employed is evident. The films from $Cu(acac)_2$ [fig.3.3 (a)] and $Cu(dpm)_2$ [fig.3.3 (b)] have a uniform and smooth morphology. The films from $Cu(hfac)_2$ [fig.3.3 (c)], on the other hand exhibit a rough, highly porous microstructure with a wide distribution of grain sizes, with an average grain size of ~500nm. These observations can be clearly

conformed from the high magnification SEM images of the films. In case of the films from $Cu(hfac)_2$ [fig.3.4 (c)] at a magnification of 2 KX only grains can be clearly seen,

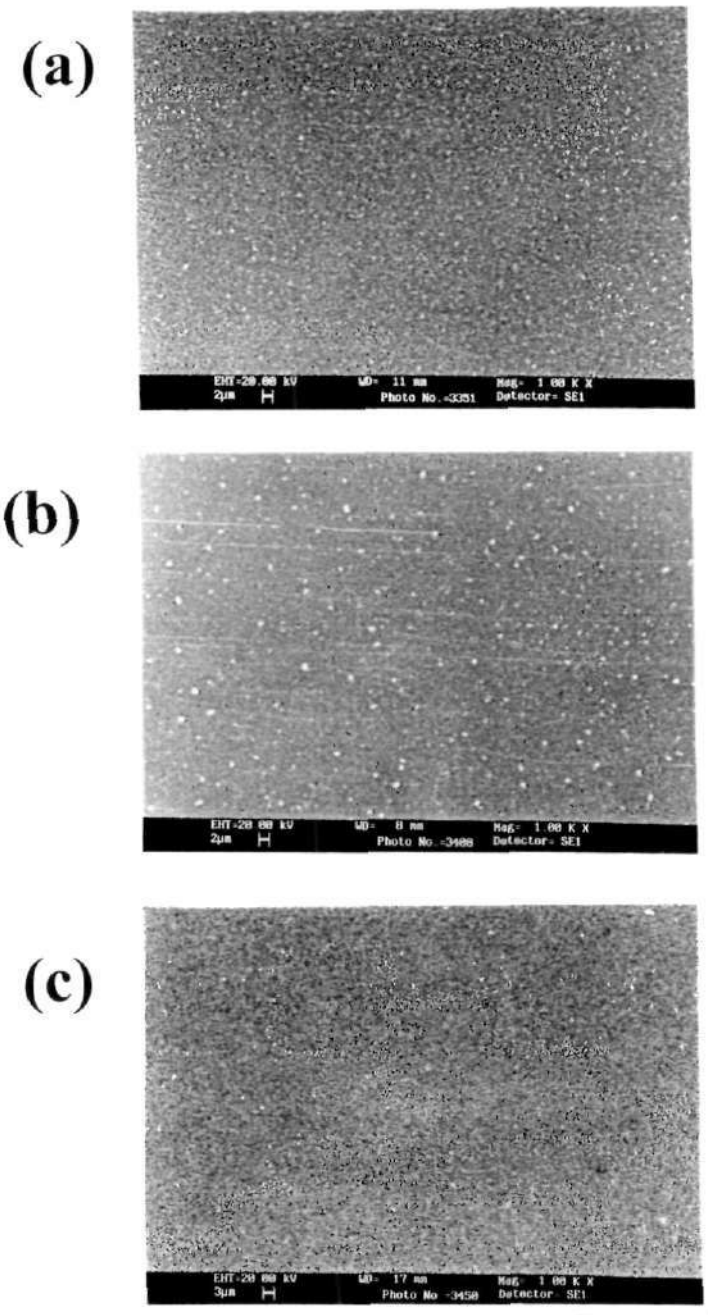

Fig.3.3 Low-magnification scanning electron micrographs of Cu films deposited at 673K from (a) $Cu(acac)_2$ (b) $Cu(dpm)_2$ (c) $Cu(hfac)_2$.

but on the other hand for the films obtained from $Cu(dpm)_2$ [fig.3.4 (b)], a smooth morphology is seen till 20 KX, and also for films of $Cu(acac)_2$ grains are visible only at 6

KX [fig.3.4 (a)]. The films deposited from $Cu(acac)_2$ show comparatively higher growth rates resulting in the reduced surface mobility of the growth species and enhanced nucleation density.

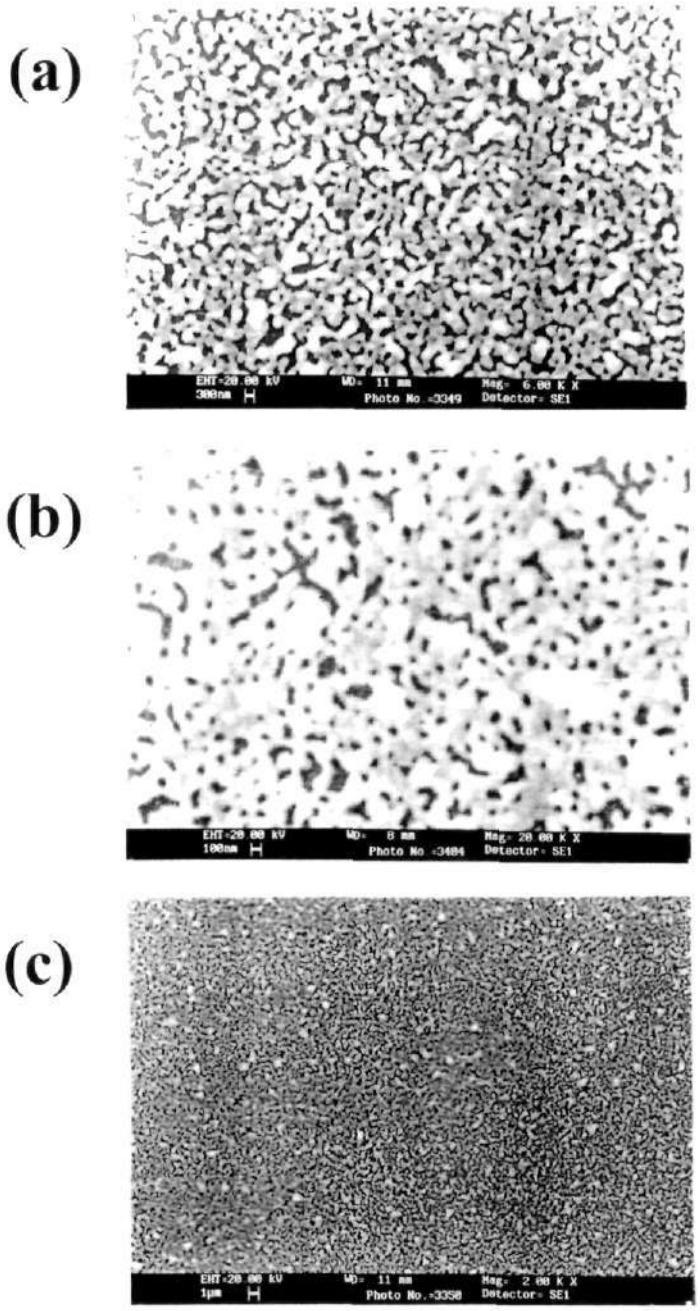

Fig.3.4 High-magnification scanning electron micrographs of Cu films deposited at 673K from (a) $Cu(acac)_2$ (b) $Cu(dpm)_2$ and (c) $Cu(hfac)_2$.

therefore relatively more dense and exhibit a smooth microstructure with high intergrain connectivity. This becomes evident from the cross sectional SEM images presented in figs.3.5 (a) and (b). The films from $Cu(hfac)_2$ are characterized by low growth rate, incorporate voids and hence show a less dense microstructure. The intergrain

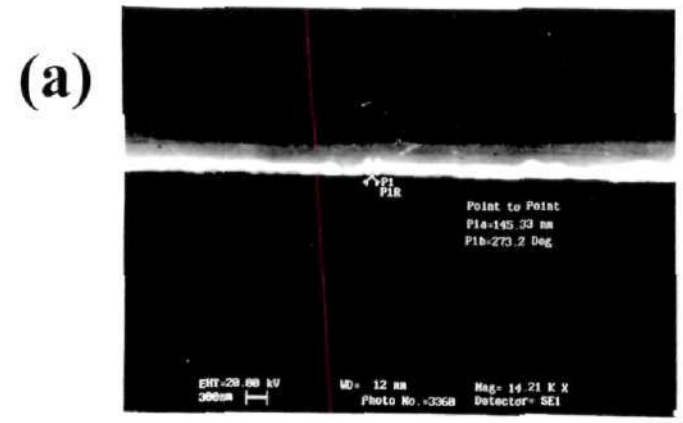

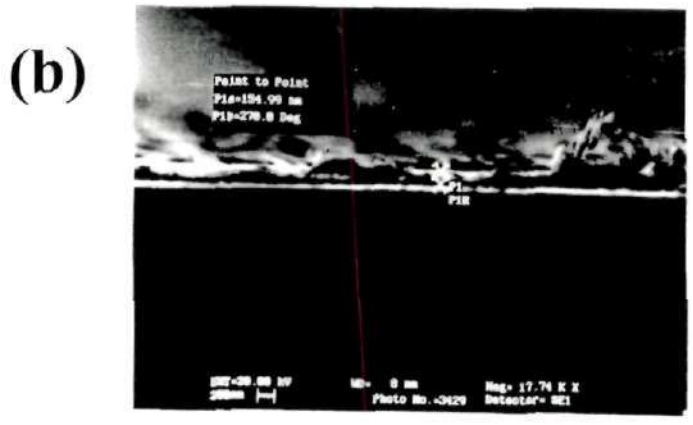

Fig.3.5 Typical cross-sectional SEM images for Cu films deposited at 673K from (a) $Cu(acac)_2$ (145.33 nm) (b) $Cu(dpm)_2$ (154.99 nm) and $Cu(hfac)_2$ (197.09 nm). The thickness of the film is given in the brackets.

connectivity in the films from $Cu(hfac)_2$ is poor because of this factor, as seen in the cross sectional SEM image of fig.3.5 (c). We obtained good copper films from $Cu(acac)_2$ precursor from 573 K to 673 K. We could not obtain copper films from $Cu(dpm)_2$ and $Cu(hfac)_2$ precursors below 673 K.

As the films obtained from $Cu(dpm)_2$ were extremly smooth and no grain were seen at high magnification in SEM, so we have carried out STM studies by employing Digital Nanoscope II scanning tunneling microscope on these films in order to know their morphology. The topview and the surface plot (in 60° perspective) are presented in fig.3.6 (a) and (b) respectively. The images reveal cauliflower like growth patterns. These images show orbicular agglomeration composed of small grains which appear to grow about a common central nucleation point. The average width of the agglomeration is around 400 nm while the grain size is ~ 40 nm. A typical agglomeration is marked as 'D-C-F-E' in fig.3.6 (a) wherein 'C' is clearly seen as its nucleation point. A line profile taken across the 'D-C-F-E' shown in fig.3.6 (c), reveals the nucleation point C as a central dark valley of ~ 20 nm depth. The 30-50 nm grains appearing as mounds grow around this point. The root mean square (rms) roughness within the agglomeration is 4.88 nm and within the grain is 1.17 nm.

The variation of average grain size, <D>, for the films obtained from $Cu(acac)_2$, determined from statistical analysis of different SEM images, is shown as a function of the deposition temperature in fig.3.7. At a low deposition temperature of 523 K, the average grain size is ~ 76 nm, with a small number of grains of sizes above 100 nm. With the increasing deposition temperature, an increasing number of larger grains is observed.

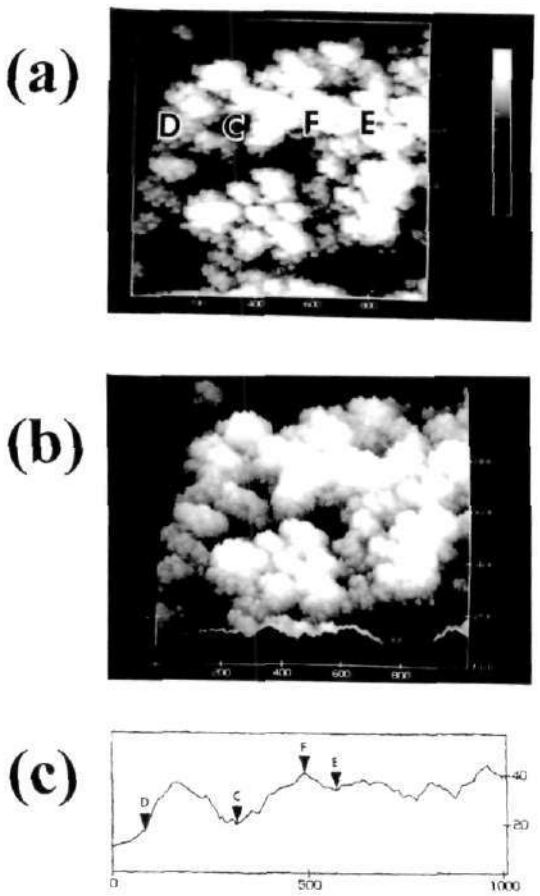

Fig.3.6 STM images of Cu films deposited on Si(100) substrates deposited at 673 K from $Cu(dpm)_2$, (a) topview, (b) surface-plot in 60° perspective and (c) line profile taken across 'D-C-F-E' as marked in (a) .

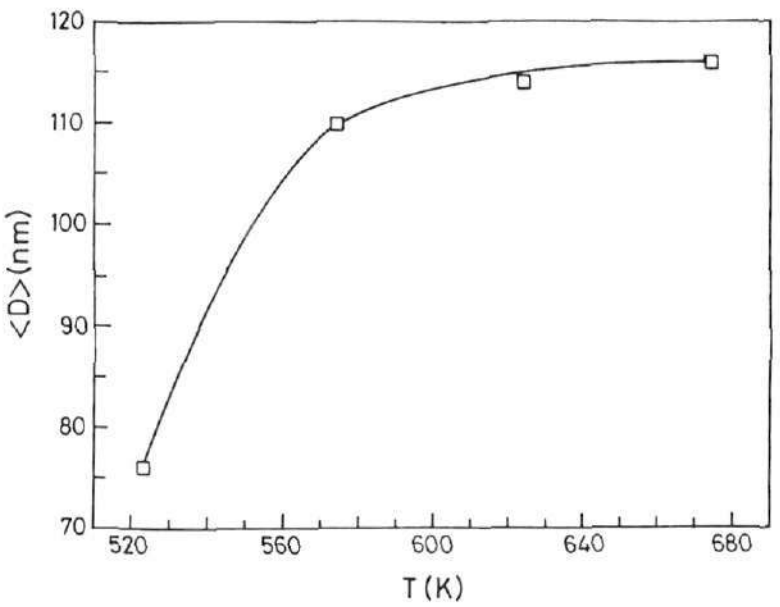

Fig.3.7 Variation of average grain size <D> with deposition temperature for Cu films deposited from $Cu(acac)_2$.

These grains grow at the expense of smaller grains and have sizes significantly above the main population of 70-80 nm grains. Thus, the observed average grain size increases with the deposition temperature. At deposition temperatures higher than 623 K, the size levels off to ~ 115 nm giving a bimodal grain size distribution. The observed saturation of average grain size at higher temperatures is due to the formation of new small grains at the different nucleation sites.

Growth Aspects

In view of the practical applications of copper films, the rate of film growth is a

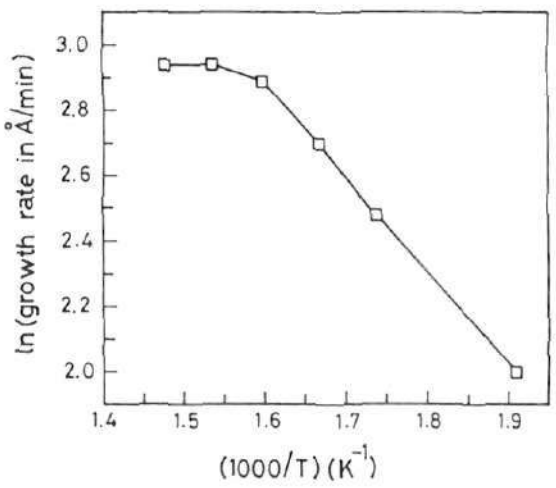

Fig.3.8 Arrhenius plot of growth rate versus deposition temperature of copper films deposited from $Cu(acac)_2$ on Si (100) substrates by nebulized spray pyrolysis.

vitally important parameter. The growth rate, d/t, of copper films from the different Cu precursors was estimated from the knowledge of the film thickness, d, attained in a known length of deposition time, t. We have compared the growth rates for the Cu depositions carried out under the similar experimental conditions such as the substrate temperature (673 K), precursor concentration (~1 mM) and the carrier gas (N_2/H_2) mixture flow rate (1 lit/min). The films from $Cu(acac)_2$ exhibited the highest growth rate of ~19 Å/min. The growth rate reduced to a low value of 3 Å/min for $Cu(hfac)_2$. In the case of $Cu(dpm)_2$, an intermediate growth rate of 14 Å/min was observed. The cause for

such differences in the growth rate of the films obtained from the different precursors is not clear at present. It is possible that the structure of the precursor molecule has some influence on the growth rate since bond breaking is essential before the metal film is deposited. It should be noted that the growth rates observed by us are smaller than the deposition rates of 200 to 400 Å/min required in real situations. In nebulized spray pyrolysis, the growth rate is determined by the concentration of the precursor, nebulized spray flow rate, carrier gas flow rate and the substrate temperature[21]. It should be possible to optimize these parameters to achieve higher growth rates.

Fig.3.8 shows the Arrhenius plot of the growth rate of the films deposited on Si(100) substrate using the $Cu(acac)_2$ precursor over the 523-673 K range. There is a linear relation over the most part of the temperature range, indicating thermally activated deposition kinetics. Around 650 K, the growth rate becomes nearly independent of the substrate temperature, suggesting the onset of diffusion-controlled growth. The activation energy, E_a, estimated from the linear segment of this plot using Arrhenius relation

$$G = A \, Exp(-E_a/RT) \qquad (1)$$

turns out to be ~ 90 kJ/mol. This value is comparable to the previously reported values of the activation energies for copper film growth by MOCVD[22,23].

Transport properties

The temperature dependence of the electrical resistivity of the films from $Cu(acac)_2$, $Cu(hfac)_2$ and $Cu(dpm)_2$ deposited under the similar deposition conditions (at 673 K) is presented in fig.3.9. All the films show metallic conduction in the 300 K-50 K range. The room temperature resistivity value is lowest (9.3 μΩcm) for the films deposited from

$Cu(dpm)_2$. This is close to the Cu films deposited by low pressure MOCVD[24], but higher than the 1.67 μΩcm value of bulk copper.

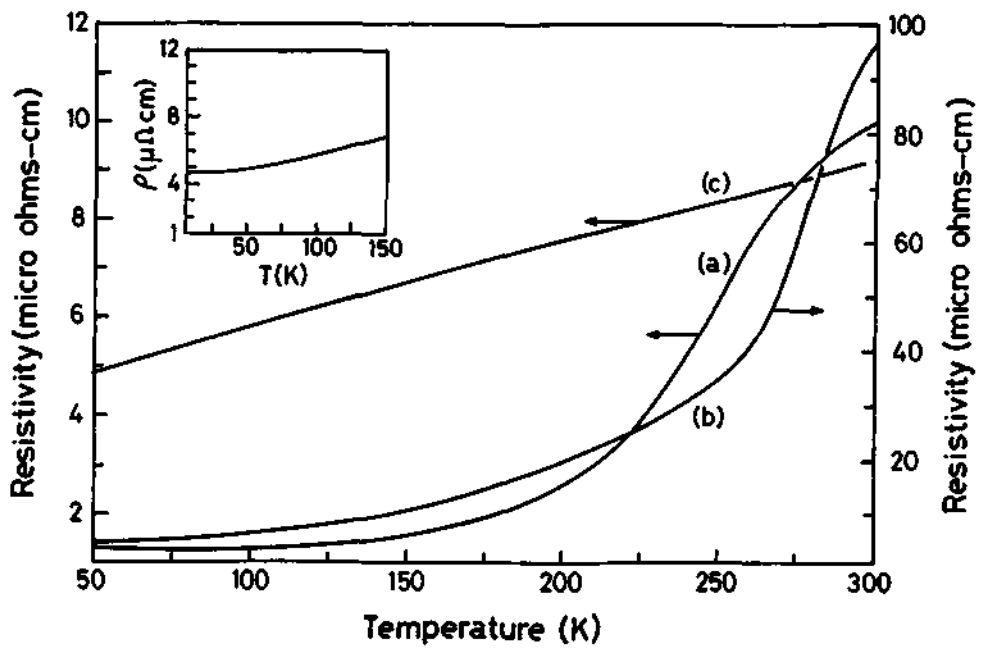

Fig.3.9 Variation of resistivity with temperature for copper films at 673 K from (a) $Cu(acac)_2$ (b) $Cu(hfac)_2$ (c) $Cu(dpm)_2$. Inset shows data (up to 4.2 K) of Cu films from $Cu(dpm)_2$.

The resistivity of the films from $Cu(hfac)_2$ is nearly two orders of magnitude larger than that for the films from $Cu(dpm)_2$ or $Cu(acac)_2$. On the basis of the structural and morphological aspects of the films deposited from the three precursors, it is possible to relate the resistivity behavior to the crystallinity and the microstructure. Thus, the high resistivity of the Cu films derived from $Cu(hfac)_2$ is likely to be due to the poor intergrain connectivity and the porous microstructure. On the other hand, the dense, fine-grained and smooth morphology of the films from $Cu(dpm)_2$ and $Cu(acac)_2$ yielded significantly lower resistivities.

The mean free path of the conduction electrons is an important quantity in determining the electrical conductivity of metals. Its value depends on the degree of perturbation of the crystalline lattice by the thermal motion of the lattice and the structural defects. The mean free path, l, of the electrons in the Cu films discussed here was obtained using the Drude relation:

$$l = [(mv_f)/(n_e e^2 \rho)] \qquad (2)$$

where e is the electronic charge, m its mass, n_e is the electron density in pure bulk copper ($8.47 \times 10^{22}/cm^3$), v_f is the fermi velocity of electrons in copper (1.57×10^8 cm/s) and ρ is the observed resistivity. The different electrical characteristics including the mean free paths of the films are listed in table I. The films derived from different precursors exhibit a positive temperature coefficient of resistivity (TCR). The TCR was obtained using equation

$$TCR = (1/\rho_1)[(\rho_2-\rho_1)/(T_2-T_1)] \qquad (3)$$

Here, ρ_1 and ρ_2 are the resistivities of the film at temperatures T_1 and T_2 respectively. The TCR value for pure copper metal is $2.91K^{-1}$, for bulk copper wire it is $0.0907\ K^{-1}$ and for copper films obtained from $Cu(dpm)_2$, it is 3.4×10^{-3} (at T_1=4.2 K, T_2=300 K)[14]. The TCR values obtained for the films from all the three precursors is presented in Table 1. Although the films deposited from $Cu(hfac)_2$ show porous morphology with a void structure, it is not a discontinuous film as reflected in its positive TCR value. For discontinuous films with islands, negative TCR is generally observed [24].

The residual resistivity ratio (RRR) defined as the ratio of the resistivity at 300 K to that at 4.2 K (i.e.$\rho_{300\ K}/\rho_{4.2\ K}$), is taken to be a direct measure of the quality of the metal films. We have carried out the low temperature measurements down to 4.2 K for the

films from $Cu(dpm)_2$ which showed the best resistivity behavior in this work (see inset of fig.3.9.). The RRR value for these films is 2, which compares well with the value for the films obtained from MOCVD[24]. Pure copper exhibits a RRR of 862.5 (calculated

Table 1 Properties of Cu/Si(100) films prepared by using different precursors.

Sample	$\rho_{(50K)}$ $\mu\,\Omega$cm	$\rho_{(300K)}$ $\mu\,\Omega$cm	$\iota_{(50K)}$ nm	$\iota_{(300K)}$ nm	TCR_{obs} (300K-50K)
Cu/Si(100) from $Cu(acac)_2$	1.3	10.7	49	6	2.8×10^{-2}
Cu/Si(100) from$Cu(hfac)_2$	9.3	98.5	7	1	3.8×10^{-2}
Cu/Si(100) from $Cu(dpm)_2$	4.9	9.3	14	7	3.6×10^{-3}
Cu/Si(100) from $Cu(dpm)_2$	4.65 ($\rho_{4.2K}$)	9.3	14	7	3.4×10^{-3} (300K-4.2K)
Cu wire	0.06 ($\rho_{4.2K}$)	1.67	1098	39.7	9.07×10^{-2} (300K-4.2K)

using resistivity values taken from CRC Handbook of Chemistry and Physics, 78th Edition, 1997-98) and for copper wire, it is 27.8. Copper films exhibiting near bulk resistivities and high RRR value have been deposited by PVD methods[25,26].

According to Matthiessen's rule, the resistivity of metals can be considered to be sum of a residual non-thermal component, ρ_o, and a thermal component, ρ_T:

i.e., $\rho_{total} = (\rho_o + \rho_T)$ (4)

Assuming $\rho_{4.2\,K} \approx \rho_o$, the temperature dependent part of resistivity of the Cu films from $Cu(dpm)_2$ is 4.65 $\mu\Omega$-cm. For bulk copper wire, this contribution is ~ 1.61 $\mu\Omega$-cm, which arises only from electron-phonon interaction. The deviation from Matthiessen's rule possibly arises from enhanced electron-phonon interactions. The high resistivity of the films compared to bulk copper can arise from (i) grain-boundary scattering (ii) surface

scattering (iii) defect scattering and (iv) impurity scattering. Typical contributions to the resistivity from the plane defects are reported to be ~ 3.1 x 10^{-8} μ Ω-cm per stacking fault and ~ 1 x 10^{-7}μ Ω-cm per twin[27,28]. As the densities of such defects in the polycrystalline metal films are of the order of 10^5 per cm^3 or less, these together have little effect on the observed resistivity[29]. Vacancies also do not influence the resistivity in a discernible manner, with a typical vacancy density of ~ 10^{-8} at 300 K[30].

The Cu films deposited from $Cu(dpm)_2$ are polycrystalline although there is high preferred (111) orientation. These contain grains of ~ 40 nm as observed in the STM images. The extent to which the resistivity is increased by grain-boundary scattering depends on the average grain size and the quality of the film. On the basis of the Mayadas-Shatzkes (MS) grain-boundary scattering model[31], the resistivity data can be analyzed by considering the influence of only the grain-boundary scattering on the excess of resistivity, assuming the Fuch's specularity parameter, p=1[32]. The grain boundary enhanced resistivity is given by:

$$\rho_{gr}(T) = [\rho_{\infty}(T)/ f(\alpha)] \quad (5)$$

where, $f(\alpha) = [1-(3/2)\alpha + 3\alpha^2 -3\alpha^3 \ln\{1+(1/\alpha)\}]$ (6)

and $\alpha = [\{l_{\infty}(T)/\langle D\rangle\}\{R/(1-R)\}]$ (7)

$$\rho_F = [(1/\rho_{gr})- \{(1/\rho_0)*A\}]^{-1} \quad (8)$$

with $A = (6 / \Pi*k)(1-p)\int_0^{\Pi/2} d\phi \int_1^{\infty} \{\cos^2 \phi/H^2 (t, \phi)\}\{(1/t^3)- (1/t^5)\}[\{1- \exp\{-ktH(t, \phi)\}\}/\{1- \exp\{-ktH(t, \phi)\}\}]dt$

where p is the probality that an electron will be specularly reflected upon scattering from the film surface, k is the reduced film thickness (the film thickness a divided by the

electron mean free path l_0), t and ϕ are integration variables and the function $H(t, \phi)$ is defined by

$$H(t, \phi) = 1+ \alpha \cos^{-1}\phi(1-t^{-2})^{-1/2} \quad (9)$$

Hence

$$(\rho_F / \rho_{gr}) = \{1- (A/f(\alpha)\}^{-1} \quad (10)$$

and $$(\rho_F / \rho_\infty) = \{f(\alpha) - A\}^{-1} \quad (11)$$

In the above equations, $\rho_\infty(T)$ is the total resistivity of the pure bulk material at temperature T, <D> is the average grain diameter in the film, R is the reflection coefficient of electrons striking the grain boundaries ($0 \le R \le 1$). $l_\infty(T)$ is the mean free path of the bulk material at temperature T without the grain boundaries.

By using the limiting form of equation (6) for $\alpha \le 1$, $f(\alpha) = (1+3/2\ \alpha)$, the equation (5) can be written as

$$\rho_{gr}(T) = \rho_\infty(T) / [\ 1+ \{(3/2)l_\infty(T)/<D>\}\{R/(1-R)\}] \quad (12)$$

where $\rho_\infty(T)$ is the resistivity of pure copper metal at temperature (T) and <D> (= 40nm) is the average grain size of copper film obtained from $Cu(dpm)_2$. Equation (12) can be written as

$$\rho_{gr}(T)<D>= \rho_\infty(T)<D> + [(3/2)l_\infty(T))\{R/(1-R)\}] \quad (13)$$

If 'd' is the thickness of the film and multiplying (13) by 'd/<D>' we get,

$$\rho_{gr}(T)(d) = \rho_\infty(T)(d) + [(3/2)l_\infty(T).\rho_\infty(T))\{R/(1-R)\}]\ (d)/<D> \quad (14)$$

In the above equation, the term $[(3/2)l_\infty(T).\rho_\infty(T))\{R/(1-R)\}](d)/<D>$ is the size effect induced grain boundary scattering. This value can be obtained from the plot of $\rho_{gr}(T)(d)$ verses (d) for different film thicknesses. The values of resistivities for films of 100, 125

and 155 nm thickness are 10.2, 9.8 and 9.3 μΩcm respectively for films obtained from $Cu(dpm)_2$. This plot gave the Y intercept as 0.26 x 10^{-6}μΩcm and slope as 7.63 μΩ cm. We have estimated the reflection coefficient, R as 0.398. The value of $l_\infty(T)$ is calculated from the knowledge of $(\rho l)_\infty$ and $\rho_\infty(T)$. The product $(\rho l)_\infty$ is assumed to have a constant value of 6.6 x 10^{-12} Ω cm ^{2} for bulk copper[24,31]. The values of α and f(α) are calculated from the equations (6) and (7) and are 0.142 and 0.829 respectively. The grain boundary resistivity ρ_{gr} is estimated from the equation (5) as 2.08 μΩ cm (by taking the ρ_∞ at 300 K for pure copper metal as 1.725 μΩ cm). The reported values of R range between 0.4-0.8 for Cu films obtained by the MOCVD technique[24]. A reflection coefficient of ~ 0.35 has been reported by Sambles et al[33] for (111) oriented Au films deposited by the PVD method. It appears that the more dense, smooth and preferentially (111) oriented microstructure of the Cu film deposited from $Cu(dpm)_2$ gives a low R value. We have not attempted to estimate exactly the surface scattering contribution to resistivity. There seems to be a definite contribution due to this mechanism as the film shows deviation from Matthiessen's rule. In the light of the above discussion, the high resistivity of Cu film from $Cu(dpm)_2$, relative to bulk Cu arises from the combined effect of surface scattering and impurity scattering. We believe that the impurity scattering term could be significant as the RRR observed for this film is quite low (~2). We have however not estimated the impurity scattering contribution.

The ambient stability of the Cu films deposited from different precursors was evaluated by studying the changes in their room temperature resistivity (ρ_{300K}) with the duration of film exposure to the ambient atmosphere. The maximum duration of exposure

was 72 hours. The results are shown in fig.3.10 where the solid lines shown are the best fits of the observed data

$$\log(\rho_f) = [A + B\,t] \qquad (15)$$

From fig.3.10, we see that all the films exhibit a linear increase in the logarithm of resistivity with the duration of exposure. The slope of such a plot can be taken as the rate of degradation of these films i.e., the fit parameter B can be treated as a rate constant to compare the relative stability of the films. Accordingly, the rate constants for the films from $Cu(acac)_2$, $Cu(hfac)_2$ and $Cu(dpm)_2$ on Si(100) substrates are 0.011, 0.016 and 0.007 sec^{-1} respectively. The films from $Cu(hfac)_2$ show fastest degradation in contrast to

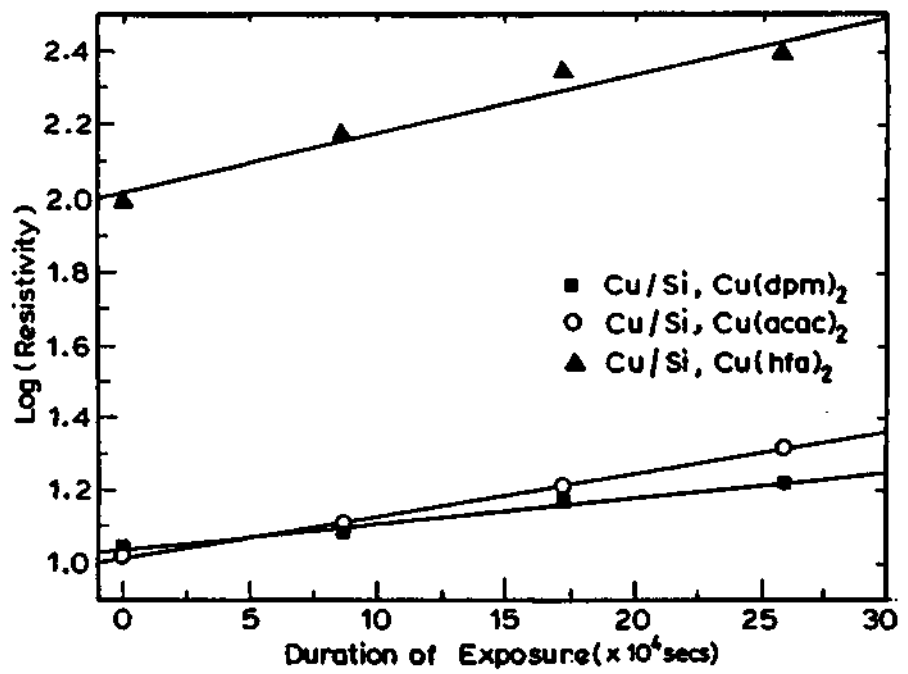

Fig.3.10 Variation of resistivity of as deposited Cu films at 673 K with duration of exposure in air.

those deposited from $Cu(acac)_2$ and $Cu(dpm)_2$. The films from $Cu(dpm)_2$ appear most stable for the range of exposure compared here, their rate constants being an order of magnitude different. The observed degradation is most likely due to the slow oxidation

of the film. It is likely that the presence of adsorbed contaminants and humidity from the ambient would affect the resistivity. It is noteworthy that the Cu films from $Cu(hfac)_2$ with a void structure and a porous surface morphology show the highest degradation.

3.4.2. Cobalt and Copper –cobalt alloy films

(a) Cobalt Films

The X-ray diffraction patterns of the Co films deposited from $Co(acac)_2$ on Si(100) and borosilicate glass at 598 K and 673 K are shown in fig.3.11. The XRD patterns are showing a polycrystalline nature with no indication of an oxide phase. The films deposited on Si(100) show a mixed fcc and hcp phase at 598 K but a fcc phase only at 673 K. On the other hand films deposited on borosilicate glass showed a mixed fcc and

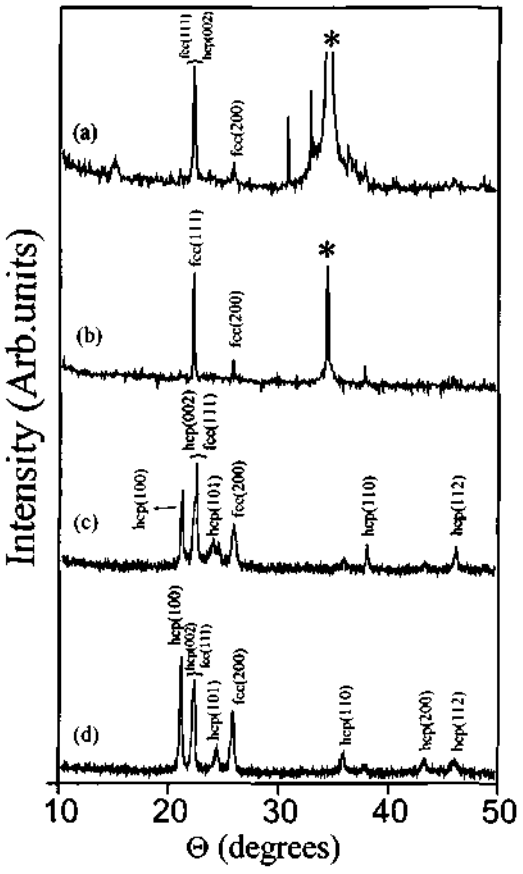

Fig.3.11 The X-ray diffraction patterns of Co films deposited on Si(100) substrates at (a) 598 K and (b) 673 K and on glass substrate at (c) 598 K and (d) 673 K `*`denotes Si(100) reflection.

hcp phases both the temperatures.

In order to conform the mixture of phases obtained at different temperatures SEM was done on the films. Fig.3.12 (a) and (b) shows SEM images of the films deposited on Si(100) and fig.3.12 (c) and (d) on borosilicate glass at 598 K and 673 K respectively. The films deposited on Si(100) at 598 K clearly reveal a needle shaped flaky morphology and granular morphology was observed for the films deposited at 673 K. The films deposited on glass show a granular and needle shaped flaky-type morphology at 598 K and 673 K respectively.

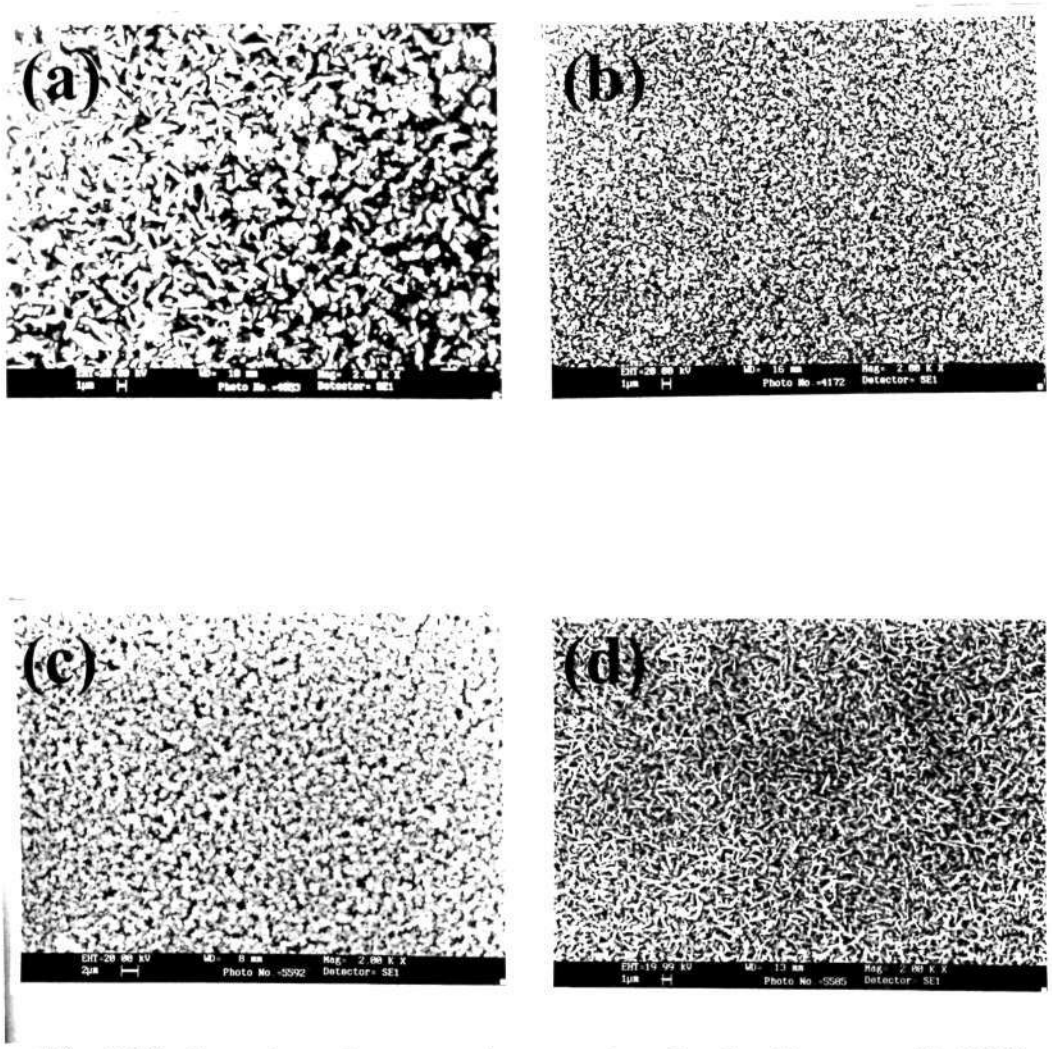

Fig.3.12 Scanning electron micrographs of Co films on Si (100) substrate at temperature (a) 598 K and (b) 673 K and on glass substrate at temperature (c) 598 K and (d) 673 K.

Electrical resistivity data of the Co films on the Si(100) and glass substrates deposited at 673 K are shown in figs.3.13 (a) and (b) respectively. The data clearly reveal the expected metallic behavior. The values of resistivity of the Co films on the Si(100)

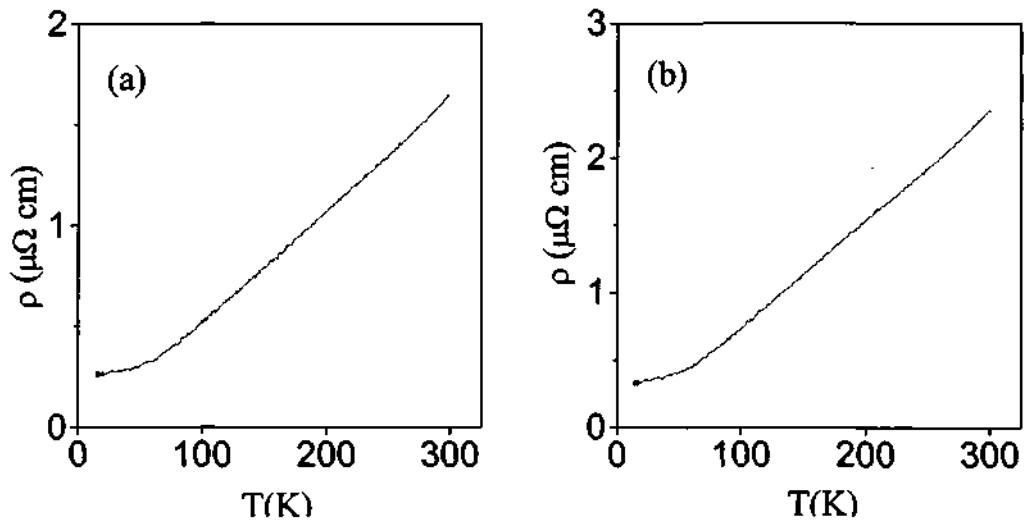

Fig.3.13 Electrical resistivity of Co films deposited at 673 K on (a) Si(100) and (b) Glass.

substrate at 300 K and 15 K are 1.646 μΩ cm and 0.258 μΩ cm respectively. The resistivity values of the films on the glass substrate are 2.347 μΩcm and 0.327 μΩcm at 300 K and 15 K respectively. The resistivity of the films on the glass substrate is somewhat higher probably because of the presence of mixed phases of Co. This low resistivity of the films on Si(100) is due to single fcc phase present.

Magnetic hysteresis loop measurements of the Co films on Si(100) and on glass substrates were recorded with the magnetic field parallel and perpendicular to the film. The results are shown in fig.3.14. The films deposited at 598 K gave good square loops when field is parallel to the film surface. The loops are not as good in the perpendicular direction as generally expected for films. The saturation magnetization values for the films deposited on Si(100) at 598 K are 30 emu/g and 21 emu/g in the parallel and

perpendicular directions respectively. For the films deposited on glass substrates, the saturation magnetization values are 65 emu/g and 53 emu/g respectively in the parallel and perpendicular directions.

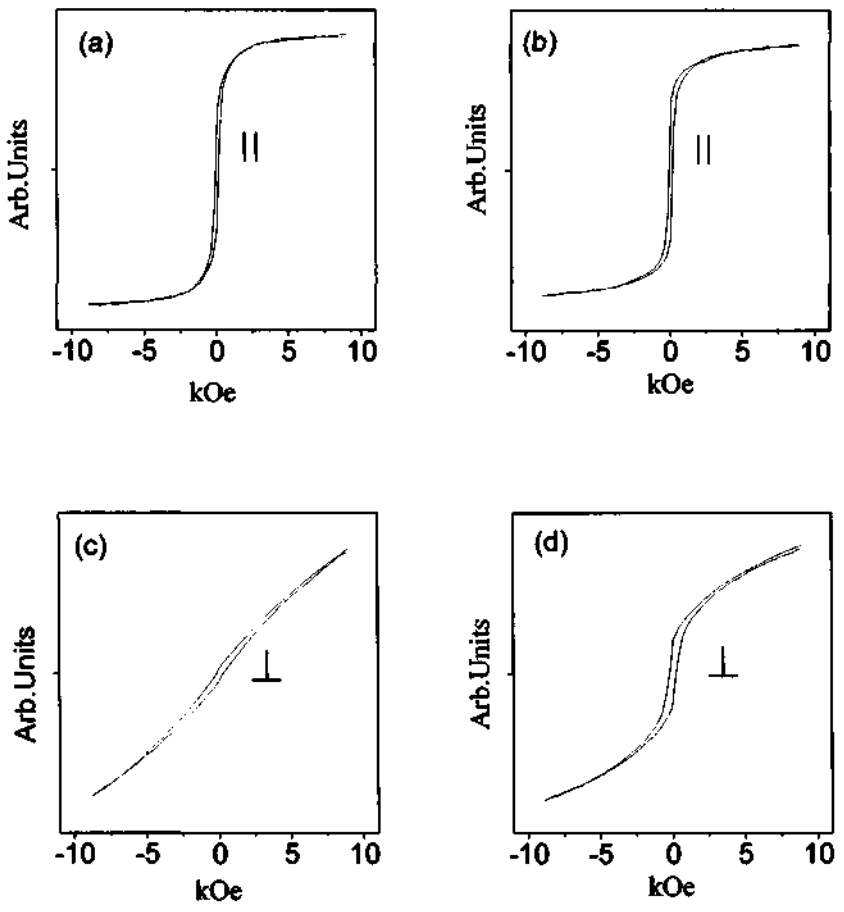

Fig.3.14 Magnetic hysteresis loops of Co films deposited at 598 K on Si(100) with field (a) parallel and (c) perpendicular; and on glass substrate with field (b) parallel and (d) perpendicular to the surface.

(b) Granular Cu-Co alloy films

In fig.3.15 (a) we show the X-ray diffraction pattern of the as-deposited films of $Cu_{82}Co_{18}$ at 673 K. On annealing the film in hydrogen at 923 K, we notice phase separation in the $Cu_{82}Co_{18}$ film as can be seen from the XRD pattern in fig.3.15 (b). In

the case of the $Cu_{50}Co_{50}$ composition, there is phase separation in the as-deposited film itself (at 673 K) as can be seen in fig.3.15 (c).

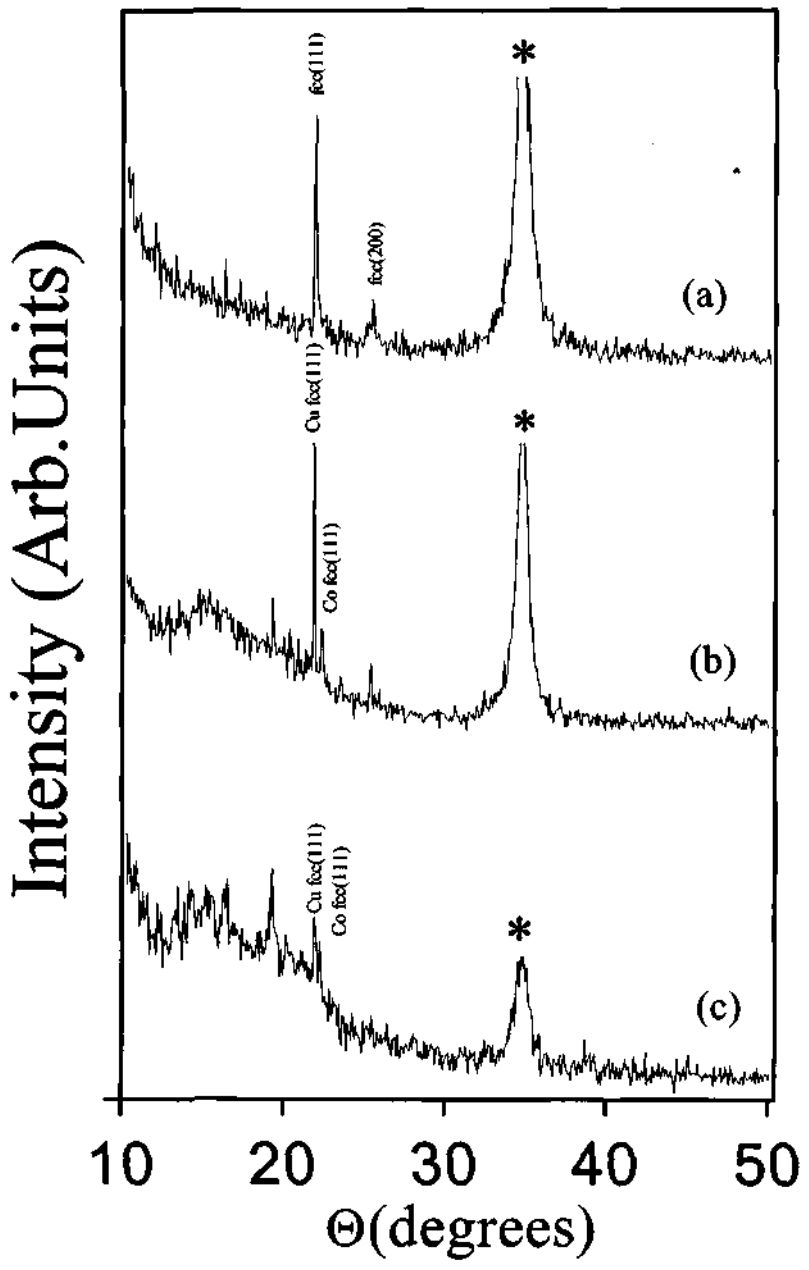

Fig.3.15 X-ray diffraction patterns of Cu-Co granular films deposited at 673 K (a) as-deposited and (b) hydrogen annealed at 923 K for the films of $Cu_{82}Co_{18}$ and (c) as-deposited film of $Cu_{50}Co_{50}$.* denotes Si(100) reflection.

Such phase separation on annealing $Cu_{82}Co_{18}$ is known in the literature[17].

Magnetic hysteresis loop measurements were carried out on the $Cu_{82}Co_{18}$ and $Cu_{50}Co_{50}$ films. In fig.3.16, we show typical hysteresis loops obtained with the $Cu_{50}Co_{50}$ film deposited on Si(100) at 673 K. The loops obtained with the field parallel and perpendicular to the film are both shown in the figure. In the parallel orientation, good square loops are obtained. The magnetization values for the $Cu_{50}Co_{50}$ film deposited at 673 K are 29 emu/g and 28.5 emu/g respectively with the field parallel and perpendicular to the film surface.

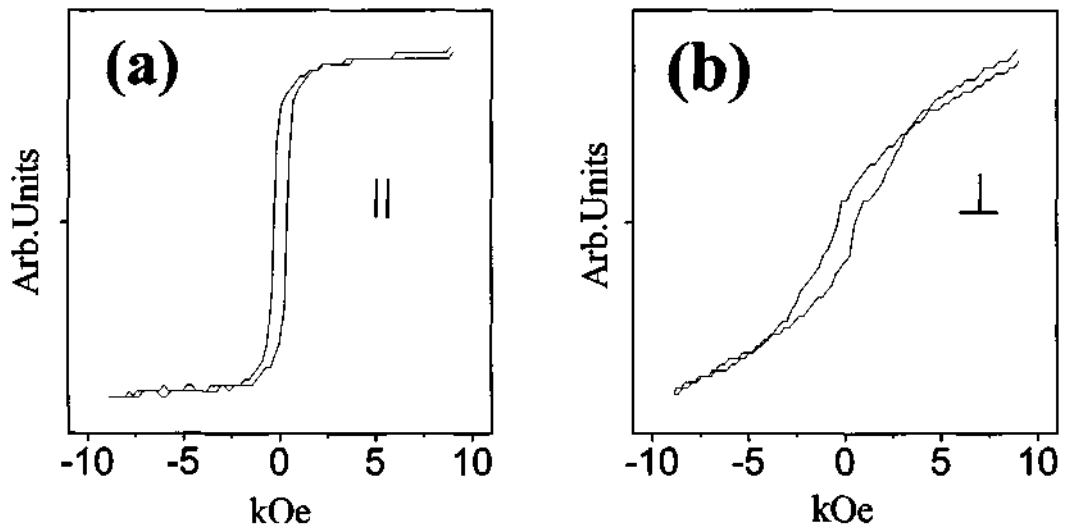

Fig.3.16 Magnetic hysteresis loops of $Cu_{50}Co_{50}$ film deposited at 673 K on Si(100) with field (a) parallel and (b) perpendicular to the surface of the film.

Magnetoresistance (MR) measurements were carried out on both the $Cu_{50}Co_{50}$ and $Co_{18}Cu_{82}$ films. The results are presented in fig.3.17. We have obtained MR of 0.28 % and 0.14% respectively for the $Cu_{50}Co_{50}$ and $Cu_{82}Co_{18}$ films at a field of 1.2 kOe at 300

K. This is quite satisfactory, considering that other workers have obtained around 3% MR at a field of 5 tesla or higher[18,19].

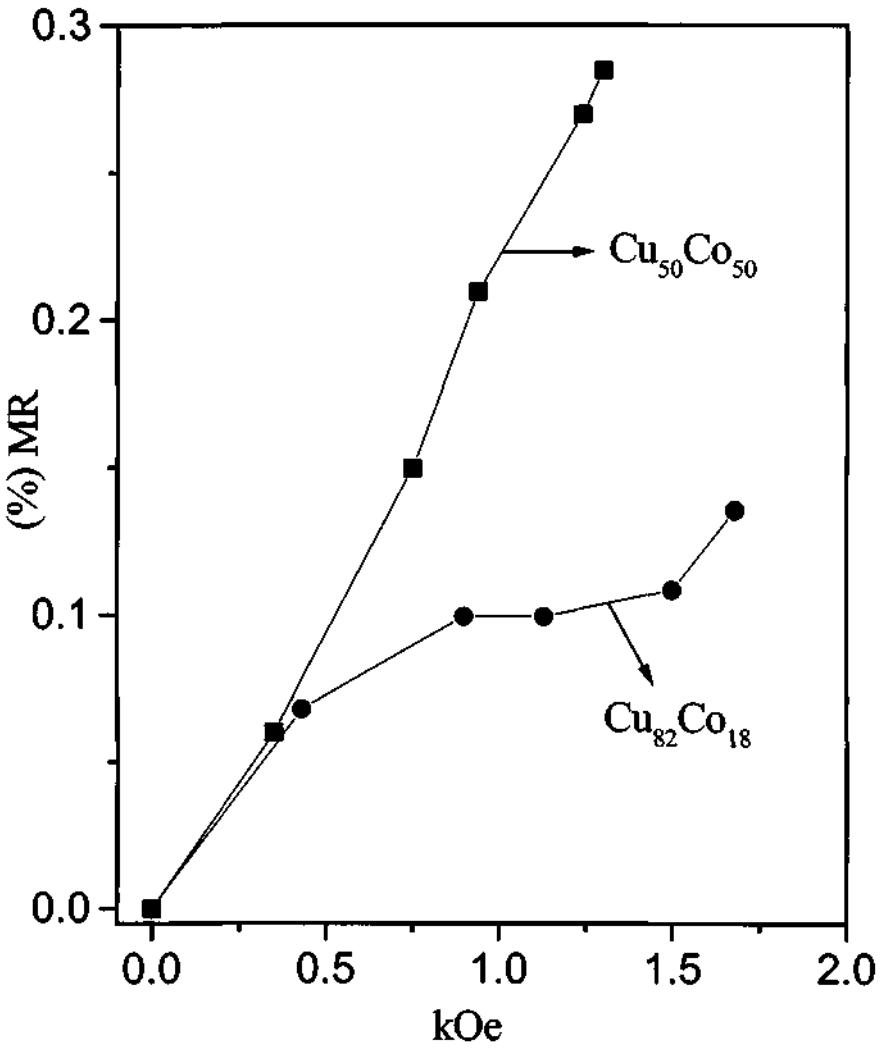

Fig.3.17 Field dependence of the magnetoresistance of the $Cu_{50}Co_{50}$ and $Cu_{82}Co_{18}$ films deposited at 673 K on Si(100).

3.5 References

1. Murarka S P and Hymes S W1995 CRC Crit. Rev. Solid State and Mater. Sci. **20** 87
2. Murarka S P, Gutmann R J, Kaloyeros A E and Lanford W A 1993 Thin Solid Films **236** 257
3. Shingubara S, Nakasaki Y and Kaneko H 1991 Appl. Phys. Lett. **58** 42
4. Li J, Blewer R and Mayer J W 1993 MRS Bulletin **18** 52
5. Hampden-Smith M J and Kodas T T 1993 MRS Bulletin **18** 39
6. Brayer J D, Swanson R M and Sigmon T W 1986 J. Electrochem. Soc. **133** 1242
7. Li J and Mayer J W 1992 Mater. Chem. Phys. **32** 1
8. Mausbach M, Ehrich H and Muller K G 1991 Mat. Sci. and Engineering **A 140**, 825
9. Thomas P A, Brodsky M H, Kaplan D and Lepine D 1978 Phys. Rev. B **18**, 3059
10. Yehoda J E , Yang B, Vedam K and Messier R J 1988 Vac. Sci. Technol. **A6**, 1631
11. Reynolds S K, Smart C J, Baran E F , Baum T H, Carlson C E and Brock P J 1991 Appl. Phys. Lett. **59**, 2332
12. Naik M B, Gill W N, Wentorf R H and Reeves R R 1995 Thin Solid Films **60**, 262
13. Chiang C M, Miller T M and Dubois L H 1993 J. Phys. Chem. **97**, 11781
14. Girolami G S, Jeffries P M and Dubois L H 1993 J. Am. Chem. Soc. **115**, 1015
15. Li M, Wang G C and Min H G 1998 J. Appl. Phys. **83**, 5313
16. Maruyama T 1997 Jpn. J. Appl. Phys. **36**, 6A, L705
17. Childress J R and Chien C L 1991 Phys.Rev. **B4**, 8089
18. Berkowitz A E, Mitchell J R, Carey M J, Young A P, Zang S, Spada F E Parker F T, Hutten A and Thomas G 1992 Phys. Rev. Lett. **68**, 3745

19. Berkowitz A E, Mitchell J R, Carey M J, Rao A P, Rao D, Starr A, Zang S Spada F E, Parker F T, Hutten A and Thomas G 1994 J. Appl. Phys. **73**, 5320

20. Wang W, Zhu F, Weng J, Xiao J and Lai W 1998 Appl. Phys. Lett. **72**, 1118

21. Langlet M and Joubert J C Chemistry of Advanced Materials, Edited Rao C N R, IUPAC 21st Century Monographs series, Blackwell Sci. Pub. Oxford, 1993, 55

22. Kim D J, Wentorf R H and Gill W N 1993 J. Electrochem. Soc. **140**, 3267

23. Yoen H Y, Park Y B and Rhee S W 1997 J. Mater. Sci.: Mater. in Electronics

24. Ramaswamy G, Raychaudhuri A K, Goswami J and Shivashankar S A 1997 J. Appl. Phys. **82**, 3797

25. Pai P L and Ting C H 1989 IEEE Elect. Dev. Lett. **10**, 423

26. Pai P L, Ting C H, Chiang C, Wei C S and Fraser D B 1990 Proceedings of the 1989 Workshop, Materials Research Society, Pittsburgh (PA) **359**

27. Siegal R W 1960 Philos. Mag. **13**, 337

28. Andrews P V, West M B and Robeson C B 1969 Phil. Mag. **19**, 887

29. Chopra K L, Suri R and Thakur A P 1977 J. Appl. Phys. **48**, 538

30. Rossiter P L and Bass J 1991 Materials Science and Technology eds. Cahn R W, Hansen P and Kramer E J (VCH Weinheim) **3A**, 257

31. Mayadas A F and Shatzkes M 1970 Phys. Rev. **B1**, 1382

32. Fuchs K 1938 Proc. Camb. Philos. Soc. **34**, 100

33. Sambles J R, Elsom K C and Jarvis D J 1982 Phil. Trans. R. Soc. London **A304**, 365

PART 4

INVESTIGATIONS OF SINGLE CRYSTALS OF RARE EARTH MANGANITES GROWN BY THE FLOATING ZONE MELTING CRYSTAL GROWTH TECHNIQUE

SUMMARY*

Rare earth manganites of the type $Ln_{1-x}A_xMnO_3$ where Ln is a rare earth and A is an alkaline earth have become known for a variety of fascinating properties such as colossal magnetoresistance (CMR), charge ordering (CO) and orbital ordering. Single crystals of manganites are necessary for many of the investigations on these materials. Single crystals of $Nd_{0.5}Ca_{0.5}MnO_3$, $Gd_{0.5}Ca_{0.5}MnO_3$, $Nd_{0.5}Sr_{0.5}MnO_3$ and $Nd_{0.45}Sr_{0.55}MnO_3$ were grown in this laboratory by the floating zone melting crystal growth technique and the crystals are characterized suitably. The crystals have been provided to coworkers for various studies.

Single crystals of $Nd_{0.5}Ca_{0.5}MnO_3$ show current-induced insulator-metal transitions at low temperatures. In addition, the charge-ordering transition temperature decreases with increasing current. The electroresistive ratio, defined as $\rho_{0.5}/\rho_I$ where $\rho_{0.5}$ is the resistivity at a current of 0.5 mA and ρ_I the resistivity at a given applied current, I, varies markedly with temperature and the value of I. Thermal hysteresis observed in $Nd_{0.5}Ca_{0.5}MnO_3$ at the insulator-metal transition indicates that the transition is first-order. The current-induced changes are comparable to those induced by magnetic fields.

*Based on this work the following papers have resulted: Europhys. Lett. (2000), J. Phys. D: App. Phys.(Communicated)

4.1 INTRODUCTION

An overview of the various aspects of rare earth manganites was presented in Part 1 of this thesis. For some of the studies on the charge ordered manganites, it is desirable to have single crystals. Good single crystals of manganites can only be prepared by the floating zone melting crystal growth technique. The technique involves melting of polycrystalline rods of the required material in hot zone and then cooling the melted system slowly by pulling it out of the hot zone in order to have crystal growth. Crystals of the following manganites were grown by floating zone melting crystal growth technique:

(a) $Nd_{0.5}Ca_{0.5}MnO_3$

(b) $Gd_{0.5}Ca_{0.5}MnO_3$

(c) $Nd_{0.5}Sr_{0.5}MnO_3$

(d) $Nd_{0.45}Sr_{0.55}MnO_3$

These crystals have been characterized by x-ray diffraction, electrical transport measurements and magnetization measurements (see section 4.3). The crystals have been used to carry out various studies. Thus, the crystals of $Nd_{0.5}Ca_{0.5}MnO_3$, $Nd_{0.5}Sr_{0.5}MnO_3$ and $Nd_{0.45}Sr_{0.55}MnO_3$ have been used for EPR studies. Brillouin Scattering studies have been carried out on crystals of $Nd_{0.5}Ca_{0.5}MnO_3$. A study of electrical properties has been carried out on crystals of $Nd_{0.5}Ca_{0.5}MnO_3$ and $Gd_{0.5}Ca_{0.5}MnO_3$. We have studied the effect of electric fields on single crystals of charge ordered $Nd_{0.5}Ca_{0.5}MnO_3$. The results of this study are presented in section 4.4.

4.2 EXPERIMENTAL

Single crystals were grown by the floating-zone furnace fitted with two ellipsoid halogen lamps (fig.4.1), having prepared the polycrystalline samples of the materials by the solid state route. Monophasic polycrystalline samples were hydrostatically pressed and sintered at 1400 ^{o}C for 24 hrs to obtain feed and seed rods of dimensions 8cm in length and 4mm in diameter. Single crystals were then grown under 2-3 l/min of airflow. The actuall process of growth is shown in fig.4.2. Fig.4.2 (a) shows the two rods when they have just started melting followed by fig.4.2 (b), which shows, as they are joined before the actuall growth is started. Fig.4.2 (c) shows when the rods are joint and crystal is being grown by pulling them downwards. The crystals thus obtained were cut and subjected to oxygen annealing for 48h. Magnetization data were obtained with a vibrating sample magnetometer operating between 300 - 50 K. Electrical resistivity measurements were carried out on crystal of dimension 4 mm in diameter and 1 mm in thickness by the standard four-probe method.

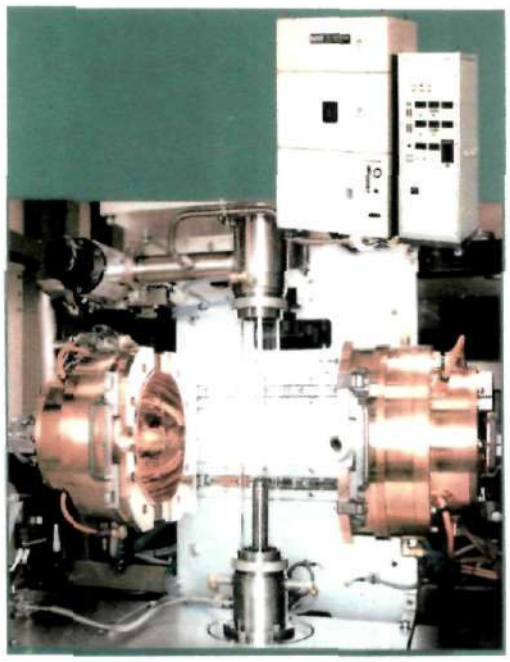

Fig.4.1 The floating zone melting crystal growth system.

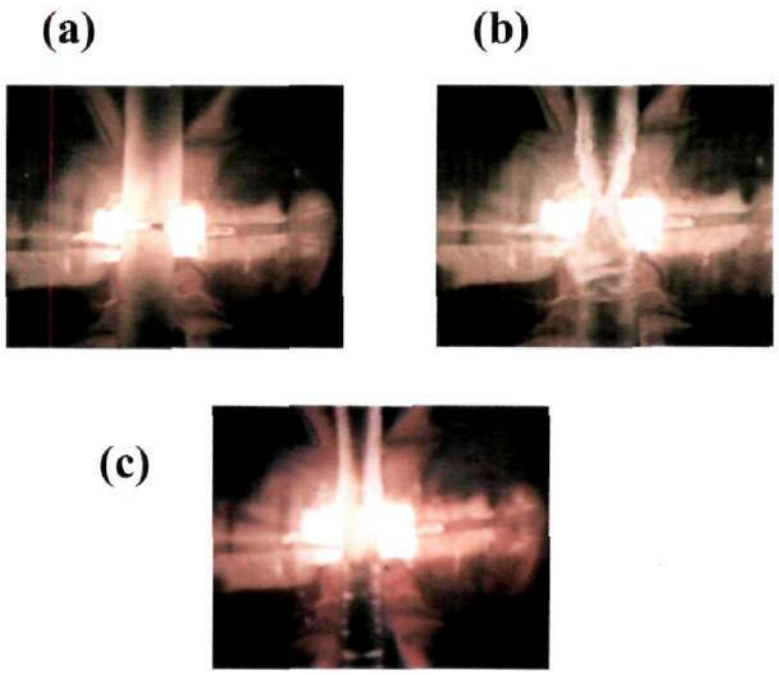

Fig.4.2 Different stages of growth of single crystals.

4.3 CHARACTERIZATION OF SINGLE CRYSTALS

$Nd_{0.5}Ca_{0.5}MnO_3$

Single crystals of $Nd_{0.5}Ca_{0.5}MnO_3$ {$<r_A>$ 1.17 Å} were grown in air by floating zone

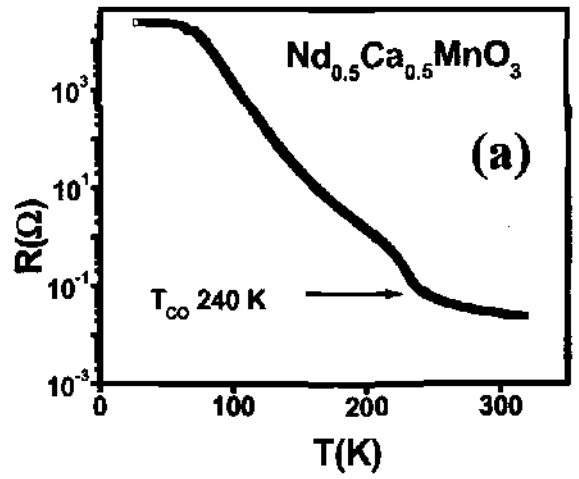

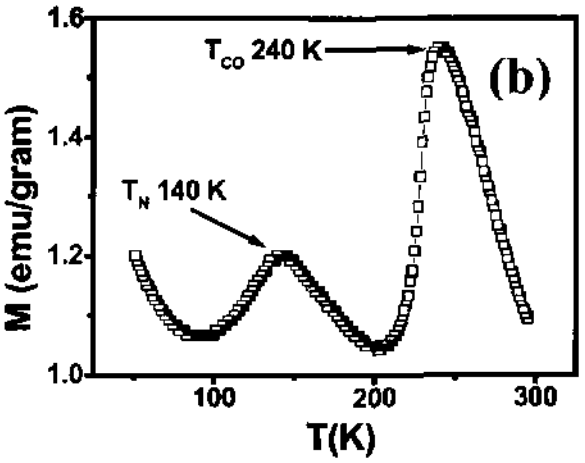

Fig.4.3 (a) Temperature variation of resistance of $Nd_{0.5}Ca_{0.5}MnO_3$ single crystal clearly shows the resistance jump at the charge ordering (T_{CO}) transition. (b) Magnetization of $Nd_{0.5}Ca_{0.5}MnO_3$ single crystal clearly shows the charge ordering (T_{CO}) and antiferromagnetic transition (T_N).

melting crystal growth technique. Later they were annealed at 900°C for 24 hrs to 48 hrs in oxygen atmosphere to have the correct Mn^{3+}/ Mn^{4+} ratio in the manganite. The magnetization and electrical transport properties of $Nd_{0.5}Ca_{0.5}MnO_3$ clearly shows the charge ordering transition (T_{CO} = 240 K) and the antiferromagnetic ordering (T_N = 140 K) in the system (fig.4.3)

Brillouin Scattering study of $Nd_{0.5}Ca_{0.5}MnO_3$ single crystals

Brillouin scattering studies on single crystals of charge ordered manganite $Nd_{0.5}Ca_{0.5}MnO_3$ were carried out by Murugavel et.al.(Europhys. Lett. 2000). The spectra show two modes at ~ 27 GHz (B-mode) and 60 GHz (S-mode). The B-mode frequency and intensity from 300 K to 27 K, covering both the charge ordering transition to 250 K and the antiferromagnetic transition, at 170 K, exactly follow the same temperature dependence as the dc magnetic susceptibility as shown in fig.4.4.

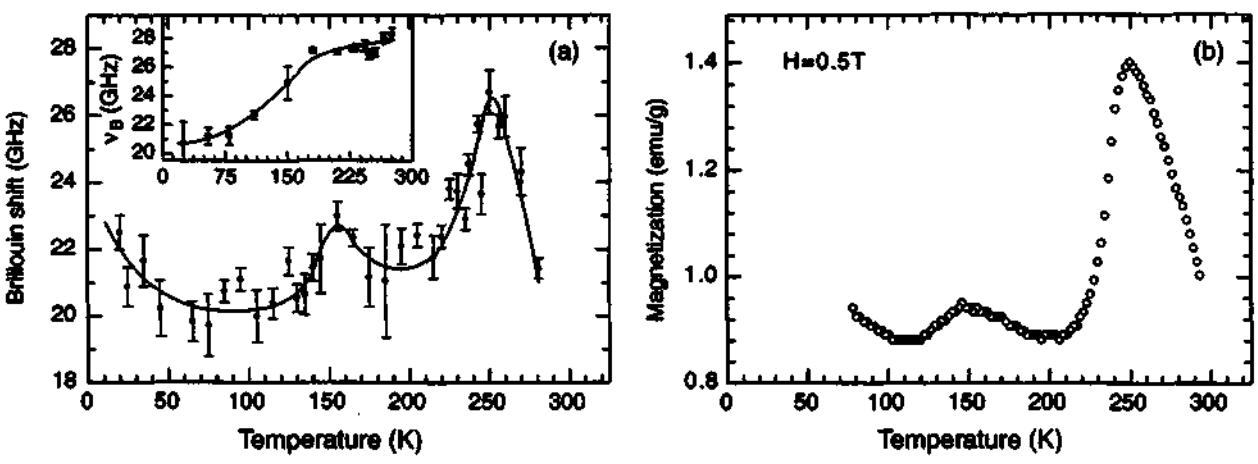

Fig.4.4 (a) Temperature dependence of the B-mode in the cooling cycle. The inset in (a) shows the temperature dependence of the B-mode in the heating cycle. (b) Temperature dependence of magnetization measured using vibrating sample magnetometer in a field of 0.5 T. The solid lines are drawn as a guide to the eye.

$Gd_{0.5}Ca_{0.5}MnO_3$

Single crystals of $Gd_{0.5}Ca_{0.5}MnO_3$ {$<r_A>$ 1.14 Å} were grown in air by floating zone melting crystal growth technique. Later they were annealed at 900°C for 24 hrs to 48 hrs in oxygen atmosphere to have the correct Mn^{3+}/ Mn^{4+} ratio in the manganite. The

magnetization and electrical transport properties of $Gd_{0.5}Ca_{0.5}MnO_3$ clearly shows the charge ordering transition (T_{CO} = 260 K) in the system (fig.4.5)

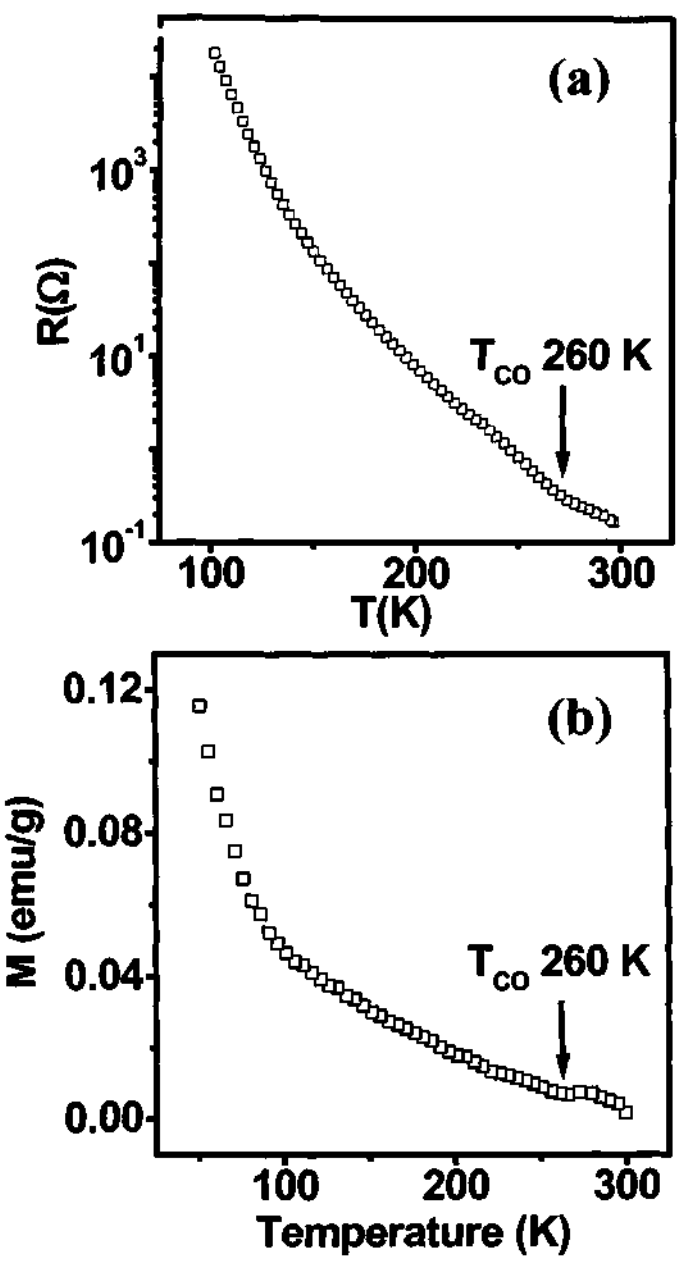

Fig.4.5 (a) Temperature variation of resistance of $Gd_{0.5}Ca_{0.5}MnO_3$ single crystal clearly shows the charge ordering transition (T_{CO}). (b) Magnetization of $Gd_{0.5}Ca_{0.5}MnO_3$ single crystal clearly shows the charge ordering transition (T_{CO}).

$Nd_{0.5}Sr_{0.5}MnO_3$

Single crystals of $Nd_{0.5}Sr_{0.5}MnO_3$ {$<r_A>$ 1.24 Å} were grown in air by floating zone melting crystal growth technique. Later they were annealed at 900°C for 24 hrs to 48 hrs in oxygen atmosphere to have the correct Mn^{3+}/ Mn^{4+} ratio in the manganite. The magnetization and electrical transport properties of $Nd_{0.5}Sr_{0.5}MnO_3$ clearly shows the ferromagnetic ordering transition (T_C = 260 K) and the charge ordering antiferromagnetic ordering transition (T_{CO} = 150K) in the system (fig.4.6). EPR studies are being carried out on these crystals.

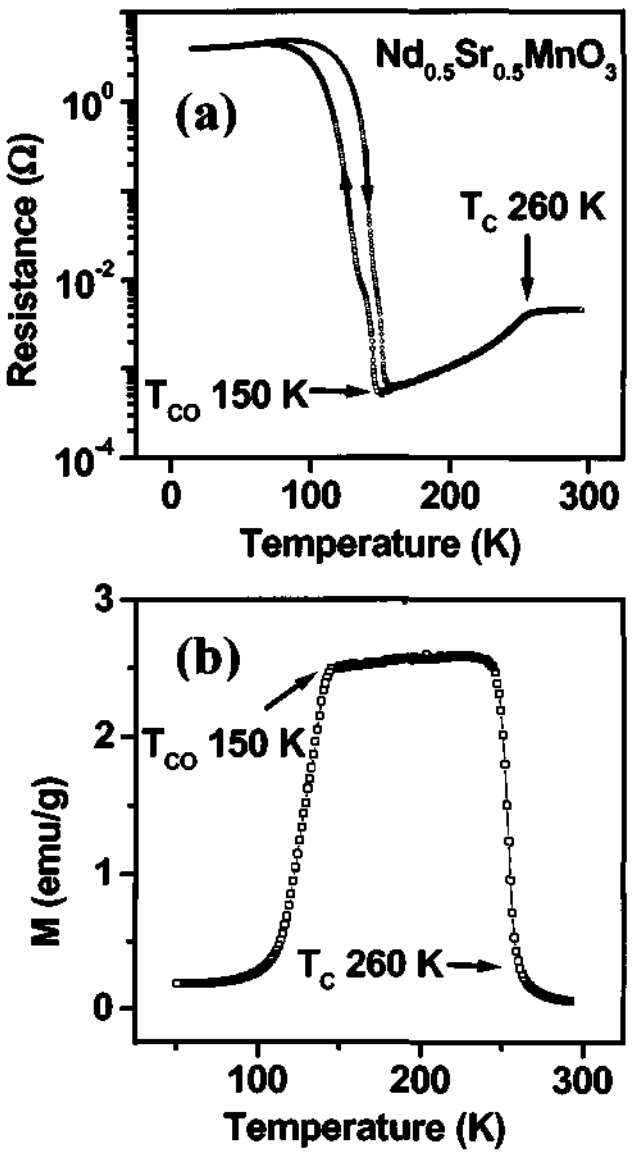

Fig.4.6 (a) Temperature variation of resistance of $Nd_{0.5}Sr_{0.5}MnO_3$ single crystal clearly shows the ferromagnetic transition (T_C) and charge ordering transition (T_{CO}). (b) Magnetization of $Nd_{0.5}Sr_{0.5}MnO_3$ single crystal clearly shows the ferromagnetic transition (T_C) and the charge ordering transition (T_{CO}).

$Nd_{0.45}Sr_{0.55}MnO_3$

Single crystals of $Nd_{0.5}Sr_{0.5}MnO_3$ {<r_A> 1.22 Å} were grown in air by floating zone melting crystal growth technique. Later they were annealed at 900°C for 24 hrs to 48 hrs

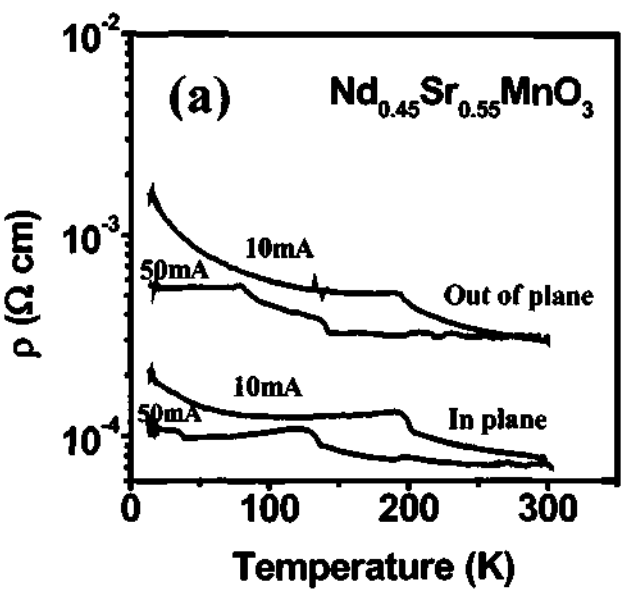

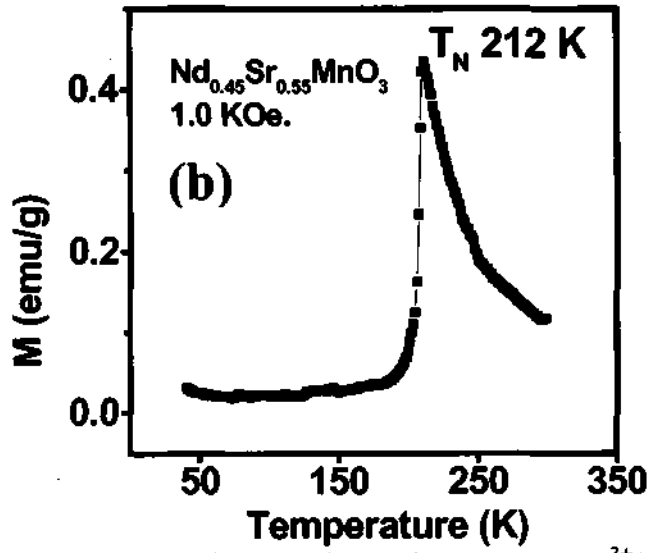

Fig.4.7 Temperature variation of resistance of $Nd_{0.45}Sr_{0.55}MnO_3$ single crystal clearly shows the antiferromagnetic transition (T_N) (b) Magnetization of $Nd_{0.45}Sr_{0.55}MnO_3$ single crystal clearly shows the antiferromagnetic transition (T_N).

in oxygen atmosphere to have the correct Mn^{3+}/ Mn^{4+} ratio in the manganite. The magnetization and electrical transport properties of $Nd_{0.5}Sr_{0.5}MnO_3$ clearly shows the A – type antiferromagnetic ordering transition (T_N = 210 K) in the system (fig.4.7). EPR studies are being carried out on these crystals.

4.4 Current-induced phase control in charged-ordered $Nd_{0.5}Ca_{0.5}MnO_3$ crystals*

In fig.4.8, we show the resistivity of a $Nd_{0.5}Ca_{0.5}MnO_3$ crystal at different applied currents when the sample is cooled from 300 K. There are four distinct features in the plot. There is a drop in the resistivity throughout the temperature range as the current, I, is increased. The temperature dependence of the resistivity changes with the increase in I. An insulator-metal transition occurs around 65 K (T_{IM}) at high values of I, beyond a

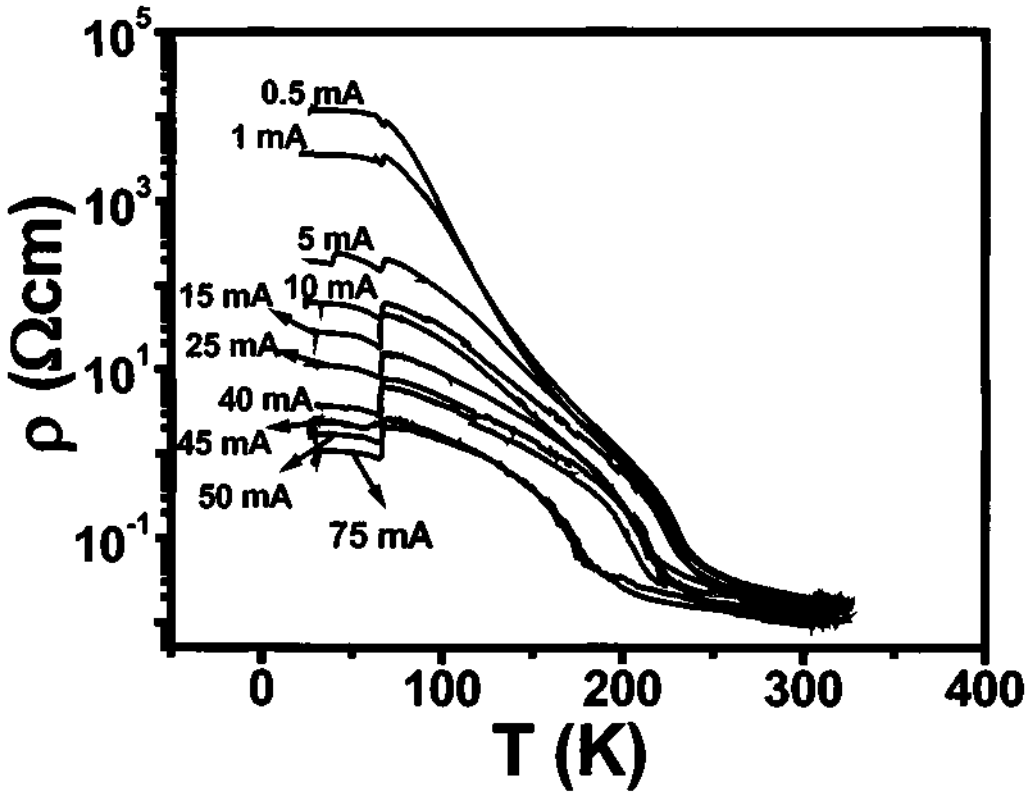

Fig.4.8 Temperature variation of resistivity of $Nd_{0.5}Ca_{0.5}MnO_3$ in cooling runs.

threshold value. The T_{co} shifts to lower values with increase in I and become constant beyond a high I value (~50mA). Such a current-induced shift in T_{CO} is indeed

* Background of this study can be found in Part 1 of the thesis

noteworthy. The plot of T_{co} against I is linear with a slope of ~1 K/mA as shown in fig.4.9. The decrease in the T_{co} could be due to the charge delocalization driven by external current , which in turn decreases lattice distortions.

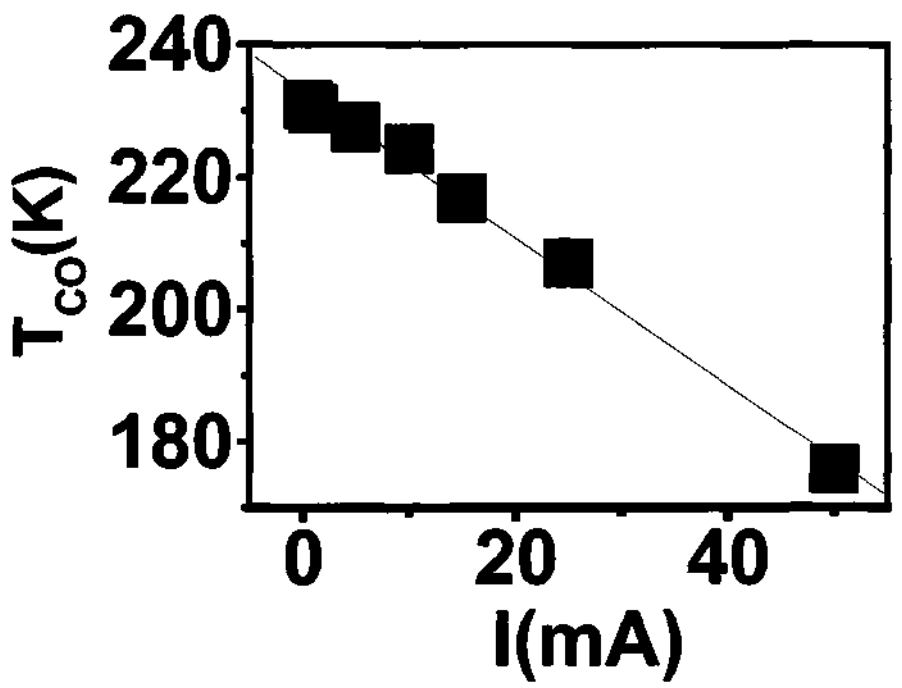

Fig.4.9 The variation of T_{co} with the applied current.

As the current through the $Nd_{0.5}Ca_{0.5}MnO_3$ crystal is increased, there is a drastic change in the resistivity. The $\rho_{0.5}/\rho_I$ ratio where $\rho_{0.5}$ is the resistivity at a current of 0.5 mA (which is the smallest I employed by us) and ρ_I the resistivity at a given applied current, I, may be considered to represent the electroresistive ratio analogous to the magnetoresistive ratio. In fig.4.10 we show the temperature variation of $\rho_{0.5}/\rho_I$ for different I values. The change in resistivity at low temperatures (~20 K) is four orders of magnitude while it is one or two orders at high temperatures ($T \approx T_{co}$). The four orders of

magnitude change in the resistivity is achieved by changing the applied current by two orders, indicating the non-ohmic behavior.

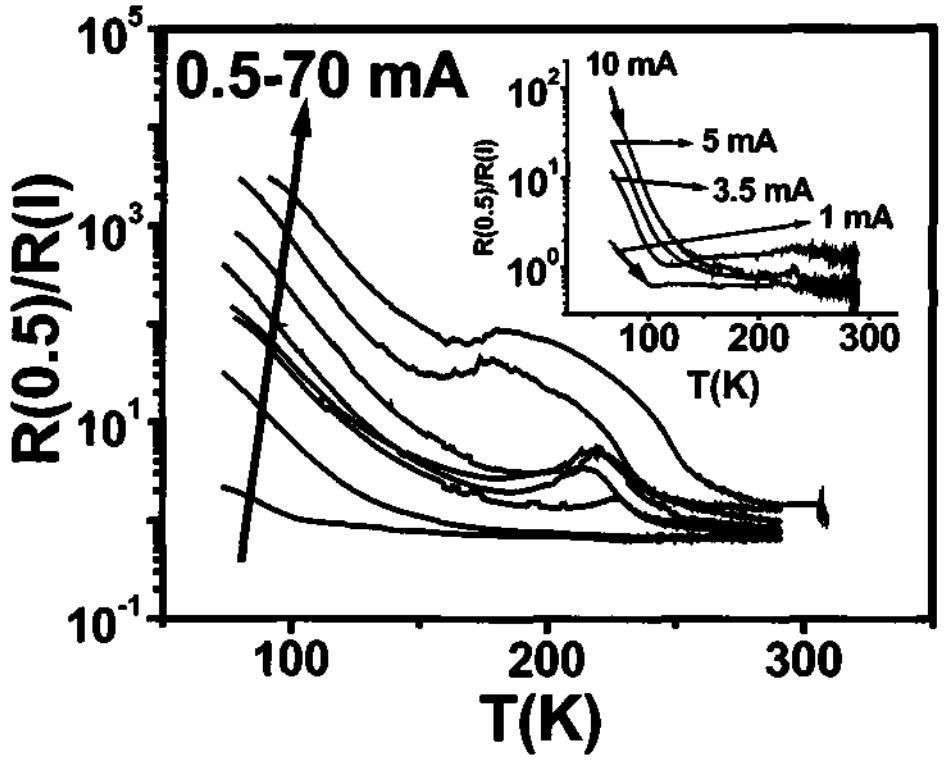

Fig.4.10 Variation of the electroresistive ratio with temperature in the cooling cycle. Inset shows the same in the heating cycle.

As the current is increased, we observe a sharp drop in resistivity of the sample at the insulator-metal transition temperature, T_{IM} (fig. 4.11) a behavior not noticed in earlier films. When the ρ-T data are recorded in the warming run without turning off the current, we observe a thermal hysteresis, which become prominent at large currents. The observation of hysteresis suggests a first-order nature of the structural change induced in the transition. In the warming run, the low resistive state persists down to a temperature T_W, lower than T_{IM} (fig.4.11). The resistivity change at T_W increases with the increasing current. Both T_{IM} and T_W are independent of the applied current as also the ratio of the

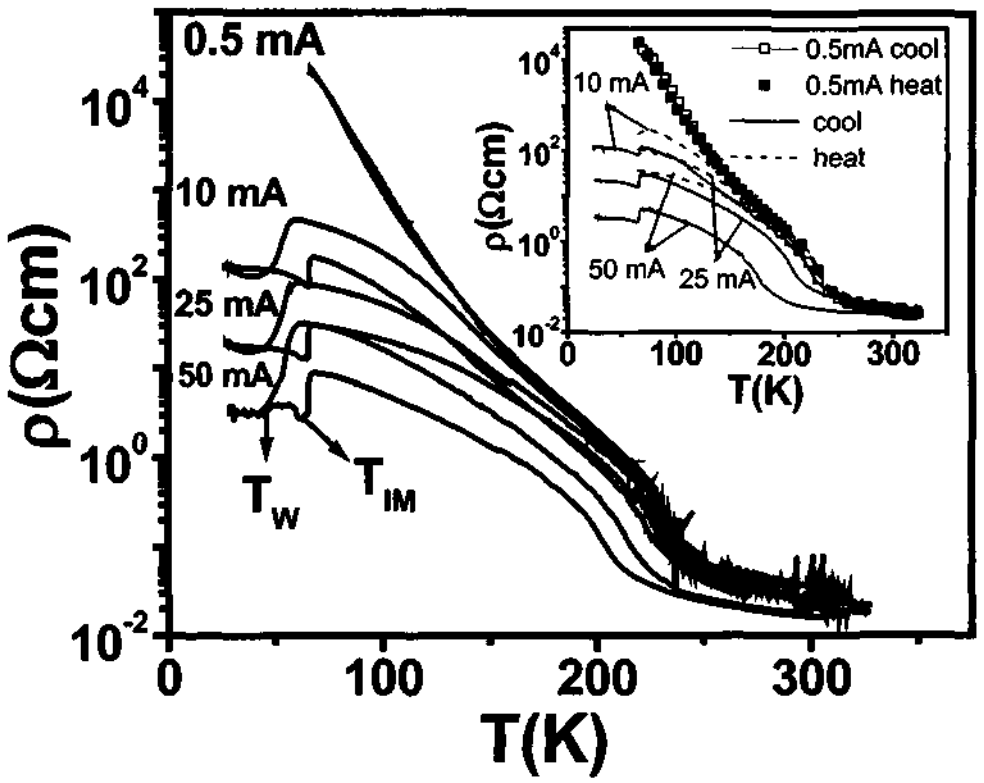

Fig.4.11 Temperature variation of resistivity of $Nd_{0.5}Ca_{0.5}MnO_3$ in the cooling and heating cycles, wherein the current is not switched off at the lowest temperature before starting the heating run. The inset shows the same with the current switched off and then switched on at the lowest temperature, before starting the heating run.

peak resistivity in the heating and the cooling runs. The inset of fig.4.11 shows the similar ratio for warming cycle. If one compares the change in the resistivity to the ratio of resistivities, the phenomenon is quite striking (fig.4.12). When the current is switched off at low temperatures, the current source is not able to pass the same current in the sample when the current is again switched on at the same low temperature due to voltage limit (V-Limit 105 V) of the source. This implies that the resistivity of the sample becomes high on switching off the current and the source meter is unable to pass the required current with the maximum voltage drop it can generate across the leads

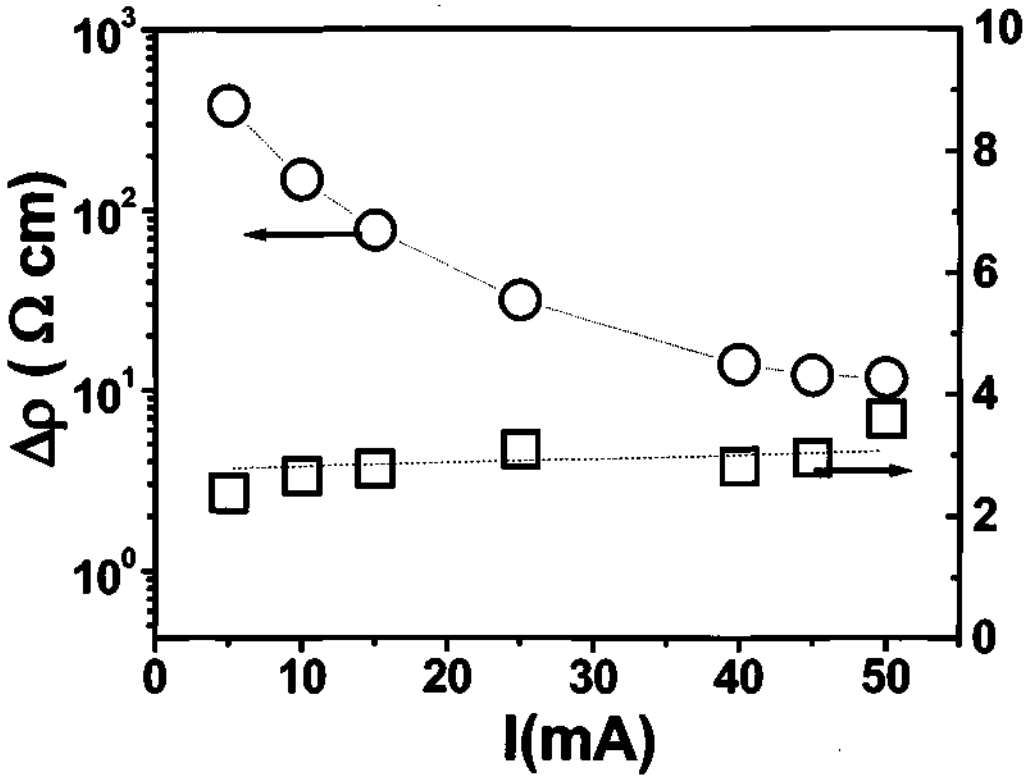

Fig.4.12 The squares represent the ratio of resistivities at the peak value in the cooling and heating runs with the current not switched off before starting measurements at the lowest temperature. Open circles represent the difference in the peak values of resistivity.

(which was possible before switching off the current). The effect of the current in the warming run is quite different from that in the cooling run, the resistivities in the former being higher. Although the resistivity of the sample has field dependence, all the ρ-T curves merge around 150 K above which the current has little effect (fig.4.11). This is in stark contrast to the cooling run data.

Based on these observations we have proposed a small model for this current induced low resistive states and shift of T_{CO} to lower temperatures. The schematic of the proposed mechanism is shown in fig.4.13. As we see from fig.4.13 (a) for a pure compound having only Mn^{3+} or Mn^{4+}, there is a completely symmetrical arrangement of

the octahedra leading to no lattice strain in the system. As we start doping the pure material, Mn^{3+} or Mn^{4+} ions get generated depending on the pure material and their ratio is determined by the amount dopant material (fig.4.13 (b)). The Mn^{3+} ion is a Jahn-Teller (JT) ion, and the corresponding distortions of MnO_6 octahedra is elongated as shown in fig.4.13 (b). This controls the lattice strain field, which in turn controls the charge ordering, and orbital ordering in this system. Since Mn^{3+} ion is JT distorted, the Mn^{4+} ions experience a strain lattice field, which tends to localise the mobile charge carries as shown in fig.4.13 (b). At room temperature these octahedra have sufficient thermal energy, so that they can rotate and tilt in order to relax the system and keep the strain at minimum. But as we start cooling the material this motion of octahedra gets frozen due to decreasing thermal energy at low temperatures. This results in increase in the lattice strain field, which in turn leads to localisation of electrons and high resistance to the material. At a particular temperature i.e. the charge ordering temperature T_{CO} there is a jump in the resistance of the material due to intense lattice strain field (fig.4.13 (c)). As we apply electric field to this material, there is an increase in the number of charge carriers due to inverse spin valve effect (section 1.4.3) which in turn makes the system more dynamic, as the electrons are moving from Mn^{3+} to Mn^{4+}. Due to this dynamicness of the system the lattice strain field gets relaxed and the resistance falls down (fig.4.13 (d)).

If we cool the system from room temperature in the presence of a electric field, the amount of lattice strain field is reduced and the material does not gets charge ordered at the normal charge ordering temperature, leading to shift of the charge ordering towards

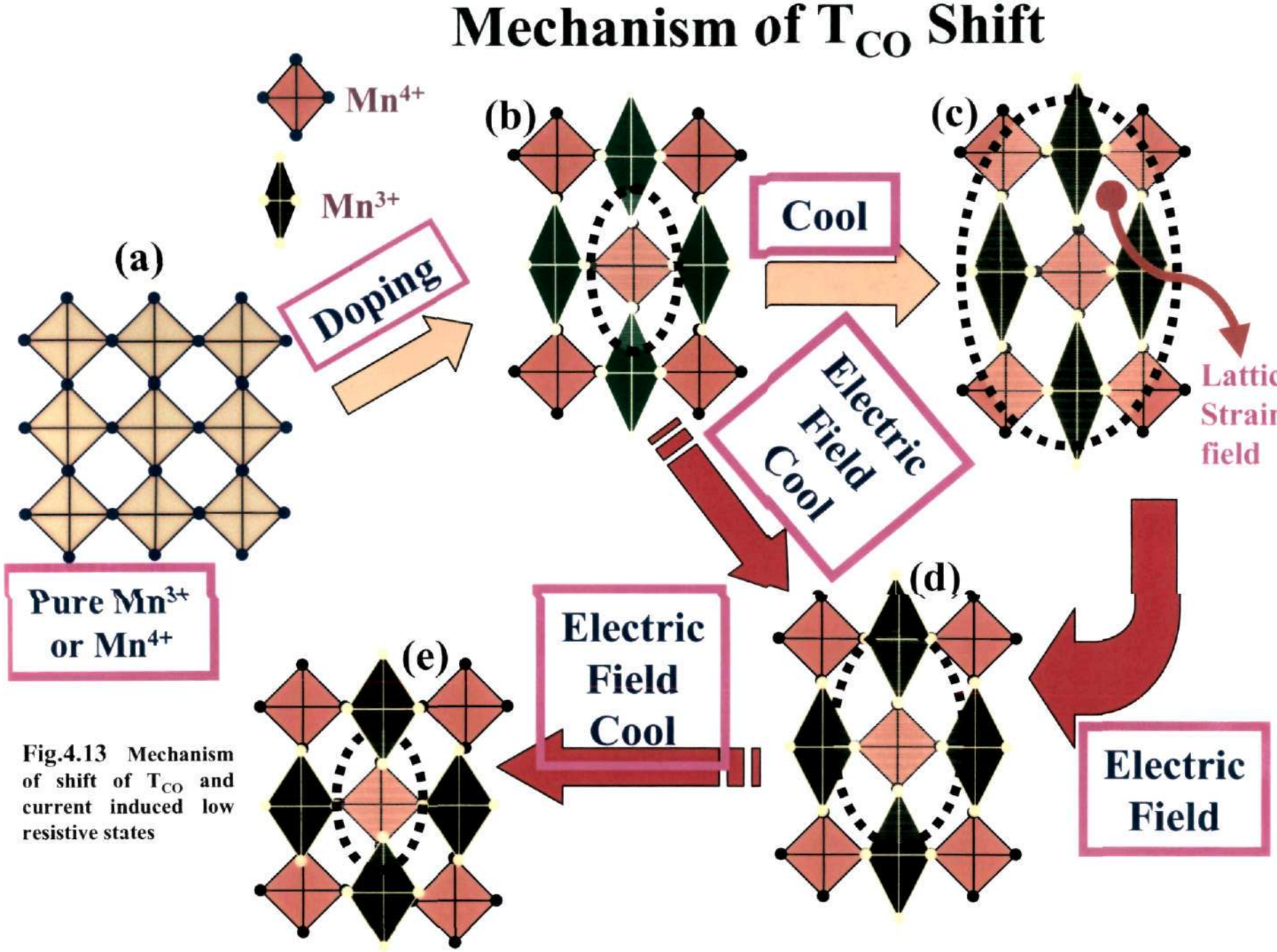

Fig.4.13 Mechanism of shift of T_{CO} and current induced low resistive states

low temperature (fig.4.13 (d)). On further application of electric field the lattice strain field is further decreased and the resistance falls further (fig.4.13 (e)).